Ground vehicle platoons: aerodynamics and flow control
An experimental and computational investigation

Craig Nolan

Submitted in fulfilment of the requirements for the
Degree of Doctor of Philosophy

James Watt School of Engineering
College of Science and Engineering
University of Glasgow

February 2023

Declaration

I certify that the thesis presented here for examination for PhD degree of the University of Glasgow is solely my own work other than where I have clearly indicated that it is the work of others (in which case the extent of any work carried out jointly by me and any other person is clearly identified in it) and that the thesis has not been edited by a third party beyond what is permitted by the University's PGR Code of Practice.

I declare that the thesis does not include work forming part of a thesis presented successfully for another degree.

I declare that this thesis has been produced in accordance with the University of Glasgow's Code of Good Practice in Research.

I acknowledge that if any issues are raised regarding good research practice based on review of the thesis, the examination may be postponed pending the outcome of any investigation of the issues.

Signature: Craig Nolan Date: February 2022

Abstract

Road transport contributes approximately 20% to the United Kingdom's greenhouse gas emissions, accelerating the effects of global warming. Since the United Kingdom, like many other countries, has pledged to reach net zero carbon emissions over the next two decades, reducing emissions from road vehicles has become a priority. A further adverse effect of road vehicle emissions is their link to serious health issues such as respiratory and cardiovascular diseases. To achieve the required substantial reduction in emissions, a multi-faceted approach will be required. In this project, one important aspect, the aerodynamics of ground vehicle platoons, is explored with the aim of expanding the understanding of road vehicle aerodynamics and exploring innovative solutions to improve road vehicle efficiency.

Vehicle platooning is a form of cooperative travelling in which vehicles drive closely together, with the intention to reduce overall air resistance, fuel consumption and vehicle emissions. Platooning, i.e., the cooperative movement of a group of individuals, is a concept that is not unique to road vehicles, but can be commonly observed in nature (e.g., a school of fish) or in sport (e.g., cyclists riding their bikes in a train). Here the trailing individuals take advantage of the sheltering provided by the leading individuals of the group. As a continuation of this observation, it would be natural to assume that road platooning is always beneficial, and that the trailing vehicles of a platoon reliably experience a reduction in drag. However, there are several examples in the literature that report a rear vehicle in a platoon receiving a drag increase. With the wide range of vehicle geometries on the roads, it is vital that additional research is targeted at understand the fundamental aerodynamic principles that lead to such adverse platooning results and understand the role that geometry plays in influencing the effectiveness of a platoon.

In the first stage of this project, the geometry dependence of platooning was explored by systematically altering the shape of a simplified ground vehicle to change its platooning behaviour from the 'classical' platooning behaviour, where the rear vehicle experiences a high drag reduction, to 'inverted' platooning behaviour, where the rear vehicle suffers an increase in drag. To this end, a large parameter study was completed using unsteady Reynolds-Averaged Navier-Stokes (URANS) simulations. A key outcome of this study was that the combination of a more streamlined rear vehicle, coupled with strong wake-impingement caused by the lead vehicle results in the most adverse platooning outcome.

The second stage of the project focused on establishing the potential of using passive flow

control to alleviate the adverse platooning effects that were observed in a platoon composed of two Ahmed bodies with 25° rear slant angles. First, the potential of plasma actuators as flow control devices was explored by experimentally characterising the performance of a serrated dielectric barrier discharge (DBD) plasma actuator. This was followed by another set of URANS simulations which considered the application of flow control in the context of a platoon of two 25° Ahmed vehicles. This covered both plasma-actuator like induced jets as well as flaps as flow control devices. The flow control devices were located at the top of the rear slant of the front vehicle and were designed to induce flow separation to increase the size of the front vehicle's wake. Using this technique a drag reduction for the rear vehicle of up to 25% compared to the configuration without flow control was achieved.

In the final stage, the effectiveness of flow control was tested experimentally in the University of Glasgow's Handley-Page wind tunnel. First the dependency of the drag coefficient of a platoon composed of two 25° Ahmed vehicles on inter-vehicle spacing and Reynolds number was investigated, showing that a significant dependency on both parameters exists. Then, flow control was introduced in the form of a flap, with the previous sets of experiments being repeated for three flap angles and two flap lengths. While the flap was not quite as effective as predicted by the URANS simulations, the flap still induced a significant reduction in drag (ca. 9%) when compared to the rear vehicle of the baseline case that was subject to inverted platooning conditions.

Acknowledgements

Firstly, I would like to take this opportunity to thank my two supervisors, Dr Angela Busse and Prof. Kostantinos Kontis, for their continuous support, wisdom and guidance throughout this project. This has been an incredible learning experience and would not have been possible without my supervisors caring and welcoming nature along with their willingness to sit and discuss queries and provide feedback on my work.

I would also like to thank Dr Richard Green for the many long days at the Handle-Page wind tunnel discussing setups and troubleshooting equipment. This advice and support proved invaluable to the project. In addition I would like to thank the other post-grads and post-docs who work at the wind tunnels, Alex, Daniele, David and Michael, for being available whenever I needed a second opinion or an extra pair of hands (especially during model installation).

I would like to express my gratitude to my friends and family for their encouragement and much needed distraction over the last few years. In particular I would like to thank Callum Roberts for always being there to talk whenever I needed it.

Finally, I have to thank my wife Claire for her tireless support, encouragement and belief. From sifting through literature looking for Reynolds numbers to lending an ear when I had a problem to work through; she has been by my side through the highs and the lows and I would not have got this far without her.

Contents

List of Figures

List of Tables

Nomenclature

Roman Symbols

$1/n_e$	Power law exponent
ΔP	Change in pressure $[Pa]$
Δs	Particle displacement between two PIV images $[m]$
Δt	Time interval between a pair of PIV images $[s]$
ℓ	Mixing length $[m]$
A	Frontal area $[m^2]$
c	Flap length $[m]$
C_B	Drag coefficient contribution of the base surface of the Ahmed vehicle
C_d	Drag coefficient
C_K	Drag coefficient contribution of the rounded leading edge surface of the Ahmed vehicle
C_R	Drag coefficient contribution of the remaining surfaces of the Ahmed vehicle e.g. not the leading edge, rear slant or base
C_S	Drag coefficient contribution of the rear slant surface of the Ahmed vehicle
C_{d0Re}	Drag coefficient of a platoon vehicle when tested at the highest Reynolds number
C_{d0}	Isolated vehicle drag coefficient
D	Drag $[N]$
d	Distance between two vehicles in a platoon $[m]$
F	Force $[N]$
F_D	Drag force $[N]$

F_L Lift force $[N]$

F_R Reaction force $[N]$

H Vehicle base height $[m]$

k Turbulent Kinetic Energy $[J/kg]$

L Vehicle length $[m]$

l Characteristic length $[m]$

M Magnification factor $[px/m]$

n Number of vehicles or participants in a platoon

P Power $[W]$

p Pressure $[Pa]$

Re Reynolds number

Re_H Reynolds number based on vehicle height

Re_L Reynolds number based on vehicle length

Re_x Reynolds number based on x

U Velocity component in the positive x direction $[m/s]$

u Characteristic velocity scale $[m/s]$

U_∞ Bulk flow velocity magnitude $[m/s]$

v Flow speed $[m/s]$

v_x x component of velocity $[m/s]$

v_y y component of velocity $[m/s]$

x Distance along a plate (used for boundary layer characterisation) $[m]$

Greek Symbols

α Flap angle $[^\circ]$

δ Boundary layer thickness $[m]$

ε Dissipation rate $[m^2/s^3]$

ε_u Error in velocity $[m/s]$

μ Dynamic viscosity of the fluid $[kg/ms]$

ν Turbulent viscosity []

ω Specific dissipation rate $[m^2/s^3]$

ω_z z component of vorticity $[s^{-1}]$

ϕ Ahmed vehicle rear slant angle $[^\circ]$

ρ Density of the fluid $[kg/m^3]$

Abbreviations

2D Two Dimensional

3D Three Dimensional

TKE Turbulent Kinetic Energy $[J/kg]$

AC Alternating Current

AEV Automated and Electric Vehicles Act

CAD Computer Aided Design

CFD Computational Fluid Dynamics

CFL Courant-Friedrichs-Lewy or convective Courant number

CNC Computer Numerical Control

DBD Dielectric Barrier Discharge

DC Direct Current

DDES Delayed Detached Eddy Simulation

DES Detached Eddy Simulation

DVSA Department of Vehicle Standards Agency

EASM Explicit Algebraic Reynolds-Stress Model

GETS Generalised European Transport System

HGV Heavy Goods Vehicle

HWA Hot Wire Anemometery

IDDES Improved Delayed Detached Eddy Simulation

KMK Kapton, Mylar, Kapton (A type of dielectric material)

LDA Laser Doppler Anemometery

LES Large Eddy Simulation

PATH Partners for Advanced Transit and Highway program

PCB Printed Circuit Board

PIV Particle Image Velocimetry

RANS Reynolds Averaged Navier-Stokes

RMIT Royal Melbourne Institute of Technology

SARTRE Safe Road Trains for the Environment

SST Shear Stress Transport

TRAIN Transient Aerodynamic Investigation

URANS Unsteady Reynolds Averaged Navier-Stokes

Chapter 1

Introduction

The road to wisdom? - Well, it's plain
and simple to express:
Err
and err
and err again
but less
and less
and less.

Piet Hein
(1905-1996)

To limit global warming to below 2°C [5], greenhouse gas emissions will need to be reduced to net zero over the next few decades. While exact timelines differ between countries, Scotland, for example, passed legislation pledging to reach net zero emissions by 2045 [6]. Achieving these reduction targets pose challenges to all sectors, however, one sector that faces some of the biggest challenges is road transport, which contributes approximately 20% to the United Kingdom's greenhouse gas emissions [7]. Unlike many other sectors such as power generation, where large reductions in greenhouse gas emissions have been achieved over the last decades [8], greenhouse gas emissions arising from road transport have increased by 6% between 1990 and 2018 [7]. The main reason for this rise in emissions is the increasing number of vehicles on the road with 328 billion miles travelled in 2018 compared to 255 billion miles in 1990 [7].

To achieve a large reduction in road transport emissions, many measures will be required, such as improving public transport, increasing the proportion of electric vehicles on the road, and improving the overall efficiency of road vehicles. The efficiency of a vehicle is measured through its power usage and is directly proportional to vehicle emissions. The power consumption of a vehicle can be defined as:

$$P = Dv \tag{1.1}$$

Where D is the drag force and v is velocity. Furthermore, the drag force can be expressed as:

$$D = \frac{1}{2}\rho v^2 C_d A \tag{1.2}$$

Where ρ is the density of air, C_d is the drag coefficient of the vehicle and A is the frontal area of the vehicle. These equations suggest that power increases as a cube of velocity and linearly with the other variables. Whilst reducing the velocity of the vehicle is an effective way to reduce power consumption, it is not practical for a number of reasons. Similarly, whilst some work design considerations can be made to reduce the frontal area of a vehicle, this saving is again limited. A much more feasible method for reducing power consumption and lowering vehicle emissions is through the reduction of the drag coefficient

One way to improve the efficiency of a road vehicle is platooning. In a platoon, vehicles follow each other at a close distance, thus sheltering each other and reducing aerodynamic drag [9]. Platooning provides advantages both to internal combustion engine powered vehicles, by reducing fuel consumption, and to electric vehicles, by extending range. Furthermore, platooning could help to improve traffic flow on congested roads by increasing traffic throughput as a result of maintaining short following distances and by using vehicle-to-infrastructure technologies to communicate between platoons and traffic lights [10].

Most platooning research is founded on the assumption that, with the development of an intelligent transport systems, closely spaced platooning could be an important tool in achieving a reduction in emissions and energy consumption. Under dry conditions, the Department for Vehicle Standards Agency (DVSA) advises maintaining at least a 2 second gap between vehicles [11]. When driving at motorway speeds ($70mph$ in the UK) this equates to an inter-vehicle distance of $62.6m$. Studies show that, at these larger distances, platooning is unlikely to be effective as significant drag reductions are only expected at short inter-vehicle distances of the order of a few vehicle lengths. However, platoons with short inter-vehicle distances may become much more feasible in the near future. Along with cruise control, modern driver aids already have the ability to match the speed of the vehicle in front, to keep the vehicle in its lane, and to perform emergency stops if the vehicle in front breaks harshly or if a pedestrian steps in front of the car [12]. Some modern cars, such as the Tesla Model Y, can even operate fully automatic on motorways. Whilst some industry professionals snub the idea, a considerable amount of the control technology required for platooning is already in existence with large companies like Google investing in the development of self driving cars and Heavy Goods Vehicle (HGV) manufacturers like Scania, Mercedes-Benz, and Volvo conducting platooning research [13–18].

Most platooning research focuses on motorway speeds when discussing real world applications. This is for a number of reasons: Motorways are designed to minimise corners and vehicles travelling on a motorway tend to maintain constant speeds for long periods of time. Motorways also have the highest speed limits of all road infrastructure and, as a result, vehicles typically achieve their highest speeds on motorways. The aerodynamic drag of a ground vehicle

increases approximately quadratically with the increase of the vehicle speed, for example, at 70mph, the aerodynamic drag of a typical heavy truck vehicle contributes approximately 65% of the total energy expenditure [19]. Therefore, motorway speeds are the speed regime where vehicle aerodynamics are at their most influential.

The transition from human-driven to driverless vehicles poses its own challenges in ensuring the safety of mixed traffic environments [20]. Therefore, we envisage a future where automated vehicles have their own, segregated, lanes on motorways, allowing them follow each other safely at much closer distances than would be possible for human-driven vehicles. This lane could be used solely for goods transport, or for passenger vehicles if it was deemed safe enough. Such a scenario would provide the perfect conditions for large scale platooning which has the potential to create significant energy savings. One example of a real-world implementation of a segregated lane for driverless vehicles is the Forth Road Bridge, connecting Edinburgh and Fife in Scotland, which is hosting the first tests for a fully automated bus route [21]. On a wider scale, vehicle automation is being specifically targeted as an area of interest as part of the United Kingdom's consultation on the rules on safe use of automated vehicles on roads [22].

To date, the largest interest in platooning research comes from the Heavy Good Vehicles sector where academic researchers, manufacturers, and fleet operators have conducted road tests to understand the feasibility of using platooning as a method to reduce the fuel consumption of a fleet of vehicles [9, 14–16, 23–25]. The main conclusion from these road tests is that forming a close platoon is achievable from a control perspective. One of the main reasons why widespread implementation of platooning is not yet possible is the regulatory framework, as legislation, such as the UK's Highway Code [26], would need to be adapted to allow vehicles in a platoon to run closely together.

Platooning of other types of road vehicles, such as passenger cars, are in a relatively early stage of research and there are a lot of open questions still to be explored. The main challenges can be split into three categories: Aerodynamics, Control and Legislation with each category consisting of several subcategories. The focus of this project is on aerodynamics. The aerodynamic interaction between vehicles in a platoon is complex and even the simplest two vehicle platoon systems are not yet fully understood. The occasionally counter-intuitive nature of platooning at times results in platoons experiencing increased drag as opposed to the desired drag reduction. This type of behaviour has been found both experimentally and numerically for a range of platoons and no real conclusions have been drawn to explain what causes it [27, 28].

As done historically, in the search for aerodynamic improvements of an isolated vehicle, a simplification of the problem was required to build a strong foundation of the fundamentals. Emphasising again that platooning is still in the early stages of development, a similar method will be undertaken. Using simplified vehicle models, this study will analyse the aerodynamics of a two vehicle platoon. By focusing on a platoon of just two vehicles, it not only allows for a gradual build up of complexity, (e.g. building upon knowledge of isolated vehicles) it

also represents a baseline scenario where adding further vehicles has been shown to have no significant effect on the fundamental flow structure whilst adding significantly more challenges to simulation and experimental work.

Whilst all three of the aforementioned challenges for platooning need to be addressed for platooning to be implemented on the roads, by first investigating the aerodynamic benefits available through platooning, a strong case for further discussion and investment in road vehicle control and legislation can be built. The key motivation and impact of this thesis is to improve the understanding of the complex aerodynamics of platoons in order to enable a realistic assessment the potential economic and environmental benefits. From here there will be a case for further investment, since, without clear and measurable incentives, governments will be unlikely to prioritise the development of new legislation.

1.1 Structure of thesis

Following this brief introduction, the structure of this thesis is as follows:

- Chapter 2 outlines the relevant literature related to the study and gives a detailed explanation of the background that helped to motivate this study. The chapter concludes with a statement of the aims and objectives that defined the scope of this project.

- Chapter 3 describes a series of Unsteady Reynolds Averaged Navier-Stokes (URANS) simulations that focused on understanding the fundamental aerodynamic differences between a platoon of two cuboids and a platoon of two 25° Ahmed bodies, a widely used simplified model of a ground vehicle. This is achieved by systematically morphing one geometry into the other.

- In chapter 4, the previously obtained knowledge is used to trial passive flow control techniques, namely flaps, in a similar computational setting as before. useful insight into the effectiveness of implementing flaps as flow control on a platoon is provided. This proved vital to focusing the later experimental work.

- Chapter 5 describes a series of platooning experiments conducted in Glasgow University's Handley Page wind tunnel facility. An experimental setup was developed based on the platooning knowledge gained from the previous investigations to conduct a series of experiments on a platoon composed of two 25° Ahmed bodies. Both the influence of inter-vehicle spacing and Reynolds number on the platoon's performance was investigated. The potential for using flow control to improve platooning outcomes was then explored using passive flow control by flaps.

- Chapter 6 provides further exploration of an alternative flow control device for platooning. The chapter initially details an experimental investigation on an electrically controllable

flow control device called a plasma actuator. The intention is to test its potential to be implemented as a flow control device on a platoon. A detailed explanation of the experimental setup and methodology is given, which was then applied to characterise the maximum jet velocity that can be produced using a plasma actuator with a serrated electrode design. A computational representation and validation of a plasma actuator-like induced jet is provided, followed by further URANS simulations where a representative jet is used as a flow control device on a two vehicle platoon.

- Finally, chapter 7 provides the concluding thoughts for the project, reflecting on the aims and objectives and outlining possible directions for future work in the field.

Chapter 2

Literature Review

In this chapter, first a review of simplified vehicle geometries for investigation of ground vehicle aerodynamics is given with particular focus on the Ahmed vehicle model, computational techniques and experimental techniques. This is followed by an overview of flow control techniques applied in the context of simplified vehicles. Finally, the literature surrounding vehicle platooning and an outline of some of the main challenges faced in this area of research will be discussed. This should provide the reader with the appropriate understanding of the background literature that underpins the work described in this thesis. In addition, some interesting outcomes found in the literature and some of the open questions in the field will be highlighted. This in turn will motivate the aims and objectives for the project which will be laid out in detail at the end of this chapter.

2.1 Simplified Vehicle Geometries

Since the first fossil fuel crisis in the 1970s, there has been a clear need for improving the aerodynamics of road vehicles. Whilst the geometries of road vehicles are quite complex, it is possible to reproduce their basic aerodynamic flow features using far more simple geometries. Many of these geometries became very popular for ground vehicle aerodynamics research including the field of platooning.

The most basic representation of a road vehicle would be a cuboid. Whilst this is an extreme simplification, it does represent some of the aerodynamic features of a Heavy Goods Vehicles (HGV). Further geometries were designed to target specific features of road vehicles. The Ahmed geometry was initially designed to highlight how varying the backlight angle effects the lift and drag coefficient of a vehicle [1]. A similar study was conducted by Howell [29] analysing the effect of leading edge angle on the drag coefficient of a model known as the Rover model. A combination of these two features can be found in the Davis model, adding a little more complexity to the geometry [30].

In recent years more complex models have increased in popularity, for example, the Dri-

vAer model [31–33] represents an estate car with re-configurable rear designs. Additionally, the Generalised European Transport System (GETS) model, which was designed to recreate the aerodynamic features of a HGV, is often used [34], along with a variety of other HGV inspired models [35–37]. Some of the aforementioned geometries in this chapter will be encountered later in this thesis. A more detailed history on the use of a wide variety of reference models can be found in the review paper by Le Good and Garry [38].

Another important factor when discussing road vehicle geometries is the Reynolds number. The Reynolds number is a non-dimensional number that describes the ratio between the inertial to the viscous forces in a flow. This is detailed in equation 2.1

$$Re = \frac{\rho u l}{\mu} \tag{2.1}$$

where ρ is the density of the fluid, u is the characteristic velocity scale (here: the free-stream velocity), l is the characteristic length of the model (not to be confused with L, used for vehicle length, later in this thesis) and μ is the dynamic viscosity of the fluid. The Reynolds number influences transition to turbulence, boundary layer thickness, the extent of flow separation and much more. Therefore, in theory, if the Reynolds number of two similar experiments are the same, the physics of the flow will also be the same. This principle of Reynolds number similarity is of particular use when designing experiments. One example of this is as follows; building a wind tunnel big enough for a full scale car model is extremely expensive, instead a scale model of said vehicle can be used and Reynolds number scaling can be utilised to match the Reynolds number of the experiment to full scale conditions. This experiment then provides and accurate prediction of what to expect at full scale conditions.

The lift and drag coefficients of many vehicles discussed in the Le Good and Garry [38] review paper show some Reynolds number dependency. One difficulty when comparing different studies in this area is the inconsistency in the selection of the characteristic length in the Reynolds number calculation. In bluff body studies, the norm is to use the base height H of the model as the characteristic length, however, for road vehicle studies the vehicle length L is also commonly used. The present project draws on literature from both topics and is primarily focused on vehicle wakes. The size, shape and length of a vehicle's wake is driven by the base height therefore, unless specified otherwise, the base height will be used as the characteristic length scale in the Reynolds number calculations.

2.1.1 Aerodynamic features of the Ahmed vehicle

One of the most popular simplified vehicle models is the Ahmed body, first developed in 1984 by Ahmed et al. [1]. This geometry is often used in fundamental research on ground vehicle aerodynamics due to its simplicity. Accurate scale models of road vehicles are expensive to manufacture and can be difficult to work with. The Ahmed body offers a simplified alternative

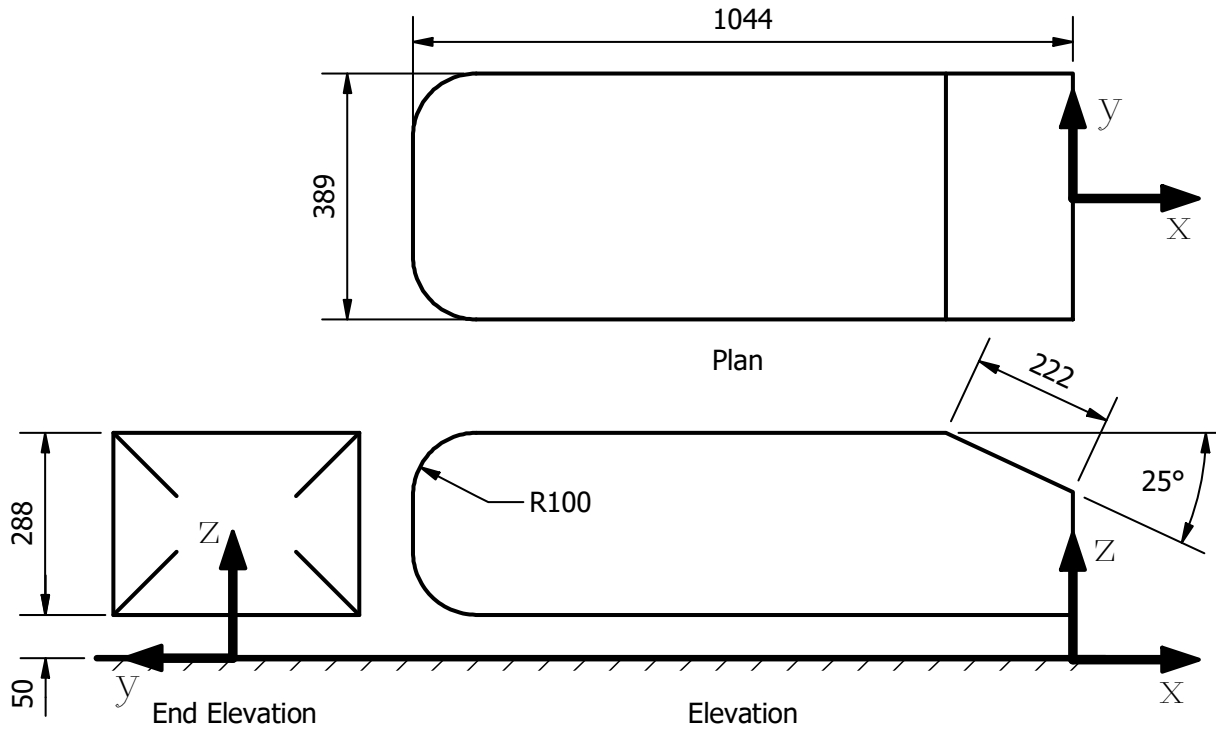

Figure 2.1: The dimensions of the Ahmed body. All units are given in millimetres. The flow is in the positive x-direction. The rear slant angle of the Ahmed body is variable; here an Ahmed body with a 25° rear slant angle is shown.

whilst maintaining many of the general flow features of a road vehicle. This enables a better understanding of general road vehicle aerodynamics and allows for a more systematic analysis of automotive design.

Figure 2.1 shows the dimensions of the Ahmed body. The Ahmed body has a rounded leading edge, to maintain flow attachment around the front of the geometry, and a re-configurable rear slant. The length of the rear slant is maintained at $222mm$, however, the slant angle, ϕ, can be varied from 0° to 40° when measured down from the horizontal. When placed in a wind tunnel, the Ahmed body is often mounted on four stilts. The size and location of the stilts varies slightly from experiment to experiment. In computational studies, the stilts are often omitted since they are difficult to model accurately and have little effect on the overall result [39].

In general, the airflow around the leading edge of the Ahmed body is clean. Stagnation occurs roughly halfway up the vertical leading edge and small separation bubbles have been observed on the flat surfaces immediately downstream of the curved leading edge. The flow is accelerated under the vehicle floor providing a slight vertical pressure difference, also known as down-force [40, 41].

As the flow moves downstream, it approaches the trailing edge slant where the flow features get notably more complex. In the $\phi = 0^\circ$ or square-back configuration, the flow over the rear of the Ahmed body separates into a large wake with two re-circulation regions. As the slant angle is increased, the flow along the centre line of the model remains attached over the rear slant.

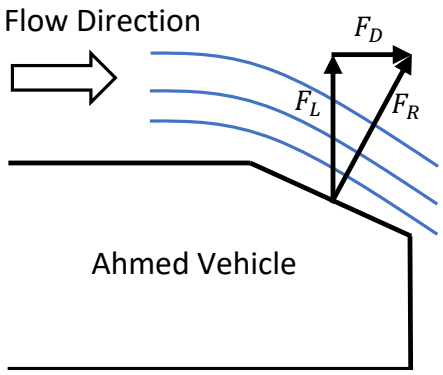

Figure 2.2: Depiction of reaction force caused by flow attachment over the trailing edge slant of an Ahmed vehicle

This, in turn, reduces the size of the wake. The drag coefficient for the Ahmed body reaches a minimum when the rear slant is around 12.5°. As the angle is increased further, the drag coefficient climbs to its peak at the “critical angle" of 30° [3, 42]. This increase in drag is due to the extra work being done on the flow to keep it attached over the trailing edge. This can be explained using Newton’s third law of motion and is outlined in figure 2.2. A force is required to cause the flow to be diverted down, this force is provided by the vehicle surface. In reaction to that, an equal force, normal to the surface exists. This force is made of a lift component and a drag component and, as the rear slant angle is increased, so too does the drag component of the reaction force.

When the rear slant angle exceeds 30°, the flow can no longer remain attached to the angled surface and detaches at the top of the rear slant. This coincides with a sharp drop in drag coefficient, as the aforementioned reaction force no longer exists, and a larger wake similar to the squareback case forms. The drag coefficient then remains fairly consistent as the rear slant angle increases to the point of becoming a squareback Ahmed vehicle once more.

The flow over the rear slant also has three dimensional components. On each side, the flow wraps around the slant forming two strong vortices off each C-pillar. At low slant angles these vortices are small but as the angle increases, the vortices grow, and at high slant angles they begin to dominate the wake structure. Corallo et al. [43] suggest that the interaction between these two vortices promotes down-wash maintaining flow attachment over the rear slant at higher angles. Corallo et al. supported this by showing how the critical angle can be altered by changing the width or aspect ratio of the model.

Figure 2.3, taken from Ahmed et al. [1], highlights how influential each surface of the Ahmed body is in contributing to the total drag coefficient of the model. It is clear that in the squareback configuration, the majority of the drag originates from the large wake causing low pressure on the base of the model. As the rear slant angle is increased, the wake decreases in size. For low angles, this improves the pressure recovery on the base causing both the base component of the drag coefficient and the overall drag coefficient to drop. As the rear slant angle continues

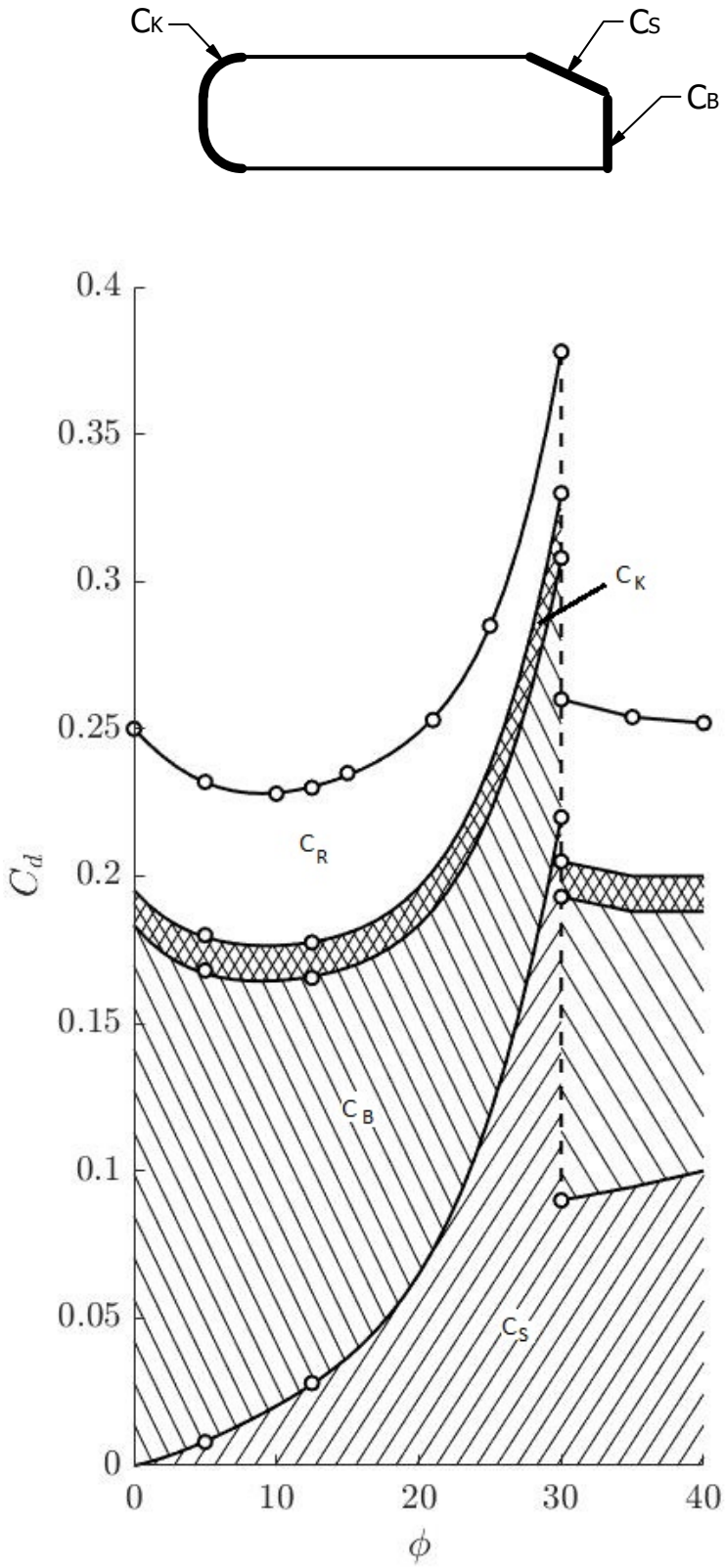

Figure 2.3: Drag coefficients of Ahmed body with budget of individual contributions of various slant angles. (Data taken from Ahmed et al. [1])

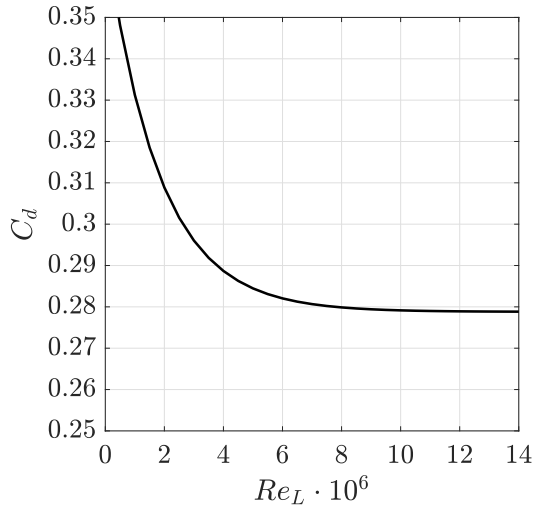

Figure 2.4: Best fit approximation of the drag coefficient over a range of Reynolds numbers for the Ahmed body with a 25° rear slant. Best fit using equation 2.2 taken from Meile et al. [2]

to increase, however, the work being done by the vehicle surfaces to maintain flow attachment gets greater. Whilst the drag component of the base continues to drop, it is outweighed by the sharply increasing drag component of the rear slant. As the angle approaches the critical angle, the drag coefficient component of the rear slant surface becomes the dominant driving factor for the total drag coefficient and the flow begins to detach at the top of the slant, creating a small bubble. Once the rear slant angle increases above the critical angle, the flow can no-longer remain attached to the surface. This produces a large wake with two main re-circulation regions which appear not too dissimilar to the 0° case. The main difference in these two cases is that that the pair of C-pillar vortices remain present in the post critical flow detachment regime [2].

The effect of the flow detachment can be observed in the drag coefficient graph shown in Figure 2.3. Once the flow has detached from the rear slant there is a sharp decrease in drag coefficient mainly due to the reduction in the drag component attributed to the flow over the rear slant. In addition to the similar structure of the flow compared to the 0° case, the drag coefficient also drops to a level just higher than that of the 0° Ahmed body. From this point forward, the flow becomes much more stable and easier to predict [39].

Whilst the squareback case is one of the simpler Ahmed body cases, there have been some interesting observations on the structure of its wake. In the study by Grandemange et al. [44] a switching behaviour was noted in the re-circulation region of the wake of the Ahmed body. This took the form of two stable modes, one consisting of one large re-circulation in the wake and the other mode being two smaller re-circulations vertically displaced from each other. This phenomenon is not specific to the Ahmed body and but has also been observed by Pavia et al. [45] on the squareback Windsor (a.k.a. Rover) model, another simplified vehicle model.

The intricacies of the aerodynamics of the Ahmed vehicle make it very susceptible to the specific flow conditions. The main way to measure this is by studying how the drag coefficient

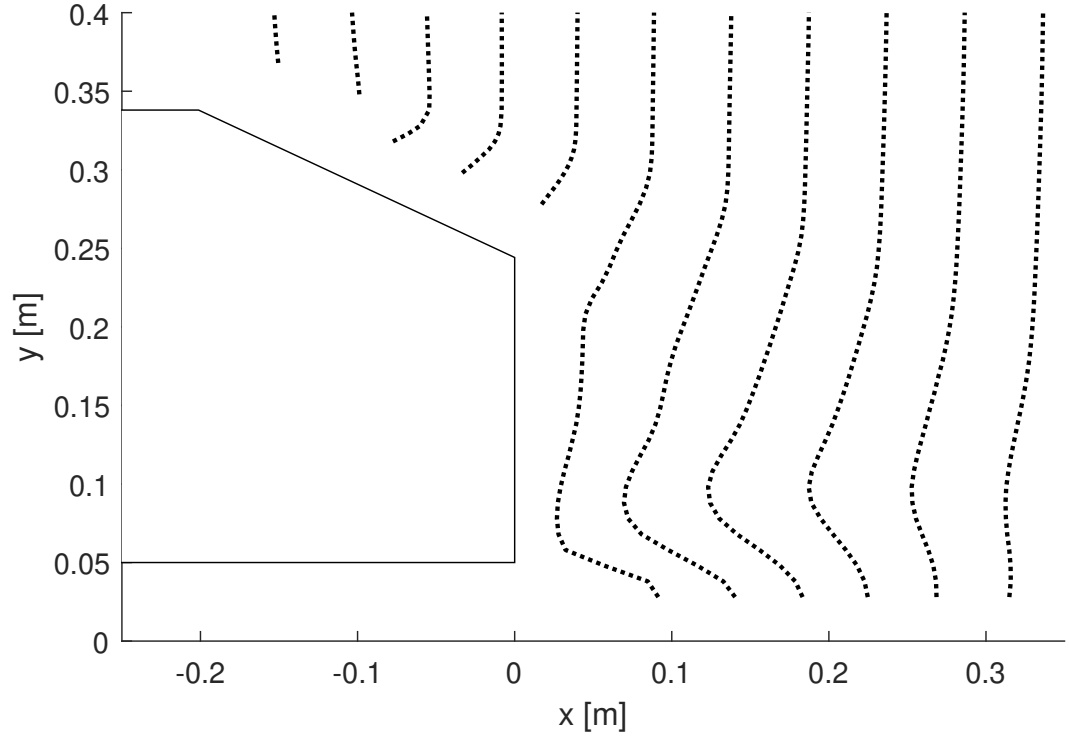

Figure 2.5: Stream-wise velocity profiles for an Ahmed vehicle with a 25° rear slant (data from Lienhart et al. [3]). This provides a visual representation of how the flow develops over the rear slant and into the recirculation region at the base of the vehicle.

changes with Reynolds number. Meile et al. [2] found that as Reynolds number increases, the drag coefficient decreases. For low Reynolds numbers, there is a rapid decrease of the drag coefficient with Reynolds number, but for high Reynolds numbers ($>9 \cdot 10^6$) the results become Reynolds number independent [42]. An empirical relationship for the dependency of the drag coefficient of Reynolds number, as described by Meile et al. [2], for the Ahmed body with a 25° rear slant is provided in equation 2.2 and visually represented in figure 2.4.

$$C_d = 0.2788 + 0.0915 \cdot exp(-Re_L \cdot 10^6/1.7971) \tag{2.2}$$

2.1.2 Experimental methods for analysing Ahmed vehicles

The results from the original experiments by Ahmed et al [1] were discussed above. Due to its importance as reference geometry for ground vehicle aerodynamics, the Ahmed body was later studied experimentally by many other groups. In the experiments of Lienhart et al. [3] the 25° and 35° Ahmed bodies were studied, with the aim of supplying a detailed set of quantitative results to be used as reference data. The conditions of this experiment were clearly defined:

The Ahmed body was placed in a $3/4$ open wind tunnel test section and mounted $50mm$ off the ground using $30mm$ diameter stilts. The test section cross section was $1.87m \times 1.40m$ resulting in a 4% blockage ratio. Three different measurement techniques were used to collect the data. Hot-Wire Anemometry (HWA) measurements were conducted in the low turbulent region at the inlet to provide accurate characterisation of the inlet boundary conditions. Laser Doppler Anemometry (LDA) was used to obtain a detailed study of the flow over the rear slant and in the wake of the Ahmed body. Finally, pressure taps were used over the rear slant, base and side panel surfaces to provide a detailed picture of the pressure coefficient in this region. The large database of results created by Lienhart et al. allows for a far more structured validation process of computational and experimental studies. One of the key figures produced by this study is the stream-wise velocity plot depicted in figure 2.5. Here, a series of hot wire measurements were performed at precise locations to provide a clear picture of the velocity profiles over a range of streamwise locations. In theory, this allows future studies to use a similar method and compare their findings thus validating the accuracy of their new readings.

Studies on the Ahmed body have only increased in recent years with experimental methods expanding to include both Particle Image Velocimetry (PIV) and Stereo PIV. For example, Grandemange et al. [46] used these methods to study the length of the recirculation region of a squareback Ahmed body over a range of yaw angles. Similar techniques were used by Zhang et al. [47] to analyse the multitude of shedding frequencies around different sections of the Ahmed body.

2.1.3 Simulation of flow past the Ahmed body

Flow past the Ahmed body has been simulated using many different numerical approaches. Due to the high Reynolds number, the flow will always be in the turbulent regime. Therefore, in the following, simulations of flow around an Ahmed vehicle will be grouped according to the chosen turbulence modelling approach: Reynolds-Average Navier-Stokes (RANS) simulations, large-eddy simulations (LES), and hybrid simulations.

Reynolds Averaged Navier-Stokes

As stated previously, the Ahmed body became popular not only for the key flow phenomena it produces but also due to its simple shape making it well suited for early Computer Aided Design (CAD) and Computational Fluid Dynamics (CFD). Despite its basic geometry, some of the complex flow features observed for Ahmed bodies have proven difficult to recreate computationally. In an early CFD study on the Ahmed body, Larsson et al. [48] made some progress predicting the drag coefficient of the Ahmed body at different rear slant angles using a zonal Navier-Stokes approach. Whilst all of the drag coefficients from $20^\circ - 40^\circ$ were slightly under-predicted, the strongest discrepancies were seen when analysing the flow field. The main vortices that develop

off of the C-pillars were captured but the simulation was not very successful in predicting the flow separation after 30°.

A decade later and simulation techniques had significantly improved. In the study by Bayraktar et al. [42] a dual experimental and computational investigation of the Ahmed body for a range of slant angles from 0° to 25° was conducted. An unsteady Reynolds Averaged Navier-Stokes (RANS) solver was used with the standard k-ε turbulence model. Whilst the simulation provided good correlation with the experimental drag coefficient data using a mesh size of 3.9 million cells, a final mesh size of 5.4 million cells was implemented to provide improved flow field resolution. Here, the simulation data matched the experimental drag coefficients accurately with only a small discrepancy between the lift coefficient results. In addition to lift and drag coefficients, this study also compared the pressure coefficient along the centre line of the Ahmed body achieving a good agreement between the experimental and simulated data sets. This study was conducted prior to the publication of the experimental data by Lienhart er al. Therefore, the analysis of the flow was still very qualitative with no clear indication on how accurate the simulation was at predicting the complex flow features at the rear of the Ahmed body.

As the amount of better defined, repeatable, experimental data increased, CFD methods began steadily improving. With such a plethora of experimental data, the Ahmed body became an important test bed and validation case for a range of simulation techniques. One of the most cost effective techniques when simulating turbulent flows is Unsteady RANS (URANS) and many different variations of Reynolds Averaged Navier-Stokes (RANS) turbulence models were developed. Guilmineau [39] compared results for 6 different turbulence models to Lienhart et al.'s experimental data for the 25° and 35° Ahmed bodies to highlight each model's strengths and weaknesses. Guilmineau found that, for the 35° Ahmed body, the flow is post critical therefore it detaches at the top of the rear slant and never reattaches. Whilst all the models matched the experimental flow data well, the Explicit Algebraic Reynolds-(S)tress Model (EASM) provided the closest match. The story was notably different for the 25° case. While for the 35° case the flow over the rear slant had matched experimental data well, for the 25° case there were clear discrepancies with most turbulence models continuing to predict large flow separation. For this case, the $R_{ij} - \omega$ and $k - \omega$ turbulence models provided the closest match of the drag coefficient to the experimental data. It is clear however, that the flow for the 25° case was still proving to be challenging to model accurately .

The $k - \omega$ Shear Stress Transport (SST) turbulence model was later adopted by Meile et al. [2] where they investigated how the simulation setup could be optimised to improve the accuracy of the results for the 25° and 35° Ahmed bodies. This paper provides a very clear set of parameters to be followed when designing a URANS simulation for flow past the Ahmed body. A uniform $40m/s$ velocity inlet was used to match the wind speeds of other experimental research for a Reynolds number of $2.8 \cdot 10^6$. A small area upstream of the model was given a full slip condition thus allowing the flow to develop into the computational domain before

interacting with a no slip condition floor. This is similar to the experimental setup in a wind tunnel where often ground plates offset from the wind tunnel floor are used. A pressure outlet was used which was set a large distance downstream to allow space for the flow to settle inside the test domain. The improvement in turbulence model combined with a more rigorous approach to building the simulation greatly improved the effectiveness of the simulation with both the flow over the rear slant and the lift and drag coefficient being withing 5% of the experimental validation data. This was a significantly improved result from previous research applying the $k-\omega$ SST turbulence model. The key takeaway from the Meile et al. [2] study is that, when implemented carefully, URANS and specifically the $k-\omega$ SST model can be an effective way to predict the drag coefficient of simplified vehicle geometries. Guilmineau [39] showed that these techniques still have their limitations when predicting the flow field, especially in and around regions of flow separation, however, the low cell counts required (less than 5 million cells) make this technique very versatile and computationally affordable.

Large Eddy Simulation

While in a RANS simulation the entire spectrum of turbulent eddies is modelled, in a large eddy simulation (LES) the motion of the large turbulent eddies is resolved, while the smaller, unresolved turbulent structures are modeled using a subgrid-scale model. The key advantage of LES over other turbulence models, such as RANS simulations, is that LES provides a much more realistic representation of the turbulence within a flow. This is because LES resolves the larger turbulence structures directly, rather than modelling their average effect on the mean flow as in RANS simulations. As a result, LES provides a more accurate representation of the turbulence and its impact on the overall flow. In the context of the Ahmed body, this is of special relevance when it comes to resolving the large-scale turbulent eddies in the near-wake of the body. However, there are also some limitations to LES. One of the main limitations is that LES simulations require a much finer grid and a much smaller time step. This results in the need of far greater computational resource than would be required for a typical RANS simulation at the same Reynolds number. This makes LES simulations very computationally intensive and time-consuming, making them much more challenging to implement for high-Reynolds number and/or complex flows [49].

However, despite the much higher physical realism provided by the LES approach to model turbulent flows, the 25° Ahmed body still presents a challenging configuration to capture computationally. Serre et al. [50] investigated, as part of a French-German collaboration, the flow past the 25° Ahmed body using a range of different LES methods. They concluded that while LES predictions were capable of providing an overall agreement with the experimental reference data, not all of the tested LES codes were capable of capturing the separation of the flow over the rear slant. Several models also led to a significant over-prediction of the drag coefficient, with C_d varying between 0.317 and 0.431 across the three tested LES models. The authors

concluded that the Ahmed body test case is challenging for all components of an LES solver. This is because of the complex flow physics that occur in the flow over the 25° Ahmed body, which include flow separation, vortex shedding, laminar to turbulent transition and large-scale turbulent structures that dominate the turbulent transport.

A big factor that has limited the application of LES to simulating the flow around the 25° Ahmed body are the high Reynolds numbers that are of interest in the context of this problem. LES at higher Reynolds numbers is very computationally expensive, especially if a wall-resolved LES is desired. Therefore, most studies published in the literature using eddy-resolved methods opt for hybrid approaches instead.

Hybrid Models

Whilst LES provides a large amount of detail, it is computationally very expensive and the computational cost rapidly increases with Reynolds number. Spalart et al. [51] proposed a compromise to enable eddy-resolved simulations at higher Reynolds number. By combining the $k-\omega$ SST URANS turbulence model with LES, significant time savings could be made. The flow near the surface in an attached boundary layer can be approximated well using RANS methods avoiding the very-fine meshes (and associated high computational cost) required for wall-resolved LES. Once the flow separates from the surface it becomes highly turbulent and LES provides significant advantages when modeling these detached eddies. This hybrid method was named Detached Eddy Simulation (DES) and has been the foundation for a large range of hybrid models. The improvement in results does come at a cost. Where the mesh size used by Meile for their RANS simulations ranged from 4.5 to 5 million cells, a mesh used for hybrid RANS-LES models is usually in the region of 30 million cells [52]. The number of cells in the mesh only increases further when moving to a pure LES simulation, drastically increasing the resolution of the flow field but also the computational cost of the simulation. This is specifically true for Reynolds numbers matching those used in wind tunnels.

Over two separate papers, Guilmineau et al. [53, 54] studied a wide range of composite RANS-LES models, comparing them to both experimental data and $k-\omega$ SST URANS data. It was found that the composite simulations improved the resolution of the flow field, bringing the predicted flow separation over the rear of the Ahmed body in-line with data collected in the Lienhart et al. [3] study. The most accurate flow field predictor was the Improved Delayed Detached Eddy Simulation (IDDES) that provided a near perfect qualitative match of the flow fields measured by Lienhart et al.

Whilst this new technique provided an improved prediction of the flow field when compared to URANS, when analysing the predicted drag coefficients, the hybrid models were less effective. Here it was $k-\omega$ SST that produced the most accurate comparison to the experimental data with the hybrid models over-predicting the drag coefficient by $20-25\%$. In addition to this, the hybrid models are between 1.5-2 times more computationally expensive [52, 55] than their

URANS equivalent. This highlights the importance of selecting the appropriate model when designing an investigation as each have their own benefits and drawbacks.

2.1.4 Conclusions

The important role that simplified vehicle geometries, like the Ahmed body, play in developing the understanding of more complex systems cannot be understated. The best way to make insight and progress is to begin with the fundamentals and slowly build the complexity, taking time to fully understand each step. This is the key to understanding any complex system and is a principle that was followed throughout the current work.

The Ahmed vehicle in particular played a key role in the early development of road vehicles providing greater insight into the effects of backlight angle on drag coefficient. Its simple shape but transferable aerodynamic properties made it a perfect test bed for vehicle related computational and experimental investigations. Experimentally, techniques such as PIV, LDA, hot wire, pressure tappings and load cell measurements have been used to characterise the forces and flow structures produced by the Ahmed vehicle. Computationally however, the Ahmed vehicle still provides challenges. The main drive to use this geometry going forward in this work comes from the vast quantity of previous research that has been conducted to understand the flow around the Ahmed body. This detailed understanding of the isolated case will play a vital role in improving the understanding of the platoon's aerodynamics.

This thesis blends both computational and experimental investigations utilising PIV, force measurements and URANS simulations. When selecting a computational method, an understand the scope of the project is required. CFD will be used to help guide the development of an experimental campaign. A wide range of test cases will be required to explore numerous configurations of different platoon inter-vehicle distances, vehicle geometries, flow control techniques and flow speeds. In total this will be in excess of 100 unique test cases resulting in tens of thousands of hours of simulation time. It is also worth remembering that this is a general sweep of input parameters, and whilst it is important to gain as accurate force and flow field data as possible, the CFD simulations will not be used to do a targeted search of a specific test case. For this reason, using the URANS method with the $k-\omega$ SST turbulence model is the best fit for the objectives for this study. This setup provides a good approximation of drag coefficients and flow field data whilst remaining comparatively computationally inexpensive when compared to the more detailed simulation approaches discussed earlier.

2.2 Ahmed vehicle flow control

Flow control is used to alter the flow around objects, to improve aerodynamic performance like lift or drag coefficients, to reduce vibrations or to change other flow characteristics such as

separation and reattachment. In general, flow control falls into two categories, passive and active flow control. For passive flow control no energy input or control loop is required. Example for passive flow control are devices that consistently alter the flow such as flaps, vortex generators, or the application of specific surface roughness areas. Active flow control requires auxiliary power input and has the potential to change and adapt to the current flow conditions via a control loop. Ideally this is done in cooperation with sensors, updating the flow control on the current flow conditions and adapting automatically to provide the desired outcome. Examples for active flow control devices are pneumatic flaps that can change in angle [56], pulsed jets of air [57,58], or surface suction [59,60].

This section is focused on the implementation of flow control on the Ahmed vehicle geometry as this will be the main geometry used in this project. Some additional examples of interesting flow control applications have been included as these also influenced the design of the investigations detailed in this thesis.

2.2.1 Passive flow control

Flaps are one of the most commonly applied passive flow control devices. Their ease of design and implementation makes them ideal for initial testing of flow control. In addition, the abrupt nature of a flap reliably influences flow separation which has a big impact on the drag coefficient of bluff bodies. The earliest example of flaps being used on a single Ahmed like vehicle comes from Khalighi et al. [61]. In this investigation, a squareback bluff body similar to the squareback Ahmed vehicle was used with rear mounted, horizontal, flaps offset from the top and bottom surfaces. Using both computational and experimental methods drag reductions of 6-20% were demonstrated.

The work was later expanded by Beaudoin et al. [56]. When compared to the Khalighi et al. study, the geometry used in this paper is a much closer representation of an Ahmed vehicle. Beaudoin et al. used a quarter scale Ahmed vehicle with a 25° rear slant for their experiments. However, the length of the rear slant was 42% longer than on a standard Ahmed vehicle. Flaps were placed on all 7 edges of the two rear panels at the base of the Ahmed vehicle. In addition to the multiple flap locations, a wide range of angles for each flap were tested. The most effective flap location was two flaps running down each side of the rear slant. This configuration had the effect of reducing the strength of the rear vortex structures and provided a 17% reduction in drag coefficient. This was closely followed by one flap mounted at the top of the rear slant promoting flow separation for which a drag reduction of 15% was measured.

The Beaudoin et al. study would later influence more computational studies on 25° and 35° Ahmed vehicles with flaps located at the top of the trailing edge slant [62–64]. A range of flap lengths and angles were explored at Reynolds numbers around $1 \cdot 10^6$. In general the best results were obtained when flaps were used to trigger separation of the flow over the trailing edge slant. For Ahmed vehicles with near critical slant angles, the flow is relatively unstable making it very

easy to promote flow detachment. For this reason, the length of flap has little influence when mounted in this location as even the smallest flap (3.6% of the rear slant length) can induce flow separation [63].

Collectively, the Khalighi et al. [61], Tian et al. [62], Siddiqui et al. [63] and Raina et al. [64] studies all used steady RANS as their computational method to simulate the effects of flow control. As discussed in section 2.1, this is a widely used method to simulate flow past the Ahmed body. Whilst these papers give a useful insight on the effects of flap size, location and angle, it has been shown in section 2.1 that unsteady RANS or DES would provide more accurate flow field estimations. The added complexity of a flap only exacerbates this point, as seen in the Khalighi et al. study where the computational and experimental results had around a 30% difference in measured drag coefficient.

Fourrié et al. [65] conducted experiments on an Ahmed vehicle with a flap mounted at the top of the rear slant, analysing the effect of flap angle on drag coefficient. A Reynolds number of around $3 \cdot 10^5$ based on vehicle height was used, as with most experimental work this is notably lower than the Reynolds numbers used in the aforementioned computational studies. They found that the most effective flap angle was 5° up from horizontal generating a 9% reduction in drag coefficient. This is in slight disagreement with the previously mentioned computational studies that found the optimum flap angle to be 5° less than horizontal whilst predicting drag coefficient reductions in the region of $15 - 20\%$. Further experimental investigations would be useful for a broader set of comparative data, in addition, more detailed simulation techniques could also be used to improve the discrepancy between experimental and computational results.

In addition to flaps, another popular passive flow control device is vortex generators. Pujals et al. [66] and later Krajnović [67] applied cylindrical vortex generators on the roof of the 25° Ahmed vehicle, $120mm$ upstream of the rear slant. One characteristic flow feature on the 25° Ahmed vehicle is a small recirculation region immediately downstream of the initial slant where the flow detaches slightly and then reattaches to the angled surface. The introduction of vortex generators increases the turbulence in the boundary layer helping the flow to stay attached over the trailing edge, eliminating the recirculation bubble. The experimental results by Pujals et al. [66] were later replicated computationally using LES by Krajnović [67] to show this technique can provide around a 10% reduction in drag coefficient.

A more novel take on passive flow control was implemented by Mahammadikalakoo et al. [68]. They used a series of different shaped slots or 'tunnels' through the vertical rear corners, traditionally called the C-pillar on a road vehicle, of the 25° Ahmed vehicle. This addition created vortical structures that increase the mixing of the shear layer and reduce the size of the recirculation region resulting in a 2.5% reduction in drag coefficient.

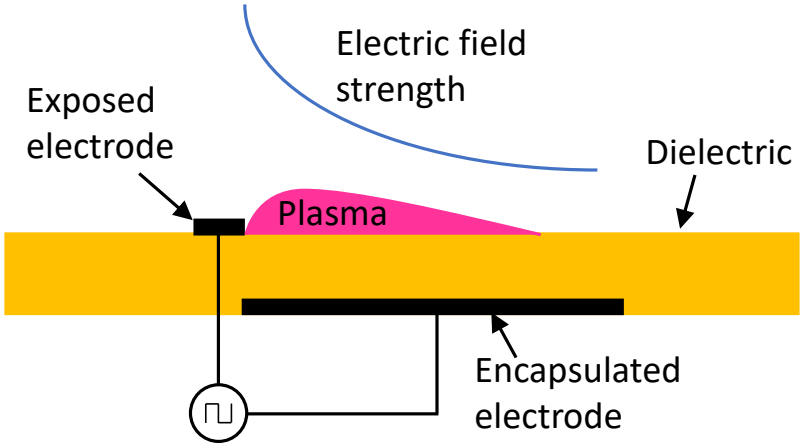

Figure 2.6: Schematic of a standard DBD plasma actuator

2.2.2 Active flow control

Active and passive flow control techniques have a similar goal however, active flow control tends to operate on a more sophisticated level. Active flow control describes a flow control process that has the ability to move or change depending on the flow structure or conditions. This can be achieved through the use of pulsed jets that can modify their pulsing frequency, or through pneumatically controlled flaps that can alter their angle depending on certain scenarios. The possibilities for these techniques are numerous however, the following section outlines some of the interesting applications seen on the Ahmed vehicle.

Plasma actuators

Using jets of air is a popular way of applying flow control to a system as they can be very versatile. Not only can their direction and magnitude be tailored to a situation, they can also be pulsed to take advantages of harmonics in flow oscillations. One way of creating jets of air is through the use of plasma actuators, an electrically controlled flow generation system.

A plasma actuator is constructed of three main parts as shown in figure 2.6. One electrode is connected to ground and encapsulated in a non-conductive, dielectric material. Above this, an exposed electrode is positioned and a high potential difference, in the order of $10^4 V$, is generated between the two electrodes. The presence of this alternating high voltage ionises the surrounding air creating a plasma film of electrons and ionised air molecules. A lateral offset is applied to the electrodes introducing an electric field component parallel to the surface. This in turn causes the ions to move parallel to the surface, towards the encapsulated electrode thus introducing momentum into the surrounding air resulting in a jet.

The most basic plasma actuator design uses two rectangular electrodes. This design has been widely studied over the last decade and has many different applications [4, 69–75]. Whilst the electrode geometry is consistent, the large variety in additional set up and input parameters

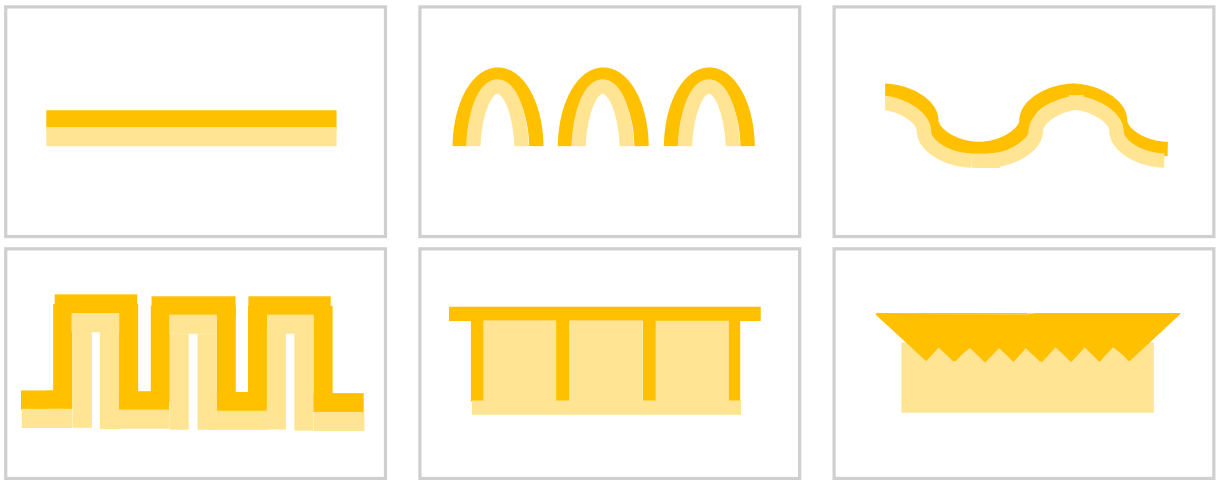

Figure 2.7: Different electrode designs for plasma actuators: Upper row (from left to right) Linear, Horseshoe, Serpentine; lower row (from left to right) Square wave, Finger and Serrated. Exposed electrode in dark orange, encapsulated electrode in light orange.

between different studies makes it extremely difficult to draw quantitative comparisons. The main differences predominantly fall into four groups: design of the exposed electrode, design of the encapsulated electrode, dielectric material properties and input electronics.

Early in the development of plasma actuator technology it was noted that changing the design of the exposed electrode can influence the generated flow in different ways. Hoskinson et al. [71] experimented with using a wire of similar thickness to a rectangular electrode and compared the induced force finding that the use of a wire produced more than double the force. This wire design was then later adopted by Kim et al. [76] and applied to an Ahmed vehicle where induced velocities of $4.2ms^{-1}$ were measured.

Electrode geometries were developed further, rather than aiming to produce a faster linear jet of air, the focus moved to producing a more three dimensional flow. Initially with a horseshoe shaped electrode [77, 78] and later serpentine [72, 79–81], square wave [73] and finger shaped electrodes [82](shown in figure 2.7), studies analysed the ability of these actuators to produce vortical structures. It was found that by altering the shape of the electric field, small pairs of vortices could be generated, this improves the mixing of the boundary layer and the bulk flow, increasing the turbulence and allowing flow to remain attached to a surface. These types of plasma actuators work in a similar way to a passive vortex generator however with the added benefit of being flush to the surface and electronically controllable making them ideal for active flow control.

When focusing more on maximising the induced jet velocity, the exposed electrode design that has seen the most success is the serrated electrode. Joussot et al. [74] and Liu et al. [75] both studied this geometry in depth in two different studies. They both found that the serrations pinched the induced air flow creating a series of higher velocity jets of around $6ms^{-1}$. Despite using a similar exposed electrode design and obtaining similar results, the input voltage and

frequency along with the material construction of the actuator differ greatly between these two studies. This again highlights the difficulty when comparing two studies as on the surface they seem similar but, with so many input variables to choose from, they can in reality be quite different.

Moving away from exposed electrodes, Erfani et al. [83] focused their study on the make up of an encapsulated electrode. They proposed a staggered encapsulated electrode that is gradually positioned higher in the dielectric material. In theory this should improve the electric field strength whilst insulating the nearest section of encapsulated electrode from the exposed electrode. With this method they were able to improve the induced velocity of a rectangular electrode from $1ms^{-1}$ to $2.8ms^{-1}$.

The Erfani et al. investigation exploits the relationship between electric field strength and dielectric material thickness. For the same material, the thinner the dielectric material, the stronger the electric field [84]. Despite this, some level of dielectric material is required as the high frequency, high voltage used to generate plasma readily breaks down the dielectric layer eventually leading to arcing. Rodrigues et al. [85] studied the effects of 4 different dielectric materials analysing the mechanical power output. This refers to the rate at which work can be done by the actuator which is defined as the measured force multiplied by the velocity output. Whilst they found an actuator using a Kapton dielectric generated the highest mechanical power for a given voltage, a Silicone dielectric was able to hold a higher voltage, ultimately surpassing the maximum mechanical power output of the Kapton actuator.

This brings us finally to input parameters, namely the input voltage and frequency. Thomas et al. [84] showed how increased voltage always resulted in increased thrust. However, they were quick to note that different dielectric materials and material thicknesses saturated at different voltage levels, ultimately imposing a mechanical cap on the maximum voltage and thrust generated.

The effect of input frequency has a lesser correlation with velocity output. Thomas et al. [84] and later Ruisi et al [69] found that the optimum frequency for induced velocity varies depending on the design of the actuator. This can also be seen by comparing the previously mentioned studies as they all use vastly different input parameters to generate their jets.

One of the main challenges with plasma actuators is measuring the near wall jets. Loadcells have been used to measure thrust generated, however, if one wishes to capture the induced velocity other techniques are required. One technique is the use of Pitot tubes; these should be made from non-conductive materials and elliptically shaped to reduce the effect of flow acceleration around the walls of the tube [86]. A more complex method would be to use Laser-Doppler Anemometry (LDA) [74], this method allows for very near wall measurements and also provides high frequency resolution of the flow. A similar data rate can be obtained by using a hot-wire probe however, the use of conductive equipment near a plasma actuator is not advised.

Accurate simulation of plasma actuators is difficult due to the complex physics of ionised

gases combined with electric fields and regular air molecules. Futrzynski et al. [87] and Bart et al. [88] created CFD models of actuator applications by adding an additional body force term to the Navier-Stokes equations creating a jet. Then, using a series of flow interrogation regions, the simulated jet was tailor to experimental data of plasma actuators. One additional observation is that the simulations maintained a no slip condition at the surface of the plasma actuator. It is extremely challenging to measure the induced velocity created by a plasma actuator at the surface however, as the flow is being influenced by a magnetic field as opposed to a regular jet of air, this could nullify the no-slip assumption.

Active flow control applications

The most common form of active flow control is through the use of pulsed jets. Similar to the flap cases discussed in connection with passive flow control (see section 2.2.1), Joseph et al. [89], Zhang et al. [90] and Wang et al. [91] all tested the implementation of jets at a variety of locations across the rear slant of the 25° Ahmed vehicle. The main conclusion from these studies was that a jet located at the beginning of the rear slant provides the highest performance as it promotes shear layer mixing and improves flow attachment along the angled surface, on average, achieving a 14% drag reduction.

In a similar vain, Bruneau et al. [60] combined pulsed jets on the C pillars of an Ahmed vehicle with suction at the top of the rear slant. This improved the flow attachment over the trailing edge of the vehicle. The addition of pulsed jets on the base helped to promote shear layer mixing around the side of the vehicle, further reducing the size of the recirculation region. This combination resulted in a drag reduction of 13%.

As touched upon in section 2.2.1, flaps are commonly used as passive flow control devices. Kim et al. [92] implemented a“bio-inspired" flap attached at the beginning of the trailing edge slant of a 25° Ahmed vehicle. The novelty in this design was that the flap was not fixed in position, like in the passive flow control cases, but was free to oscillate in the unsteady wake of the vehicle. It was shown that a drag saving of 19% could be achieved using this method and that a light, stiff material was best suited for this application.

Plasma actuators have also been used as flow control on the Ahmed vehicle. Kim at al. [76] implemented a wire design, producing jets of air to close the small separation bubble that forms as the flow over the Ahmed body detaches slightly over the trailing edge slant. This provided a maximum drag reduction of 10%.

2.2.3 Other examples of flow control application

Naturally, flow control devices are not unique to the Ahmed vehicle and have been used on a wide range of bluff body geometries. This final section will briefly discuss some, non Ahmed vehicle related, studies that were also of particular interest during this research and show the

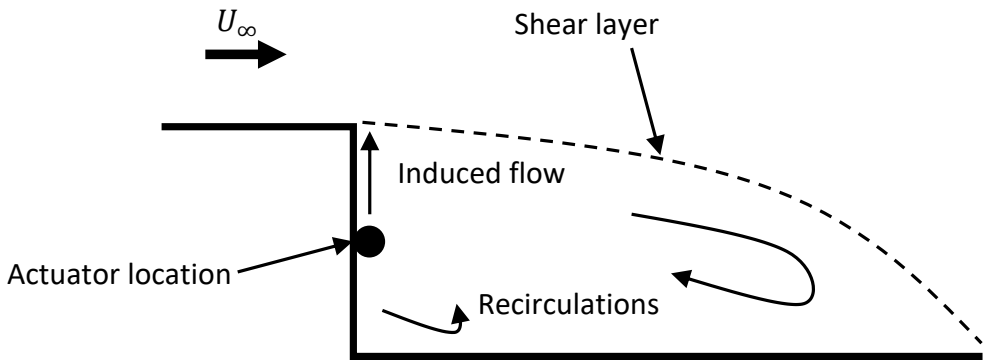

Figure 2.8: Schematic of plasma actuator implementation on a backwards facing step. Drawing based on data from a study by D'Adamo et al. [4]

wide range of options when implementing flow control techniques. Choi et al. [93] and Clapperton et al. [94] both utilised surface normal jets on two different cylindrical geometries to trip the boundary layer development and subsequently delay separation. This technique resulted in a drag saving of 15% and highlights further how constant jets can be utilised to influence the flow and promote shear layer mixing for better flow manipulation.

For more extreme bluff body cases where the flow separates over a sharp trailing edge, drag reduction can be obtained by the use of pulsed jets to excite modes in the shear layer. The most classic example of this type of geometry is the backwards facing step. D'Adamo et al. [4] used a plasma actuator positioned on the base of the step, directing a jet vertically into the shear layer, as shown in figure 2.8. When pulsing the actuator close to the shear layer's natural frequency of $10Hz$, they were able to disrupt the shear layer in such a way that the size of the wake and the reattachment length were reduced. A similar result was found by Oxlade et al. [95] for a configuration where the jets were directed in the streamwise direction.

On a similar trend, Roy et al. [82] applied flow control to the rear of a lorry type model. As before, this model had a sharp trailing edge resulting in abrupt flow separation. At a Reynolds number of $1 \cdot 10^5$, Roy et al. were able to reduce the drag of the lorry by 14% by adding three, finger type, plasma actuators on the exposed sides at the rear of the model. The actuators produced jets with a velocity of approximately 20% of the free stream velocity but also with a strong three dimensional component to promote shear layer mixing and therefore reduce the length of the wake. A similar method was later adopted by Lo et al. [96] who implemented a linear actuator at the rear of a fully articulated HGV model obtaining a similar result.

Vernet et al. [78] later used a similar lorry model, however, the focus of this study was flow control at the leading edge. Again using plasma actuators, at a Reynolds number of $5 \cdot 10^6$, they were able to maintain flow attachment over the curved surfaces of the leading edge, reducing the drag especially under yaw conditions.

Further information on a variety of active flow control techniques and analysis of their ap-

plication can be found in the review papers by Cattafesta et al. [97] and Wojewodka et al. [98].

2.2.4 Conclusions

When working with the Ahmed vehicle it has been shown that, even the application of a fairly rudimentary flap can serve as an effective form of flow control. There are two main flow control designs for the 25° case, the first is to promote flow detachment over the rear slant, reducing the base pressure, and the second is to encourage boundary layer mixing to enhance flow attachment and shrink the small separation bubble that forms at the beginning of the trailing edge slant. Both methods have been proven to be effective ways to reduce the drag of the Ahmed vehicle.

When promoting separation, a simple flap at the beginning of the rear slant is sufficient. However, when attempting to improve flow attachment there are a much larger range of options. Whilst vortex generators have proven effective, a more elegant solution is the use of jets or plasma actuators. Whilst these techniques are less invasive to vehicle design it can prove challenging to generate a jet with enough momentum to influence the free stream, something that will only become more difficult as model size and free-stream velocity are increased to full scale conditions.

2.3 Platooning

In the context of transportation, platooning refers to the driving of two or more vehicles as a group for a prolonged period of time. Platooning can help to use roads more efficiently improving traffic flow, but the aspect of platooning of most interest to this project are the potential aerodynamic benefits of two or more road vehicles following each other closely.

An early example of platooning research was conducted by Zabat et al. in association with the Partners for Advanced Transit and Highways (PATH) Program in California in 1995 [23]. The purpose of their wind tunnel investigation was to measure how vehicle drag was affected by vehicle spacing for platoons of 2, 3 and 4 vehicles. The PATH Program was founded to investigate ways to reduce air pollution, and platooning was highlighted as one way to improve vehicle efficiency which is directly correlated with a reduction in emissions. In their study, Zabat et al. used one-eighth scale models of the 1991 GM Lumina APV (a minivan). This work showed the effectiveness of platooning as a drag reduction and fuel saving concept. At short inter-vehicle distances, the platoon members received drag reductions of between 40% and 80%, depending on the number of vehicles involved and location in the platoon. As the inter-vehicle distance grew, the benefits seen on the front vehicle in the platoon reduced fairly quickly, returning to a value similar to the isolated case at a distance of around 1 vehicle length. For the rear vehicles however, drag reduction in the order of 20% were still visible at the largest inter-vehicle distance tested of 3 vehicle lengths. These tests were carried out at a Reynolds number of $4 \cdot 10^5$, whilst

this is lower than usually seen in a real world setting the results undeniably highlight the great potential of this technique.

In a later study, Tsuei and Savaș [99] expanded on the drag measurements taken by Zabat et al. in a wind tunnel investigation of platoons of cuboids and of 1/20th scale models of the 1997 Buick LeSabre. Again, in this investigation platoons of 2, 3 and 4 vehicles were tested. In line with the previous result, considerable drag reductions were observed with the greatest drag reduction occurring for the platoon of 4 vehicles. It was also worth noting that the cuboid model, the less streamlined of the two vehicle models used, recorded greater reductions in drag coefficient when compared to the Buick model. These two early investigations provided promising results and influenced the full scale road tests that followed.

2.3.1 Road tests

In an early investigation by Tadakuma et al. [100, 101], they showed that the positive effect of platoons seen in experimental data could be translated to real world applications. Using an oval track, they ran a platoon of two sedan cars and a platoon of a microbus followed by a sedan. The vehicles drove at $25ms^{-1}$ and inter-vehicle distances of $10m$ to $60m$ were trialed. They found that the microbus-sedan platoon was the most efficient, resulting in a drag reduction of 30% for the rear vehicle at a distance of $30m$. This drag reduction translated to a 5% fuel save for the platoon.

Whilst the effectiveness of platooning has been proven to translate well to full scale testing, the practical feasibility of platooning has also needed to be determined. In the road tests of the Safe Road Trains for the Environment (SARTRE) project [14], a platoon composed of two trucks and three saloon cars was tested. To create a fully functioning platoon, all vehicles were fitted with proximity sensors and control technology was used that was readily available on the open market. This study demonstrated that it is possible for the vehicles in the platoon to follow each other safely at close spacing using current technology. This also proved the practical feasibility of platooning in realistic traffic environments with particular emphasis on the ability to leave all road networks untouched.

The PATH study also developed their testing further, moving to a field test of a platoon of 3 tractor-trailer lorries [9]. An electronic platoon control system was tested in not only accelerating, decelerating and maintaining a constant speed but also conducting maneuvers such as joining a pre-existing platoon or splitting a platoon thus showing the versatility of platooning when implementing a control system. Gaps of $4-10m$ were tested and fuel savings of $10-14\%$ were recorded. It was noted that strong winds made the results fairly inconsistent highlighting one of the biggest difficulties with road testing as there are a number of additional, uncontrollable, factors for this type of investigation. A summary of the PATH program was provided by McAuliffe et al [24].

More examples of the use of control systems for on the fly platoon generation are discussed

in the two papers by Liang et al. [15, 16]. Using 3 HGV's on a motorway in Sweden, they investigated further how platoons can co-exist with other vehicles on a motorway. They were also able to generate a fuel saving of 20% over the course of an $11km$ journey.

Finally, Nuszkowski et al. [25] trialed a two vehicle box truck platoon. Using both a measurement of fuel usage and by taking air velocity readings at the front of each truck, they were able to report a 10% fuel save for the rear vehicle in the platoon. Whilst this is a sizable fuel saving, they did note that current highway laws would consider the inter-vehicle distance used to achieve this drag reduction as unsafe and at the designated safe distance the fuel save was reduced to 8%. This again highlights another struggle for platooning as current legislation makes it difficult to achieve the best possible outcomes.

These road tests are fundamental to the further development of platooning. They very clearly indicate that the ability to generate drag reductions through platooning is already feasible, along with all the technology required to make their integration into regular traffic possible. Obviously, busier roads will slightly reduce the efficiency of each platoon,however, even when traveling at safe distances, measurable gains can be made. The studies outlined primarily focused on HGVs as they are best suited for this drag reduction technique. However, their success highlights that more investigations are necessary on a wider range of geometries and vehicles to fully understand the scope of possible gains achievable from platooning.

2.3.2 Classical platooning

When investigating the fundamental aerodynamic properties of platoons, it is important to start with vehicle geometries that are simple and well understood. This allows to build up the complexity gradually and to evaluate each change in geometry individually. In the study by Uystepruyst et al. [102], a platoon of four cuboid vehicles was analysed using large-eddy simulations (LES) at $Re_H = 10^5$. The spacing between the geometries is denoted as d/L where d is the distance between the vehicles and L is the length of the vehicle. Uystepruyst et al. investigated the effects of changing the location of a single vehicle in the platoon where the baseline separation was $d/L = 0.4$. In this configuration the lead vehicle experienced a 15% reduction in drag. A much larger drag reduction of $70-75\%$ was observed for the middle vehicles with the rear most vehicle receiving a lower drag reduction of 60%. This is a classical example of the behaviour we would expect from a platoon: the lead vehicle receives a small drag reduction due to the reduced pressure difference caused by the presence of a vehicle in its wake and in doing so, shelters the following vehicles which as a result experience large drag reductions. The cuboid case was designed to mimic HGVs and the results were similar to experimental tests on HGVs [103] and the HGV road tests discussed in section 2.3.1 showing the applicability of simplified models when used in this context.

The theme of targeting HGV-like geometries was continued in a study by Robertson et al. [104] where an experimental study of a platoon of eight lorries at a Reynolds number of $3 \cdot 10^5$,

based on vehicle height, was conducted. Three inter-vehicle distances were investigated, $d/L = 0.5, 1.0$ and 1.5. At $d/L = 0.5$ the lead vehicle received a 15% reduction in drag coefficient, whilst at the higher separation distances the drag coefficient was relatively unchanged. Moving down the platoon however, large drag reductions were measured for all following vehicles at all spacings considered. The largest reduction in drag coefficient was observed for the second vehicle when the lorries were closest together. In this setup the second lorry experienced a 65% drag reduction. Robertson et al. continued this work with a second paper [105] focusing on the unsteady oscillations in and around the platoon. It was noted that two main transitory oscillations exist. A strong low frequency oscillation of several vehicle lengths was measured over the whole platoon,independent of vehicle spacing, whilst a secondary higher frequency oscillation was present between the vehicles with a wavelength of around 0.5L.

The experimental data collected by Robertson et al. was later used to validate two Computational Fluid Dynamics (CFD) studies on platoons composed of eight lorries [36, 37], thus providing one of the most complete sets of comparable data in the field of platooning. Initially, He et al. [36] used delayed detached eddy simulations (DDES) to simulate the platoon at a Reynolds number of $3 \cdot 10^5$ in alignment with the experimental data. Whilst there was some slight variation between the simulated and experimental drag coefficients for the isolated vehicle case, the results from the platoon case were extremely consistent between simulations and experiments. The only other discrepancy between experimental and simulated data was found for the final vehicle in the platoon where the simulation over-predicted the drag value by around 10%. Whilst DDES was able to predict the drag forces with good accuracy, the low frequency oscillations present in the Robertson et al. [105] study were not captured.

Zhang et al. [37] further built upon this work using improved delayed detached eddy simulations (IDDES) to analyse the effects of a lorry platoon running through a tunnel. As in the previous studies, significant reductions in the drag coefficient were observed for all vehicles in the platoon with the middle vehicles receiving the greatest benefits. When entering a tunnel, the drag coefficient for each vehicle in the platoon increased with the leading four vehicles being the worst affected. Whilst the drag coefficients increase in the tunnel compared to standard road / open air conditions, it is the normalised drag compared to vehicles in isolation travelling through a tunnel that needs to be considered. As the drag coefficient of an isolated lorry driving in a tunnel is also increased when compared to driving in open air, platooning in tunnels proved to be even more effective way to reduce drag with the best performing lorry experiencing only 30% of the drag experienced by a lorry travelling in isolation through a tunnel.

Further experimental work on HGV models was carried out by Törnell et al. [18] where a fully articulated two lorry platoon was analysed both computationally and experimentally. As seen in the previous studies, drag benefits were observed for both vehicles in the platoon. The highest drag reductions were achieved when the vehicles were close together $(d/L = 0.18)$ with the front and rear lorries receiving a 30% and 40% drag reduction respectively. As the inter-

Author	ϕ	Re_H	Method
Watkins and Vino [27]	30	$6.34 \cdot 10^5$	Experimental
Uystepruyst et al. [108]	30	$3.90 \cdot 10^5$	Computational
Mirzaei et al. [109]	25	$3.00 \cdot 10^5$	Computational
Gnatowska et al. [110]	25	$0.39 \cdot 10^5$	Both
Bruneau et al. [111]	0	$0.15 \cdot 10^5$	Computational

Table 2.1: Overview of Ahmed geometry platoon investigations from the literature.

vehicle distance was increased, the drag coefficient values for both vehicles gradually increased approaching the drag coefficient of an isolated lorry. A Reynolds number dependency study was also conducted and the system was found to be Reynolds number independent for values greater than $1.5 \cdot 10^6$, when using vehicle height as a reference value. The lead vehicle received up to a 60% higher drag coefficient at lower Reynolds numbers with the rear vehicle also observed a drag increase at lower Reynolds numbers, however, only in the region of $5-10\%$. Finally, Törnell el al. analysed the effects of small yaw angles and found that using a lateral offset between the vehicles in the platoon can improve the efficiency when traveling in a cross-wind.

2.3.3 Ahmed geometry platoons

All of the research outlined in sections 2.3.1 and 2.3.2 focused on the benefits of HGV platoons. With this in mind, it would be reasonable to expect that (almost) any group forming a platoon would experience a reduction in drag since platooning is a strategy also found in the context of road cycle racing [106, 107], motor racing, swimming, and even nature in the flight of flocks of birds or schools of fish. Whilst it is easy to assume that a platoon of vehicles would always result in drag reduction, this is not a trivial result as there are many exceptions and the flow regimes around these platoons are extremely complex.

The current section analyses the results of Ahmed vehicle platoons, a common simplified vehicle geometry discussed in length in section 2.1. In this section we will explore a number of examples where platoons do not provide a drag reduction for the rear vehicle. We have given this phenomenon the term 'inverted platooning' as where we would traditionally expect to see a rear vehicle having a drag reduction when platooning, said vehicle instead receives a drag increase.

As discussed in section 2.1 an advantageous way to analyse complex aerodynamic systems is through the use of simplified vehicle geometries. The Ahmed body is the most studied and well understood simplified vehicle geometry so naturally, there are a number of platooning investigations that also utilise this geometry. An overview of these studies is outlined in table 2.1, highlighting the Reynolds number and method used.

An early example of an Ahmed vehicle platoon is the experimental study by Watkins and Vino [27]. Two Ahmed bodies with a 30° rear slant were used and the investigation measured the lift and drag coefficients over a wide range of vehicular spacing. At short distances ($d/L < 1$),

where classically the platoon is most efficient, the rear vehicle receives a large increase in drag in the order of $25-35\%$ whilst the front vehicle is the one to see the benefits, receiving a drag reduction of around 55%. This is the opposite of what was observed in other platooning studies. The authors conclude that the result is counter intuitive however, they note that as traffic spacing is likely to decrease in the future, further efforts should be made to improve the understanding of this phenomenon. They also suggest that the strong rear vortices produced by the Ahmed vehicle could be one reason for the increase in drag.

Whilst it is counter-intuitive, there is enough evidence to support the results that, for some platooning cases, the rear vehicle receives a drag increase when part of a platoon. Through the use of LES, Mirzaei et al. [109] provided deeper insight into the flow structures of this complex system in order to further understand the underlying reasons behind the drag increase. Two 25° Ahmed bodies were analysed at three inter-vehicle distances of $d/L = 0.3, 0.5$ and 1. Mirzaei validates their results using the Watkins study although it is important to note that the two studies use a different geometry and Reynolds number(See Table 2.1). This is reflected in the results as Mirzaei measures a drag reduction for both vehicles at $d/L = 0.3$ and 1 with the rear vehicle having a maximum normalised drag coefficient of 1.007 at $d/L = 0.5$. The general trends seen in both papers are similar however, with the rear vehicle consistently having the higher drag of the two vehicles. Mirzaei provided a detailed description of the flow features around the vehicles and noted that the wake impingement produced an area of high pressure on the leading edge of the rear vehicle, however, the root cause of the inverted platoon conditions remained unclear.

Following this, a combined experimental and computational study on the 25° Ahmed vehicle platoon was carried out by Gnatowska et al. [110]. A comparison between steady-state RANS simulation and experimental data was made at a Reynolds number of $0.39 \cdot 10^5$. This highlights one of the biggest challenges in platooning research as there are not many wind tunnels with long enough test sections to house a platoon at high Reynolds numbers. Despite this, the experimental results were qualitatively very similar to the results provided in the Watkins paper discussed earlier, with the rear vehicle observing a 20% increase in drag at $d/L = 0.4$. Another interesting outcome from this study was that whilst the RANS simulation was able to correctly predict the presence of inverted platooning, there was not much correlation between the experimental and computational results. This could indicate that the turbulence is too complex for a steady-state solver.

Further computational research on an Ahmed vehicle platoon was conducted by Bruneau et al [111]. In this study, a platoon of two squareback Ahmed vehicles was investigated. In addition, some active flow control in the form of two horizontal jets at the rear corners of the front vehicle in the platoon were applied. The jet velocity was 0.6 of the free stream velocity. Whilst the front vehicle in the platoon received a 20% drag reduction, the drag coefficient of the rear vehicle increased by 3% when compared to an Ahmed platoon without flow control.

This was followed by another study by Bruneau et al. [111] where a RANS approach was

implemented using a platoon of two and three squareback Ahmed vehicles at three separation distances of $d/L = 0.2, 0.5$ and 1. The study was conducted at a Reynolds number of $0.15 \cdot 10^5$, whilst this is the lowest of the papers discussed, the results show that the squareback variation of the Ahmed vehicle performs better in a platoon than the versions with a rear slant. For all inter-vehicle distances analysed, both vehicles are shown to have drag reductions of at least 10% with a maximum drag reduction of 36% for the rear vehicle at $d/L = 0.2$. Whilst this could be due to Reynolds number effects, it suggests that the larger wake produced by the squareback Ahmed vehicle (as discussed in 2.1) provides a better shelter for the rear vehicle, improving the performance of the platoon.

In a slightly more unique study using an Ahmed vehicle platoon, Uystepruyst et al. [108] investigated how wake structures effect passing vehicles. This is essentially a look at platooning whilst the vehicle's centre planes are laterally offset. Through the application of URANS, two 30° Ahmed vehicles were analysed for a d/L range of -2 to 2. The primary focus was to understand the lateral forces on vehicles as they pass one another however, it was interesting to note that the rear most vehicle consistently saw an increased drag coefficient despite the offset. This is noteworthy as it suggests that the rear vehicle interfering with the recirculating region of the front vehicle is not the sole cause for inverted platooning conditions.

In recent years there has been an upturn in the number of computational investigations into Ahmed vehicle platoons, all of which are in agreement with the inverted platooning result [112]. It has been shown that the addition of more vehicles has diminishing returns on the overall performance of the platoon but can be used to limit the extent of inverted conditions for vehicles in the middle of the platoon [113, 114].

2.3.4 Additional inverted platooning results

Inverted platooning conditions is not a unique result effecting only platoons of Ahmed vehicles. In an experimental investigation, Le Good et al. [28] analysed how platoons are affected by vehicle shape. Here the MSM vehicle model was used at a Reynolds number of $0.7 \cdot 10^5$ based on the vehicle length, a Reynolds number at the lower end for platooning studies (note that whilst some effort has been made to convert all Reynolds numbers to be referenced with respect to model height, obtaining additional details such as name and dimensions of the MSM model was challenging therefore this value was not converted). The MSM vehicle was designed to be a stylised but simplified version of a passenger vehicle and has a much smaller and more streamlined shape when compared to HGVs. Whilst the HGV-based research exclusively showed platoons improving aerodynamic efficiency, platoons of 2, 3 and 4 MSM vehicles provided drag penalties for all vehicles involved. This highlights how inverted platooning conditions are not solely a property of the Ahmed vehicle and can occur when other geometries are used for platooning.

As part of their study, Le Good et al. investigated the influence of a modification of the vehicle geometry. The MSM vehicle was modified to have any combination of square leading

and trailing edges, reducing the streamlined nature of the original vehicle. It was shown that by giving the lead vehicle a square back, the size of the wake was increased, and all of the platoon members received drag savings. These drag reductions were further improved by adding square edges to the ends of all inter-vehicle platoon members. Le Good et al. concluded that whilst a low drag geometry is advantageous for isolated vehicles, a streamlined shape appears to hinder a vehicle's effectiveness in a platoon.

This idea is further supported in the study by Gheyssens et al. [34] where the $k-\omega$ SST RANS solver was used to analyse the effect that the radius of the vehicle's leading edge has on a platoon of three Generalised European Transport System (GETS) vehicles. The GETS model closely resembles the geometry of a cuboid, therefore, when the leading edge radius was small, all of the vehicles in the platoon obtained a drag reduction. This is in line with the cuboid platooning results quoted in the previously mentioned Uystepruyst et al. [102] study. As the leading edge radius was increased however, the rear most vehicle began to see an increase in drag similar to the inverted platooning conditions discussed in the Le Good et al. [28] research. This highlights the sensitivity of platooning to geometric shape and why it is important to improve the understanding of this interaction.

Le Good et al. [115] built upon this work further in their experiment of a platoon of three Windsor vehicles at a Reynolds number of $2.78 \cdot 10^5$. Using simplified vehicle models, such as the Windsor vehicle, is key to understanding the fundamentals of the complex aerodynamics of a platoon. By adjusting the trailing edge slant, Le Good further identified the sensitivity of platoons and the geometries that tend to provide drag reductions. 27 unique combinations of 0°, 10° and 25° slant angles were used and the mean drag reductions for the platoons ranged from 12% to 21%. Although the mean drag for each platoon decreased, not all of the vehicles in the platoon received a drag reduction. This provided an interesting insight where although inverted platooning conditions were present, the platoon as a whole benefited from one vehicle playing a, somewhat, sacrificial role.

To understand this relationship further, Macaskill et al. [116] used 4 different Windsor model configurations analysing 7 different platoon combinations to understand the effects of vehicle geometry on platooning. The 4 geometries consisted of a combination of two leading edge geometries (one stepped and one flat) and two trailing edge geometries (one squareback and one with a 25° slant). Here all of the platoons displayed inverted platooning conditions however it was noted that the optimum distance between the vehicles varied depending on the vehicle geometry. Macaskill highlighted this as a potential downfall to the implementation of platooning given the wide range of vehicle geometries on the roads today.

The phenomenon of inverted platooning is not restricted to simplified vehicles or experiments at low Reynolds numbers. Ebrahim et al. [103] used a RANS computational method with a $k-\varepsilon$ turbulence model to simulate a platoon of 2 and 3 Nissan Leaf 2016s at a Reynolds number of $5.23 \cdot 10^5$. The leaf is a small electric hatchback and the visualisations provided show

Author	Method	Model (ϕ)	Re_H	n range
Džijan et al. [118]	RANS $k-\varepsilon$	Race Car	$9.38 \cdot 10^5$	2
Ebrahim et al. [103]	RANS $k-\varepsilon$	Nissan Leaf 2016	$5.23 \cdot 10^5$	$2-3$
Gnatowska et al. [110]	RANS $k-\varepsilon$	Ahmed (25°)	$0.39 \cdot 10^5$	2
Bruneau et al. [111]	RANS $k-\omega$	Ahmed (0°)	$0.15 \cdot 10^5$	$2-3$
Gheyssens et al. [34]	RANS $k-\omega$ SST	GETS	$5.92 \cdot 10^6$	3
Uystepruyst et al. [108]	URANS $\zeta-f$	Ahmed (30°)	$3.90 \cdot 10^5$	2
He et al. [36]	DDES	HGV	$3.00 \cdot 10^5$	8
Zhang et al. [37]	IDDES	HGV	$3.00 \cdot 10^5$	8
Mirzaei et al. [109, 119]	LES	Ahmed (25°)	$3.00 \cdot 10^5$	2
Uystepruyst et al. [102]	LES	Cuboid	$1.00 \cdot 10^5$	4

Table 2.2: Overview of computational platooning investigations from the literature.

that it produces a very small wake. When in a two vehicle platoon, the small wake is perfect for creating inverted platooning conditions with the rear vehicle receiving a 5% increase in drag at a distance of $d/L = 0.25$. In this case however, the addition of a third vehicle provided a large enough change resulting in each vehicle in the platoon receiving a drag reduction. This result was then built upon further by Ebrahim et al. [117] using the DrivAer model where again, inverted conditions were observed.

Džijan et al. [118] also used the RANS $k-\varepsilon$ method to analyse a platoon of race cars. Naturally, race cars are designed to be very low drag in isolation therefore, in accordance with the work by Le Good et al., should also exhibit inverted platooning conditions. for d/L values greater than 2, the two vehicles have little to no influence on each other. However, in the region of $d/L = 0.5$ to $d/L = 1.5$ the rear vehicle receives a drag increase of up to 7%. In addition to this, for all distances up to $d/L = 2$, the front vehicle has a lower drag coefficient than the rear vehicle. This goes some way to highlighting the importance of further research in this area. Whilst there is some understanding of what geometries perform poorly in platoons, there is currently no in depth explanation to why this is the case.

2.3.5 Computational methods for platooning

A key factor that makes platooning research particularly challenging is the size of the platoon. Having multiple models requires larger simulation domains and the complex flow features can very quickly drive up cell counts making simulations computationally expensive. An overview of the computational research on platooning is given in table 2.2, it is worth noting the wide range of computational methods used.

Applying a steady state RANS method is a very computationally efficient way to tackle this problem. A number of papers adopted this technique paired with the $k-\varepsilon$ turbulence model [103, 110, 118]. One of the main benefits of this technique is that good approximations of drag values can be obtained with relatively small mesh sizes, keeping computational costs

low. Gnatowska et al. [110] made use of this in their study using a tetrahedral mesh of 600,000 cells. Whilst the computational results showed a qualitative match to experimental results, the drag coefficients predicted by the simulation were not in agreement. This could indicate that the turbulence model used was not accurate enough however this result could also be caused by inadequate cell density. Ebrahim et al. [103] and Džijan et al. [118] took cell density to the other extreme. Both studies utilised mesh sizes in excess of 25 million cells. Whilst the drag values predicted by these simulations were near matches to the associated experimental drag values, these simulations are much more computationally expensive somewhat defeating the purpose of using a simplified turbulence model.

One of the more optimum turbulence solvers for RANS simulations when analysing isolated vehicles was the $k-\omega$ SST solver discussed in section 2.1. This solver was able to achieve good accuracy with drag coefficient estimations at a relatively low cell count of around 4 million. Gheyssens et al [34] and Bruneau et al. [111] both applied this method to platooning simulations of simplified vehicles. Despite its benefits in isolated vehicles, Bruneau et al. found that their simulation became grid independent at the much higher cell count of 755 million cells. Gheyssens used a tetrahedral meshing scheme with far fewer cells and were still able to achieve good agreement with experimental results.

Uystepruyst et al. [108] analysed the results of three different mesh densities using URANS with the $\zeta - f$ solver. Not only did they find that the results from their 6 million and 8 million meshes to be very similar, both mashes showed good similarities with experimental data.

Another computational method often applied is LES. This model simulates the turbulent kinetic energy in significantly more detail than RANS methods however it is usually significantly more computationally expensive. Uystepruyst et al. [102] and Mirzaei et al. [109] both utilised this technique to simulate platoons of simplified vehicles.

In order to avoid excessive cell counts, hybrid URANS-LES methods are more commonly used. In this method, the eddies are characterised using LES with URANS being applied to the near wall flow. He et al. [36] and Zhang et al. [47] used DDES and IDDES respectively to analyse the turbulent flows around a platoon of 8 lorries. These two techniques are similar with both investigations using comparable platoon sizes and domain sizes. Whilst both methods achieved good agreement with the experimental drag data referenced, the IDDES method acheived this with 34.9 million cells when compared to 52 million cells used in the DDES investigation. Both simulations provided a significant improvement in the detail and reliability of the flow visualisation however the DDES method was unable to capture the lower frequency oscillations observed in the associated experimental validation case [105].

It is clear that the cost of stimulating a platoon requires some trade-offs. Using LES, Mirzaei et al. [119] considered a way to analyse two vehicles in a long platoon of Ahmed vehicles. Two computational regions were considered: the first included an entire Ahmed vehicle with a rear half upstream and a front half downstream, the second was comprised of only the inter vehicle

space with the trailing edge of the front car and the leading edge of the rear car included in the domain. The two domains consisted of 8.5 and 4.2 million cells respectively, a significant decrease on similar LES studies. Whilst drag measurements are difficult to obtain when incomplete vehicles and wakes are simulated, the streamlines and turbulence intensity between both computational regions were in good agreement showing that this technique can be a useful tool for purely flow physics related investigations.

Another way to optimise platooning investigations was conducted by Ebrahim et al. [120] where they analysed wake generators as a way to both reduce computational costs and as an alternative in wind tunnel investigations. Ebrahim found that, for a platoon of two Ahmed vehicles with a 25° trailing edge slant, when the lead vehicle was half of the usual Ahmed body length the drag coefficients for both vehicles were relatively unchanged. As one would expect, the shorter lead vehicle was slightly less reliable however the results stayed within 5% of the results of a similar simulation using two full length models. Whist this study shows promise, it was carried out using the steady state RANS $k-\varepsilon$ RKE method that, as discussed previously, has had varying success at simulating the complex flow features of platoons accurately. Despite this, Ebrahim et al. provided a convincing validation case for each of the bluff body generators discussed, comparing not only drag coefficients but also lift coefficients, stream-wise velocity plots, surface pressures and velocity fields. All of this was achieved using a computationally efficient 4.6 million cell mesh.

In general, most computational studies compare drag coefficient data to experimental data as a way to validate their results. To provide a more in depth comparison, some investigations also compare lift coefficients, shedding frequencies and surface pressure measurements [34, 36, 103]. This extra layer of detail when validating is extremely useful for platooning studies as the flow structure is particularly complex. Where RANS simulations perform well at predicting drag values of vehicles in isolation, it has been shown to be less effective at predicting turbulent wake flow [2]. This could have a knock-on effect impacting the quality of the simulations for vehicles further downstream in the platoon.

The simulations discussed have a wide range of platoon members from 2 vehicles to 8 vehicles. Obviously these tho extremes will require different domain sizes for their computational investigation. In general, the domain began $3-5$L upstream of the first vehicle and ended $7-9$L downstream of the last vehicle. Whilst the extra length added to the number of cells in the domain, the variety of domain sizes had no notable effect on the results discussed. The main driver for increased cell count was not the domain size but the addition of refinements. Prism layers proved to be an effective method of capturing flow near the vehicle walls with staggered volume refinement radiating out from the vehicles.

2.3.6 Experimental methods for platooning

Where the length of a platoon can cause some issues for computational investigations, it is even more critical for experimental work. Most wind tunnel investigations are limited by cross sectional area or blockage, where test section length is less important. For platooning, test section length is the limiting dimension making it difficult to conduct experiments using full length vehicles. Even when using scaled models, wind tunnels capable of housing a platoon of more than 2 vehicles with variable vehicle-separation distances is hard to find. Whilst scaled models can help combat the space issue, the use of scaled models makes it challenging to achieve higher Reynolds numbers. A HGV on a motorway operates at a Reynolds number in the region of 10^8, in comparison, most experimental investigations reach around 10^5.

Using the Coventry University low speed, open test section, closed loop return wind tunnel, Le Good et al. were able to perform two independent platooning investigations. The test section length of this tunnel is $2.5m$. Le Good et al. [28] used 5 models in their first platoon study resulting in a Reynolds number of $0.7 \cdot 10^5$ (with respect to vehicle length). A bespoke, six axis, overhead force balance was used to measure the forces of one vehicle in the platoon with the other vehicles mounted on a ground plate. For this setup the force balance does not traverse. One drawback to this method is that the distance from the leading edge of the ground plate to the first vehicle changed depending on the platooning configuration being measured. The same setup was later used by Le Good et al. for 3 Windsor vehicles [115]. Fewer models allowed the models to be larger resulting in a Reynolds number of $2.78 \cdot 10^5$.

An alternative solution to wind tunnel testing was applied by Robertson et al. [104, 105] in two separate investigations of an 8 vehicle, $1/20^{th}$ scale, lorry platoon. Here, moving model experiments were conducted using the Birmingham Transient Aerodynamic Investigation (TRAIN) rig facility. Models are mounted on a $150m$ long track and can reach speeds of $75ms^{-1}$. A $20m$ suspended ground plate at the interrogation region was also installed. Static hole probes were installed on the models at various locations on the leading edge, trailing edge, roof and sides and were sampled at $5kHz$ to measure static pressure and 3 component velocities. This was later used to calculate the drag forces for each vehicle. Using this setup running at $25ms^{-1}$, a Reynolds number of $3 \cdot 10^5$ was achieved, something that would have been significantly harder to execute for an 8 lorry platoon in a traditional wind tunnel.

The majority of wind tunnel experiments use either single or 3 axis loadcells to measure forces on vehicles. This causes complications for platooning investigations as independent loadcells are needed for each vehicle. Additionally, if the effect of vehicle spacing is being investigated, a system needs to be put in place to allow the model and all associated mounts and measurement equipment to move with it. Watkins et al [27] used an internally mounted, 6 component, force balance to measure the forces on the movable vehicle. The experiments were conducted in the $9m$ long test section of the Royal Melbourne Institute of Technology(RMIT) Industrial, closed jet, Wind Tunnel. Two Ahmed vehicles were studied and thanks to the size

of this wind tunnel, $2mx3m$ cross section, a much higher than typical Reynolds number was achieved ($Re_H = 6.3{\cdot}^5$).

Törnell et al. [18] used both force balances and pressure taping for their experiment of two 1:6 scale HGVs. The highly detailed lorry models were $2.7m$ in length and were investigated at the Volvo Cars Aerodynamic Wind Tunnel. This tunnel includes a $5.3m \times 1m$ rolling road section. The force measurements for each model were taken one at a time using a force balance under the rolling road section and were averaged over 20s. Pressure sensors were mounted on the front, rear, sides and top of the models. time-resolving sensors were used on the measurement model and average sensors were applied to the other. Pressure taps were not mounted on any of the corners as these areas are very sensitive.

2.3.7 Conclusions

After analysing all of the previous results, it is clear that vehicle platooning has the potential to provide large drag reductions for road vehicles. Not only is the technology already available, the potential for savings is great. Unfortunately however, some challenges still remain. Where traditionally it is assumed that all slip-streaming will result in drag reductions, it is clear that there are a wide number of cases where that statement does not hold true. Whilst all of the studies measured a mean drag reduction, there were some results where the platoon would cause one or more vehicles to have an increase in drag, a term that we cave coined as inverted platooning. A number of studies have attempted to understand the causes of this somewhat counter intuitive interaction, however, no concrete answer has yet been determined. This highlights the need for further research in this area as improved understanding of this complex system has the potential to unlock large drag savings for road vehicles.

One of the main limiting factors in the field currently is that most studies are focused on maximising the drag savings instead of understanding the fundamental aerodynamics. Whilst Törnell et al. [18] investigated the effect of Reynolds number on a platoon, drawing any field wide conclusions is challenging as this appears to be the only test of its kind. This leads onto another difficulty in this field which is the diversity of investigations. With such a large array of variables such as Reynolds number, vehicle spacing, number of vehicles and even the vehicle models themselves, drawing parallels between studies is difficult, in turn making it difficult to make progress.

In our opinion, the key areas for future development of this research topic have to focus on understanding inverted platooning, only then will the efficiency and effectiveness of platooning really be able to progress. Testing focused on understanding why some platoons perform better than others, be it by altering vehicle spacing, speed, geometry or something else entirely, is key. Initially, it was prudent to show the benefits that platooning could provide to help encourage future studies however that fact is now very clear from the research discussed and it is time to focus more on understanding the complex aerodynamic systems involved.

In order to achieve this, future work should focus more on basic 2 vehicle platoons using simplified models. Mirroring how vehicle aerodynamics was investigated in the past, the use of simplified vehicles will allow the key flow physics to be more evident. This also makes comparison between research groups far easier as there is more consistency between studies. What was also becoming clear from the papers discussed was that additional vehicles in the platoon did not enhance the understanding of the physics of the platoon. Whilst extra vehicles improved the drag savings, the lead vehicle acts in a very similar way regardless of the number of vehicles behind, with the middle vehicles all experience very similar results to each other. Therefore, the additional information gained does not outweigh the added complexity for either experimental or computational methods. Experimentally a 2 vehicle platoon can achieve a much greater range of Reynolds numbers when compared to a longer platoon in the same facility (excluding the TRAIN facility) and a simulation of a 2 vehicle platoon can focus their cell budget more closely on the complexity when compared to a longer platoon.

In summary, platooning has undeniable potential to significantly reduce vehicle emissions and energy usage in the near future however there are still a number of unanswered questions that need to be solved before this can become a reality.

2.4 Project aim and objectives

As shown in the literature review, platoons have been investigated for a wide range of vehicles. However, due to the absence of a consistent approach between different studies, it is often unclear what causes the differences observed between different platoon configurations, such as ‘classical’ versus ‘inverted’ platoons. The main aim of this thesis is to create a better baseline knowledge of the flow around simplified vehicle geometries and to provide deeper understanding of the fundamental aerodynamics of platoons for future, more complex, designs. The secondary aim of this thesis is to explore whether flow control can help to alleviate or eliminate cases of adverse platooning performance.

One of the bigger problems with platooning, e.g., in the inverted cases, is that whilst in general a platoon as a whole is more efficient than two vehicles driving in isolation, if one or more vehicles are suffering an increase in drag it will be difficult to persuade individual road users to take part in a platoon. This is why the secondary aim is important. Whilst the addition of flow control could, in some cases, reduce the total performance of the platoon, a situation where all vehicles in a platoon are receiving some benefit will be much more favourable for the adoption of platooning by the wider community.

Focusing on vehicle platoons composed of two vehicles, a range of basic geometric features will be explored to provide a fundamental understanding of the cause of inverted platooning and give suggestions on how it is best avoided. There are many geometric parameters which affect the aerodynamic performance of ground vehicles. To limit the number of parameters,

the current study will focus on two-body platoons composed of Ahmed bodies of uniform size. Other geometric parameters, such as vehicle size, will also influence the behaviour of a platoon, but they are beyond the scope of the current study. The Ahmed body configuration has been chosen since it is one of the best documented cases for a simplified ground vehicle geometry in the scientific literature.

The specific objectives are outlined in the following bullet points:

- Investigate the geometric features, namely leading and trailing edge geometry, that create inverted platooning and provide a better understanding of its causes.
- Experimentally characterise a plasma actuator to asses its potential as a flow control device.
- Computationally explore the potential of different methods of flow control (flaps, plasma actuators) and how they can be used to alter the performance of a platoon
- Provide an experimental proof of concept for platoons with flow control.

Chapter 3

Shape dependency of platooning

3.1 Introduction

As discussed in chapter 2.3, ground vehicles can experience both 'classical' platooning and 'inverted platooning' conditions. In general, classical platooning conditions are to be preferred as they yield consistent drag reductions at close inter-vehicle spacing. However, there is no clear conclusion regarding what geometric features are causing inverted platooning. Watkins and Vino [27] hypothesise that the rear vortex structure of the front vehicle is the cause of increased drag on the following vehicle at close spacing. Mirzaei et al. [109] imply that the pressure induced by an impinging wake is the cause of the inverted platooning conditions, and Le Good et al. [115] simply conclude that inverted platooning is an 'interesting paradox'.

In this study, the influence of vehicle geometry on a platoon composed of two bodies is investigated with the aim to establish which geometry features trigger the change from 'classical' to 'inverted' platooning conditions. The inspiration for this study came from comparing two studies, one of a series of cuboids that displayed classical platooning conditions [102], and the other a platoon of Ahmed bodies that resulted in inverted platooning [27]. Whilst the outcomes between the studies were very different, the geometries used are remarkably similar as the addition of leading edge rounding and a rear slant being the only operations needed to transform a cuboid into a Ahmed vehicle. Therefore, in the present study, a cuboid geometry is systematically morphed into the more complex geometry of the Ahmed body with a 25° slant angle, a geometry known to produce inverted platooning conditions. The systematic, step-wise change in geometry gives insight to the specific geometric features that affect the change in drag experienced by members of a platoon.

This chapter is structured as follows. In section 2 the design of the investigation is outlined including the numerical model setup and computational method used. Section 3 outlines the results from both homogeneous and heterogeneous platoons and is followed by a discussion of the geometry features causing 'inverted' platooning conditions in section 4. Conclusions are given in section 5.

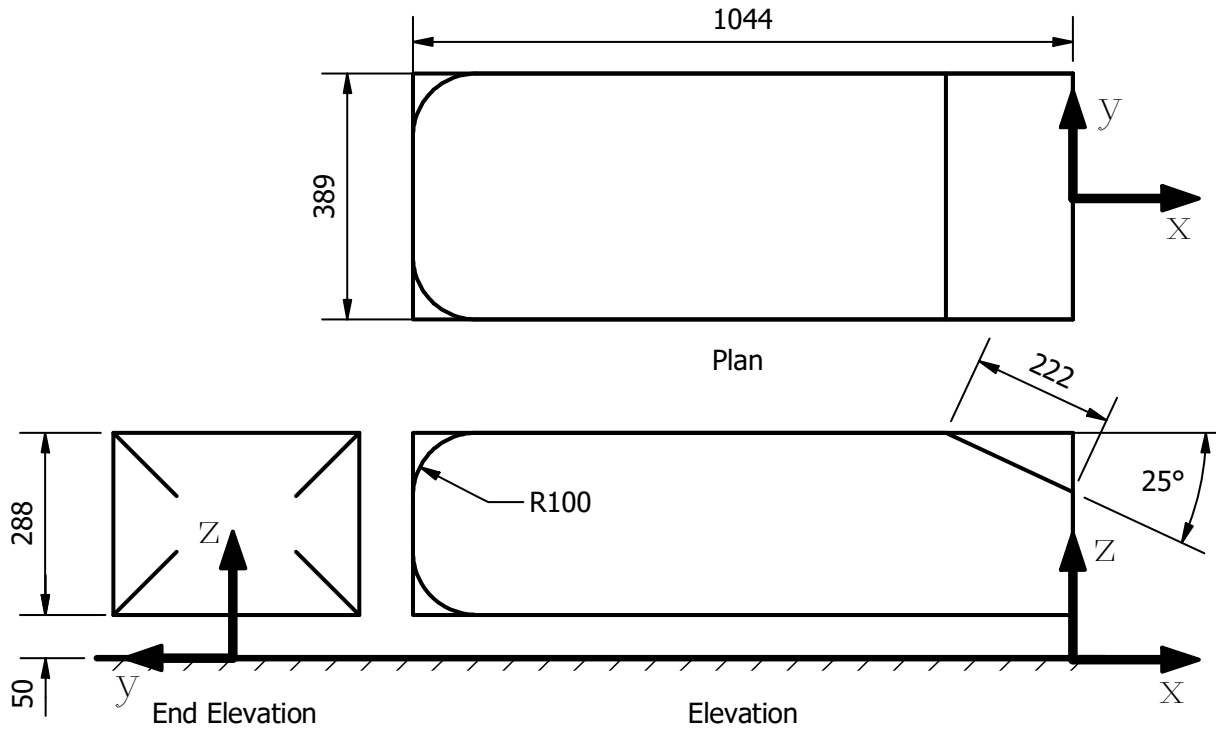

Figure 3.1: Basic vehicle geometry; all dimensions given in units of millimetres. By introducing leading edge rounding and a rear slant a Cuboid can be morphed into an Ahmed body with 25° rear slant angle.

3.2 Methodology

3.2.1 Design of investigation

In this investigation four different simplified ground vehicle bodies were studied. The vehicle geometries are derived from the cuboid [102] and the Ahmed body [27, 109] (see Figure 3.2). All geometries have identical overall dimensions, i.e. length, width and height, and they differ in their leading and trailing edge (see Figure 3.1). Stilts have been omitted from the geometries to reduce the computational cost, additionally, in the study by Guilmineau [39], it was shown that the removal of the stilts had little effect on the profile of the wake or the drag coefficient of an Ahmed vehicle in a URANS simulation.

Whilst a platoon of cuboids displays classical platooning conditions [102], the two simple geometric modifications that transform a cuboid into an Ahmed body with 25° trailing edge slant angle, namely a rounded leading edge and a slanted trailing edge (see figure 3.2 (d)), are sufficient to alter the performance and outcome of the platoon. From the literature discussed previously, the 25° Ahmed body is known to display inverted platooning conditions at short spacing [109].

The purpose of this study is to systematically investigate how the rounded leading edge and the slanted trailing edge influence the type of platooning behaviour. To this end, two intermedi-

(a) (b) (c) (d)

Figure 3.2: The basic vehicle geometries used in the current study: (a)0° Cuboid, (b)25° Cuboid, (c)0° Ahmed, (d)25° Ahmed.

platoon type	reference name	front geometry	rear geometry
1	Cuboid-0° – 0°	00° Cuboid	00° Cuboid
2	Ahmed-25° – 25°	25° Ahmed body	25° Ahmed body
3	Ahmed-0° – 0°	00° Ahmed body	00° Ahmed body
4	Cuboid-25° – 25°	25° Cuboid	25° Cuboid
5	Cuboid-0°-Ahmed-0°	00° Cuboid	00° Ahmed body
6	Cuboid-25°-Ahmed-0°	25° Cuboid	00° Ahmed body
7	Ahmed-0°-Cuboid-0°	00° Ahmed body	00° Cuboid
8	Ahmed-25°-Cuboid-0°	25° Ahmed body	00° Cuboid

Table 3.1: Overview of investigated platoon configurations. Platoon configurations 1 to 4 are homogeneous platoons while configurations 5 to 8 are heterogeneous.

ate geometries are introduced: a body which combines the leading-edge geometry of the cuboid with the 25° rear slant angle of the Ahmed body (in the following named Cuboid 25° - see figure 3.2 (b)), and a body which combines the leading-edge geometry of the Ahmed body with a 0° trailing edge (in the following named Ahmed 0° - see figure 3.2 (c)). This geometry is also known as the squareback Ahmed body. Note that supports for mounting the Ahmed body are not included in the current study in order to facilitate the morphing of the Cuboid geometry to the Ahmed body.

Eight different two-vehicle platooning configurations are investigated (see Table 3.1). The first four platoons are homogeneous, i.e. the two vehicles in the platoon are identical. The remaining four configurations are heterogeneous platoons which are used in the second part of the current study to further clarify the relative impact of the trailing edge of the front vehicle and the leading edge of the rear vehicle on the platoon performance.

For each platoon, a range of inter-vehicle distances was investigated. Based on previous studies, the change between 'classical' and 'inverted' platooning conditions occurs for short inter-vehicle distances with $d/L \leq 1$. Therefore, this study focuses on six different separation distances, d/L =0.2, 0.4, 0.5, 0.6, 0.8 and 1.0 in order to characterise the platoons' performance over this range.

3.2.2 Numerical method

In total, 48 simulations were carried out to obtain the aerodynamic coefficients for all platoon types in Table 3.1 at the six different inter-vehicle distances. A further four simulations were

conducted to obtain the drag coefficients of the isolated vehicle geometries for comparison. All simulations were conducted as unsteady Reynolds-averaged Navier-Stokes simulations using SimCenter STAR-CCM+ by Siemens PLM Software version 15.04.010. In the context of the present simulations the incompressible, unsteady Reynolds-averaged Navier-Stokes equations are solved using the finite volume method. The segregated flow solver was chosen in STAR-CCM+, which employs a pressure-velocity coupling algorithm [121].The $k-\omega$ SST model was chosen since this has been successfully used in previous investigations of flow over the Ahmed body [2, 39].

The incompressible Navier-Stokes equations are a set of partial differential equations that describe the motion of an incompressible fluid. In the Reynolds-averaged Navier-Stokes (RANS) approach to simulating turbulent flows, the Reynolds decomposition is used to decompose the velocity and pressure fields into mean and fluctuating parts:

$$U_i = \langle U_i \rangle + U_i', \qquad p = \langle p \rangle + p'. \tag{3.1}$$

By applying averaging to the continuity and the Navier-Stokes equations, the Reynolds-averaged Navier-Stokes equations (also know as the mean flow equations) are obtained, see equations (3.2) and (3.3), which describe the behaviour of the averaged velocity and pressure fields.

$$\frac{\partial \langle U_i \rangle}{\partial x_i} = 0 \tag{3.2}$$

$$\frac{\partial \langle U_i \rangle}{\partial t} + \frac{\partial \langle U_i \rangle \langle U_j \rangle}{\partial x_j} = -\frac{1}{\rho}\frac{\partial \langle p \rangle}{\partial x_i} + \nu \frac{\partial^2 \langle U_i \rangle}{\partial x_j \partial x_j} - \frac{\partial \langle u_i' u_j' \rangle}{\partial x_j}, \tag{3.3}$$

where ρ is the density and ν the kinematic viscosity. In the Reynolds-averaged Navier-Stokes equations, the influence of the velocity and pressure fluctuations on the flow are represented by the Reynolds Stress Tensor $\langle u_i' u_j' \rangle$. As a result, the mean flow equations are not a closed set of equations, and further inputs are required to generate a complete set of equations that can be solved by application of numerical methods.

Most RANS modelling approaches start from the Boussinesq hypothesis, which is also known as the turbulent viscosity hypothesis. This hypothesis states that the deviatoric Reynolds stress is proportional to the mean rate of strain tensor $\bar{S}_{ij}$. The definition of the deviatoric Reynolds stress is given in equation (3.4).

$$a_{ij} = \langle u_i' u_j' \rangle - \frac{2}{3} k \delta_{ij} \tag{3.4}$$

In the Boussinesq hypothesis a new quantity, the 'turbulent viscosity' ν_t is introduced as given in equation (3.5).

$$a_{ij} = -2\nu_t \bar{S}_{ij} \tag{3.5}$$

This hypothesis is based on two underlying assumptions: firstly that transport effects can be neglected and secondly that the turbulent stress and mean rate of strain tensor are aligned. Whilst neither of these assumptions are true in general, they do provide an approximation for the Reynolds stress tensor and only the turbulent viscosity, which is in general a function of space and time, remains to be modelled.

The most widely used approach to obtain the turbulent viscosity is the use of 'two-equation' RANS models. These models provide closure to the (unsteady) RANS equations, by the means of two further model equations. There are two main families of two-equation turbulence models, the k-ω and the k-ε model families which are named after the corresponding two model equations. The general approach for these two-equation models starts from a mixing length approximation, which relates the turbulent viscosity to a mixing velocity and a mixing length as given in equation (3.6).

$$\nu_t = u^* \ell^*. \tag{3.6}$$

For both the k-ε and the k-ω models, the mixing velocity is determined from the turbulent kinetic energy (see equation 3.7) for which a transport equation needs to be solved (k equation)

$$u^* \sim k^{1/2}, \qquad \text{where} \qquad k = \frac{1}{2}\langle u_i' u_i' \rangle \tag{3.7}$$

To obtain the mixing length, an additional transport equation needs to be solved for the dissipation rate ε or specific dissipation rate ω. The corresponding mixing length definitions are given in equation (3.8) for the $k-\varepsilon$ and in equation (3.9 for the $k-\omega$ model.

$$\ell^* \sim \frac{k^{\frac{3}{2}}}{\varepsilon} \tag{3.8}$$

$$\ell^* \sim \frac{k^{\frac{1}{2}}}{\omega} \tag{3.9}$$

By substituting the relationships for u^* and ℓ^* into equation (3.6), the turbulent viscosity (or eddy viscosity) is defined as function of k and either ε or ω as shown in equations (3.10) and (3.11) where C_μ is an empirical constant ($C_\mu = 0.09$)

$$\nu_t = C_\mu \frac{k^2}{\varepsilon} \tag{3.10}$$

$$\nu_t = C_\mu \frac{k}{\omega} \tag{3.11}$$

In this study, the k-ω SST model is used. In the Shear Stress Transport (SST) variation of the k-ω turbulence model, the k-ω model is used in the near wall regions and k-ε model is used in the bulk flow. The k-ω SST model combines the benefits of the k-ω model's ability to much more accurately predict turbulent flows subject to adverse pressure gradients and flow separation

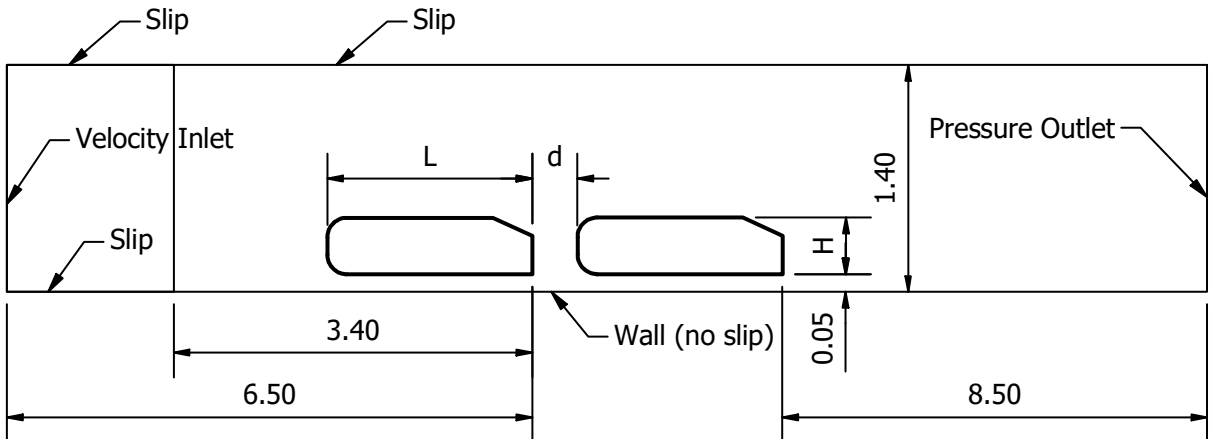

Figure 3.3: Flow domain for a wind tunnel of width $1.87m$ (dimensions in meters, not to scale). Based on flow domain in Meile et al. [2]

with the lower sensitivity of the k-ε model used for free-stream conditions.

The model equation for turbulent kinetic energy is given in equation (3.12).

$$\frac{\partial k}{\partial t} + \langle U \rangle \nabla k = \nabla(\frac{\nu_t}{\sigma_k}\nabla k) + P - \varepsilon \tag{3.12}$$

The model equation for dissipation rate is an empirical equation given in(3.13).

$$\frac{\bar{D}\varepsilon}{\bar{D}t} = \nabla(\frac{\nu_t}{\sigma_\varepsilon}\nabla\varepsilon) + C_{\varepsilon 1}\frac{P\varepsilon}{k} - C_{\varepsilon 2}\frac{\varepsilon^2}{k} \tag{3.13}$$

where $C_\mu = 0.09$, $C_{\varepsilon 1} = 1.44$, $C_{\varepsilon 2} = 1.92$ $\sigma_k = 1.0$ and $\sigma_\varepsilon = 1.3$ are modeling constants.

The model equation for specific dissipation rate is given in equation (3.14).

$$\frac{\bar{D}\omega}{\bar{D}t} = \nabla(\frac{\nu_t}{\sigma_\omega}\nabla\omega) + C_{\omega 1}\frac{P\omega}{k} - C_{\omega 2}\frac{\omega^2}{k}, \qquad \text{where} \qquad \omega = \frac{\varepsilon}{k} \tag{3.14}$$

The modeling constants are given as: $C_\mu = 0.09$, $C_{\omega 1} = 0.555$, $C_{\omega 2} = 0.833$, $\sigma_k = \sigma_\omega = 2$. A more detailed explanation of each process can e found in the work by Pope [49].

A schematic of the simulation domain is given in figure 3.3. Boundary conditions are chosen similar to typical conditions for wind-tunnel based platoon experiments where the vehicles are mounted above a ground plate. At the inlet boundary, a uniform free-stream velocity of $40m/s$ and an inlet turbulence intensity of 1% is applied. The working fluid is air with density set to $1.18415kg \cdot m^{-3}$ and a dynamic viscosity of $1.85508 \cdot 10^{-5} Pa \cdot s$. The Reynolds number calculated using the base height is $7.35 \cdot 10^5$ or $2.67 \cdot 10^6$ based on length of the body and is similar to the values used in other URANS-based studies of the Ahmed body [2, 39].

The no-slip boundary starts $2.26L$ upstream of the front vehicle, allowing the boundary layer to grow to a thickness of $30mm$ by $x = -1.4L$ (note that $x = 0$ is the base of the front vehicle). This is similar to the flow conditions used in a study on a single Ahmed body by Meile et

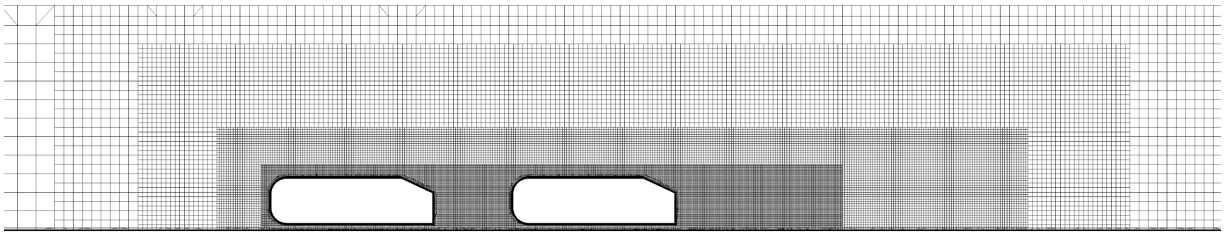

Figure 3.4: Illustration of volumetric refinements over the platoon vehicles and their wakes. Further detail on the meshing scheme can be found in appendix A.

Number of cells	Time step [s]	Maximum CFL
$0.5 \cdot 10^6$	0.0008	0.847
$1.0 \cdot 10^6$	0.0007	0.966
$2.1 \cdot 10^6$	0.0006	0.960
$3.6 \cdot 10^6$	0.0005	1.081
$8.0 \cdot 10^6$	0.0004	1.127

Table 3.2: Simulation time steps and associated CFL numbers for each case in the mesh dependency study.

al. [2]. The side and top boundaries are set to full-slip boundary conditions and a pressure outlet is employed as the outlet boundary. In all cases the total length of the simulation domain was extended to at least $5.75L$ behind the rear vehicle to allow sufficient space for any residual unsteadiness to subside.

Meshes were generated using the STAR-CCM+ inbuilt trimmed cell mesher which creates a flow aligned grid of hexahedral elements with minimal cell skewness. For modelling the near-wall flow, a high wall-y+ approach was employed and prism layers were used on the wall boundaries for improved resolution of the boundary layers. Whilst a low wall-y+ approach would provide more detail of the boundary layer development, at a high Reynolds number it is computationally expensive to achieve. Additionally, the high wall-y+ approach using the $k-\omega$ SST model is the established and widely recognised model for this type of vehicle study [2, 50, 53, 54]. Nested volumetric refinements were used to resolve the complex flow structures over the vehicles, in the inter-vehicle gap and in the vehicle wakes (Figure 3.4). A more detailed description of the mesh refinement study is given in appendix A.

A validation and grid dependency study was undertaken on the Isolated 25° Ahmed body. Here the prism layers were kept constant to ensure a consistent value of wall-y+ and the surrounding cells in the grid were systematically reduced in size such that the number of cells in the mesh doubled for each new simulation. The time step was also adjusted to maintain a maximum convective Courant number (CFL) of around 1, further details of this are given in table 3.2. The lift and drag coefficient results of the range of mesh resolutions tested are given in figure 3.5 with the chosen mesh having around 3.6 million cells.

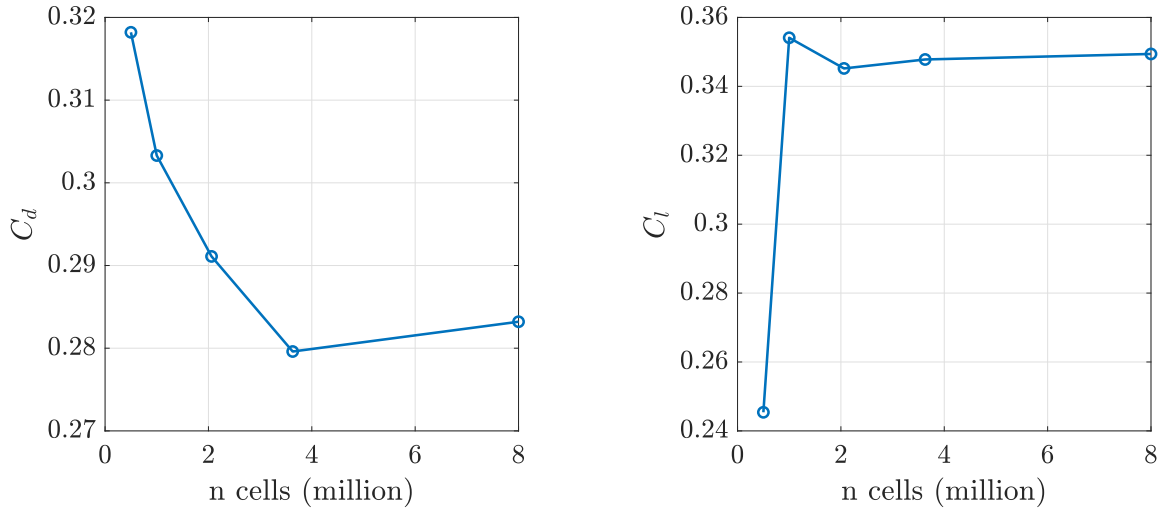

Figure 3.5: a) Drag coefficient and b) lift coefficient for the isolated 25° Ahmed body over a range of mesh densities as part of a grid dependency study.

This mesh was then extended to include a second vehicle for the platooning scenarios. This method was implemented as there are currently limited validation cases for platoons and an abundance of validation cases for the Isolated Ahmed body. This minor adaption of the validated mesh resulted in the final mesh for the platooning case to be approximately 4 million cells.

The simulations were ran with a time-step of $0.0005s$ using a second order implicit time stepping scheme. Once the flow was fully developed, drag coefficient values were averaged for a minimum of 2 seconds. The isolated lift and drag coefficients of the Ahmed 25 body were 0.336 and 0.279 respectively. This is within the range of values expected for the Ahmed body at this Reynolds number [2]. Figure 3.6 shows the streamwise velocity profiles for the 25° Ahmed vehicle compared to the experimental data provided by Lienhart et al. [3]. Here, the simulation closely matches the experimental data. Over the rear slant the simulation predicts a slightly higher velocity, suggesting that it favours flow attachment more than what was measured experimentally. In addition, the counter flow section of the recirculation region extends slightly further downstream than indicated experimentally. For the Cuboid, the simulated drag coefficient of 0.921, is in agreement with other, similar, studies [108]. The isolated drag coefficients and absolute drag values for the four vehicle geometries used in this chapter can be found in table 3.3

3.3 Results

In this section, first the results for the homogeneous platoon configurations will be discussed. Then, the heterogeneous platoon configurations will be used to gain further insight into the geometry-dependency of platoon aerodynamics. Only the velocity magnitude is shown in the

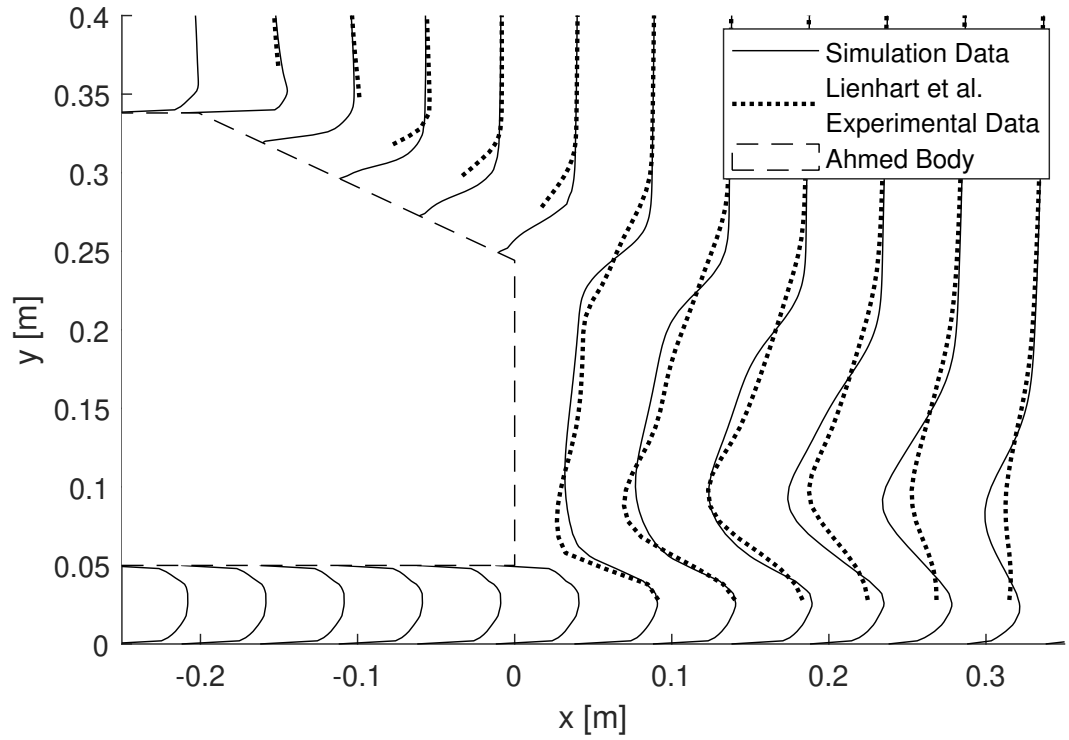

Figure 3.6: Comparison of simulated and experimental stream-wise velocity profiles for an Ahmed vehicle with a 25° rear slant (experimental data from Lienhart et al. [3]).

Geometry	Drag coefficient	Drag (at $40m/s$)
0° Cuboid	0.922	$97.9N$
25° Cuboid	0.901	$95.6N$
0° Ahmed	0.251	$26.6N$
25° Ahmed	0.279	$29.6N$

Table 3.3: Drag coefficient and absolute drag for each geometry in the shape dependency chapter. Drag force calculated at $40m/s$.

Case	Front						Rear					
	0.2	0.4	0.5	0.6	0.8	1.0	0.2	0.4	0.5	0.6	0.8	1.0
Cuboid-$0^\circ - 0^\circ$	92.7	92.9	92.1	92.1	92.7	93.4	17.8	26.0	29.2	32.7	39.7	44.8
Ahmed-$25^\circ - 25^\circ$	8.7	10.4	11.9	14.7	20.9	26.7	40.4	42.2	41.7	39.9	34.0	30.9
Ahmed-$0^\circ - 0^\circ$	90.0	89.9	90.8	91.3	92.0	92.7	29.2	37.9	41.9	49.5	53.5	59.6
Cuboid-$25^\circ - 25^\circ$	14.5	14.1	13.9	13.9	16.8	20.0	20.7	29.4	29.7	31.4	33.5	31.8

Table 3.4: Absolute drag for each vehicle in the homogeneous platoons. Drag force in Newtons calculated at $40m/s$.

Case	Front						Rear					
	0.2	0.4	0.5	0.6	0.8	1.0	0.2	0.4	0.5	0.6	0.8	1.0
Cuboid-$0^\circ - 0^\circ$	0.87	0.88	0.87	0.87	0.87	0.88	0.17	0.24	0.28	0.31	0.37	0.42
Ahmed-$25^\circ - 25^\circ$	0.08	0.10	0.11	0.14	0.20	0.25	0.38	0.40	0.39	0.38	0.32	0.29
Ahmed-$0^\circ - 0^\circ$	0.14	0.13	0.13	0.13	0.16	0.19	0.20	0.28	0.28	0.30	0.32	0.30
Cuboid-$25^\circ - 25^\circ$	0.85	0.85	0.86	0.86	0.87	0.87	0.28	0.36	0.40	0.47	0.50	0.56

Table 3.5: drag coefficient for each vehicle in the homogeneous platoons.

velocity plots to avoid repetition as little additional insight was found by analysing the individual velocity components in the wake of each vehicle.

3.3.1 Homogeneous platoons

The drag coefficients of the front and rear members for the homogeneous platoon configurations are presented in figure 3.7 as a function of the inter-vehicle spacing d/L. In all cases, the drag coefficients are normalised by the drag coefficient C_{d0} for the corresponding isolated vehicle under the same flow conditions, i.e., for $C_d/C_{d0} < 1$ a platoon member experiences drag reduction, while for $C_d/C_{d0} > 1$ its drag is increased. The drag coefficients and absolute values of drag at $40ms^{-1}$ are given in tables 3.5 and 3.4 respectively.

The cuboid is a bluff body with a C_{d0} of 0.91 and separation is triggered at its sharp leading edges. As expected, the cuboid-0°-0° platoon exhibits classical platooning behaviour, i.e., the rear vehicle experiences a high drag reduction which gradually reduces with increasing spacing, whilst the front vehicle only achieves a small reduction in drag. This is consistent with the results of Uystepruyst et al. [108].

The Ahmed-25°-25° platoon also behaves as expected by displaying inverted platooning conditions. The results are similar to the study by Watkins & Vino [27]: the rear vehicle experiences a drag increase which peaks at short spacing (here $d/L = 0.4$). Its drag then gradually decreases with d/L. In contrast, the front vehicle experiences a substantial drag reduction at short spacing which reduces as d/L increases.

Introducing a rear slant angle to the cuboid does not change its fundamental platooning behaviour: the cuboid-25°-25° displays classical platooning conditions with the rear vehicle receiving most of the benefit from the platooning. The rear vehicle thus performs significantly better when compared to the Ahmed-25°-25° platoon, however, the front vehicle still receives

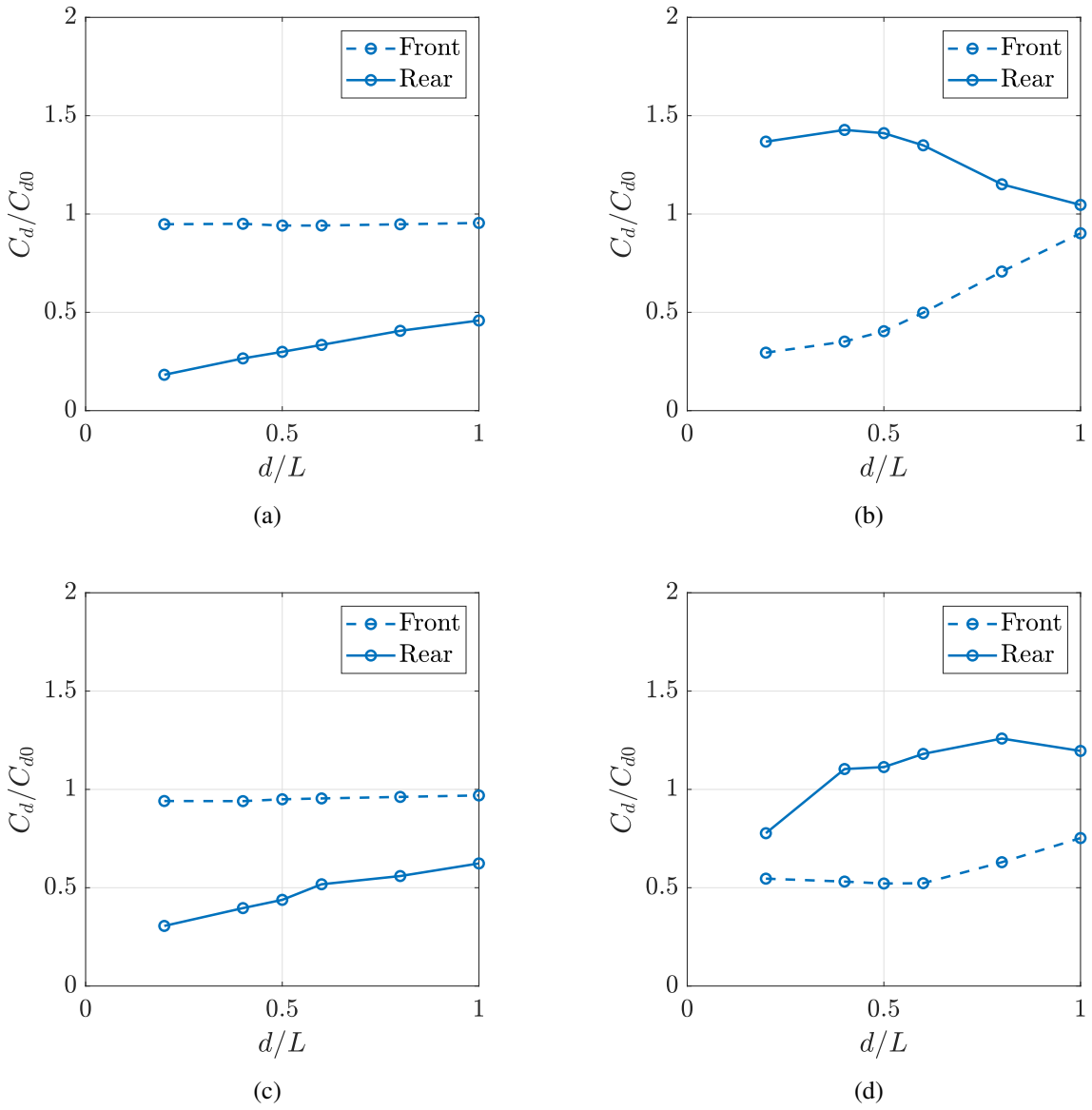

Figure 3.7: Normalised drag coefficient as a function of inter-vehicle spacing for different homogeneous platoons. (a) Cuboid-0°; (b) Ahmed-25°; (c) Cuboid-25°; (d) Ahmed-0°

Case	Front						Rear					
	0.2	0.4	0.5	0.6	0.8	1.0	0.2	0.4	0.5	0.6	0.8	1.0
Cuboid-0°-Ahmed-0°	93.5	91.8	92.2	93.0	93.7	94.4	16.0	21.1	23.5	25.2	27.7	29.0
Cuboid-25°-Ahmed-0°	90.9	91.0	91.7	92.2	93.0	93.6	23.1	27.7	28.0	28.8	29.2	28.3
Ahmed-0°-Cuboid-0°	13.0	12.8	12.8	13.1	15.2	18.0	22.5	34.0	33.0	34.4	40.9	47.3
Ahmed-25°-Cuboid-0°	2.7	6.3	7.3	8.6	13.9	20.4	54.7	50.8	59.1	65.9	83.3	90.0

Table 3.6: Absolute drag for each vehicle in the heterogeneous platoons. Drag force in Newtons calculated at $40m/s$.

Case	Front						Rear					
	0.2	0.4	0.5	0.6	0.8	1.0	0.2	0.4	0.5	0.6	0.8	1.0
Cuboid-0°-Ahmed-0°	0.88	0.86	0.87	0.88	0.88	0.89	0.15	0.20	0.22	0.24	0.26	0.27
Cuboid-25°-Ahmed-0°	0.86	0.86	0.86	0.87	0.88	0.88	0.22	0.26	0.26	0.27	0.28	0.27
Ahmed-0°-Cuboid-0°	0.12	0.12	0.12	0.12	0.14	0.17	0.21	0.32	0.31	0.32	0.39	0.45
Ahmed-25°-Cuboid-0°	0.03	0.06	0.07	0.08	0.13	0.19	0.52	0.48	0.56	0.62	0.78	0.85

Table 3.7: Drag coefficient for each vehicle in the heterogeneous platoons.

very little drag reduction. As a whole this platoon performs slightly worse than the cuboid-0°-0° platoon. The front vehicle remains relatively unaffected by the introduction of the trailing edge slant and the rear vehicle receives up to a 70% drag reduction compared to the maximum of 80% drag reduction for the simple cuboid platoon.

The final homogeneous platoon is the Ahmed-0°-0° configuration. This is arguably the most interesting platoon as it displays a combination of classical and inverted platooning conditions. When the spacing between the vehicles is very short, both vehicles experience some drag reduction, similar to the cuboid platoons. However, as the spacing between the vehicles increases, so too does the drag for the rear vehicle. When the distance between the vehicles, d/L, is greater than 0.5, the normalised drag for the rear vehicle exceeds 1 and inverted platooning conditions similar to the Ahmed-25°-25° platoon are observed.

3.3.2 Heterogeneous platoons

In a homogeneous platoon it can difficult to attribute some aspects of the platooning behaviour to specific geometry features, such as the trailing edge of the front vehicle or the leading edge of the rear vehicle, since both vehicles in the platoon are identical. The introduction of heterogeneous platoons allows for further comparison and analysis of the influence that different geometrical features have on platoon aerodynamics. The Absolute drag and drag coefficients of each vehicle in the platoon are given in tables 3.6 and 3.7 respectively.

The Cuboid-0°-Ahmed-0° platoon shown in figure 3.8 is a more complex result than the previous, homogeneous, platoons. The front vehicle experiences minimal drag reduction whilst the rear vehicle obtains a substantial reduction in drag which is highest at the closest spacing, similar to classic platooning conditions. As the inter-vehicle distance increases the regime swaps to inverted platooning. Overall, the behaviour is quite similar to the Cuboid-0°-Cuboid-0° and

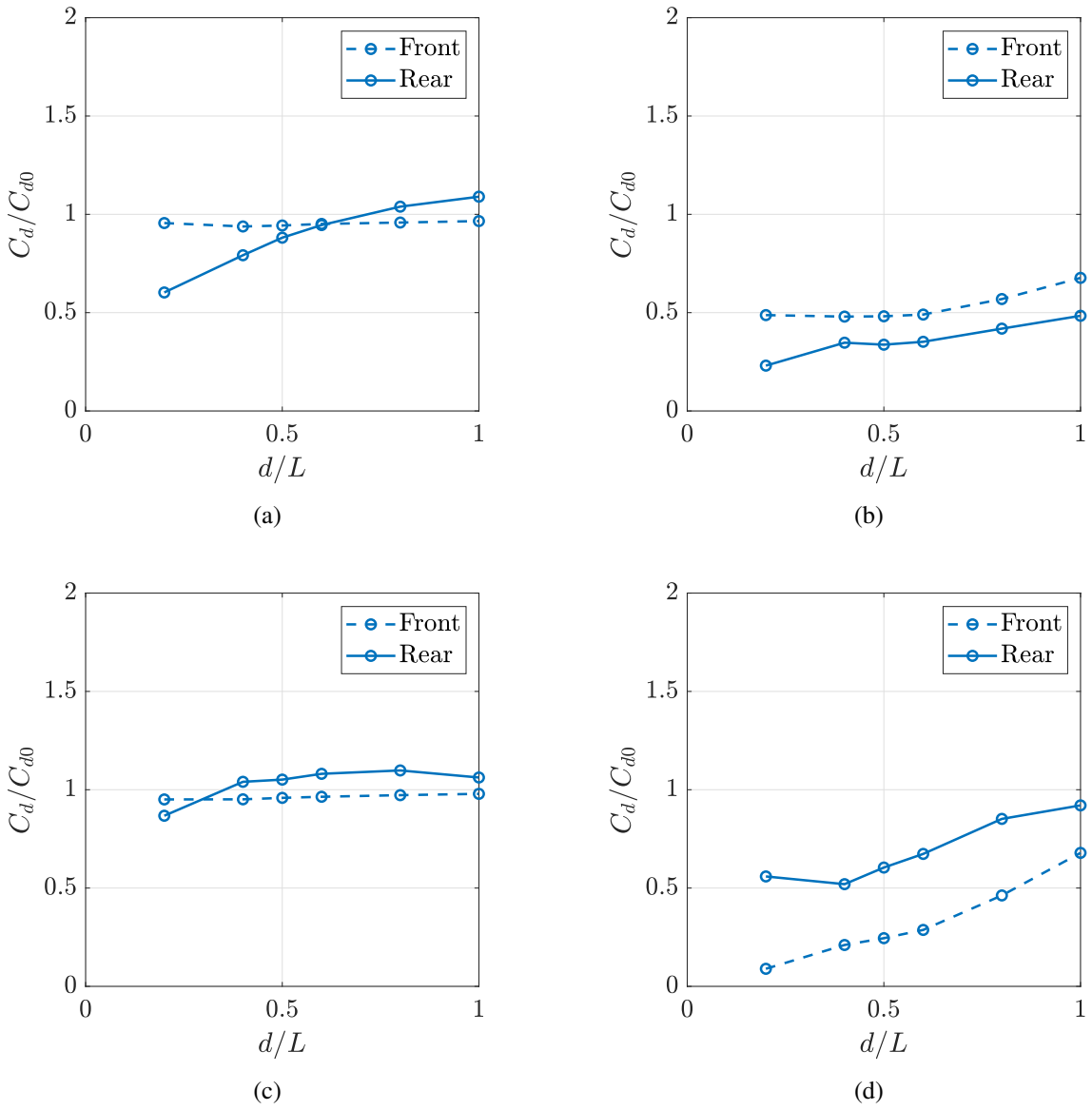

Figure 3.8: Normalised drag coefficient as a function of inter-vehicle spacing for different heterogeneous platoons. (a) Cuboid-0°-Ahmed-0°; (b) Ahmed-0°-Cuboid-0°; (c) Cuboid-25°-Ahmed-0°; (d) Ahmed-25°-Cuboid-0°.

Cuboid-25°-Cuboid-25° platoons, although the drag reduction experienced by the rear Ahmed body in the Cuboid-0°-Ahmed-0° platoon is significantly lower than for a cuboid in the same position. Keeping this in mind, when comparing the Ahmed-0°-0° platoon, the Ahmed-0° rear vehicle receives a much higher drag reduction due to the introduction of the Cuboid-0° as the front vehicle in the heterogeneous configuration.

When the two vehicles swap positions, the Ahmed-0°-Cuboid-0° combination remains an example of classical platooning conditions. However, unlike the other classical platooning configurations discussed above, for this combination *both* vehicles receive significant reductions in drag. Whilst the rear vehicle still experiences higher drag reduction compared to the front vehicle, the front vehicle also receives substantial benefits. Furthermore, significant drag reduction is sustained over a wider range of inter-vehicle distances and, for both vehicles, the drag is still clearly reduced at $d/L = 1$. The drag for the Ahmed-0° front vehicle is very similar to the drag of the front vehicle in the Ahmed-0°-0° platoon. The Cuboid-0° rear vehicle is also similar to the two previous homogeneous Cuboid platoons, performing slightly worse than the Cuboid-0°-Cuboid-0° platoon but better than the Cuboid-25°-Cuboid-25° platoon.

More complex behaviour is exhibited by the Cuboid-25°-Ahmed-0° platoon shown in figure 3.8. This platoon is most effective when the vehicles are spaced at $d/L = 0.2$. At this spacing, only the rear vehicle experiences a drag reduction whilst the front vehicle has a drag very close to the value under isolated conditions. This is similar to the classical platooning examples discussed previously. As the vehicle spacing increases, the drag of the rear vehicle increases and exceeds its C_{d0} value at $d/L = 0.6$ before decreasing again and approaching C_{d0}, a characteristic more consistent with inverted platooning conditions. In contrast, the drag of front vehicle remains largely unaffected by the platooning and close to C_{d0} for all inter-vehicle distances.

This result is best compared to the Cuboid-0°-Ahmed-0° platoon discussed above: The only geometric difference between these platoons is the introduction of a trailing edge slant on the front vehicle. This geometric change does not influence the drag reduction of the front vehicle, however, it has a strong effect on the rear vehicle. The rear Ahmed-0° vehicle in the Cuboid-25°-Ahmed-0° platoon performs significantly worse, receiving a much lower drag reduction at small separations and exceeds C_{d0} for distances above $d/L = 0.4$. The rear-slant angle on the front body, therefore, can have a strong impact on the rear body, provided that the front body has a rounded leading edge.

The final heterogeneous platoon is the Ahmed-25°-cuboid-0° case shown in figure 3.8. Both vehicles experience high drag reductions at the shortest vehicle spacing and their drag slowly increases as a function of vehicle spacing, approaching the reference value under isolated conditions. The drag dependency of the rear vehicle is similar to other platoon configurations discussed above where classical platooning behaviour was observed. However, the front vehicle experiences a greater drag reduction than the rear vehicle at all spacings, and therefore this platoon clearly differs from classical platooning behaviour, where the rear vehicle is expected to

receive the higher benefits from platooning.

Overall, the drag behaviour of the front vehicle shows similar trends to the drag of the front vehicle in the Ahmed-25°-25° platoon, although the drag reductions by the front vehicle in the Ahmed-25°-cuboid-0° are higher.

3.4 Discussion

In the following, the results for the drag coefficients will be discussed with the aid of flow visualisations to draw conclusions regarding the geometry-dependency of the platooning behaviour. In the contour plots to provided, the streamwise direction is denoted as x and is normalised against vehicle length, L ($1.004m$). The vertical direction is given as y and has been normalised with respect to vehicle height, H ($0.288m$). This allows for the relative length and height any flow features to be easily relatable to the dimensions of the vehicle.

Three section planes are provided to help illustrate the 3D nature of the flow. Primarily, a streamwise plane along the centre-line of the platoon is used to depict the flow separation at the trailing edge of the front vehicle and the flow interactions between the two vehicles. A spanwise plane at $x = 0.08L$ is used to show the presence and extent of trailing edge vortices generated by the front vehicle. This is important as it was a flow feature highlighted in the literature as a possible cause of inverted platooning conditions [27]. Finally, a spanwise plane at $y = 0.15m$ is given. This height was selected as it is situated bellow the trailing edge slants of any vehicle. The intention of this plane is to provide a more representative comparison of flow separation around the edges of the vehicles and to highlight, in detail, the full extent of downwash effects caused by both the introduction of a trailing edge slant and rear vortices.

3.4.1 Effect of the front vehicle geometry

First, the effects of the front vehicle are considered. When the platoon is led by a bluff body such as the two cuboid geometries, the flow separates at the leading edges of the front vehicle and a large wake is formed. The extent of the wake can be seen in both the spanwise (see figures, 3.13, 3.14, 3.15 and 3.16) and streamwise direction (see figure 3.9) with thick shear layers developing off of each sharp leading edge. In this case, the shedding mechanism off of the front vehicle is highly turbulent. This is highlighted in figures 3.11 and 3.12 where the turbulent kinetic energy is significantly higher for the lead cuboid type vehicles than for the lead Ahmed type vehicles. This large wake provides efficient sheltering for the rear vehicle yielding, in most cases, a substantial drag reduction for the rear vehicle, with a few exceptions where a drag penalty emerges at longer spacing. However, whilst a bluff-body as a lead vehicle is desirable from the perspective of the rear vehicle, in the overall efficiency considerations the high absolute drag of a cuboid-shaped body needs to be taken into account.

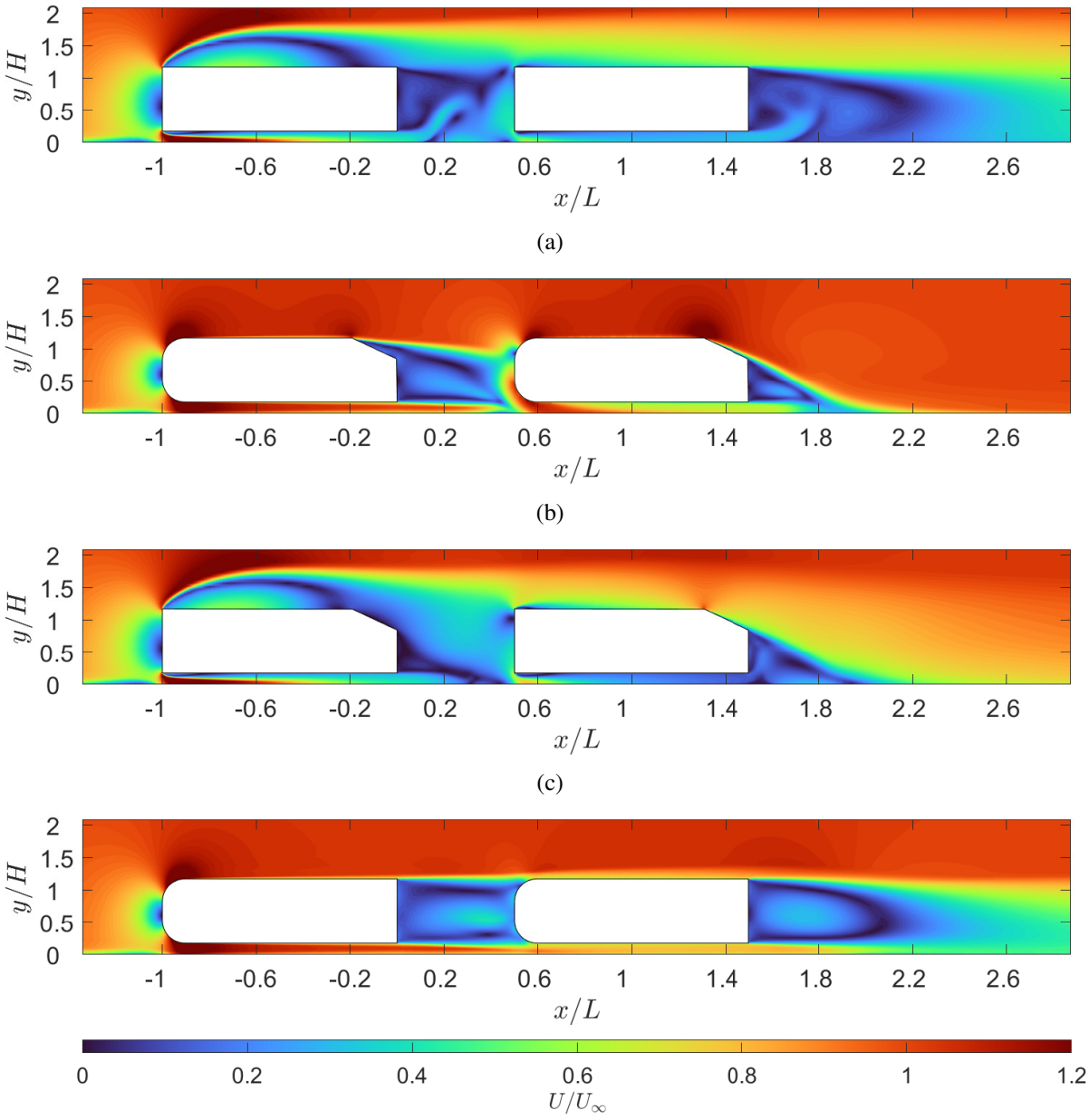

Figure 3.9: Normalised mean velocity magnitude for different homogeneous platoons at $d/L = 0.5$. (a) Cuboid-0°; (b) Ahmed-25°; (c) Cuboid-25°; (d) Ahmed-0°. Flow is from left to right.

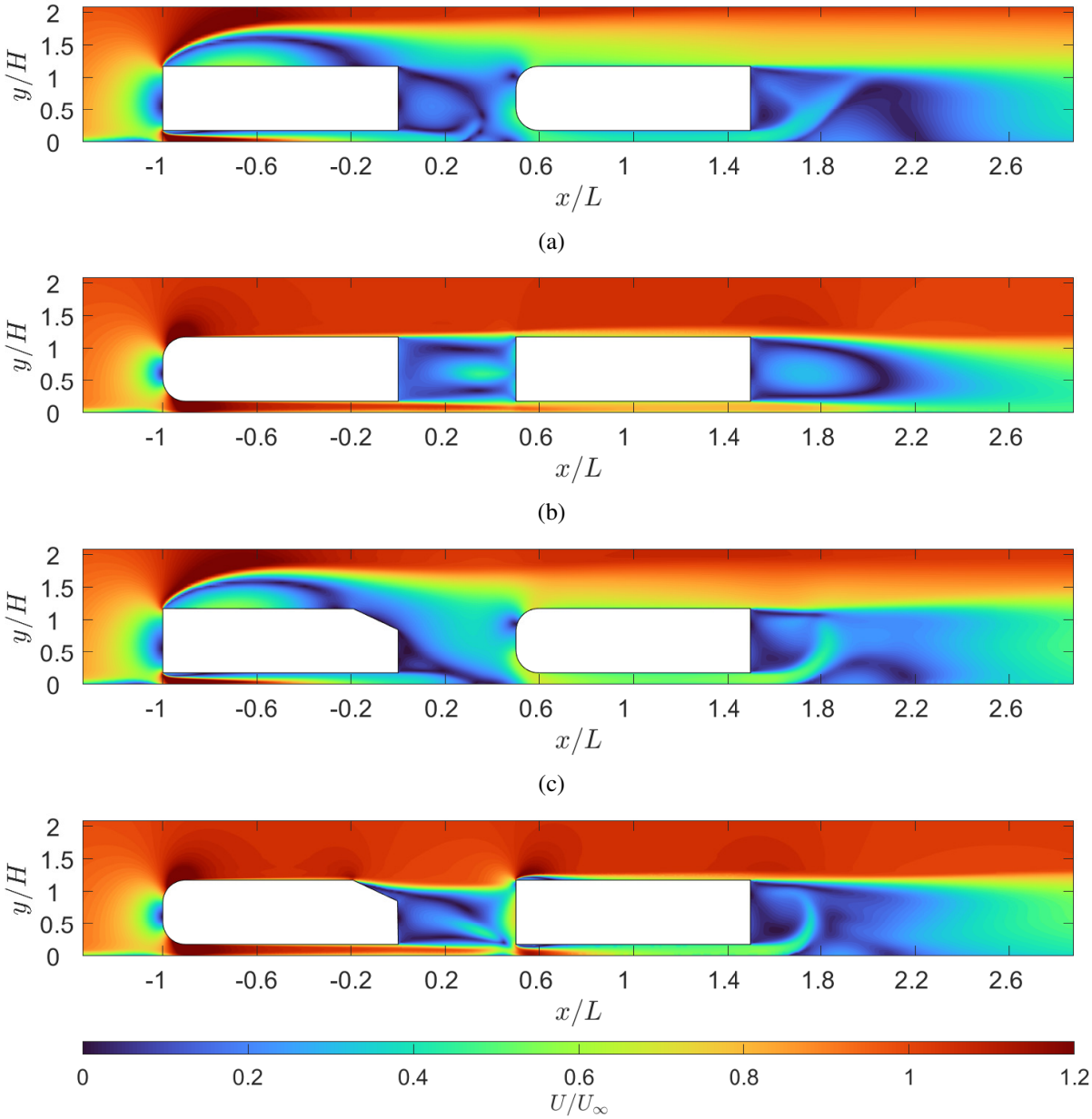

Figure 3.10: Normalised mean velocity magnitude for different heterogeneous platoons at $d/L = 0.5$. (a) Cuboid-0°-Ahmed-0°; (b) Ahmed-0°-Cuboid-0°; (c) Cuboid-25°-Ahmed-0°; (d) Ahmed-25°-Cuboid-0°. Flow is from left to right.

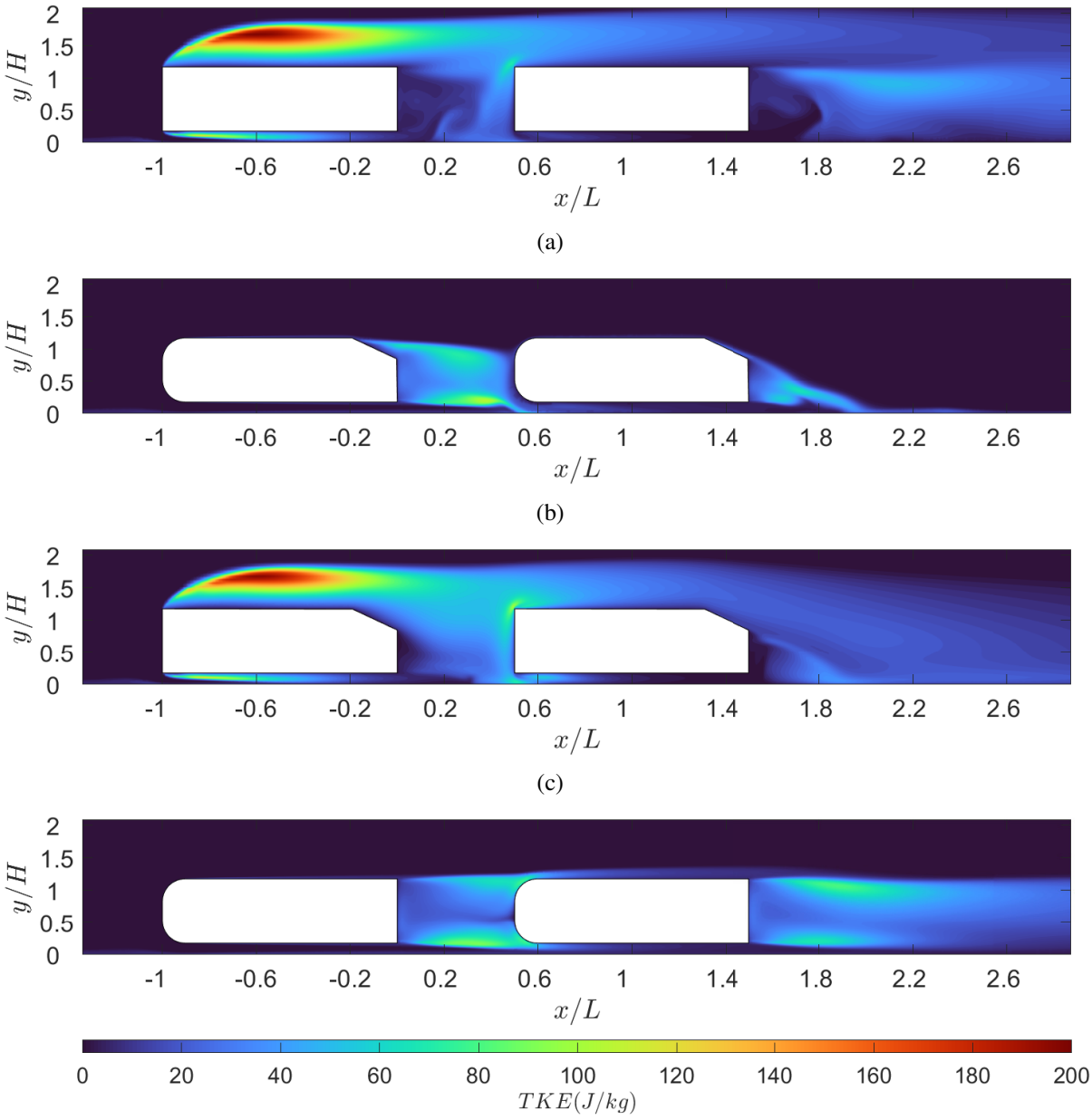

Figure 3.11: Turbulent kinetic energy for different homogeneous platoons at $d/L = 0.5$. (a) Cuboid-0°; (b) Ahmed-25°; (c) Cuboid-25°; (d) Ahmed-0°. Flow is from left to right.

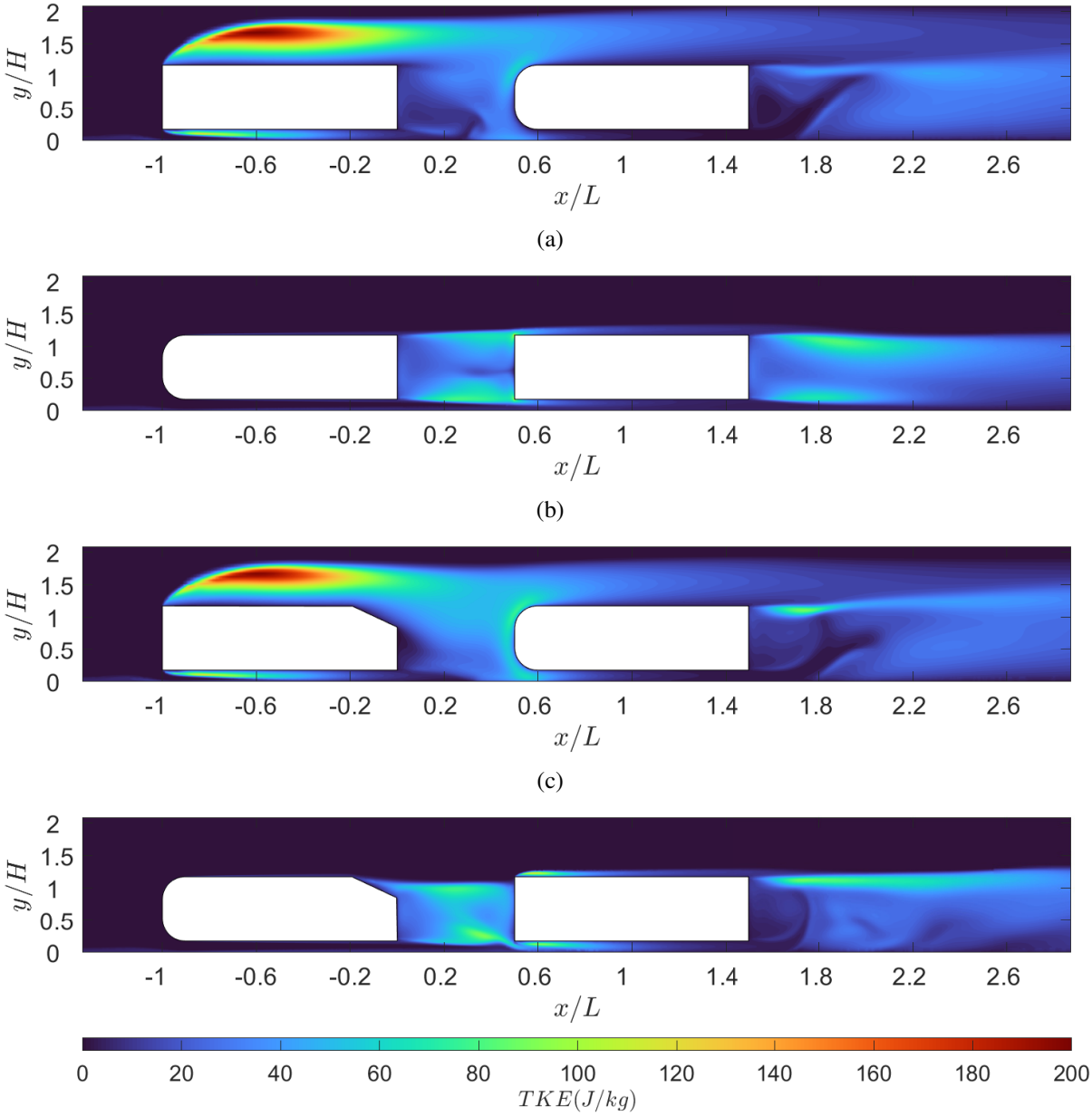

(a)

(b)

(c)

(d)

Figure 3.12: Turbulent kinetic energy for different heterogeneous platoons at $d/L = 0.5$. (a) Cuboid-0°-Ahmed-0°; (b) Ahmed-0°-Cuboid-0°; (c) Cuboid-25°-Ahmed-0°; (d) Ahmed-25°-Cuboid-0°. Flow is from left to right.

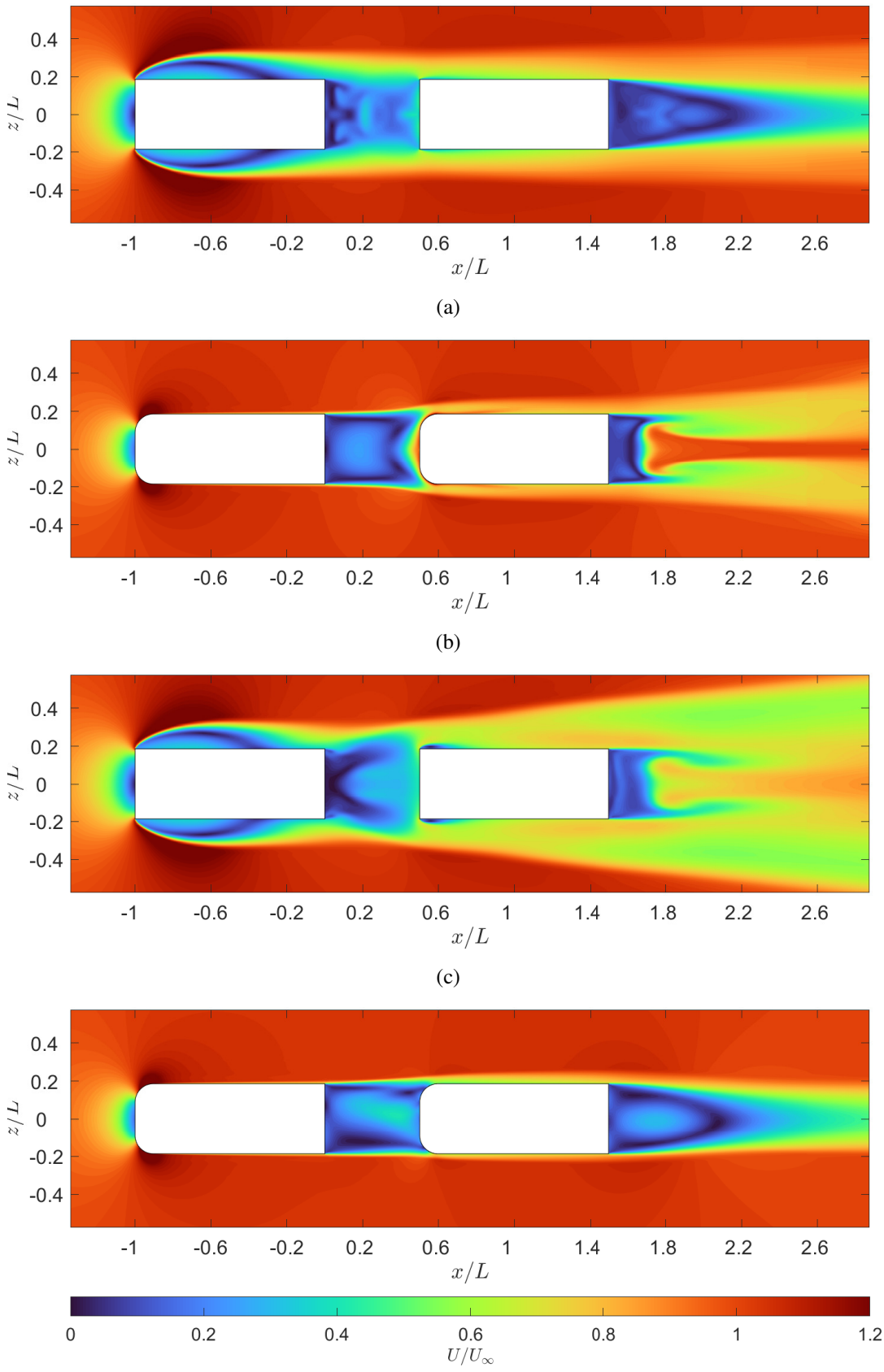

Figure 3.13: Normalised mean velocity magnitude on a horizontal plane at $y = 0.15m$ for different homogeneous platoons at $d/L = 0.5$. (a) Cuboid-0°; (b) Ahmed-25°; (c) Cuboid-25°; (d) Ahmed-0°. Flow is from left to right.

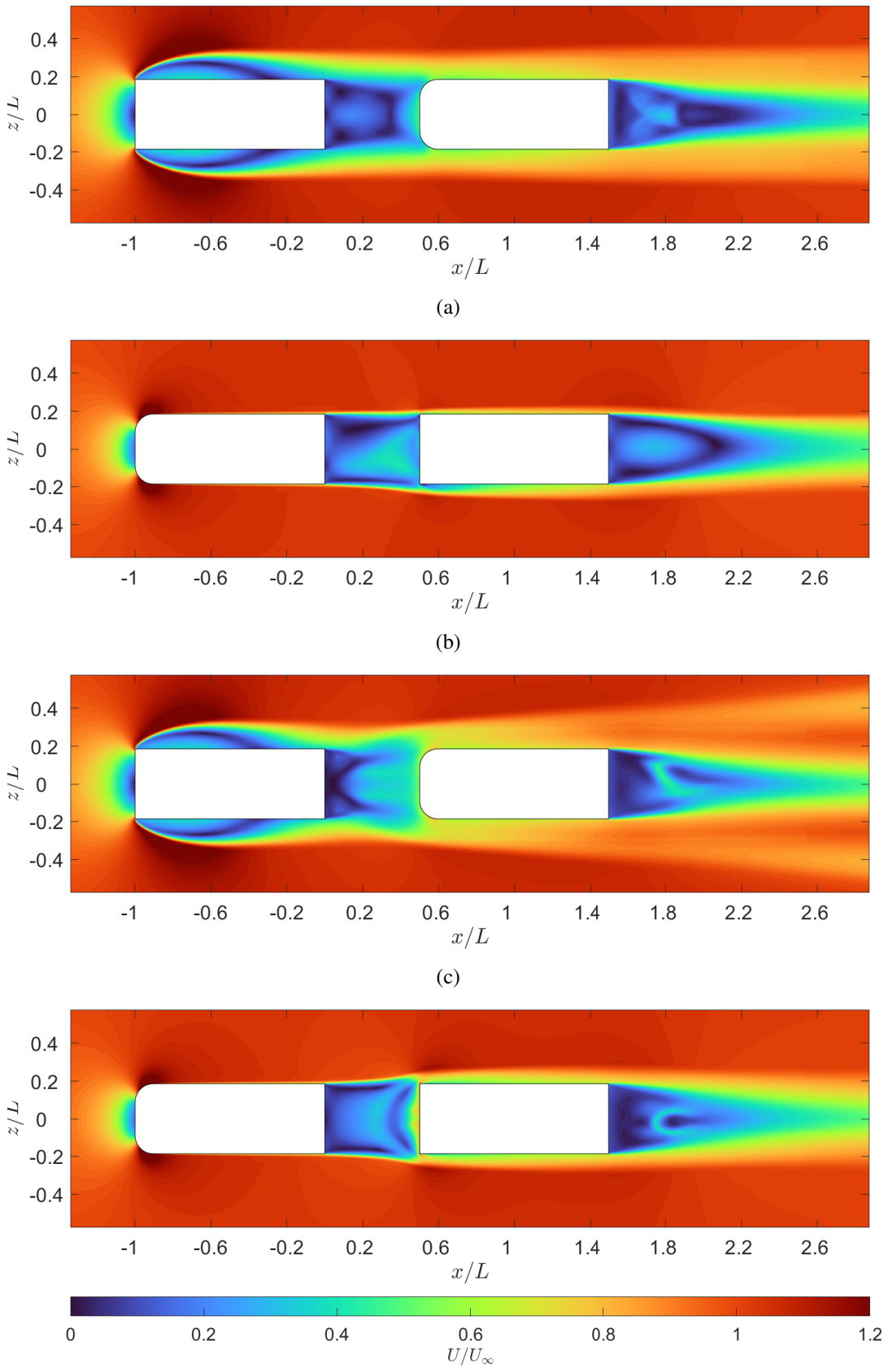

Figure 3.14: Normalised mean velocity magnitude on a horizontal plane at $y = 0.15m$ for different heterogeneous platoons at $d/L = 0.5$. (a) Cuboid-0°-Ahmed-0°; (b) Ahmed-0°-Cuboid-0°; (c) Cuboid-25°-Ahmed-0°; (d) Ahmed-25°-Cuboid-0°. Flow is from left to right.

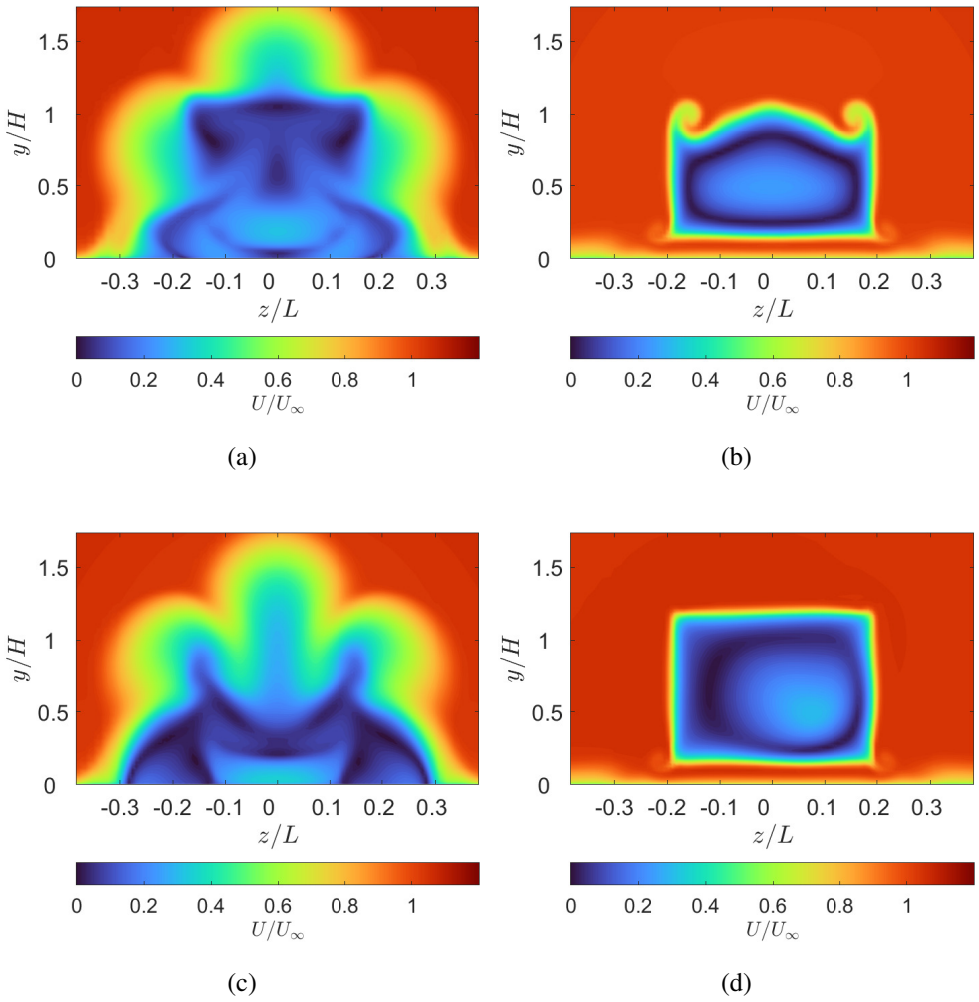

Figure 3.15: Normalised mean velocity magnitude on a spanwise plane at $x = 0.14L$ for different homogeneous platoons at $d/L = 0.5$. (a) Cuboid-0°; (b) Ahmed-25°; (c) Cuboid-25°; (d) Ahmed-0°. Flow is from left to right.

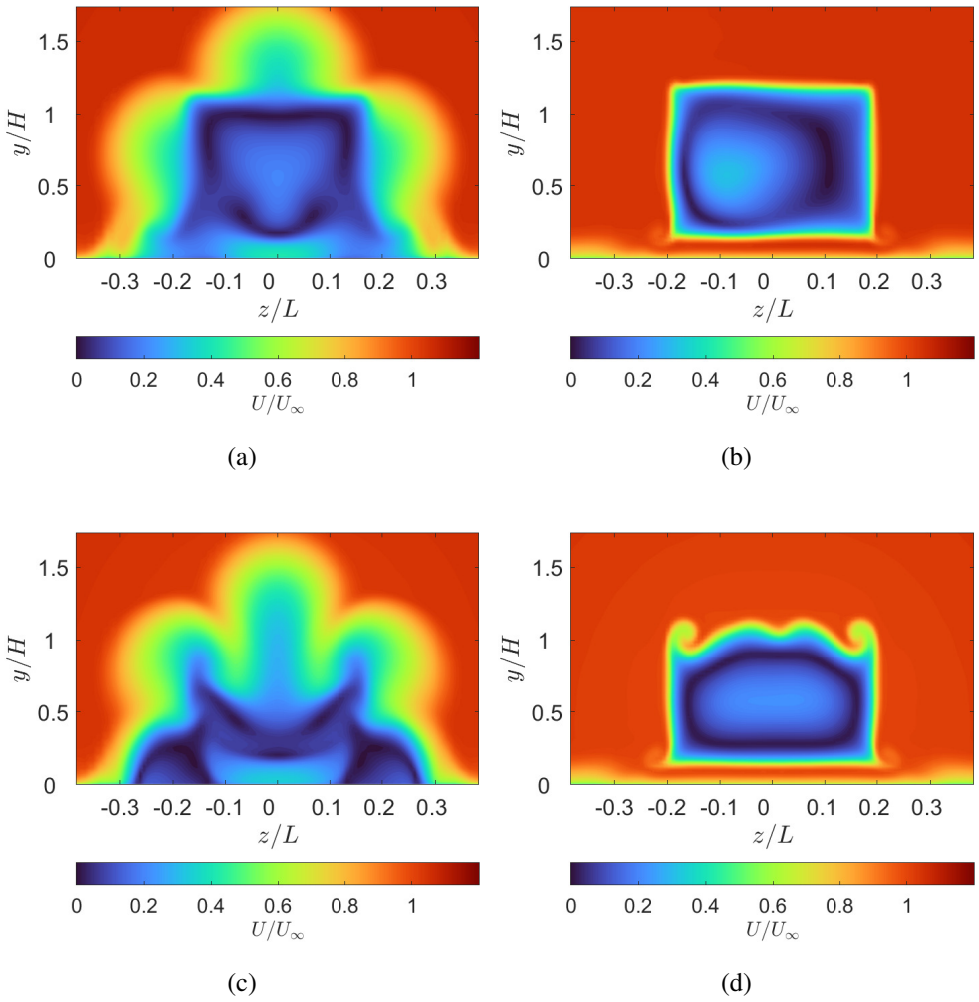

Figure 3.16: Normalised mean velocity magnitude on a spanwise plane at $x = 0.14L$ for different heterogeneous platoons at $d/L = 0.5$. (a) Cuboid-0°-Ahmed-0°; (b) Ahmed-0°-Cuboid-0°; (c) Cuboid-25°-Ahmed-0°; (d) Ahmed-25°-Cuboid-0°. Flow is from left to right.

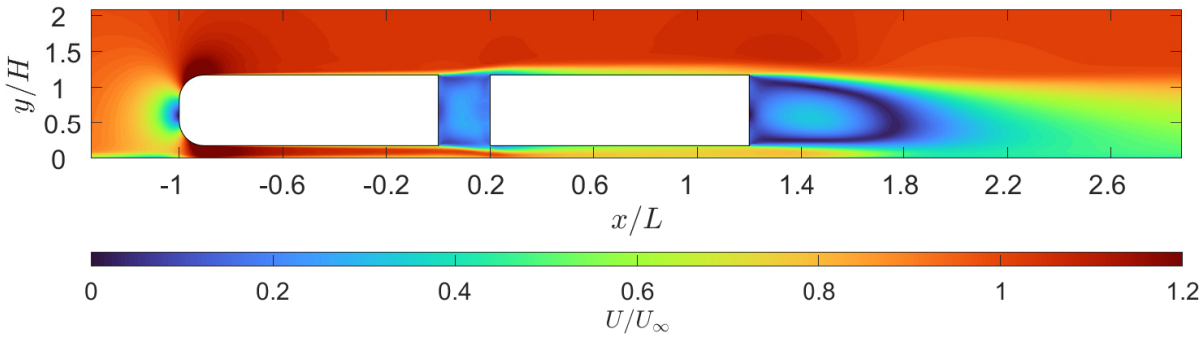

Figure 3.17: An Ahmed-0°-Cuboid-0° platoon at a vehicle spacing of $d/L = 0.2$ exhibiting stable flow reattachment on the leading edge of the rear vehicle. Flow is from left to right.

When the platoon is led by a more streamlined shaped, such as the Ahmed body with its rounded leading edges, the flow remains attached over most of the front vehicle and detaches only over its trailing edge. This results in a much lower turbulent kinetic energy, smaller wake, and less efficient sheltering of the trailing vehicle. The outcomes for platoons with a streamlined front vehicle are thus much more varied - both classical and inverted conditions are observed. In this scenario, the platoon's efficiency is much more influenced by the flow in the inter-vehicle gap, i.e. geometrically it depends much more strongly on the trailing edge of the front vehicle and the leading edge of the rear vehicle.

Finally, the addition of a trailing edge slant on the front vehicle creates a smaller wake which often, but not exclusively, results in inverted platooning conditions. The critical angle for flow separation over the Ahmed geometry, as detailed in the study by Ahmed et al. [1], is 30°, therefore the flow tries to stay attached over the 25° trailing edge resulting in greater wake impingement on the rear vehicle, increasing its drag (see figure 3.10). A similar result was reported in the paper by [109] where the flow structure of a platoon of two Ahmed-25° vehicles was analysed. Additionally, the introduction of a trailing edge slant creates vortices stemming from the C-pillar (see figure 3.15). This causes the front vehicle's wake to spread more in the spanwise direction as seen in figure 3.13.

3.4.2 Response of the rear vehicle

When the rear vehicle has a sharp leading edge, it provides the flow a stable point for re-attachment (see Figure 3.17). The presence of a more stable reattachment location significantly reduces the likelihood of inverted platooning and promotes high drag reduction for both vehicles.

With a rounded leading edge, the rear vehicle tends to perform significantly worse. For every configuration where the rear vehicle had a rounded leading edge, cases of inverted platooning was observed. This is primarily due to the wake impingement on the rounded leading edge that can be seen in both the streamwise and spanwise directions in figures 3.10 and 3.14. This was

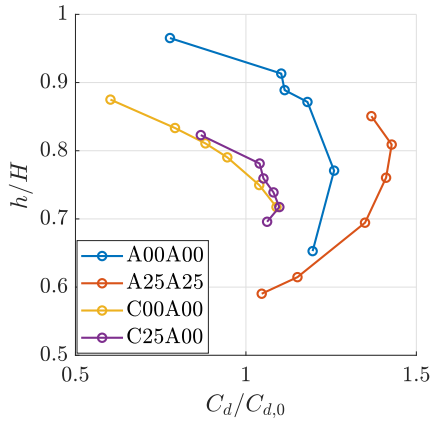

Figure 3.18: Normalised drag coefficient as a function of wake impingement location in the vertical axis on the leading edge of the rear geometry.Values taken from platoons at $d/L = 0.5$. A00 is the abbreviation for the Ahmed-0° vehicle, A25 is the Ahmed 25° vehicle, C00 is the Cuboid-0° vehicle and C25 is the Cuboid-25° vehicle. These abbreviations were used to make the legend of this figure more legible.

also observed when analysing the turbulent kinetic energy. In figures 3.11 and 3.12 the shear layer is highlighted by the area of increased turbulent kinetic energy, here the wake impingement on the leading edge of the rear vehicle is more noticeable.

As the flow transitions from recirculating wake to free stream, a stagnation zone forms on the leading edge of the rear vehicle. In order to analyse how the stagnation location effects the drag coefficient of the rear vehicle in more detail, first, a standardised definition of how to measure the location of stagnation should be provided. Using the centre plane of the platoon as a reference, when the flow impinges on the leading edge of the rear vehicle, some flow is diverted over the top of the vehicle with the rest being forced down the leading edge and under the vehicle. Moving from one regime to the other along the leading edge of the rear vehicle, the flow slows to a stagnation point and then changes direction. With this knowledge the shear stress along the centre line of the rear vehicle can be analysed. As with the flow direction, the wall shear stress also passes through a zero point when the flow stagnates. This allows us to measure the vertical height of the stagnation on the leading edge of the rear vehicle. The effects of stagnation location were also analysed in a paper by Mirzaei et al. [109] however, here they describe the wake impingement or stagnation location as simply the region on the centre plane where high pressure stagnation occurs.

When the stagnation location is very high, e.g., in the Ahmed-0°-0° case at $d/L = 0.2$, little to no drag increase is observed. Similarly, when the stagnation location is low, like in the Ahmed-25° $-$ 25° configuration at $d/L = 1$, the flow around the rear vehicle is similar to the flow over an isolated Ahmed-25° therefore, there is little difference in the drag coefficient. It appears that when the stagnation location is somewhere in between these two points, the effect of the wake impingement is strongest resulting in a sharp increase in drag. Whilst this appears to

hold true, the location of stagnation on the rear vehicle when the peak drag is measured changes on a case by case basis. The results of this in seen in figure 3.18.

From analysing figure 3.18 more closely, it can be hypothesised that any interaction of the shear layer arising from the wake of the front vehicle with the rounded leading edge of the rear vehicle negatively effects the rear vehicle. The isolated Ahmed vehicle generates a large amount of pressure recovery at the front of the vehicle by having high velocity attached flow over the rounded leading edge. The shear layer impingement disrupts this flow and reduces the velocity, increasing the drag of the rear vehicle.

The final geometric change was the introduction of a trailing edge slant on the rear vehicle. This had the effect of reducing the absolute drag of the rear vehicle, however it had no significant effect the platoon as a whole. Altering the trailing edge geometry of the rear vehicle does not influence the drag coefficient of front vehicle as it is too far downstream. It also has no effect on the platooning regime meaning that it does not dictate whether a specific platooning configuration displays classical or inverted platooning conditions.

Finally, the presence of the rear vehicle can also impact on the drag experienced by the front vehicle. The drag of an isolated Ahmed body is dominated by the pressure drag contribution over its rear. The presence of a bluff trailing body (cuboid geometry) promotes pressure recovery for the front Ahmed body and results in a significant reduction of the front vehicle's drag at short spacing. This effect is most prominent for the Ahmed 25° geometry, where, in addition, the presence of a bluff rear body triggers separation of the flow over the trailing edge slant angle of the front vehicle. In contrast, if the platoon is lead by a cuboid, no significant change in drag can be achieved for the front vehicle, since its total drag is dominated by the pressure drag contribution over its sharp leading edge.

3.5 Conclusion

The influence of vehicle geometry on the occurrence of 'inverted platooning' conditions, i.e., platoons where the trailing vehicle experiences an increase in drag, was investigated for two-body platoons formed of simplified model vehicles. It emerges that several geometry aspects can give rise to 'inverted platooning'. It is very unlikely to occur when the leading vehicle is a bluff body, such as a cuboid, whose large wake provides effective sheltering for the trailing vehicle. However, when the leading vehicle is more streamlined, such as the Ahmed body, the flow in the inter-vehicle gap governs the platoon's behaviour. The flow in the inter-vehicle gap is strongly determined by the wake of the front vehicle, but its impact on the platoon's behaviour is also affected by the leading edge geometry of the rear vehicle.

The main aim of this study was to identify a cause for the rear geometry experiencing a drag increase whilst in a platoon and to identify what geometric features are causing the increase in drag. As expected, there is more than one factor that contributes to increasing the drag of the

rear geometry.

If the leading edge of the front geometry is sharp, the resulting wake can be so large that any other geometric differences have very little effect on the overall platoon. This is the main cause for most of the classical platooning cases, especially those using cuboids.

When the leading edge of the front geometry is curved, the flow is able to remain attached and the geometric features at the interface between the front and rear geometries plays a much larger role. When the rear geometry also has a rounded leading edge, the wake impinges on this surface disrupting the attached flow and significantly reducing the pressure recovery seen in the isolated case. The maximum drag for the rear geometry comes when the curved leading edge passes through the boundary between the recirculation region of the wake and the free stream. This effect is only amplified when the front geometry has a trailing edge slant. The trailing edge slant causes a much smaller wake and the pressure gradient of the wake is much more concentrated. Without the trailing edge slant, the wake is much more unstable so the pressure difference is spread out over a much larger surface area on the leading edge of the rear geometry. This often still results in an increase in drag, however, the increase is amplified by the presence of a trailing edge slant.

If the rear geometry has a blunt leading edge the effects of wake impingement discussed previously can be neglected. The sharp leading edge provides a stable location for the flow to reattach and often benefits both the lead and trailing vehicles. Its effectiveness is again reduced when the lead vehicle has a trailing edge slant, however, most cases still yield classical platooning conditions.

For four vehicle geometries, there are a total of 4 possible homogeneous platoons and 12 possible heterogeneous platoons. In this study, 8 heterogeneous platoons were omitted. These consisted of: Cuboid 0° - Cuboid 25°, Cuboid 0° - Ahmed 25°, Cuboid 25° - Cuboid 0°, Cuboid 25° - Ahmed 25°, Ahmed 0° - Cuboid 25°, Ahmed 0° - Ahmed 25°, Ahmed 25° - Cuboid 25° and Ahmed 25° - Ahmed 0°. Whilst it was impractical to run all of the permutations, it is hypothesised that the statements presented regarding flow physics over these platoons will hold true such that, the platoons led by a cuboid type vehicle will produce a large wake resulting in more sheltering and platoons led by Ahmed type vehicles will show inverted conditions if the rear vehicle is also an Ahmed type vehicle.

Although the cuboid geometries performed better in the platoon, they also have much higher drag coefficients when in isolation and this adversely affects the platoon when considering its absolute drag. Despite this, when looking to design a platoon, it may be possible to introduce flow control on a more streamlined lead geometry to create a more beneficial wake structure that reduces the negative effects associated with wake-impingement on a streamlined rear body in the platoon.

Chapter 4

Flow control for platoons: computational investigation

4.1 Introduction

As discussed in the literature (section 2.3) and in chapter 3, a platoon of two 25° Ahmed vehicles results is the most obvious case of inverted platooning conditions. In this chapter the implementation of flow control on a platoon of two 25° Ahmed vehicles will be explored. This will be done computationally through the use of URANS simulations. The objective of this chapter is to improve the understanding of how a simple flow control device will influence the complex aerodynamics of the platoon. Additionally, the methods used to reduce the inverted platooning conditions displayed by the Ahmed platoon will be identified.

The results from chapter 3 highlighted how small changes in vehicle geometry can significantly alter the efficiency of a platoon. Many of these cases displayed inverted platooning conditions and whilst, in general, the level of drag increase for one vehicle was offset by the level of drag reduction for the other vehicle (see, e.g., figure 3.7), this is still not an optimum outcome.

The main objective of platooning is to improve the efficiency of road vehicles. For a business with multiple vehicles, e.g., an operator of a fleet of HGVs, forming a platoon that, as a whole, is more efficient than multiple vehicles in isolation is a useful technique to implement. However, for the widespread adoption of platooning, it would be desirable if individual vehicles travelling in the same direction could be combined into a platoon, not just vehicles operated by the same business. In this scenario where multiple individual vehicles work together to form a platoon, it is vital that each vehicle in the platoon receives some benefit, otherwise many individuals would be hesitant to join a platoon.

The homogeneous platoon of two 25° Ahmed vehicles exhibited the most extreme case of inverted platooning in the shape dependency study conducted in chapter 3. One difference of particular interest was the change in drag coefficients from the platoon of two 25° Ahmed ve-

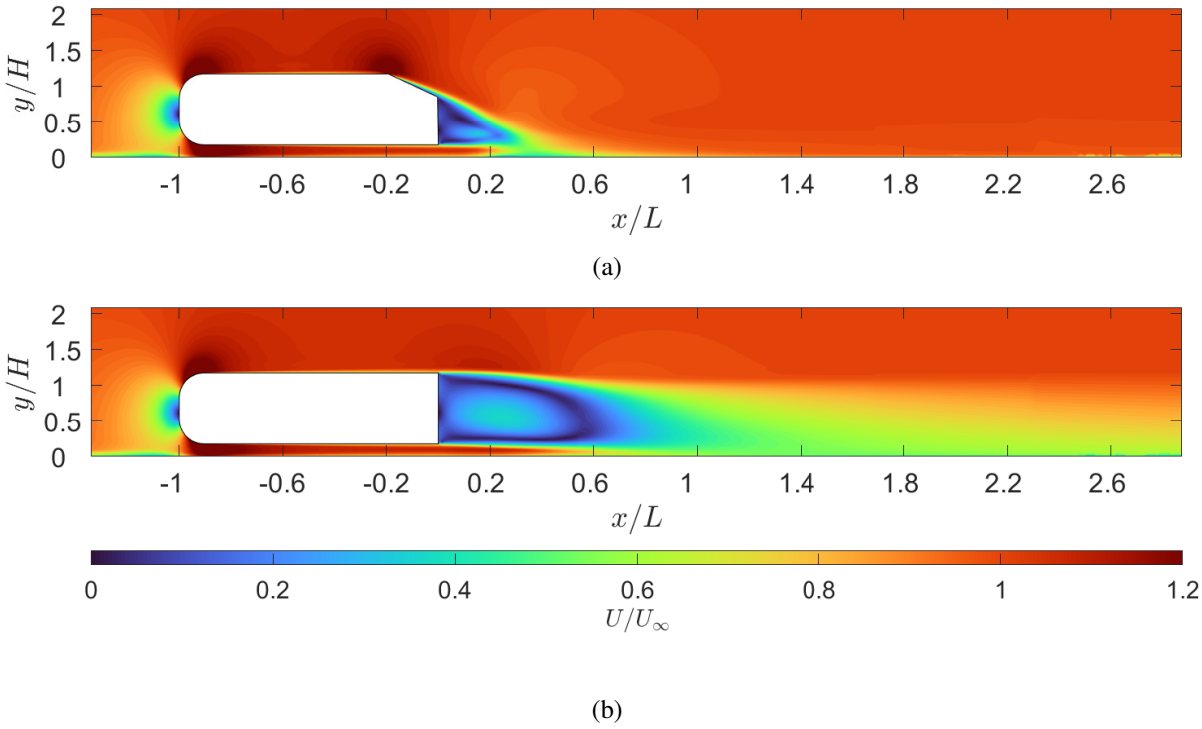

(a)

(b)

Figure 4.1: Average normalised velocity field comparison of the (a) 25° and (b) squareback Ahmed vehicles in isolation. This highlights the increased size of the wake produced by the squareback Ahmed vehicle when compared to the 25° Ahmed vehicle. Flow is from left to right.

hicles to two squareback Ahmed vehicles. This modification resulted in both the front and rear vehicles in the platoon to receive a drag reduction at $d/L = 0.2$. This provides the grounds for the hypothesis that the negative effects caused by platooning 25° Ahmed vehicles could be mitigated if the wake of the front vehicle was modified to provide more sheltering to the rear vehicle.

The difference in wake structure between the squareback and 25° Ahmed vehicle configurations in isolation was explored in detail as part of section 2.1, a visual comparison is also provided in Figure 4.1. Fundamentally, the difference in wake structure stems from the cause and location of flow separation. Whilst the flow remains attached over the rear slant of the 25° case, creating a small recirculation region in the wake, the flow over the squareback case has no angled surface to follow. Instead the flow detaches over the rounded edge at the rear of the vehicle, significantly higher than in the 25° case, resulting in a much higher and longer recirculation region.

Whilst changing the geometry of a vehicle is an effective way to influence the flow, it does not lend itself well to practical application. A more elegant method to achieve similar results would be through the application of flow control to mimic the wake generated by the squareback vehicle geometry. This would allow a vehicle to change its wake when part of a platoon by activating the flow control, while maintaining the ability to return to its normal wake conditions

when travelling in isolation.

A simple way to introduce this behaviour is through the use of flaps. Flaps are a standard, flow control device that have been used numerous times on isolated Ahmed vehicles. They are often used to control flow separation on the isolated case and alter the wake of the vehicle. A range of flap lengths and angles were investigated in order to characterise their performance in a platooning setting. This also allows for an assessment of the flow control's behaviour prior to a full wind tunnel investigation.

4.2 Methodology

In this section, the basic flow control approaches will be discussed. The flow control device was applied to the front vehicle in the platoon only, since, as described above, the aim is to modify the flow in the inter-vehicle gap. The computational approach, domain size and meshing scheme have all been kept consistent from the study outlined in chapter 3 and a detailed explanation of this setup was provided in section 3.2.2. To incorporate the addition of flow control devices into the simulation, some modifications were made to the simulation, these will be detailed later in this section. The investigation was conducted using a URANS method incorporating the $k-\omega$ SST turbulence model in Simcenter Star-CCM+ version 15.04.010. An inlet flow speed of $40ms^{-1}$ was used on a full scale Ahmed vehicle resulting in a Reynolds number of $7.35 \cdot 10^5$ based on vehicle height.

4.2.1 Flaps

Flaps have been utilised on many occasions across the automotive field to improve the aerodynamic efficiency and stability of road vehicles [122, 123]. More specific to the Ahmed vehicle, flaps have been used to induce flow separation over the trailing edge of the vehicle resulting in a reduction of the drag coefficient [56, 62–65]. They have also been used in other locations around the base of the vehicle to shrink the size of the wake and provide some pressure recovery. Notably, Kim et al. [92] used flaps in a semi active manner. Instead of mounting the flaps at a fixed angle, they were allowed to move freely providing a drag reduction of 19%.

The above are all examples of flap implementation on isolated vehicles. This study is one of the first to implement flow control of any kind on a platoon therefore the use of flaps will provide a good baseline for what can be achieved by even the most basic form of flow control. In addition, their robust and well studied nature will provide a more transferable application to both wind tunnel and real world testing as their implementation is far less complex than other flow control methods.

The flaps were mounted on the front vehicle at the top of the slant as outlined in figure 4.2. Three flap angles were used, measured from horizontal (see α in figure 4.2) these were $0°, 10°$

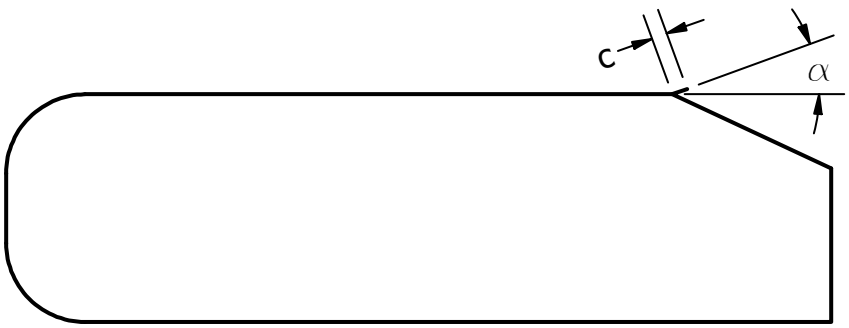

Figure 4.2: Location and dimensions of flap for flow control. c is the given flap length and α is the given flap angle. Flow is from left to right.

and 20°. These angles were selected as this is the range of flap settings where the isolated 25° Ahmed vehicle performs best [56, 61–63, 65]. To our knowledge, this is the first study in which flaps were added to the Ahmed 25° platoon therefore, guidance was taken from the isolated case. The width of the flap was equal to the width of the Ahmed vehicle and three flap lengths of $5mm$, $10mm$ and $20mm$ ($0.005L$, $0.01L$ & $0.02L$ respectively) were investigated. Again, flap lengths were inspired from the aforementioned literature on the isolated 25° Ahmed body however, the flap lengths used between these studies were less consistent. There is additional motivation in the automotive industry to keep flow control devices small as to maintain the correct aesthetic in any given vehicle design. For this reason, the selected flap lengths were at the smaller end of what is seen in the literature.

When implementing the flap some assumptions had to be made to improve the efficiency of the simulation. To model the flap, a baffle was used. This is a solid surface of zero thickness, something that is obviously not achievable in an experimental environment. This technique and its applications are laid out in more detail in the StarCCM+ user guide [121]. In reality, the flap would be made of a stiff, thin, material in the region of $1mm$, however, the smallest cell size in the original volume mesh was $12mm$. To accurately simulate the flow around such a thin geometry, the minimum cell size would need to be in the region of $0.1mm$. This would result in not only a drastically modified mesh from the validation case, but also a significant increase in the number of cells and computational expense. For these reasons, the use of a baffle was employed to approximate a flap. A small region of the mesh around the flap was refined further to more accurately model the flow separation. This was the same modification described earlier in this section and resulted in the mesh size increasing from $4.3m$ cells, as used for the original mesh in chapter 3, to $4.6m$ cells.

4.3 Scope of investigation

Table 4.1 gives an overview of the platooning configurations that were explored as part of this flow control study. To the best of our knowledge, flow control has never been applied to a platoon

reference name	front geometry	rear geometry	flow control details
Ahmed-25° – 25°	25° Ahmed vehicle	25° Ahmed vehicle	none
Flap-5 – 10°	25° Ahmed vehicle	25° Ahmed vehicle	5*mm* flap at 10°
Flap-10 – 10°	25° Ahmed vehicle	25° Ahmed vehicle	10*mm* flap at 10°
Flap-20 – 0°	25° Ahmed vehicle	25° Ahmed vehicle	20*mm* flap at 0°
Flap-20 – 10°	25° Ahmed vehicle	25° Ahmed vehicle	20*mm* flap at 10°
Flap-20 – 20°	25° Ahmed vehicle	25° Ahmed vehicle	20*mm* flap at 20°

Table 4.1: Overview of investigated platoon configurations with associated flow control description

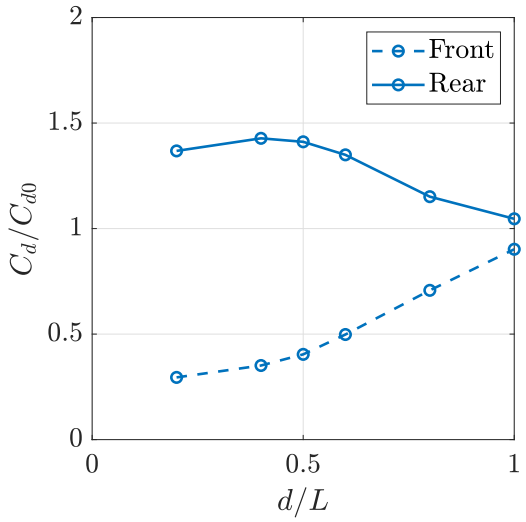

Figure 4.3: Normalised drag coefficient of the baseline platoon of two 25° Ahmed vehicles over a range of inter-vehicle distances.

in this manner before. Therefore, this test space was required to gain a broad understanding of how flow control affects the platoon's performance.

4.4 Results and discussion

In this section, a detailed characterisation of the baseline platoon of two 25° Ahmed vehicles will be provided. Following this, the implementation of flow control targeted at modifying the wake of the front vehicle in a platoon can improve the baseline result through the use of flaps will be assessed.

4.4.1 Baseline platoon

Figure 4.3 shows the normalised drag coefficient of the baseline platoon. A large increase of up to 43% is seen for the rear vehicle between $d/L = 0.2$ and $d/L = 0.6$. In contrast, the front vehicle receives a sizable drag reduction in the order of 70% at $d/L = 0.2$, reducing to 50% by

Total	Leading edge	Trailing edge slant	Base	Other surfaces
0.279	0.012	0.142	0.086	0.039

Table 4.2: Breakdown of the component of drag coefficient attributed to each surface on the Isolated 25° Ahmed vehicle

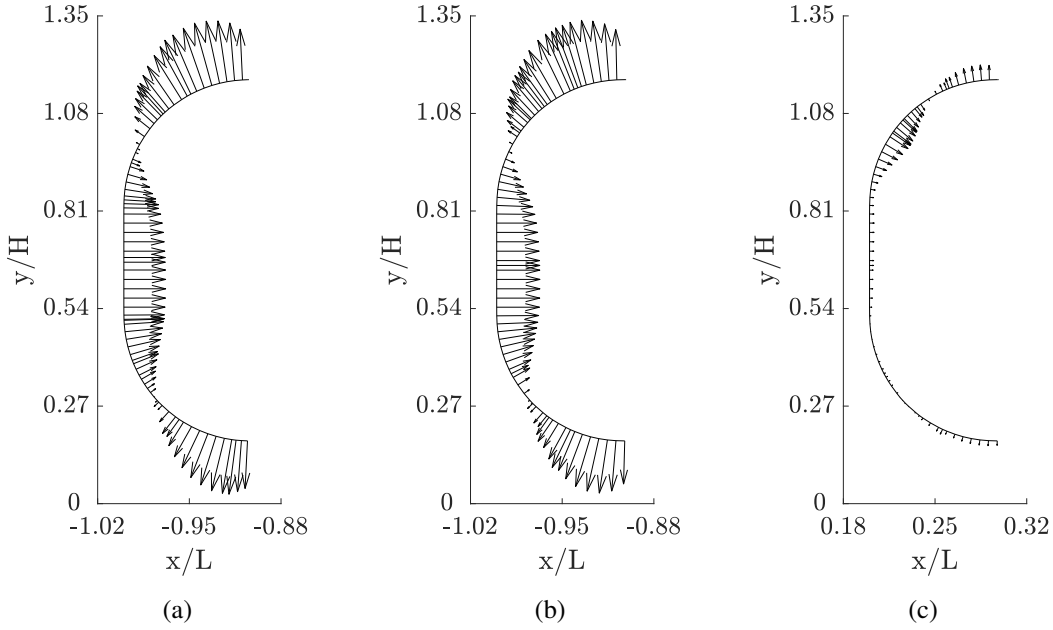

Figure 4.4: Wall normal pressure distribution across the centre plane on the leading edge of (a) an isolated Ahmed vehicle (b) the front vehicle in the baseline platoon (c) the rear vehicle in the baseline platoon at $d/L = 0.2$.Here an arrow facing into the surface represents a pressure greater than the reference pressure and an arrow pointing away from the surface denotes a pressure less than the reference pressure. The length of each arrow describes the magnitude of the pressure difference.

$d/L = 0.6$. For both vehicles, the normalised drag coefficient slowly returns to 1 as the inter-vehicle distance is increased. As discussed previously in chapter 3, this platoon is one of the most obvious cases of inverted platooning and was analysed in detail. The conclusion of this analysis was as follows: the increase in drag coefficient occurs due to the interaction of the shear layer produced by the front vehicle impinging on the rounded portion of the leading edge of the rear vehicle.

When in isolation, the leading edge of the Ahmed vehicle contributes a relatively low component of the overall drag of the vehicle. This can be seen in figure 2.3 and table 4.2. Whilst the stagnation on the flat leading edge does produce drag, the accelerated flow around the curved faces provides a large amount of pressure recovery. In addition, the trailing edge of the vehicle (trailing edge slant and base combined) produces upwards of 80% of the total drag due to the attached flow over the rear slant when set at 25°.

Figure 4.4 shows a comparison of the pressure distribution on the centre plane between the isolated Ahmed vehicle and the front and rear vehicles of the baseline platoon. This plot is based

on the plots often used to show pressure distribution around a circular cylinder [124]. This plot actually shows the difference in pressure between the measured and reference pressures, the usual convention for this type of plot is as follows: for pressures greater than the reference pressure, the difference is positive therefore the pressure lines point normal into the surface; for pressures lower than the reference pressure, the difference in pressure is negative and the lines point normal away from the surface. In this situation, 'positive' pressure denotes pressure pushing on the surface and 'negative' pressure denotes pressure pulling on the surface. The length of each line indicates the magnitude of the difference between the total pressure and the reference pressure.

Again here, the extent of the pressure recovery generated by the flow moving over the rounded portion of the leading edge of an isolated Ahmed vehicle is apparent. It is also important to note that this is only the centre plane and there are in-fact two additional curved surfaces on the side of the Ahmed vehicle also providing some pressure recovery at the front of the vehicle.

When comparing the front vehicle of the baseline platoon to the isolated case, they are almost identical. This is to be expected as the inflow for both vehicles is similar. When comparing this to the rear vehicle however(sub-figure (c)), the flow disruption caused by the platoon is clearly visible. In general, the magnitude of the difference in total pressure is significantly reduced by platooning. Whilst the pressure difference on the flat portion of the leading edge is reduced, a sizable portion of the pressure recovery over all of the curved surfaces is also lost. This, combined with the large spike in pressure where the wake from the front vehicle impinges on the leading edge of the rear vehicle, results in a dramatic increase in drag in this region of the rear vehicle.

A similar mechanism applies at the trailing edge of the front vehicle, thus providing the drag reduction seen in figure 4.3. Where, in isolation, the trailing edge produces a large component of the vehicle's drag (as highlighted in table 4.2), the presence of a second vehicle close behind the front vehicle increases the base pressure on the front vehicle. This actually has two effects, primarily, this produces some pressure recovery on the flat portion of the base, reducing the drag. In addition, at short inter-vehicle distances of $d/L \leq 0.6$, the additional pressure at the base induces some flow separation over the trailing edge slant. The combination of these two mechanisms results in drag reductions of $50-70\%$

As the vehicles move further apart, (from $d/L = 0.6$ to $d/L = 0.8$) the drag coefficient of the rear vehicle falls sharply. The larger distance between the vehicles reduces the base pressure on the front vehicle therefore, at $d/L = 0.8$, the flow over the trailing edge of the front vehicle begins to reattach the the surface. This can be seen in figure 4.5 where a comparison of the average normalised velocity field for the baseline platoon at $d/L = 0.6$ and $d/L = 0.8$ is provided. This reattached flow significantly reduces the levels of wake impingement on the leading edge of the rear vehicle resulting in a swift reduction in drag coefficient.

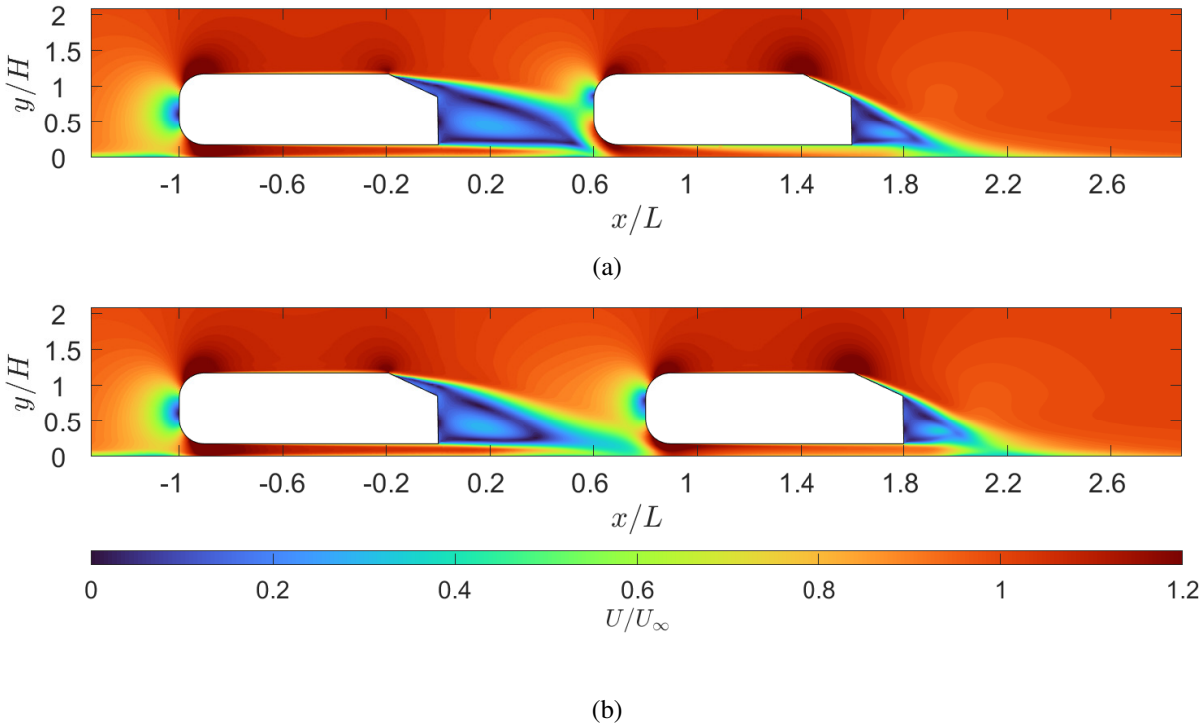

Figure 4.5: Average normalised velocity field comparison of the baseline platoon at (a) $d/L = 0.6$ and (b) $d/L = 0.8$. The flow direction is left to right.

Case	Front						Rear					
	0.2	0.4	0.5	0.6	0.8	1.0	0.2	0.4	0.5	0.6	0.8	1.0
Ahmed-25° – 25°	0.08	0.10	0.11	0.14	0.20	0.25	0.38	0.40	0.39	0.38	0.32	0.29
Flap-5 – 10°	0.12	-	0.13	-	-	0.20	0.28	-	0.31	-	-	0.32
Flap-10 – 10°	0.14	-	0.14	-	-	0.20	0.22	-	0.32	-	-	0.32
Flap-20 – 0°	0.12	-	0.13	0.14	0.16	0.20	0.28	-	0.32	0.33	0.35	0.23
Flap-20 – 10°	0.16	0.15	0.15	0.15	0.18	0.21	0.20	0.28	0.31	0.32	0.34	0.29
Flap-20 – 20°	0.18	-	0.18	0.17	0.20	0.22	0.22	-	0.32	0.33	0.32	0.30

Table 4.3: Drag coefficient for each vehicle for the platoons with flaps as flow control.

In general, the platooning effects between the two vehicles become weaker as the inter-vehicle distance grows, thus causing the drag coefficient of both vehicles to tend towards the drag coefficient of an isolated vehicle.

4.4.2 Platoons with flow control: Flaps

The previous section highlights how wake impingement on the rear vehicle results in inverted platooning conditions. Through the implementation of a simple flap at the trailing edge of the front vehicle, it is hypothesised that the shear layer can be diverted over the rear vehicle thus reducing the drag of said vehicle. In this section the effect of flap length and angle on the drag coefficient of both vehicles in the platoon will be studied.

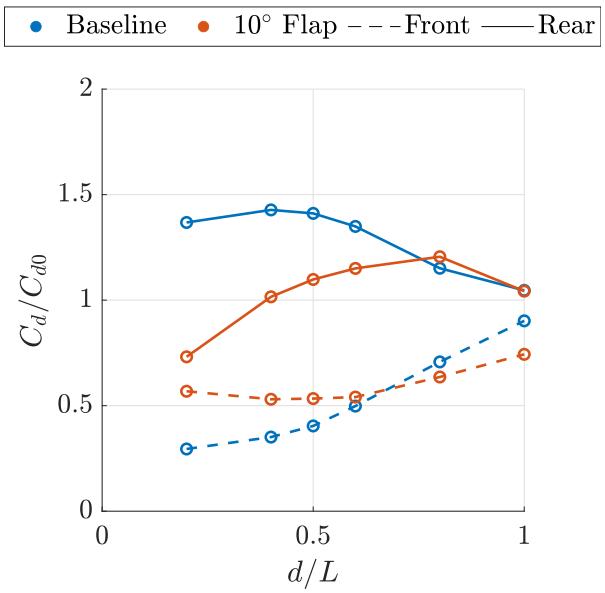

Figure 4.6: Normalised drag coefficient of the baseline platoon compared to the drag coefficients of a platoon of two 25° Ahmed vehicles where the front vehicle has a 20*mm* flap set at $\alpha = 10°$. All values are normalised with respect to an isolated 25° Ahmed vehicle.

Proof of concept

Initially, a 20*mm* flap at 10° incline from the horizontal was added to the lead vehicle of the 25° Ahmed vehicle platoon to promote flow separation. Figure 4.6 shows the effect that this flap has on the normalised drag coefficient compared to the baseline platoon. In this section, all values are normalised with respect to the isolated 25° Ahmed vehicle to highlight the true effect of the flow control. The drag coefficients for each vehicle in the platoons discussed in this chapter are given in table 4.3.

At short spacing the flap is most effective. For the rear vehicle at $d/L = 0.2$ the introduction of a flap on the lead vehicle reduces the drag coefficient by 45% when compared to the baseline case and 25% when compared to the isolated Ahmed vehicle. As the inter-vehicle distance is increased the effectiveness of the flap is reduced. The drag coefficient of the rear vehicle gradually increases and, by $d/L = 0.8$, has returned to a similar value to the baseline case.

For the front vehicle, the flap has the opposite effect. At short spacing the front vehicle performs slightly worse than the baseline case, however, over the range of inter-vehicle distances tested, the drag coefficient remains mostly unchanged. This suggests that the consistent flow separation created by the flap results in the front vehicle being less effected by the rear vehicle. This reduced dependency on the platooning configuration culminates in a drag reduction when compared to the baseline at $d/L = 0.8$ and $d/L = 1.0$.

In general, for an isolated 25° Ahmed vehicle, causing the flow to detach over the trailing edge slant improves the efficiency of the vehicle. This was shown in the studies by Tian at al. [62] and Raina et al. [64] and is also visible in the drag coefficient results at larger inter-

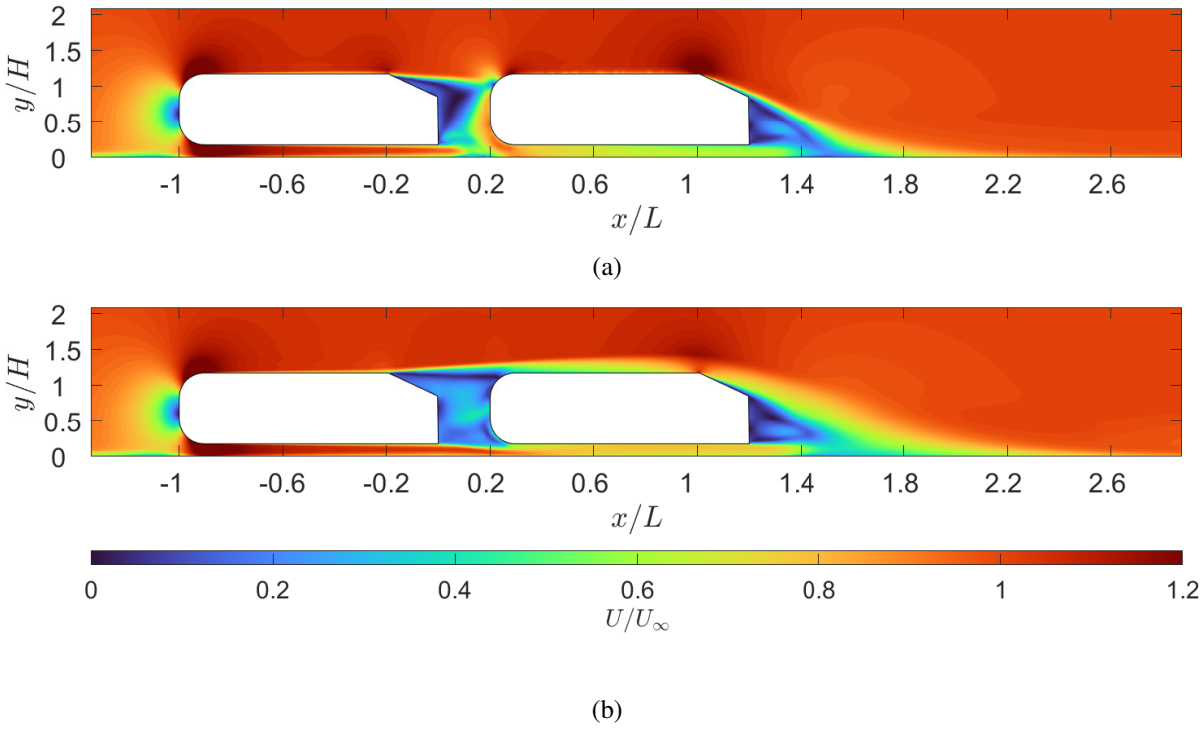

Figure 4.7: Average normalised velocity field comparison of the (a) baseline and (b) 20*mm*, 10°, flap cases at $d/L = 0.2$. The flow goes from left to right

vehicle distances from the current study, where platooning effects are less prevalent.

Figure 4.7 compares the mean velocity field, normalised with respect to the free stream velocity, between the baseline case and the initial flap configuration. This is used to highlight how the added flap modifies the wake of the front vehicle along the center plane. For the baseline case, the additional base pressure produced by the presence of the rear vehicle is sufficient to cause some flow separation over the trailing edge slant of the front vehicle. The addition of the flap provides a stable detachment point for the flow resulting in a larger, more controlled wake. This also alters the stagnation location on the leading edge of the rear vehicle.

In the baseline case, the wake impinges on the curved leading edge of the rear vehicle resulting in a large spike in pressure, as seen in figure 4.4. This is mitigated by the introduction of the flap as the entire leading edge of the rear vehicle is being sheltered. Whilst this also removes a lot of the pressure recovery aspect, which would be generated by the attached flow over the curved leading edge for an isolated vehicle, the associated drop in pressure due to the sheltering offsets this resulting in a net drag reduction. This interaction is highlighted when analysing the turbulent kinetic energy in figure 4.8. The highly turbulent shear layer is deflected over the leading edge of the rear vehicle by the flap where-as, in the baseline case, the turbulent wake of the front vehicle impinges directly into the rounded leading edge of the rear vehicle.

The introduction of the flap also impacts the 3D nature of the flow by eliminating the presence of the C pillar vortices as seen in figure 4.10. This is also seen in the literature of isolated Ahmed vehicles with flaps and is not as a result of the platooning [56, 61–63, 65]. At short

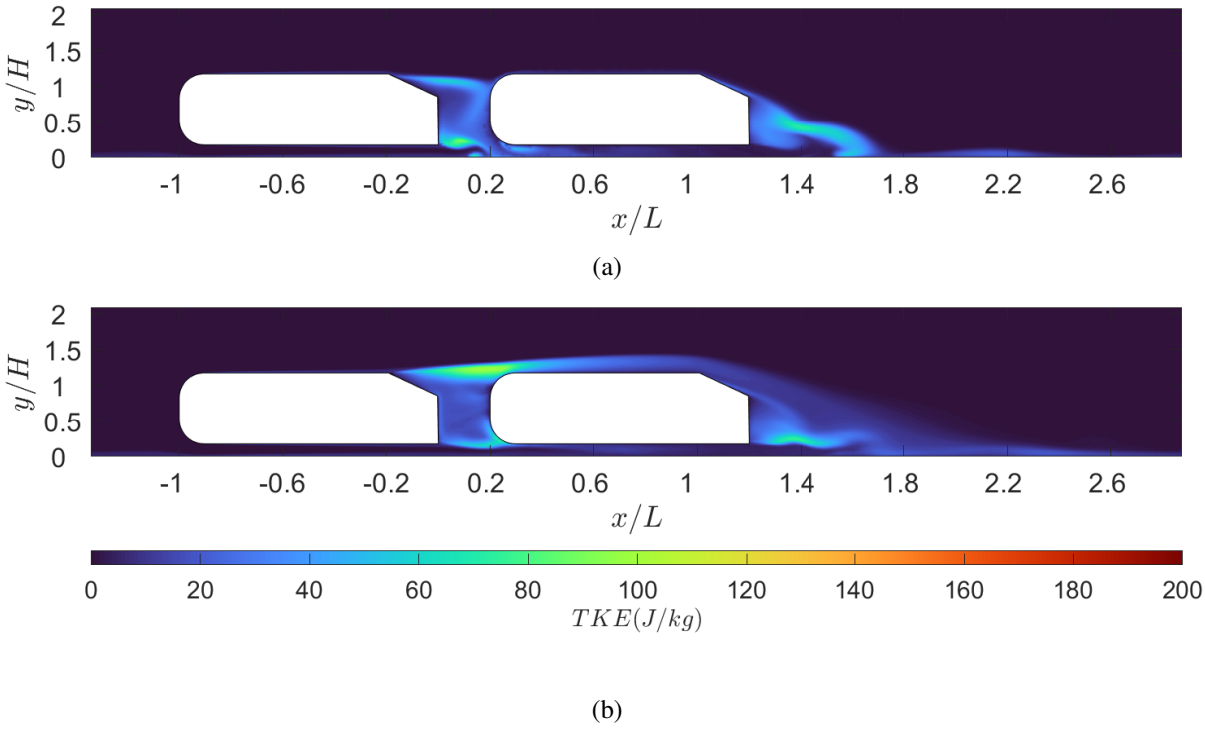

Figure 4.8: Turbulent kinetic energy field comparison of the (a) baseline and (b) 20*mm*, 10°, flap cases at $d/L = 0.2$. The flow goes from left to right

inter-vehicle distances, the flap maintains a much taller recirculation across the entire span of the vehicle. This results in improved flow reattachment in the spanwise plane for the flap case when compared to the baseline, further improving the performance of the rear vehicle in the platoon (see figure 4.9).

As the vehicles move further apart, the rounded leading edge of the rear vehicle in the flow control case begins to be affected more by the wake generated by the front vehicle, in particular the wake impingement caused by the upper shear layer. The resulting wake impingement at $d/L = 0.6$ is shown in figure 4.11. The intensity of the wake impingement remains significantly less for the platoon with flow control than in the baseline case. despite this, at this spacing, the rear vehicle does receive an increase in drag of 15% when compared to an isolated vehicle. This is still lower than the 35% drag increase seen in the baseline case and further highlights the importance of the stable flow attachment over the rounded leading edge of the Ahmed vehicle.

Finally, moving to the largest spacing, the difference in velocity field, shown in figure 4.12, is at its most prominent. When looking at the baseline case, the flow remains attached over both vehicles' rear slants and is a very close match to two Ahmed vehicles in isolation. The only difference is the slightly higher location of stagnation on the leading edge of the rear vehicle compared to the isolated vehicle case. This similarity is seen in the drag coefficient measurements as both vehicles have a normalised drag coefficient of approximately 1. In contrast, for the platoon with flow control, the flap on the front model continues to promote flow separation over the trailing edge slant leading to a large wake and continued wake impingement on the rear

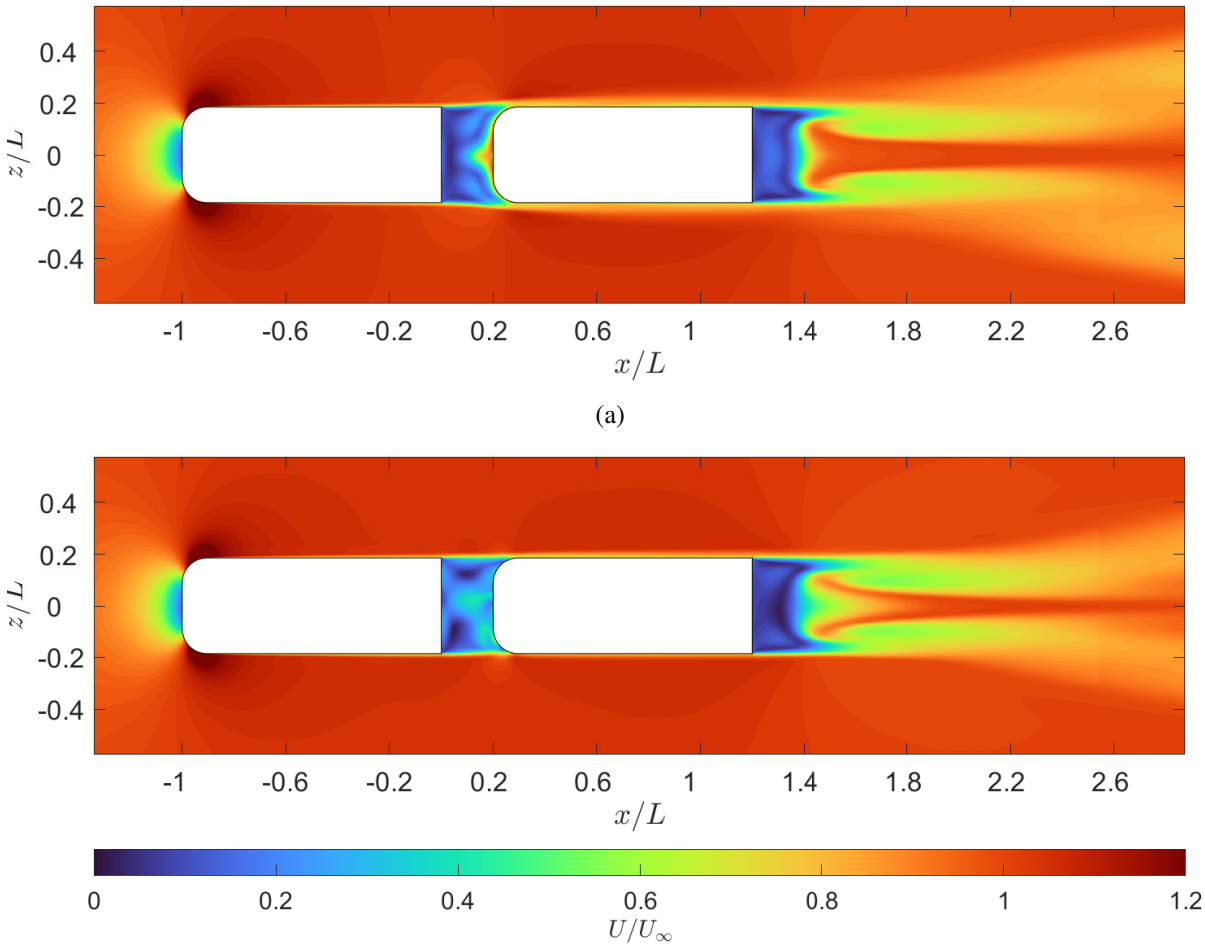

Figure 4.9: Average normalised velocity field comparison on a spanwise plane at $y = 0.15m$ of the (a) baseline and (b) 20mm, 10°, flap cases at $d/L = 0.2$. The flow goes from left to right

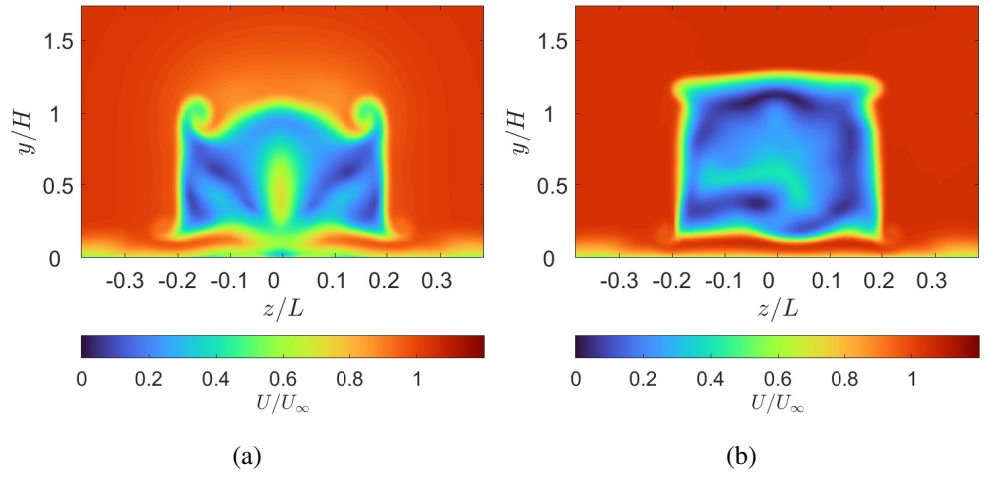

Figure 4.10: Average normalised velocity field comparison on a spanwise plane at $x = 0.15m$ of the (a) baseline and (b) 20mm, 10°, flap cases at $d/L = 0.2$. The flow goes from left to right

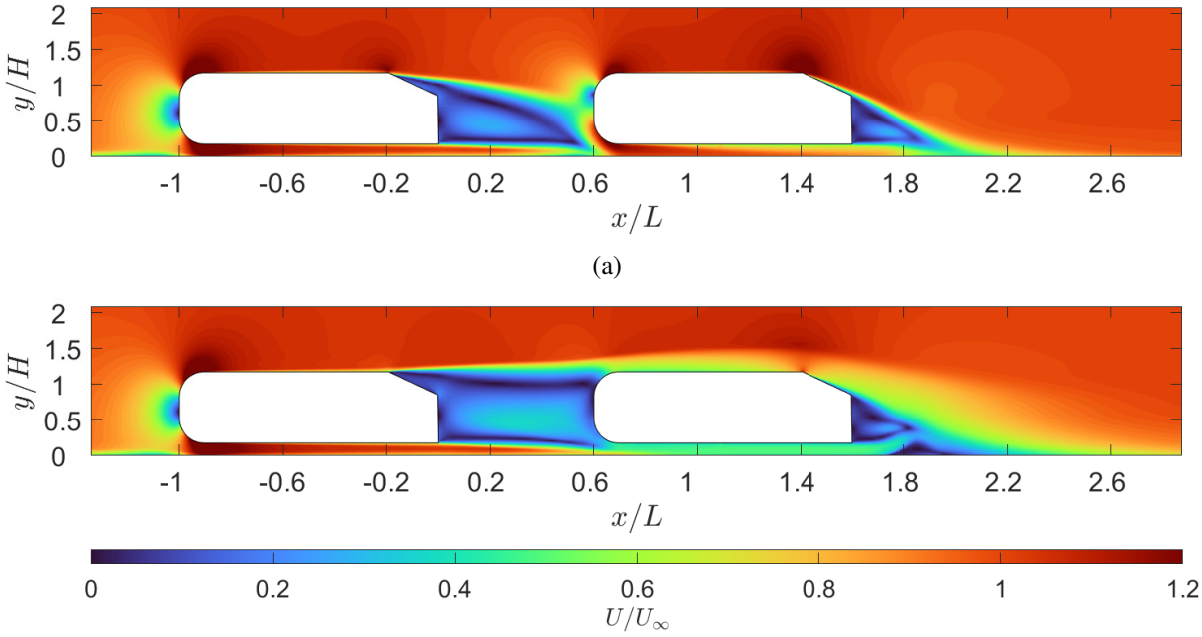

(a)

(b)

Figure 4.11: Average normalised velocity field comparison of the (a)baseline platoon and the (b)platoon where the front vehicle has a 20*mm*, 10°, flap at $d/L = 0.6$.The flow goes from left to right

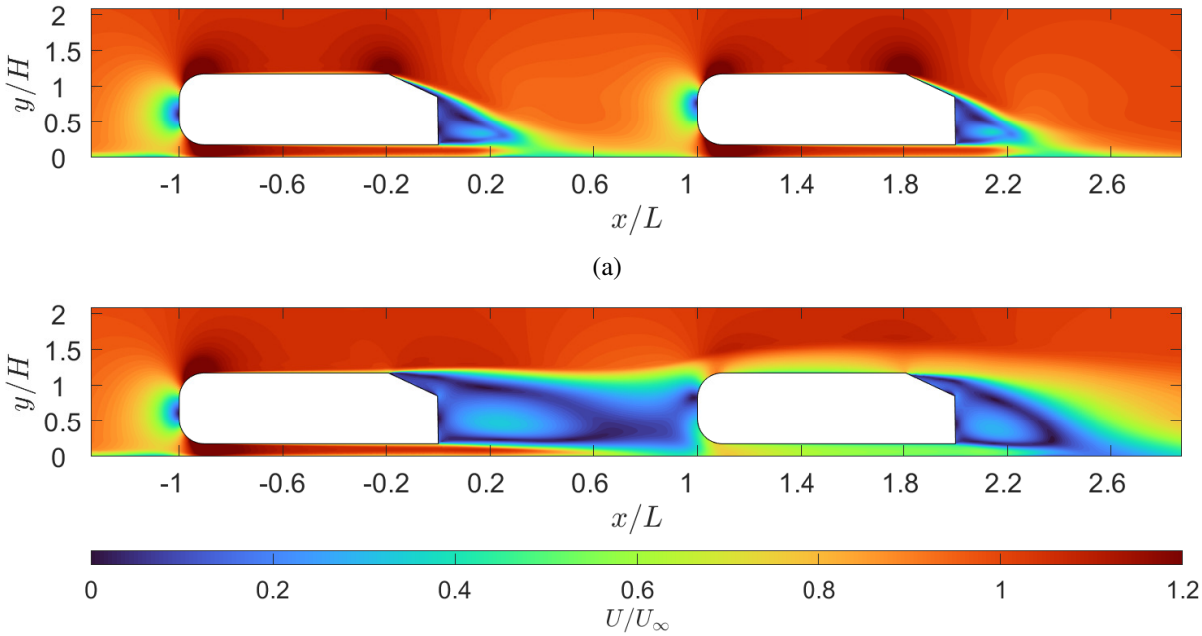

(a)

(b)

Figure 4.12: Average normalised velocity field comparison of the (a) baseline platoon and (b) the platoon with a 20*mm*, 10° flap at $d/L = 1.0$.

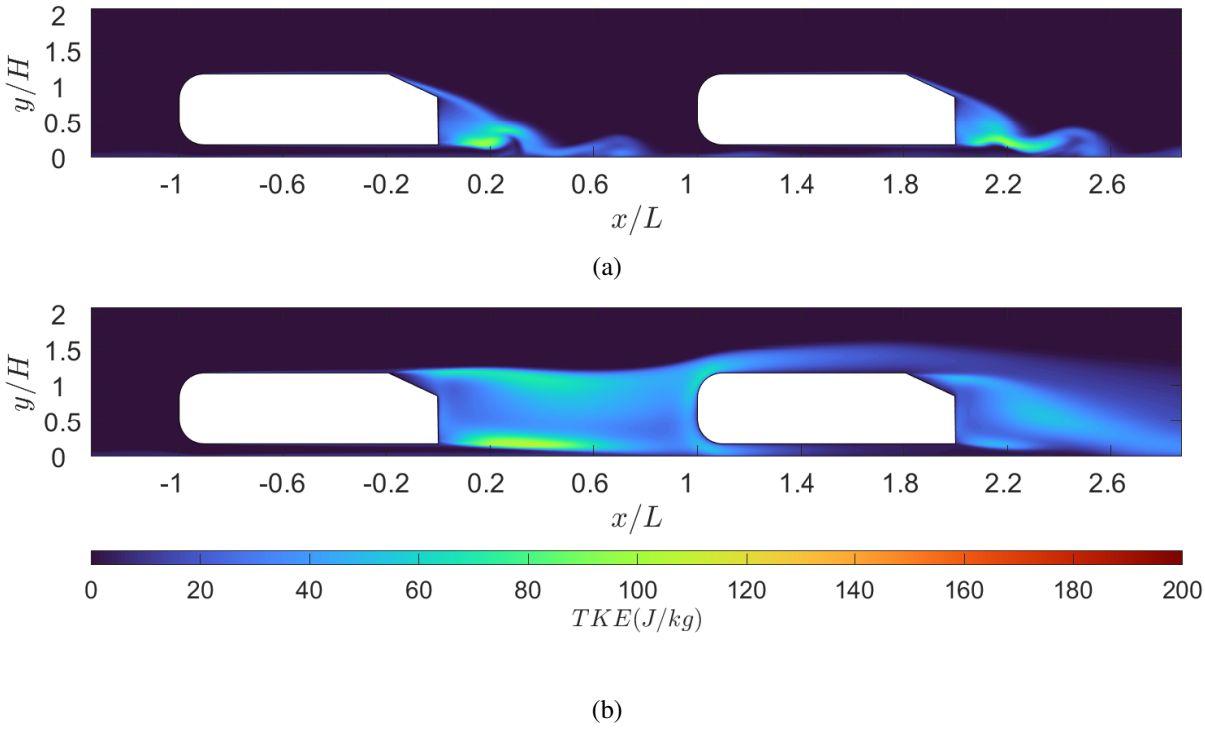

Figure 4.13: Turbulent kinetic energy field comparison of the (a) baseline and (b) 20*mm*, 10°, flap cases at $d/L = 1.0$. The flow goes from left to right

vehicle. This would result in an increase in drag for the rear vehicle, however, the increased turbulent kinetic energy in the wake of the front vehicle creates low velocity flow over the top of the rear vehicle causes the flow at the trailing edge of the rear vehicle to detach (see figure 4.13). This in turn reduces the drag component of this surface and compensates for the increase in drag caused by the wake impingement at the front of the vehicle.

The extended wake can also be seen in the spanwise direction. The lack of rear vortices can be seen in figure 4.13. This causes the recirculation region in the wake of the front vehicle to be much longer and wider, having a much larger influence on the flow structure of the rear vehicle despite the similar drag coefficient.

Effect of flap angle

In the next section, the influence of the flap angle was tested by considering three different flap angles 0°, 10°, and 20° . Initially the flap at 10° was studied as this is the optimum angle for an isolated 25° Ahmed vehicle [56], the additional angles (one above, one below) were added to better characterise the effects of flap angle of the platoon.

Figure 4.16 compares the drag coefficient of the baseline case to the three flap angles for a 20*mm* flap. The drag coefficients for each vehicle in the platoons discussed in this chapter are given in table 4.3. As seen in the previous comparison, the drag coefficient of the front vehicle with a flap is much less affected by the distance between the vehicles in the platoon when

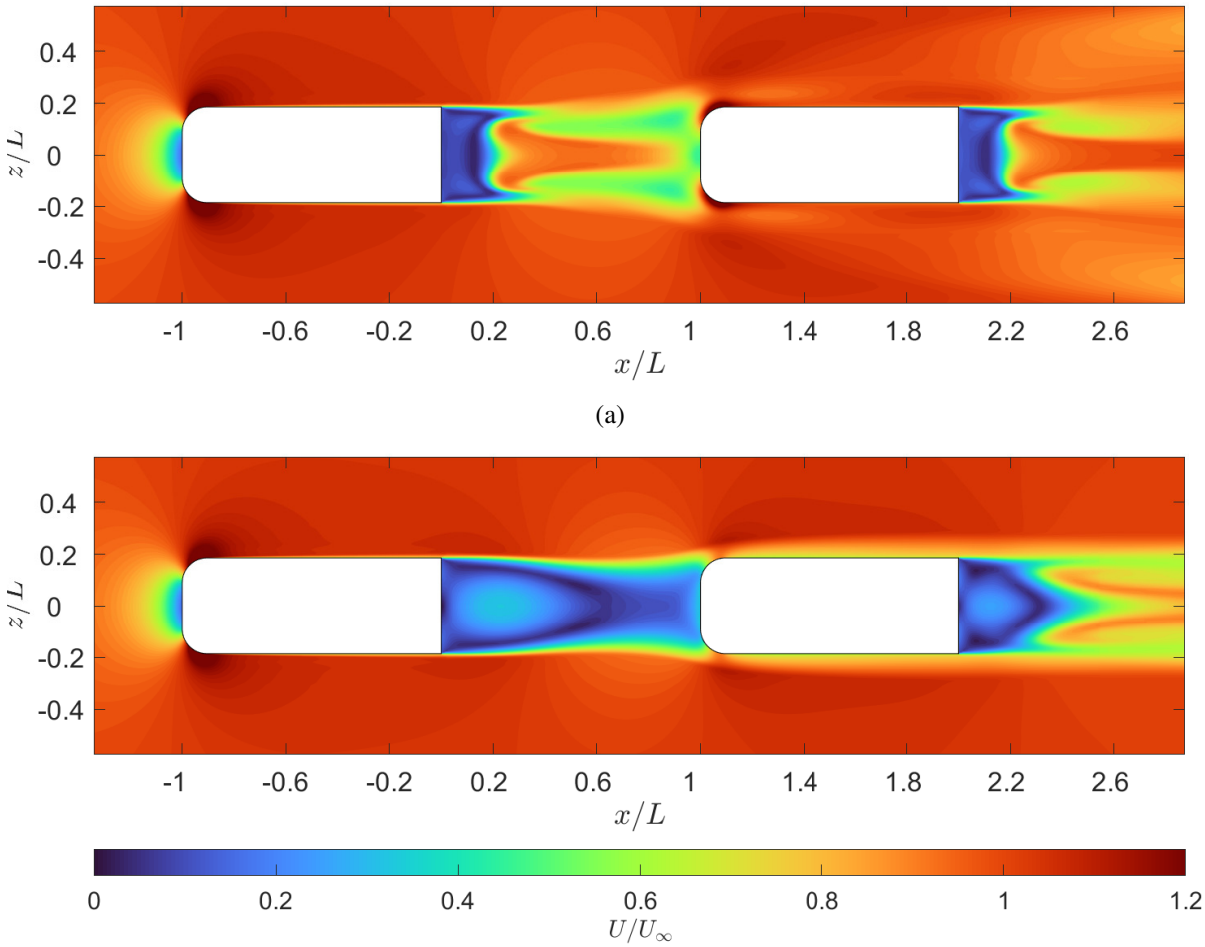

Figure 4.14: Average normalised velocity field comparison on a spanwise plane at $y = 0.15m$ of the (a) baseline and (b) 20mm, 10°, flap cases at $d/L = 1.0$. The flow goes from left to right

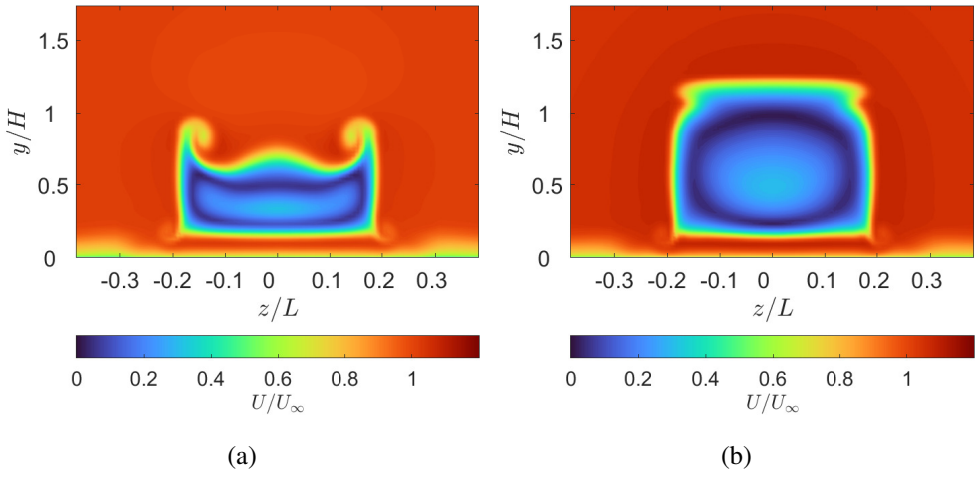

Figure 4.15: Average normalised velocity field comparison on a spanwise plane at $x = 0.15m$ of the (a) baseline and (b) 20mm, 10°, flap cases at $d/L = 1.0$. The flow goes from left to right

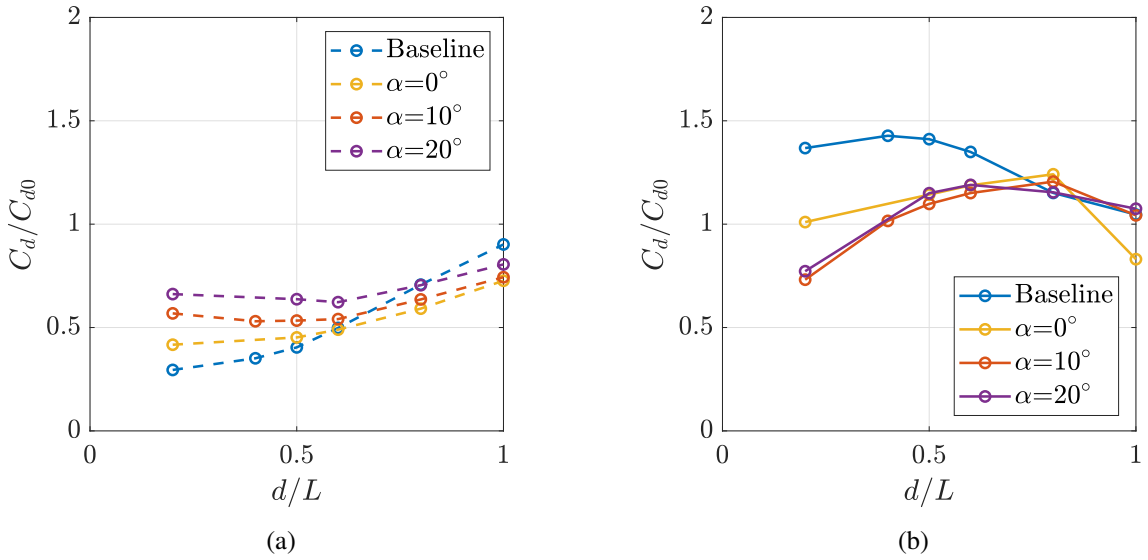

Figure 4.16: Normalised drag coefficient as a function of inter-vehicle spacing at different flap angle settings for the (a)front and (b)rear vehicles in a platoon of two 25° Ahmed vehicles.

compared to the baseline case. This holds true for the additional flap cases as, in general, the drag coefficient of the flap cases only gradually increase as inter-vehicle distance increases. At short spacings, all of the flap cases perform slightly worse than the baseline case. The flap cases have a drag reduction ranging from roughly 50% to 25%. In comparison, the front vehicle in the baseline case at $d/L = 0.2$ has a 70% reduction in drag coefficient. However, by $d/L = 1.0$, the baseline platoon has a drag reduction of only 5%, when compared to an isolated vehicle, with the flap cases all still receiving a reduction in drag coefficient from 23%, for the 20° case, to roughly 25% for the 0° and 10° cases.

The reasoning behind the difference in drag for the front vehicle is fairly intuitive. The drag reduction on the baseline case is caused by the positive pressure generated by the rear vehicle resulting in flow detachment. As the flap angle is increased, the increased base pressure is less influential in causing flow detachment resulting in less pressure recovery and less benefits for the front vehicle. Similarly, at the longest spacing of $d/L = 1.0$ the flow separation caused by the flap results in a drag reduction when compared to the baseline. This is due to the front vehicle in the baseline case no longer experiencing the benefits of the platoon and flow separation. At this stage, the benefits of the flap are very similar to the implementation of a flap on an isolated vehicle where it is suggested that to 10° case would perform best out of the three flap angles tested in this investigation. This is detailed in the experiment conducted by Beaudoin et al. [56].

The results for the rear vehicle are a little more complex. The obvious outlier in the data is the 0° flap case, as the 10° and 20° cases produce almost identical drag measurements for all the inter-vehicle distances tested. Upon closer consideration, all three flap cases have fairly similar results from $d/L = 0.4$ to $d/L = 0.8$ with only the shortest and longest inter-vehicle distances showing a significant dependency on the flap angle.

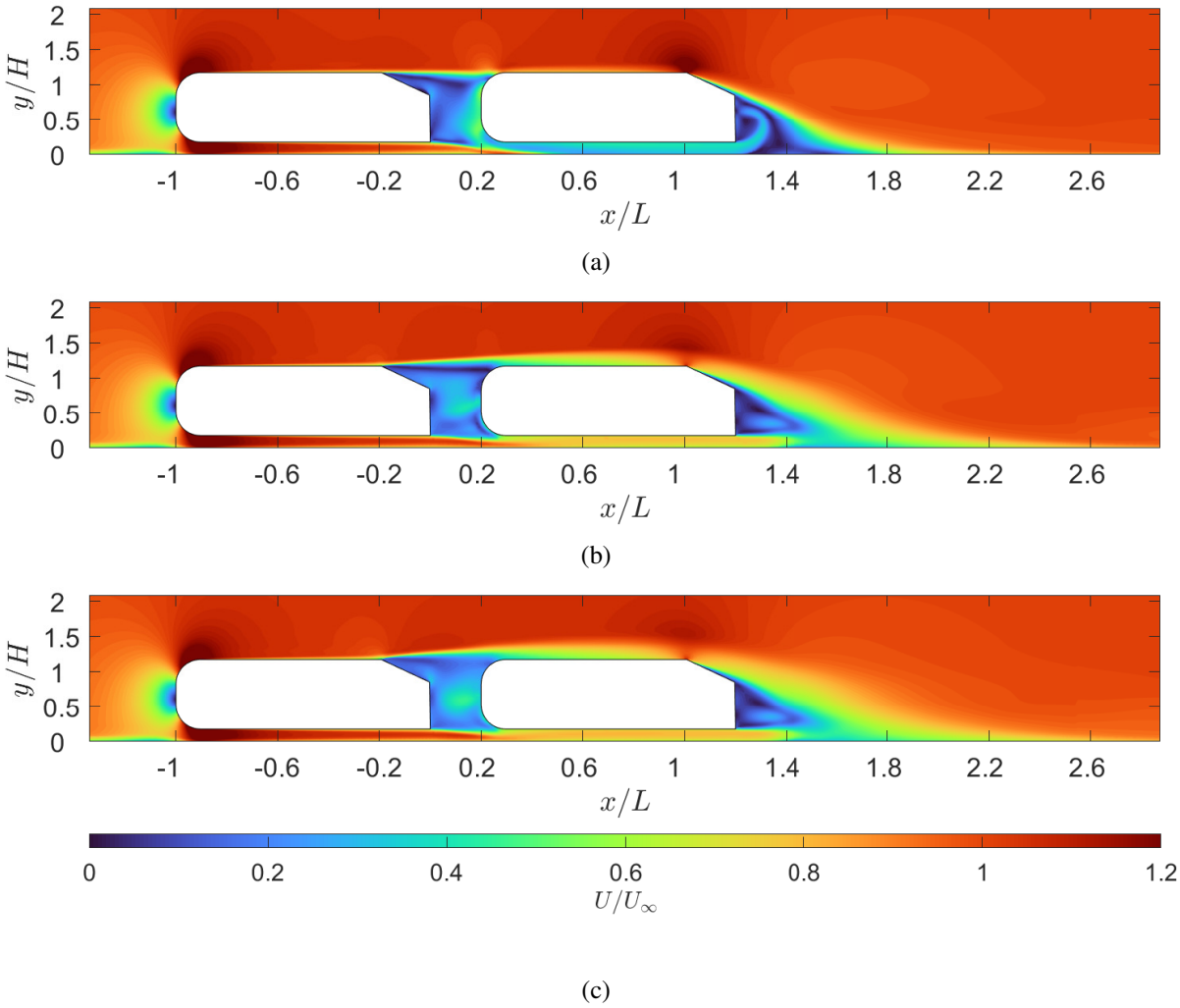

Figure 4.17: Average normalised velocity field comparison of the (a) 20*mm*-0°, (b) 20*mm*-10° and (c) 20*mm*-20°, flap cases at $d/L = 0.2$.flow goes from left to right

As with the previous data, in general, the introduction of a flap on the front vehicle results in significant drag reductions for the rear vehicle when compared to the baseline. This is especially true at $d/L = 0.2$ and the benefits are gradually reduced as the vehicles move further apart with the results converging around $d/L = 0.8$ excluding, of course, the 0° flap case at $d/L = 1.0$.

Figure 4.17 compares the velocity fields of the three flap cases at $d/L = 0.2$. The subtle differences between the three cases help to shed light on the similarities in drag results. The outlier from said drag results was the 0° case. Whilst this configuration produced a drag reduction compared to the baseline, it performed worse than the other flap cases. This is primarily due to wake impingement: The lower flap angle does not deflect the shear layer in the wake over the rear vehicle as much as the other flap configurations. This results in some wake impingement on the rear vehicle as it is visible that the free stream is briefly deflected down towards the curved leading edge of the rear vehicle and is further highlighted by the turbulent kinetic energy shown in figure 4.18. When considering the 10° and 20° cases, it is clear that these flap angles are high

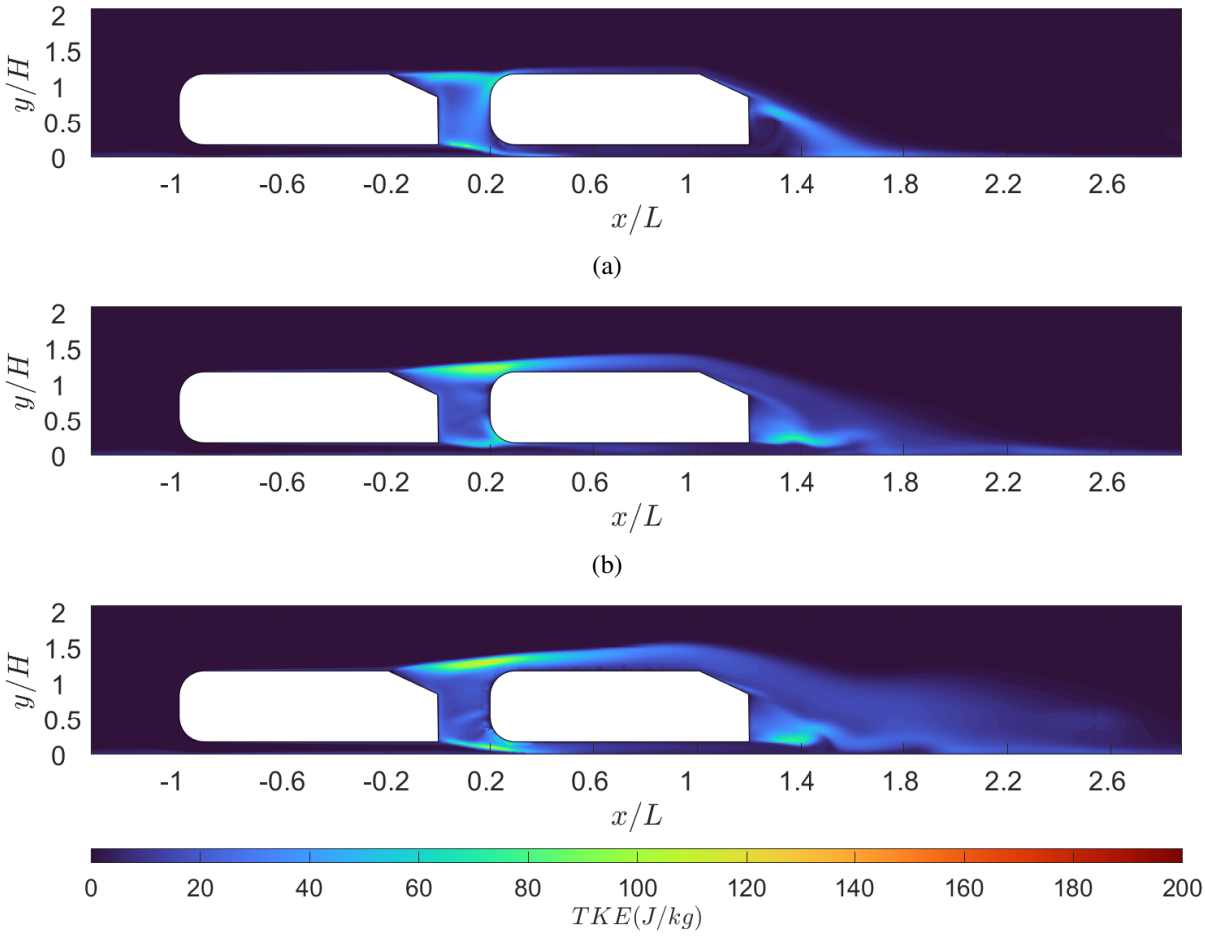

Figure 4.18: Turbulent kinetic energy field comparison of the (a) 20*mm*-0°, (b) 20*mm*-10° and (c) 20*mm*-20°, flap cases at $d/L = 0.2$.flow goes from left to right

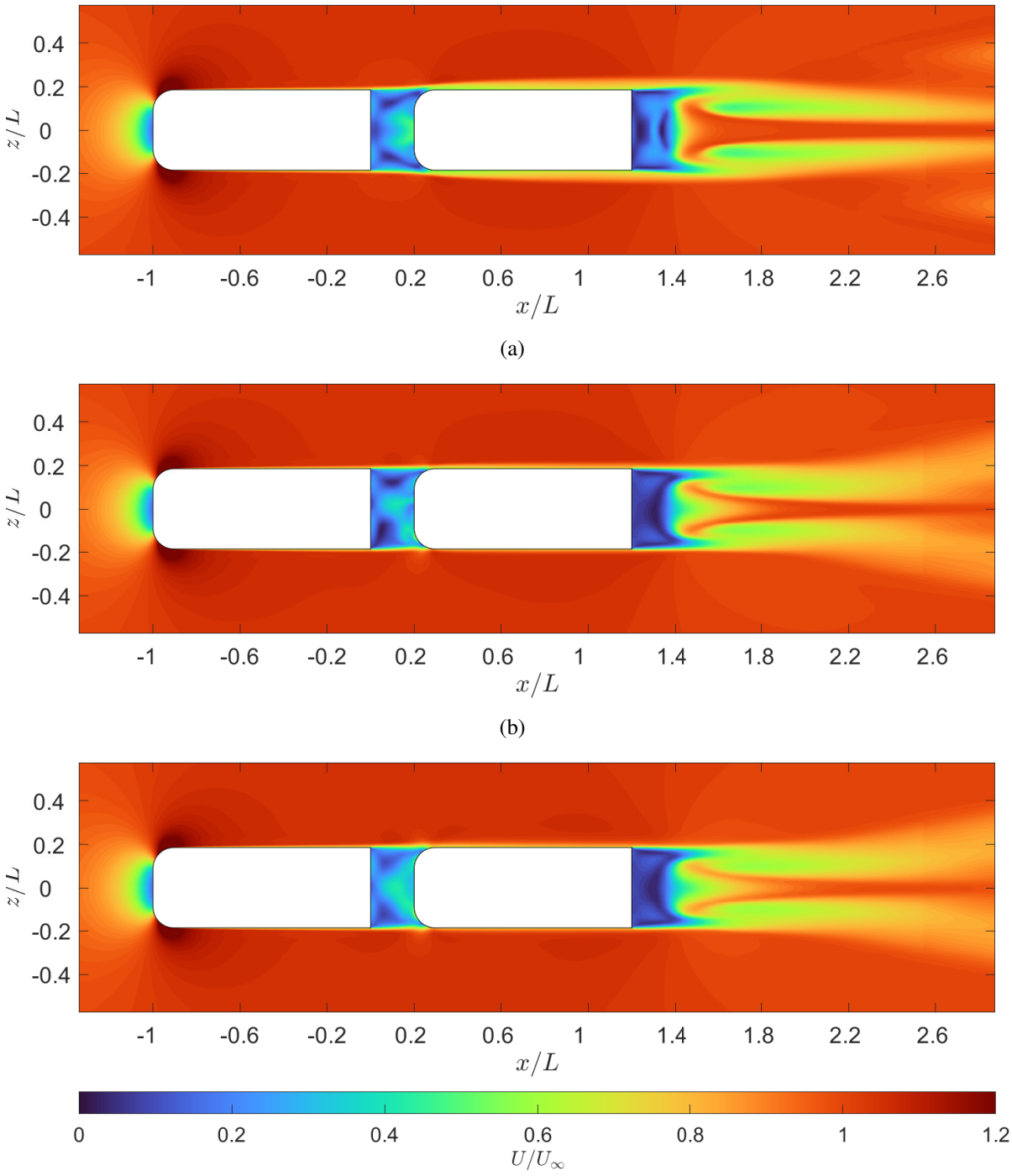

Figure 4.19: Average normalised velocity field comparison on a spanwise plane at $y = 0.15m$ of the (a) 20mm-0°, (b) 20mm-10° and (c) 20mm-20°, flap cases at $d/L = 0.2$.flow goes from left to right

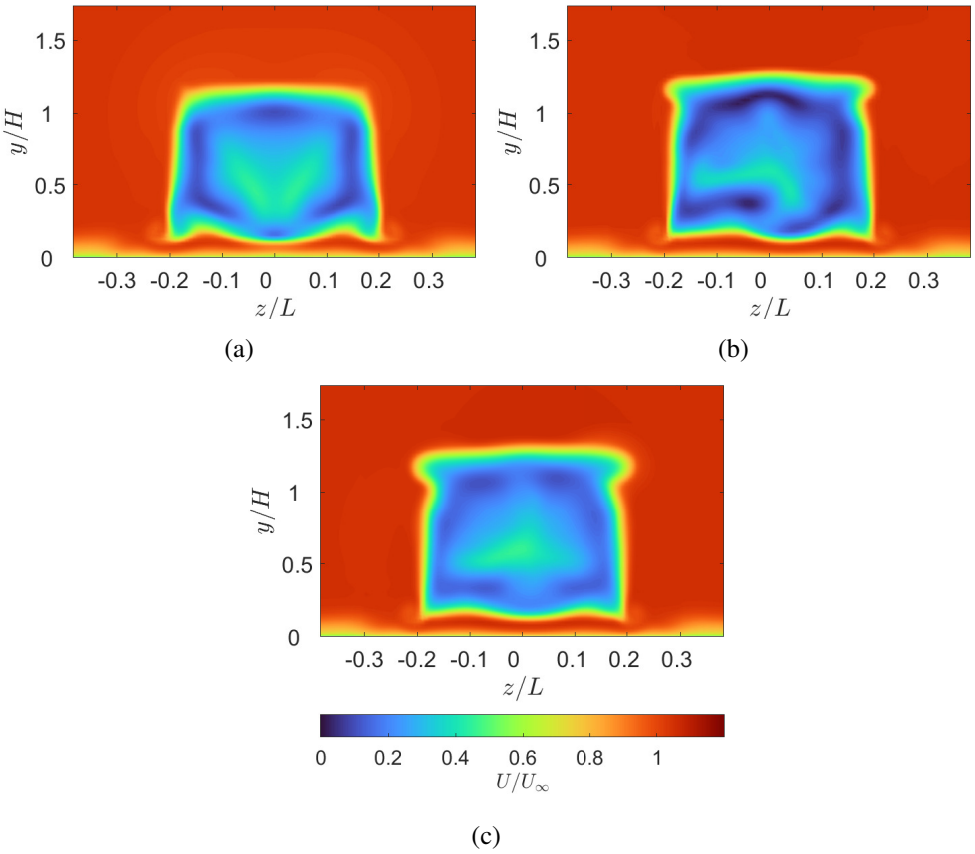

Figure 4.20: Average normalised velocity field comparison on a spanwise plane at $x = 0.15m$ of the (a) 20mm-0°, (b) 20mm-10° and (c) 20mm-20°, flap cases at $d/L = 0.2$.flow goes from left to right

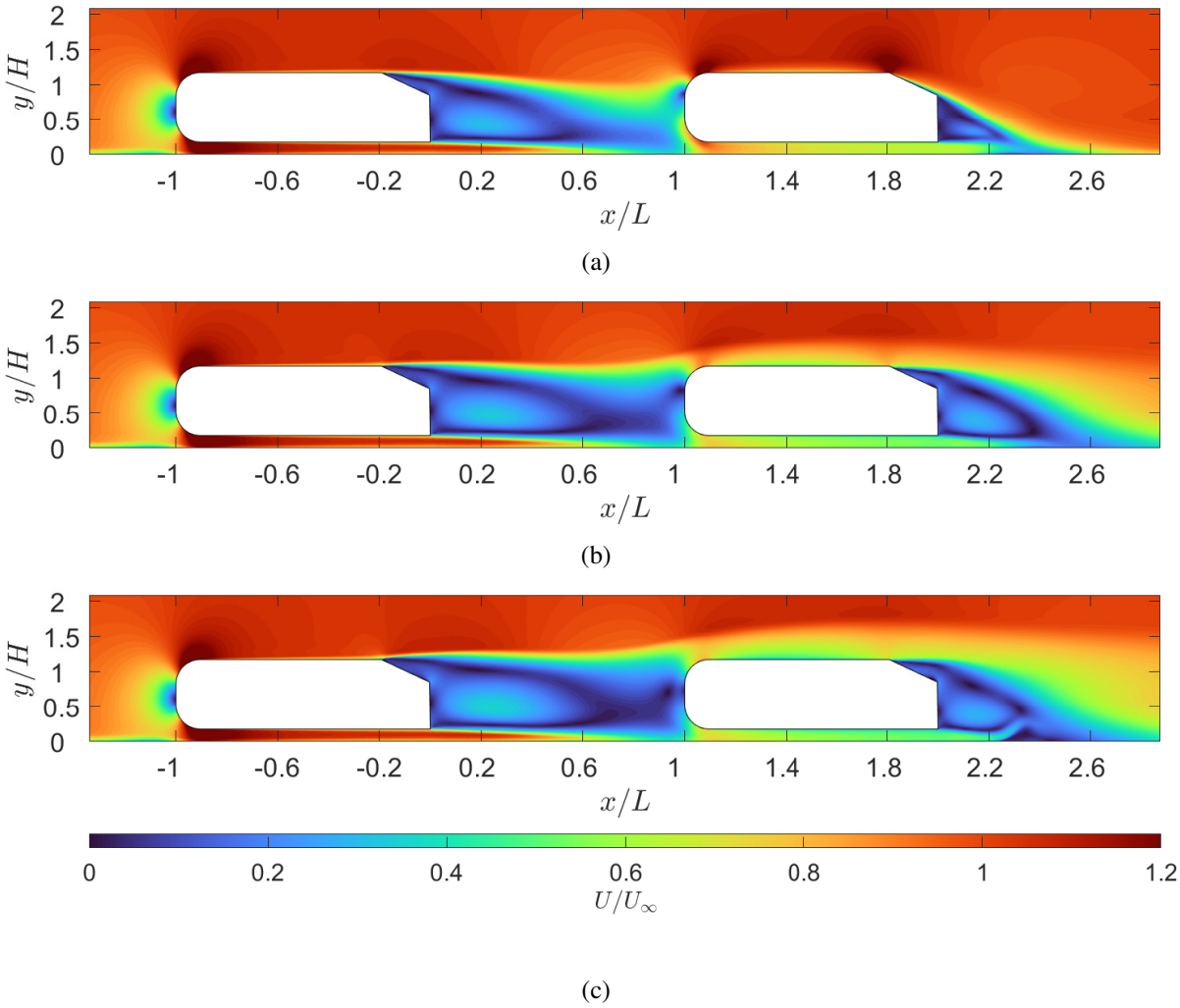

Figure 4.21: Average normalised velocity field comparison of the (a) 20*mm*-0°, (b) 20*mm*-10° and (c) 20*mm*-20°, flap cases at $d/L = 1.0$.The flow goes from left to right

enough to fully divert the turbulent shear layer over the rear geometry resulting in larger drag reduction.

As this shorted inter-vehicle distance, the difference in flow structure in the spanwise direction is much less noticeable as seen in figure 4.19 and 4.20. This is to be expected as the flap is designed mostly to effect the flow in the streamwise direction.

The other outlying case at $d/L = 1.0$ is shown in figure 4.21. Again, the 0° case produces a different result for the rear vehicle. However, in this case the outcome is a drag reduction when compared to the other two flap angles. As with previous platoons, the main cause of this difference is focused around how the wake interacts with the leading edge of the rear vehicle. The larger flap angles produce longer recirculation regions, which causes the shear layer to produce wake impingement on the leading edge of the rear vehicle over a larger range of inter-vehicle distances. This also results in much higher turbulent kinetic energy on the leading edge of the rear vehicle, further disrupting the structure of the flow (see figure 4.22). For the 0° case

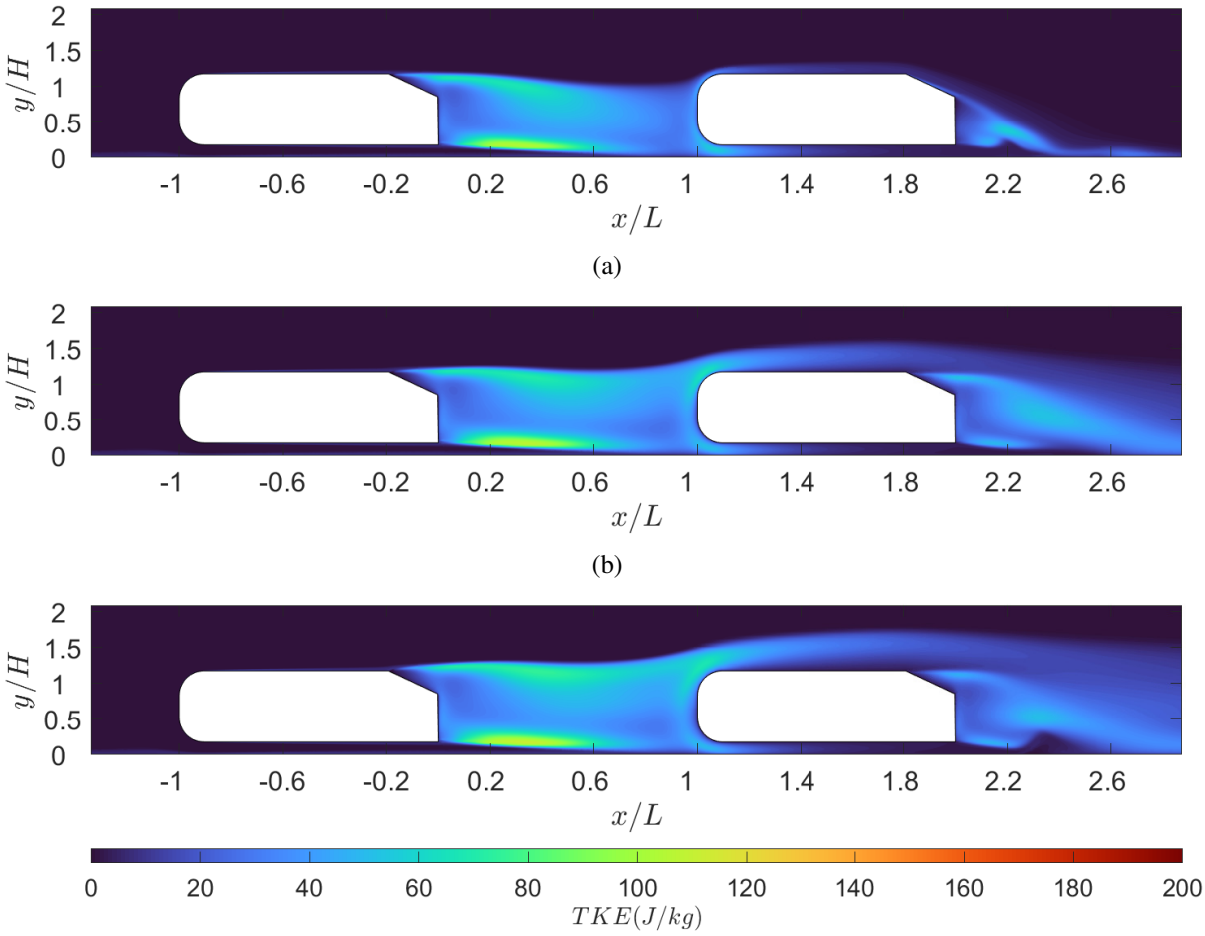

Figure 4.22: Turbulent kinetic energy field comparison of the (a) 20*mm*-0°, (b) 20*mm*-10° and (c) 20*mm*-20°, flap cases at $d/L = 1.0$.flow goes from left to right

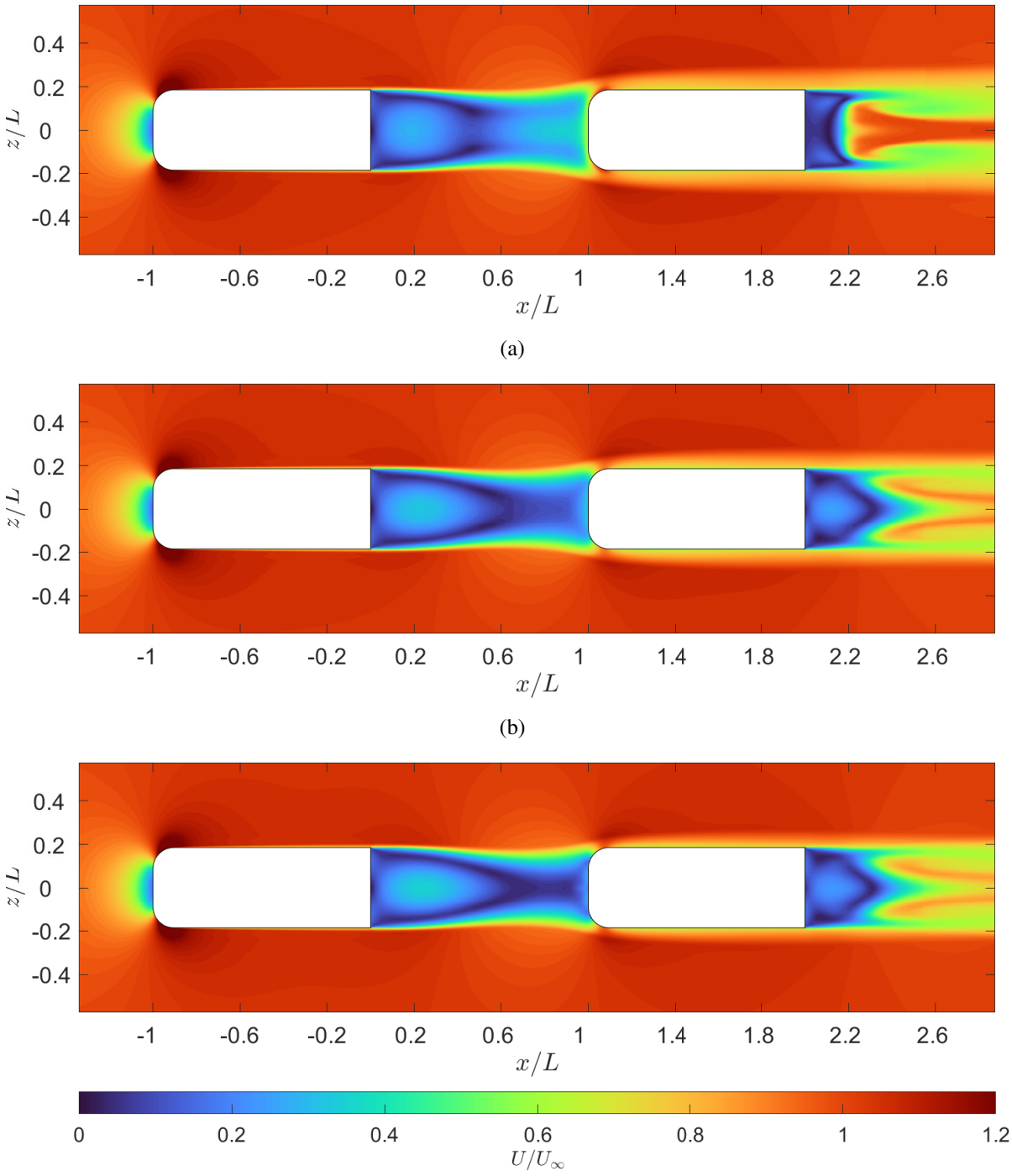

Figure 4.23: Average normalised velocity field comparison on a spanwise plane at $y = 0.15m$ of the (a) 20mm-0°, (b) 20mm-10° and (c) 20mm-20°, flap cases at $d/L = 1.0$.flow goes from left to right

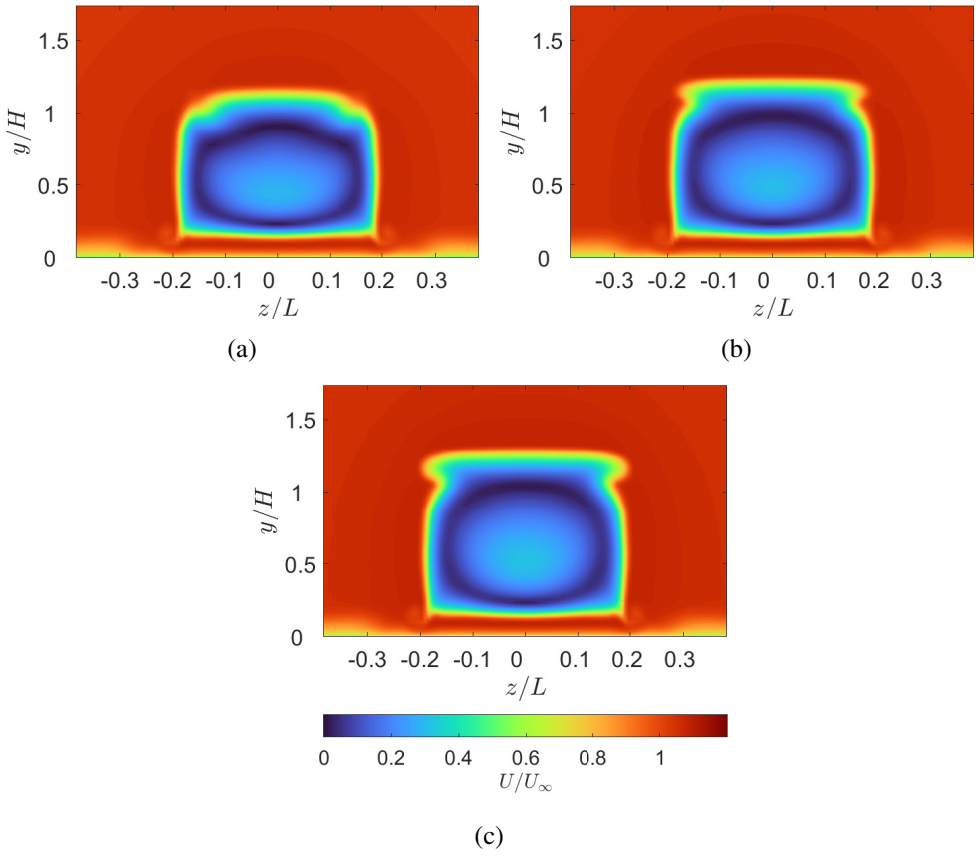

Figure 4.24: Average normalised velocity field comparison on a spanwise plane at $x = 0.15m$ of the (a) 20mm-0°, (b) 20mm-10° and (c) 20mm-20°, flap cases at $d/L = 1.0$.flow goes from left to right

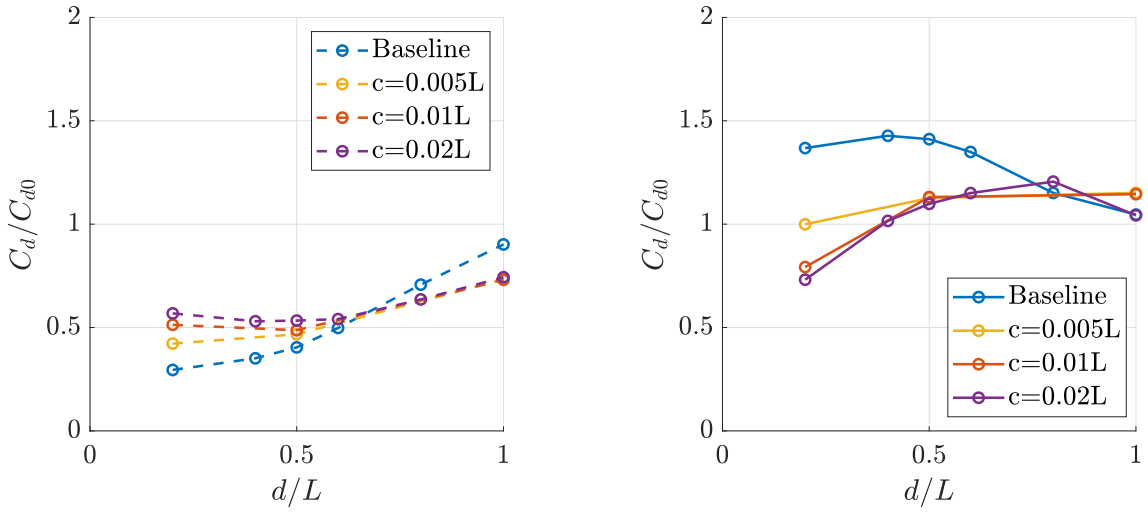

Figure 4.25: Normalised drag coefficient as a function of inter-vehicle spacing for different flap lengths for the (a) front and (b) rear vehicles in a platoon of two 25° Ahmed vehicles. Flap angle for each case is set as $\alpha = 10°$.

at $d/L = 1.0$, the rear vehicle has cleared the shear layer and recirculation region of the lead vehicle. The lower flap angle also results in increased dissipation of the turbulent kinetic energy. This allows the flow over the leading edge of the rear vehicle to be more similar to an isolated Ahmed vehicle, the difference hear being that the incoming flow speed has been reduced. This combination of lower incoming velocity and pressure recovery due to flow attachment over the rounded leading edge results in the rear vehicle performing better than the other two flap cases.

In the spanwise direction the flow structure remains much more consistent (as discussed previously for shorter inter-vehicle distances). The spanwise velocity fields are shown in figures 4.23 and 4.24, the width of the recirculation is unaffected by varying flap angle with only subtle changes in the height and flow speeds.

These results suggests that a further increase in the flap angle will not result in an additional drag reduction for the rear vehicle. The maximum potential at short inter-vehicle distances ($d/L \leq 0.2$) has already been achieved by diverting the shear layer over the rounded leading edge of the rear vehicle and the longer wakes produced by high flap angles have a negative effect on the rear vehicle at larger inter-vehicle distances ($d/L \geq 1.0$).

Effect of flap length

Finally, the influence of the flap length was tested for a constant flap angle of 10° by varying the flap length from $0.005L$ to $0.02L$ ($5mm - 20mm$). As can be observed from the results shown in figure 4.25, the relationship between flap length and drag coefficient, and flap angle and drag coefficient are remarkably similar, for this reason, only representative inter-vehicle distances were studied. The drag coefficients for each vehicle in the platoons discussed in this chapter are given in table 4.3. As the flap length is increased, less of the flow detachment is caused by the

increased base pressure provided by the rear vehicle and more of the detachment is due to the flap. This reduces the level of pressure recovery for the front vehicle and, as a result, increases the drag coefficient for the front vehicle with a flap when compared to the baseline case. As the vehicles move further apart, the influence of the platoon is reduced. At this point, the results for each flap length converge on each other and by $d/L = 1.0$ they all produce a 15% drag reduction when compared to the baseline case.

A similar behaviour is seen for the rear vehicle. Mirroring the flow features of the 0° case shown in figure 4.17, the shortest flap at $d/L = 0.2$ is unable to fully deflect the shear layer over the curved leading edge of the rear vehicle resulting in some wake impingement and a higher drag coefficient when compared to the longer flap lengths. Nevertheless, the short flap is still able to provide a 25% drag reduction for the rear vehicle when compared to the baseline case at $d/L = 0.2$ with the two longer flaps generating a 44% reduction for the same spacing. Similarly to the front vehicle, the results very quickly converge as inter-vehicle spacing is increased and for $d/L = 0.8$ and above all three flap lengths approximately match the baseline case.

4.5 Conclusions

The aim of this chapter was to asses the effectiveness of introducing simple flow control to the trailing edge of the front vehicle in a two vehicle platoon. In addition, it was explored whether simple forms of flow control could manipulate the wake in such a way that it would not only result in a average drag reduction for the platoon as a whole, but also a reduction in drag for each individual member of the platoon.

It was shown that, by promoting flow separation, a drag reduction of up to 50% could be achieved for the rear vehicle compared to the baseline case at $d/L = 0.2$. Through the use of flaps, both vehicles in the platoon received a drag reduction at $d/L = 0.2$. However, whilst the flow control in general provided drag reductions when compared to the baseline platoon, the rear vehicle still suffered some drag penalties when in a platoon compared to isolated conditions. It appeared that once the flow was fully separated and the shear layer of the front vehicle had cleared the rounded leading edge of the rear vehicle, the addition of extra flap length or a higher flap angle had no additional benefits to the rear vehicle. Furthermore, increased angle or length of flap tended to reduce the benefits of platooning for the front vehicle.

In summary, the conclusions are somewhat contradictory, in one respect the addition of flow control provided large drag reductions for the rear vehicle, especially at shorter inter-vehicle distances. In contrast, the flow control devices used had a far lesser influence over the flow than anticipated, especially at larger inter-vehicle distances, and altering their setup resulted in little modification to the final outcome of the platoon. An important next step is to experimentally validate the effectiveness of the current flow control by conducting wind tunnel investigations. This will allow us to gauge how reliable the simulation data is and provide clear next steps for

the further development of flow control techniques for platoons.

Chapter 5

Flow control for platoons: experimental investigation

5.1 Introduction

The results presented in chapter 4 showed great promise for the addition of flow control devices on the lead vehicle of a platoon to eliminate or ameliorate 'inverse' platooning cases. While these simulations provide useful insight, there is currently no known experimental research that implements flaps as a flow control device on platoons and thus a validation of the results was not possible. For this reason, it is vital that a matching body of experimental work is also conducted before fully assessing the effectiveness of platoons with flow control.

To this end, wind tunnel investigations were conducted in Glasgow University's Handley Page wind tunnel for a range of Reynolds numbers from $1 \cdot 10^5$ to $3 \cdot 10^5$. Two 25° Ahmed vehicles in a platoon were used as the baseline case against which two modified setups could be compared: first a geometric modification was made to the lead vehicle to transform it into a squareback Ahmed vehicle. This was followed by the addition of flaps to a 25° Ahmed lead vehicle to determine their effectiveness for flow control. Results were obtained using load cells for force measurements and Particle Image Velocimetry (PIV) for flow visualisation.

The following experimental campaign was informed based upon the simulations conducted in chapters 3 and 4 however, due to the reduced Reynolds number achieved in the following experiments, no direct comparison between these sets of results can be drawn. There is very limited knowledge of Reynolds number effects on platoons however, some predictions can be given based upon the Reynolds number dependence of the isolated Ahmed vehicle. As the Reynolds number decreases, the isolated drag coefficient of the 25° Ahmed body increases. Whilst it is expected that this will hold true for the front vehicle in the platoon, the length of the front vehicle's wake will vary with Reynolds number and it is currently unclear how this will effect the rear vehicle downstream. In the research by Törnell et al. [18], the Reynolds number dependency of a platoon of two HGVs was studied. Here the drag coefficient of the rear vehicle

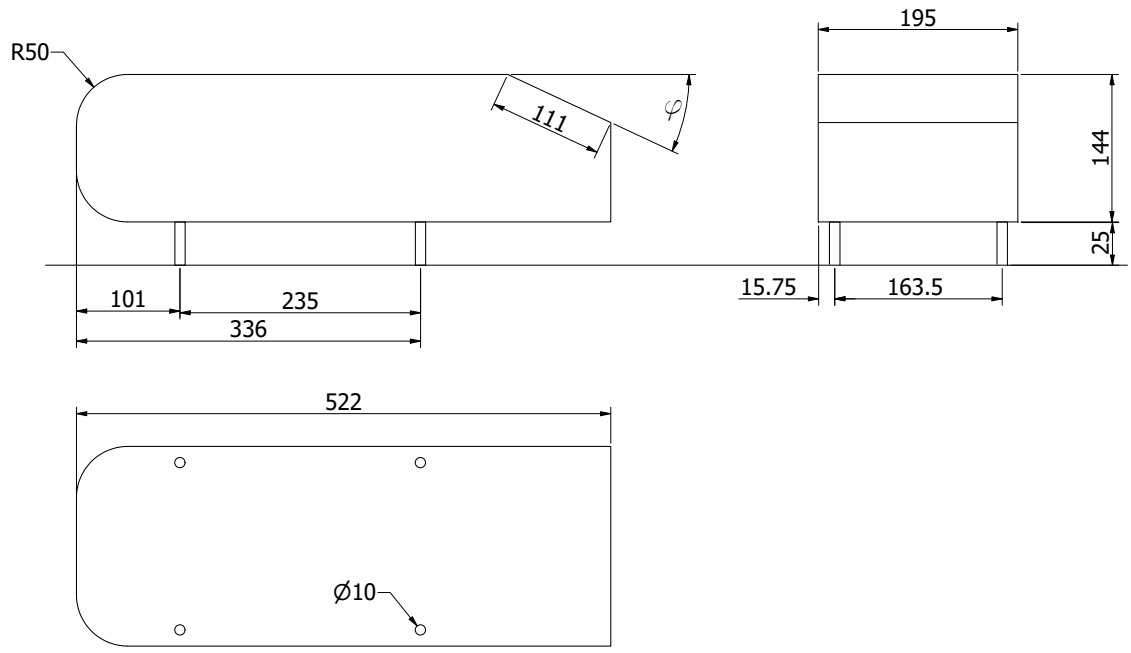

Figure 5.1: Schematic drawing of the Ahmed body at 50% scale as used in the experiments. All dimensions are given in millimetres.The depicted rear slant angle here is $\phi = 25^{\circ}$

was unchanged as Reynolds number was increased. This suggests that drag reductions for the rear vehicle would be increased at lower Reynolds numbers, conversely, drag increases for the rear vehicle would be reduced at lower Reynolds numbers.

5.2 Design of experiment

5.2.1 Model design

The models used in the platoon are two Ahmed bodies. This geometry was first used in a study by Ahmed et al. [1] where the effect of the rear slant angle on the drag coefficient of a simplified ground vehicle was investigated (see section 2.1). The geometry has a rounded leading edge, a cuboid middle section and a re-configurable slant at the rear as shown in figure 5.1. It is widely used in research as it produces flow characteristics similar to a road vehicle whilst maintaining a very simple geometry (see discussion in section 2.1).

For this experiment, as in many wind-tunnel based platooning studies, the test section length was a limiting factor. Therefore, to maximise the productivity of the investigation, half-scale models of the Ahmed body were used, the associated dimensions of which are shown in Figure

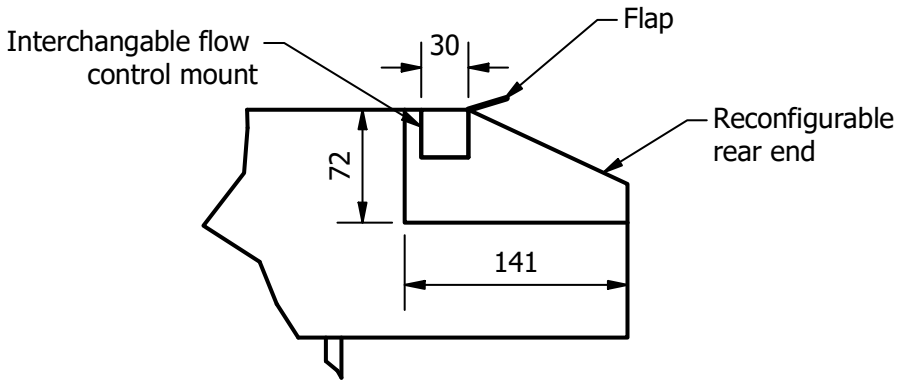

Figure 5.2: Detail schematic of re-configurable rear end and flow control mount for the front vehicle in the platoon. All dimensions are given in millimetres.

5.1. Both vehicles were mounted with a 25*mm* offset on a ground plate using 10*mm* diameter stilts attached to the underside of the vehicle in outboard locations, mimicking the original experiment by Ahmed et al. [1]. The rear model is a standard Ahmed body with a 25° rear slant angle. The front model was designed to be re-configurable with both 0° (squareback) and 25° rear slant options being used in this investigation. The front model also has a cut out slot that allows for a range of flow control devices to be mounted as detailed in Figure 5.2. Both models are hollow, made of wood and finished with paint to create a smooth surface.

5.2.2 Flow control design

A range of flaps were used as flow control devices in this investigation. The flaps were only installed on the front vehicle in the platoon and were located at the top of the trailing edge slant as shown in figure 5.2. The flaps were manufactured from 1*mm* thick aluminium and were mounted using nylon hinges. 10*mm* and 25*mm* flap lengths were used (0.02L and 0.05L respectively) and they were tested for 0°, 10° and 20° angles up from horizontal. A generic nylon control horn was fastened to the flap and connected to a custom control horn using two clevis fasteners joined by a 3*mm* diameter threaded rod. The custom control horn was mounted on the model upstream of the flap and was designed with three holes, one for each flap setting, to provide accurate repeatability between test runs.

5.2.3 Experimental setup

The experiments were conducted in the University of Glasgow's Handley-Page wind tunnel. This is a closed loop wind tunnel with a octagonal test section of 2.1m $\times$ 1.6m cross section and 3.2*m* length. The design of this experiment was heavily influenced by the study conducted by Kim et al. [76] who studied flow over a single, half scale, Ahmed body. A photograph of the installed platoon in the wind tunnel is shown in figure 5.3.

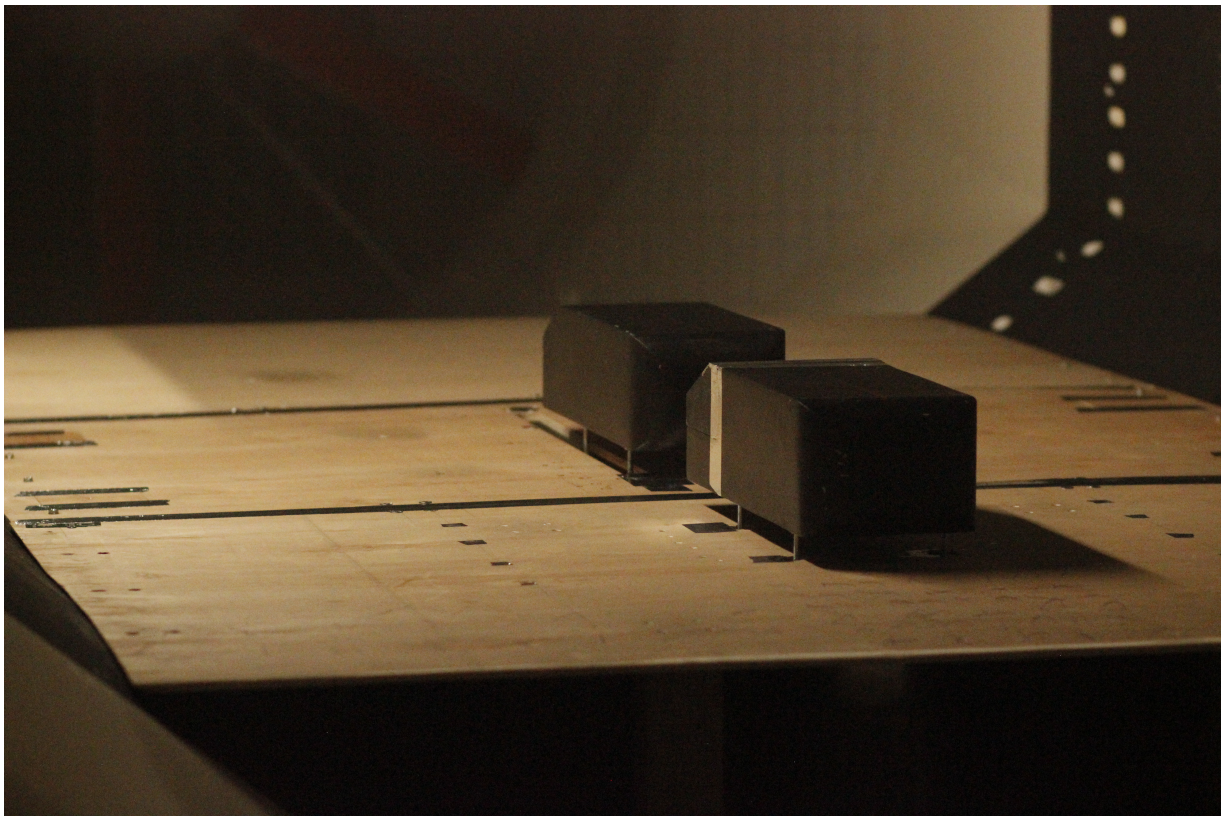

Figure 5.3: Photograph of the baseline platoon installed in the University of Glasgow's $5' \times 7'$ Handley-Page wind tunnel. Visible are the two 25° Ahmed vehicles and three sections of ground plate.

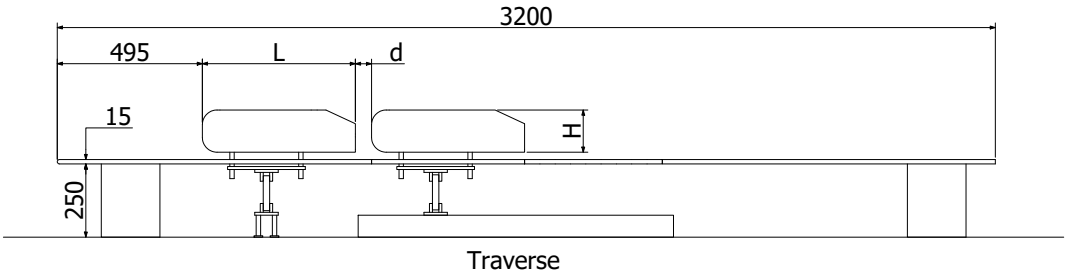

Figure 5.4: Schematic of layout for platooning experiment in the wind tunnel. The flow direction is from left to right. All dimensions are in millimetres. Additional ground plate supports and loadcell fairings have been omitted from the drawing for clarity

In order to produce a consistent, well-defined, boundary layer, a 10*mm* thick, wooden ground plate was mounted in the wind tunnel 250*mm* above the wind tunnel floor, thus providing a good comparison to both simulated and real world data as outlined by Hucho et al. [125]. The load cells for the drag force measurement on each vehicle were mounted beneath the ground plate, but still inside the wind tunnel, and were protected by aluminium fairings. The setup shown in figure 5.4 equates to a blockage of 5%. This is within the limits of wind tunnel blockage for road vehicles as outlined by Barlow et al. [126] meaning that no blockage corrections are required. The ground plate was manufactured in three sections, since the maximum length was restricted by the wind tunnel door, and spanned the full width of the wind tunnel. Each section had four legs that attached to the floor and aluminium brackets attached to the walls of the wind tunnel to ensure the ground plate did not warp or flex. The sections were secured together with aluminium brackets and 0.05*mm* aluminium tape was used to provide a smooth transition at the plate interfaces. The total length of the ground plate was 3200*mm*. The leading edge of the ground plate was sanded to an elliptical shape to reduce the length of the leading edge separation bubble. The extent of the bubble was assessed both visually, through the use of tufts, and using a static pressure rake (shown in figure 5.5) to ensure the flow had fully settled upstream of the front vehicle in the platoon; for further discussion see sections 5.2.4 and 5.2.5.

The front vehicle was mounted 495*mm* downstream of the leading edge of the ground plate. The rear vehicle was mounted on a slider to allow for variable separation distance between the two vehicles. Five evenly spaced distances between the vehicles, from $d/L = 0.2$ to $d/L = 1$, were tested. Two slots were cut in the middle section of the ground plate to facilitate the movement of the rear vehicle and associated load cell and mounts. Hatches were made of different lengths to fill the gaps in each slot for a range of vehicle locations. These were secured with 0.05*mm* aluminium tape during the experiments.

5.2.4 Scanivalve calibration

For the boundary layer characterisation, pressure measurements were made using a Scanivalve 48 channel mechanical pressure scanner. The Scanivalve has two chambers that are separated by a flexible diaphragm, one chamber is connected to a reference pressure whilst the other is connected to the input pressure. A mechanical valve is used to switch between each of the 48 possible pressure inputs of the system, of which 15 were used. As the pressure in the input pressure chamber changes, the diaphragm flexes and, through the use of strain gauges, this deflection is measured as a voltage fluctuation.

In order to first calibrate the Scanivalve it was connected to a Furness Controls FCO502 Pressure Supply. The Furness pressure supply allows for a predefined pressure difference to be set in the Scanivalve providing a calibration for the output voltage. This is achieved by connecting the zero as a reference pressure and the output of the pressure calibrator to the input of the Scanivalve. A FLUKE 922 digital airflow meter was also used to measure the input

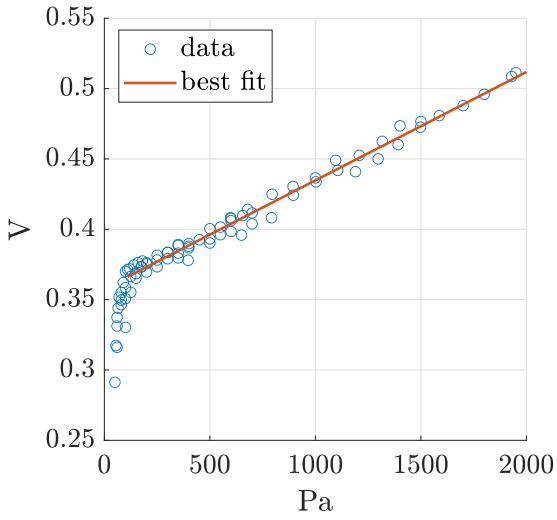

Figure 5.5: Scanivalve voltage output for applied pressure calibration. Pressure scanner is only accurate for pressures over 100*Pa* after which a linear relationship emerges.

pressure difference which was accurate to 1 Pa. Figure 5.5 shows how the voltage changes with pressure. The Scanivalve is only accurate for pressures over 100 Pa, after this point a linear relationship emerges. Some scatter was observed in the results which is to be expected from a mechanical system. One of the biggest challenges with pressure readings is that the chambers do not hold their pressure over long times leading to a drift in the voltage. To combat this, a semi-instantaneous voltage reading was taken using an in-house data acquisition system sampling at 2kHz for 5s.

5.2.5 Boundary layer characterisation

The boundary layer was characterised using the pressure rake shown in figure 5.6. This rake consisted of 2 total pressure tubes and 13 static pressure Pitot tubes. Measurements were taken along the centreline of the ground plate at 165mm, 330mm, 495mm, 808mm, 1121mm, 1226mm, 1330mm, 1435mm and 1539mm downstream of the leading edge with no vehicle models installed. These locations were selected as they fall either into the separation bubble at the leading edge of the ground plate or correspond to the notional leading edge location of each model position.

These measurements were taken to provide a general picture of the boundary layer as it develops along the ground plate. The pressure rake being used has a moderate vertical resolution which was sufficient to ensure that the boundary layer growth along the ground plate does not reach a point where the boundary layer impinges on the leading edge of any vehicle. However, the resolution is not fine enough to provide an exact measurement of the boundary layer thickness.

Figure 5.7 depicts profiles of the streamwise component of velocity at a range of locations

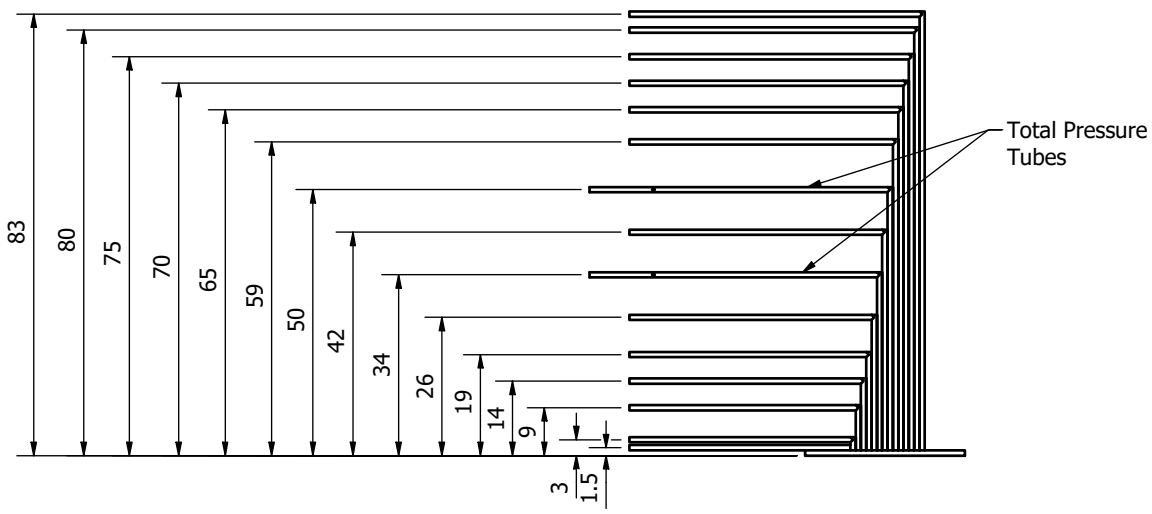

Figure 5.6: Schematic of the Pitot tube rake used to measure the boundary layer thickness on the ground plate. All units in millimetres.Predominantly static pressure tubes, the two total pressure tubes are marked thus allowing for flow velocity calculations.

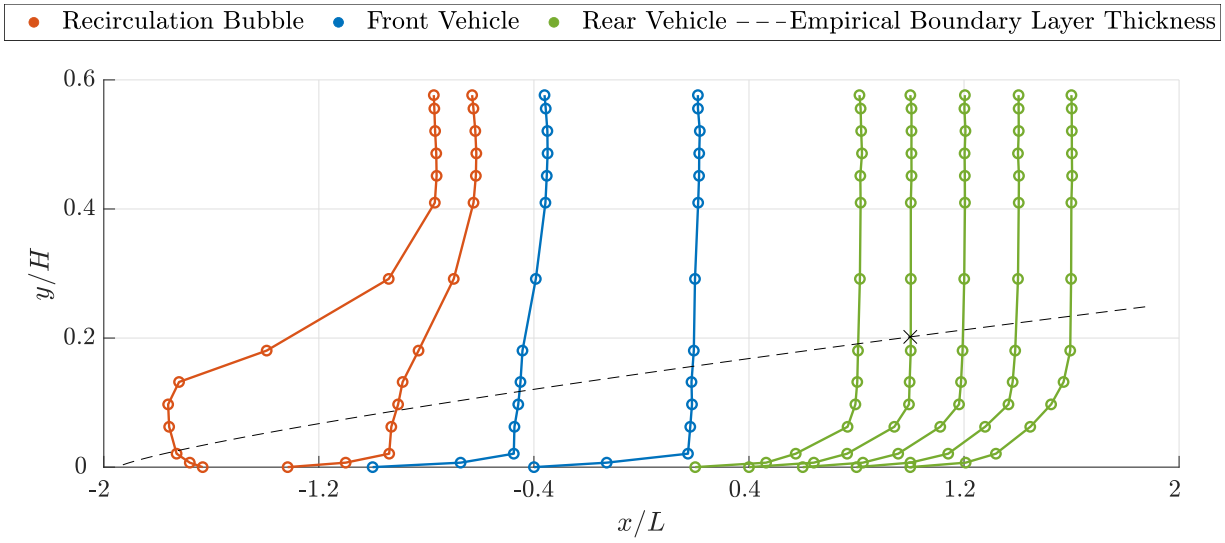

Figure 5.7: Stream-wise velocity measurements from a Pitot tube rake at a range of locations along the ground plate compared to empirical calculations for boundary layer thickness. The zero point of each line is at the location the measurement was taken. The dashed line denotes the empirical boundary layer thickness and it begins at the leading edge of the ground plate. The X marker is the empirical boundary layer thickness at the leading edge of the vehicle at its farthest point downstream e.g. $d/L = 1.0$ or $x = 1.539m$.

along the plate. The first two readings from the rake fall clearly in the recirculation bubble with reversed flow being measured. Pitot tubes are designed to measure pressures of oncoming flow [127] therefore, the readings in this reversed section, although useful to show that the flow has reversed, are not indicative of the actual pressures or associated flow speeds present. From there, the boundary develops downstream as normal. An empirical approximation is given using equation 5.2 ([128]),

$$\delta = 0.38\frac{x}{Re_x^{1/5}} \tag{5.1}$$

where δ is the boundary layer thickness, x is distance from the leading edge of the ground plate and Re_x is the associated Reynolds number based on x and wind-tunnel velocity. The results based on the empirical approximation (5.2) are in reasonable agreement with the measured data. Empirically, when the rear vehicle is at its furthest point downstream from the leading edge of the ground plate, the boundary layer thickness is calculated as $29mm$. This would slightly impinge on the lower part of the model that sits $25mm$ above the ground plate. The measurements suggest that the true boundary layer thickness is slightly less than this, however, as mentioned previously, the resolution of the rake is not fine enough to give a precise value of boundary layer thickness. In any case, the extent of the boundary layer thickness could cause some unforeseen effects on the rear vehicle when in the farthest platooning location (e.g. at $d/L = 1.0$). This should be taken into account when analysing the drag coefficients for this configuration.

An empirical representation of the velocity profiles are given in figure 5.8. The residual nonuniformity of the boundary layer at the leading edge of the front vehicle can be seen in more detail here. This will effect the drag coefficient of the front vehicle of the platoon as the higher peak velocity will result in an increase in drag force. Further downstream, the velocity profile becomes more uniform and the boundary layer can be approximated using a power law. The general equation to approximate the boundary layer is given in equation 5.2.

$$U = U_{y_0}(\frac{y}{y_0})^{\frac{1}{ne}} \tag{5.2}$$

Where U is the velocity in the streamwise direction, U_{y_0} is the freestream velocity (in this case $31ms^{-1}$ was used) at the height y_0 above the ground plate and $1/n_e$ is the power law exponent. The power law exponent determines the shape of the velocity profile within the boundary layer and can be influenced by factors such as the Reynolds number and surface roughness. The Reynolds number increases as the boundary layer develops down the ground plate therefore, depending on the measurement location, the shape of the boundary layer will vary. One way to approximate the value of n_e is discussed in the report by Johnson and Bushnell [129] and is given in equation 5.3.

$$n_e = 2log_{10}(Re_x) + 1 \tag{5.3}$$

For the range of Reynolds numbers along the ground plate, this results in an n_e value of

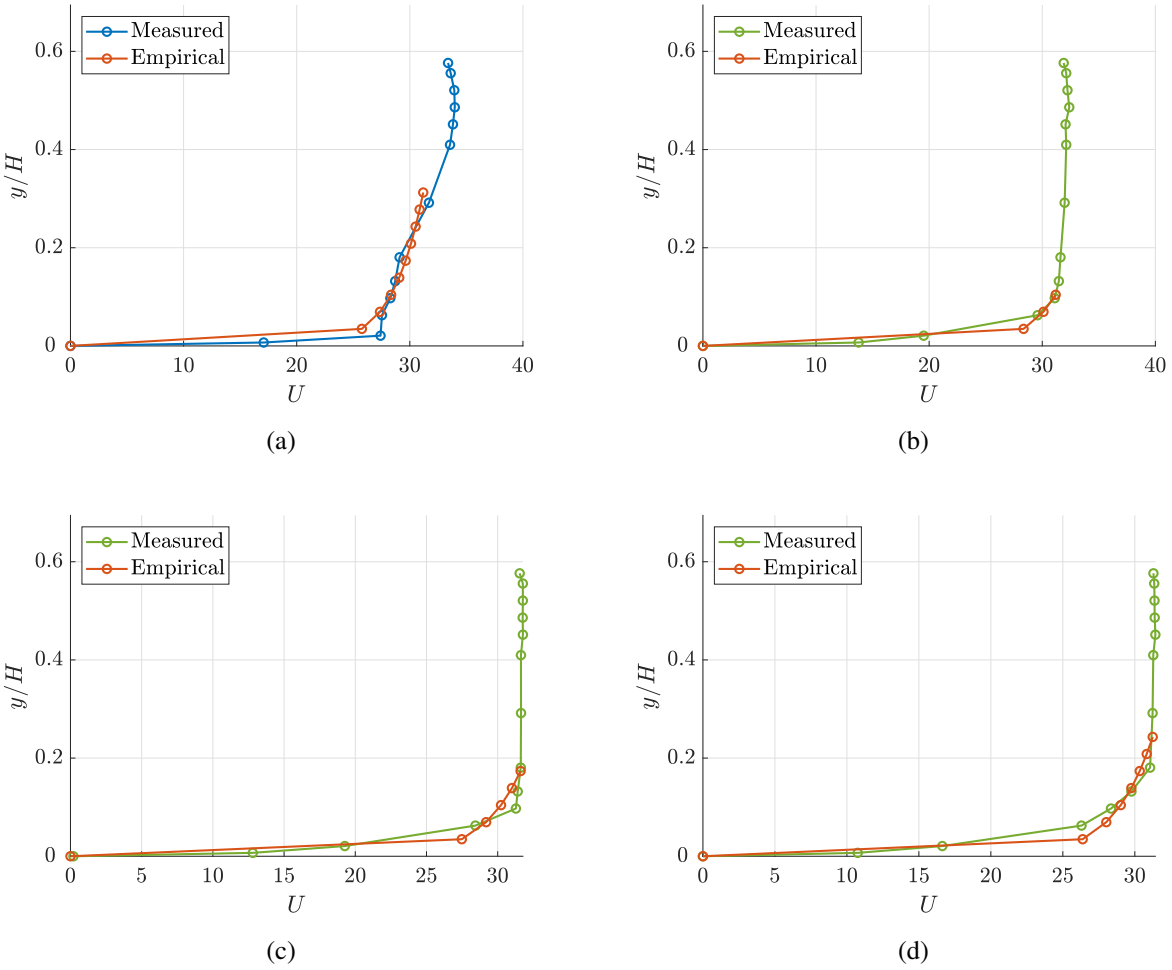

Figure 5.8: Boundary layer profiles with empirical approximation for a range of distances downstream of the leading edge of the flat plate. Representative locations of the leading edge of the (a) front vehicle and the rear vehicle at (b) $d/L = 0.2$, (c) $d/L = 0.6$, (d) $d/L = 1.0$. Boundary layer measurements were taken at $Re = 2.88 \cdot 10^5$. No models were installed inside the tunnel during the measurements.

ref. location	Re_x	n_e	y_0
Front	$1.0 \cdot 10^6$	11.0	0.042
$d/L = 0.2$	$2.2 \cdot 10^6$	11.7	0.014
$d/L = 0.6$	$2.6 \cdot 10^6$	11.8	0.020
$d/L = 1.0$	$3.0 \cdot 10^6$	12.0	0.031

Table 5.1: Overview of isolated Ahmed body experiments.

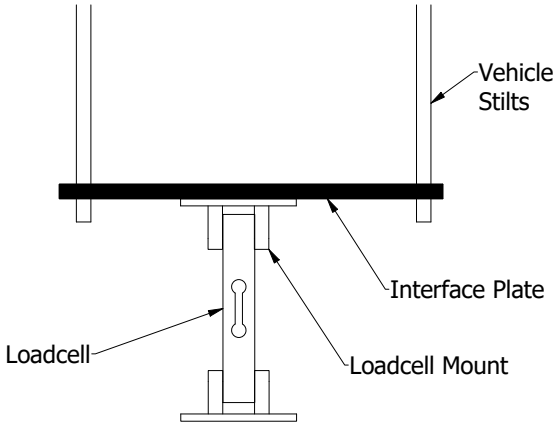

Figure 5.9: Schematic showing the system for attaching the load cell to the vehicle model and to the wind tunnel floor. The vehicle stilts pass through the ground plate and are connected to the underside of the vehicle model (not shown).

between 11 and 12. A value of 11.5 was selected for the empirical formulae to best represent the boundary layer profile. The inputs to generate each velocity profile are given in table 5.1. Another result worth noting is that the free stream velocity does not equal the quoted $30ms^{-1}$ discussed previously. Due to the changing temperatures inside the wind tunnel facility, the wind speed selected varied slightly to maintain a consistent Reynolds number.

5.2.6 Load cell setup

Force measurements for each model were taken using a A&D single axis LCB03K003MEX load cell rated at 3kg. Custom clamp style mounts were precisely manufactured to secure each side of the load cell. One mount was connected straight to the wind tunnel floor and the other was connected to an interface plate. The stilts from the vehicle models were fastened in the corners of the interface plate and the load cell was mounted directly under the centre of gravity of the vehicle as shown in figure 5.9.

The load cells were connected to a 10V power supply. The load cell output voltage was amplified by 500$\times$ and passed through a 20kHz filter. Finally, the signal was passed into the University of Glasgow's in-house data acquisition system and a sampling rate of 2kHz was selected. This sampling rate is similar in order of magnitude to other studies discussed in section 2.3.6, such as Tropea et al. [86] and Robertson et al. [104].

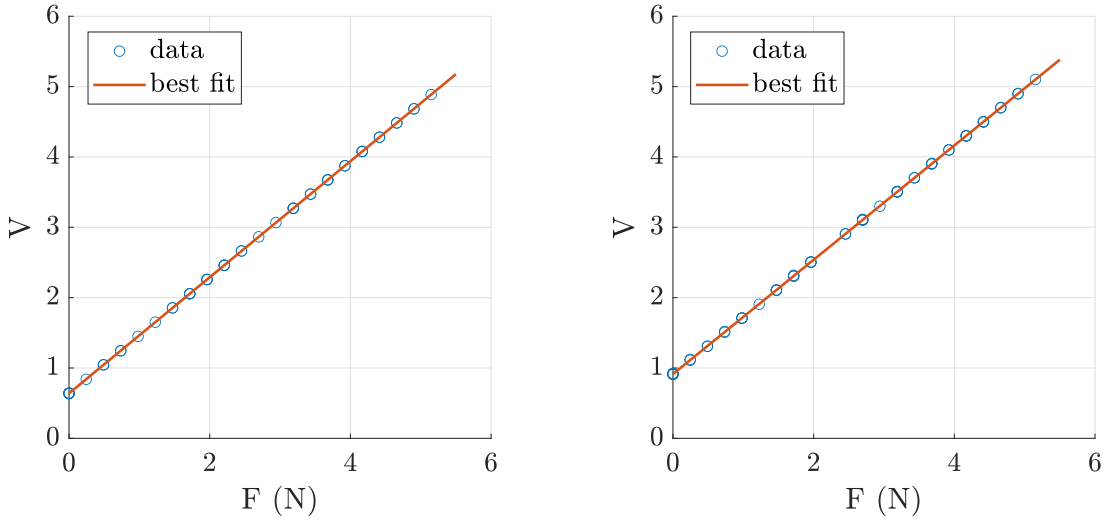

(a) Load cell 1

(b) Load cell 2

Figure 5.10: Voltage output versus applied force measured during the calibration of the load cells. It is worth noting that each data point was measured on three separate occasions. Each measurement is shown individually in the above graphs, however, they are indistinguishable from the other measurements taken at the same force.

Load cell calibration

Before the load cells were installed in the wind tunnel they were calibrated using the following procedure: The load cell was mounted as a cantilever beam and weights of different values were suspended from the load cell and then removed to imitate cyclic loading. The weights used were also calibrated using a Gram, TRFF HRB-E 203 electronic precision balance that was accurate to ± 0.001g. Figure 5.10 shows how the voltage changes with respect to applied force for each load cell. Every load cell is different due to the sensitive nature of the strain gauges and manufacturing process. Therefore, it is expected that the relationship between voltage and force slightly varies between load cells. It is evident from figure 5.10 is that both load cells have little to no drift and are very precise. The manufacturer's data sheet for the load cell gives an error of ± 0.6g.

5.2.7 PIV setup

Equipment setup

Flow field measurements were taken in the inter-vehicle gap along the longitudinal centre plane of the models using Particle Image Velocimetry (PIV). A La Vision Imager CX camera with a 50mm focal length lens was mounted on a tripod normal to the centre plane outside of the tunnel. This camera has a 16MP chip and a field of view of approximately 0.12m^2 was selected. There are many factors that affect the size of the field of view ranging from light sheet intensity to particle size and camera resolution. Whilst having the full flow field covering both models in

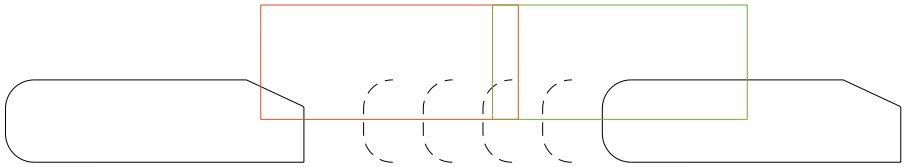

Figure 5.11: Schematic showing PIV fields of view for the wind tunnel experiments. Each field of view is $0.45m \times 0.175m$. Their streamwise locations begin at $x = -0.08m$ and $x = 0.325m$. They are set $0.15m$ above the ground plate.

one image would have been desirable, this would have led to a low resolution of the flow. The chosen field of view provided a good compromise with only two distinct interrogation regions being required to cover the flow over the rear of the lead vehicle, in the inter-vehicle gap, and over the front of the rear vehicle as shown in figure 5.11.

A Litron Lasers, Bernoulli PIV Series, 200-15PIV, pulsed Nd:YAG laser (manufacturer Litron Lasers Ltd) was used to generate the light sheet for the PIV measurements. This is a 15Hz, class 4 laser that produces a 200mJ beam per pulse. A Pea Soup, Dragon, seeder was used which, according to manufacturer specifications, produces particles of size $0.2 - 0.3\mu$m.

Post-processing

The LaVision, DaVis 10.2 software was used to implement a cross correlation method to post process the PIV image pairs, turning them into a grid of velocity vectors. For this process, an interrogation window of 16×16 pixels with a 50% overlap was used. The time interval between each image in a pair is called the Δt and can be calculated using equation 5.4. Here, Δs is the maximum distance one seeding particle moves between each image and v is the speed of the flow.

$$\Delta t = \frac{\Delta s}{v} \tag{5.4}$$

After calibrating the camera using the Lavision DaVis software, the magnification factor, M, was $11.6px/mm$. Between each image in a pair, ideally each particle should remain within the $16 \times 16px$ interrogation window selected. To ensure this is the case, the Δt was sized based on a maximum particle displacement of $8px$ or, using the above px/mm measurement, $0.69mm$. At a wind tunnel speed of $30ms^{-1}$, this equates to a Δt of $23\mu s$. This method is consistent with other PIV investigations [130, 131].

$$\varepsilon_u = \frac{0.1}{M\Delta t} \tag{5.5}$$

The uncertainty in the PIV measurement, ε_u,can be estimated using equation 5.5 and was

calculated to be $0.4ms^{-1}$. A displacement error of 0.1 pixels was assumed for the PIV regions.

A comparison between a raw PIV image and the final PIV figure is provided in figure 5.12. Here two regions have been highlighted where it was not possible to get data. Region 1 is a reflection off of the window on the opposite side of the test section. This was located far enough above the models to not be an issue as in the final PIV image it was cropped out.

Region 2 is the leading and trailing edges of the models. As the PIV camera was mounted a finite distance from the models, there will always be some level of perspective distortion at the edges of the image. The PIV light sheet intersects the models along the centre plane, the light sheet appears thicker on the front vehicle due to the trailing edge slant. As the light sheet enters the wind tunnel through the roof, it is passed through prism and lens to spread the beam into the sheet used for PIV. Coincidentally, this diverging sheet is angled normal to the trailing edge of the front vehicle resulting in increased reflections in this region when compared to the rear vehicle.

It is clear that the model can be seen in three dimensions behind this centre plane. As the illuminated particles flow over the centre plane of the model, this perspective prevents any data from being captured in these areas. This can be seen in the final PIV image where the models have been masked and a line has been drawn to indicate the centre plane where the laser light sheet intersects the models.

Additionally, as a 2D slice of 3D flow was taken, only velocities on the xz plane were captured. This is standard for 2D PIV and means that the velocity magnitude is calculated using only the x and z components of the velocity.

The final PIV image shows the average velocity magnitude on the xz plane for a total of 900 image pairs per case. No further post processing was done on the images. It was determined that no interpolation was required to 'fix' bad data points as the vector data for this test campaign was of high enough quality and any residual noise was removed in the averaging process.

Figure 5.13 shows the convergence of the velocity at four selected locations in the PIV. This convergence was taken from the example case shown in figure 5.12 where the front vehicle has a $25mm$ flap set at 10° and a free stream velocity of $30ms^{-1}$. The convergence process is carried out using a summed average approach. The locations were chosen to show a range of flow conditions throughout the region of interest. The two points in the free stream converge quickly, after only 200 images. The point at $y/H = 1.35$ is in the unsteady shear layer produced by the detached flow off of the front vehicle. As expected, this area takes far longer to converge, reaching a steady velocity at around 800 images. The final interrogation point, at $y/H = 1.10$, is in the recirculation region. Whilst this is more unsteady than the free stream, the velocity converges after 400 images.

(a)

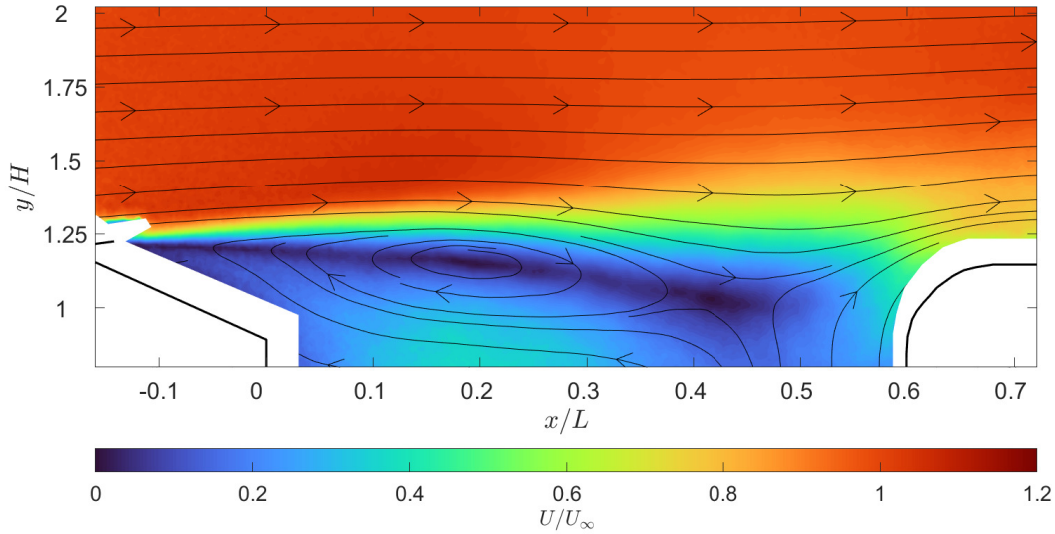

(b)

Figure 5.12: Examples of a (a) raw and (b) post-processed PIV image. Region 1 highlights some reflections from inside the test section and Region 2 highlights the perspective distortion causing the models to be seen isometrically.

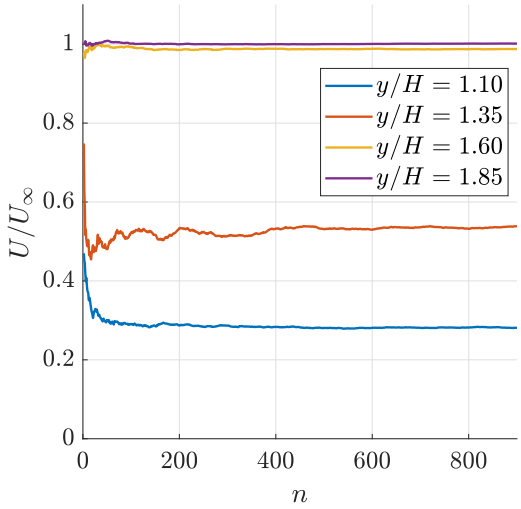

Figure 5.13: PIV convergence for a series of locations at varying heights. Convergence is taken as a summed average for up to 900 image pairs.

5.2.8 Methodology

Measurements were conducted at three different wind tunnel speeds: 10, 20 and 30m/s. Since the Ahmed body displays the aerodynamic characteristics of a bluff body, the base height H was used as the reference length scale, in line with other bluff body studies, when calculating the Reynolds number. The Reynolds numbers associated with the selected wind tunnel speeds are $0.96 \cdot 10^5$, $1.92 \cdot 10^5$ and $2.88 \cdot 10^5$.

For the platooning investigations, the inter-vehicle separation distance d is normalised with respect to vehicle length L. In this experiment, 5 separation distances were chosen, $d/L = 0.2$, 0.4, 0.6, 0.8 and 1.0 as outlined in table 5.3. The maximum inter-vehicle spacing is limited by the length of the wind tunnel test section (here: 3.2m) as in many other experimental platooning studies. The selected range of inter-vehicle distances covers the area of highest interest since inverted platooning conditions are most commonly observed at short inter-vehicle distances as discussed in section 2.3.4. This trend was also confirmed by the simulations discussed in chapters 3 and 4.

To allow the drag coefficient data to be normalised, drag coefficients for each vehicle were taken in isolation at every location in the wind tunnel (see table 5.2). Following this, the baseline platoon data was collected (see table 5.3), followed by a heterogeneous platoon consisting of a squareback Ahmed front vehicle and a 25° Ahmed rear vehicle (see table 5.4). Finally, the experiments on platoons with flow control were conducted (see table 5.5). Measurements for each configuration were repeated at least three times and the flow in the wind tunnel was allowed to settle between each run.

For each run, the output signal was sampled for 120s at 2kHz. An example of part of the output signal from one of the load cells is shown in figure 5.14. Some vibrations and noise were

ref no	reference name	d/L	wind tunnel velocity
1	Isolated Front Vehicle 10	N/A	$10m/s$
2	Isolated Front Vehicle 20	N/A	$20m/s$
3	Isolated Front Vehicle 30	N/A	$30m/s$
4	Isolated Rear Vehicle 0.2_10	0.2	$10m/s$
5	Isolated Rear Vehicle 0.2_20	0.2	$20m/s$
6	Isolated Rear Vehicle 0.2_30	0.2	$30m/s$
7	Isolated Rear Vehicle 0.4_10	0.4	$10m/s$
8	Isolated Rear Vehicle 0.4_20	0.4	$20m/s$
9	Isolated Rear Vehicle 0.4_30	0.4	$30m/s$
10	Isolated Rear Vehicle 0.6_10	0.6	$10m/s$
11	Isolated Rear Vehicle 0.6_20	0.6	$20m/s$
12	Isolated Rear Vehicle 0.6_30	0.6	$30m/s$
13	Isolated Rear Vehicle 0.8_10	0.8	$10m/s$
14	Isolated Rear Vehicle 0.8_20	0.8	$20m/s$
15	Isolated Rear Vehicle 0.8_30	0.8	$30m/s$
16	Isolated Rear Vehicle 1.0_10	1.0	$10m/s$
17	Isolated Rear Vehicle 1.0_20	1.0	$20m/s$
18	Isolated Rear Vehicle 1.0_30	1.0	$30m/s$

Table 5.2: Overview of isolated Ahmed body experiments.

ref no	reference name	d/L	wind tunnel velocity
19	Baseline Platoon 0.2_10	0.2	$10m/s$
20	Baseline Platoon 0.2_20	0.2	$20m/s$
21	Baseline Platoon 0.2_30	0.2	$30m/s$
22	Baseline Platoon 0.4_10	0.4	$10m/s$
23	Baseline Platoon 0.4_20	0.4	$20m/s$
24	Baseline Platoon 0.4_30	0.4	$30m/s$
25	Baseline Platoon 0.6_10	0.6	$10m/s$
26	Baseline Platoon 0.6_20	0.6	$20m/s$
27	Baseline Platoon 0.6_30	0.6	$30m/s$
28	Baseline Platoon 0.8_10	0.8	$10m/s$
29	Baseline Platoon 0.8_20	0.8	$20m/s$
30	Baseline Platoon 0.8_30	0.8	$30m/s$
31	Baseline Platoon 1.0_10	1.0	$10m/s$
32	Baseline Platoon 1.0_20	1.0	$20m/s$
33	Baseline Platoon 1.0_30	1.0	$30m/s$

Table 5.3: Overview of baseline platoon experiments. Platoon consists of two Ahmed vehicles with a 25° rear slant.

ref no	reference name	d/L	wind tunnel velocity
34	heterogeneous Platoon 0.2_10	0.2	$10m/s$
35	heterogeneous Platoon 0.2_20	0.2	$20m/s$
36	heterogeneous Platoon 0.2_30	0.2	$30m/s$
37	heterogeneous Platoon 0.4_10	0.4	$10m/s$
38	heterogeneous Platoon 0.4_20	0.4	$20m/s$
39	heterogeneous Platoon 0.4_30	0.4	$30m/s$
40	heterogeneous Platoon 0.6_10	0.6	$10m/s$
41	heterogeneous Platoon 0.6_20	0.6	$20m/s$
42	heterogeneous Platoon 0.6_30	0.6	$30m/s$
43	heterogeneous Platoon 0.8_10	0.8	$10m/s$
44	heterogeneous Platoon 0.8_20	0.8	$20m/s$
45	heterogeneous Platoon 0.8_30	0.8	$30m/s$
46	heterogeneous Platoon 1.0_10	1.0	$10m/s$
47	heterogeneous Platoon 1.0_20	1.0	$20m/s$
47	heterogeneous Platoon 1.0_30	1.0	$30m/s$

Table 5.4: Overview of heterogeneous platoon experiments.Platoon consists of a square back Ahmed vehicle at the front and a 25° Ahmed vehicle at the rear.

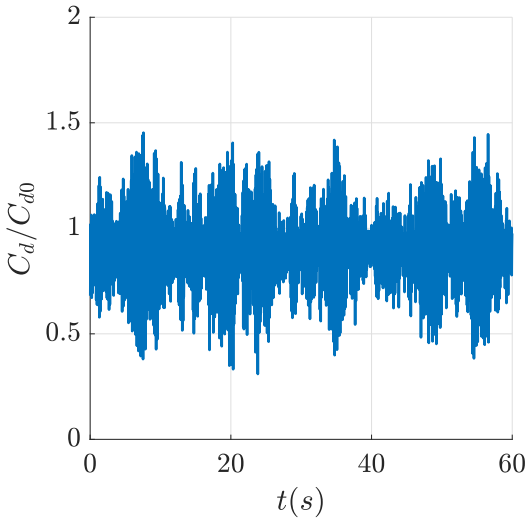

Figure 5.14: Example for an output signal of the instantaneous normalised drag coefficient of the front vehicle in the baseline platoon at $d/L = 1.0$

ref no	reference name	d/L	flap angle	wind tunnel velocity
48	Flow Control 00_0.2_10	0.2	0°	$10m/s$
49	Flow Control 00_0.2_20	0.2	0°	$20m/s$
50	Flow Control 00_0.2_30	0.2	0°	$30m/s$
51	Flow Control 10_0.2_10	0.2	10°	$10m/s$
52	Flow Control 10_0.2_20	0.2	10°	$20m/s$
53	Flow Control 10_0.2_30	0.2	10°	$30m/s$
54	Flow Control 20_0.2_10	0.2	20°	$10m/s$
55	Flow Control 20_0.2_20	0.2	20°	$20m/s$
56	Flow Control 20_0.2_30	0.2	20°	$30m/s$
57	Flow Control 00_0.4_10	0.4	0°	$10m/s$
58	Flow Control 00_0.4_20	0.4	0°	$20m/s$
59	Flow Control 00_0.4_30	0.4	0°	$30m/s$
60	Flow Control 10_0.4_10	0.4	10°	$10m/s$
61	Flow Control 10_0.4_20	0.4	10°	$20m/s$
62	Flow Control 10_0.4_30	0.4	10°	$30m/s$
63	Flow Control 20_0.4_10	0.4	20°	$10m/s$
64	Flow Control 20_0.4_20	0.4	20°	$20m/s$
65	Flow Control 20_0.4_30	0.4	20°	$30m/s$
66	Flow Control 00_0.6_10	0.6	0°	$10m/s$
67	Flow Control 00_0.6_20	0.6	0°	$20m/s$
68	Flow Control 00_0.6_30	0.6	0°	$30m/s$
69	Flow Control 10_0.6_10	0.6	10°	$10m/s$
70	Flow Control 10_0.6_20	0.6	10°	$20m/s$
71	Flow Control 10_0.6_30	0.6	10°	$30m/s$
72	Flow Control 20_0.6_10	0.6	20°	$10m/s$
73	Flow Control 20_0.6_20	0.6	20°	$20m/s$
74	Flow Control 20_0.6_30	0.6	20°	$30m/s$
75	Flow Control 00_0.8_10	0.8	0°	$10m/s$
76	Flow Control 00_0.8_20	0.8	0°	$20m/s$
77	Flow Control 00_0.8_30	0.8	0°	$30m/s$
78	Flow Control 10_0.8_10	0.8	10°	$10m/s$
79	Flow Control 10_0.8_20	0.8	10°	$20m/s$
80	Flow Control 10_0.8_30	0.8	10°	$30m/s$
81	Flow Control 20_0.8_10	0.8	20°	$10m/s$
82	Flow Control 20_0.8_20	0.8	20°	$20m/s$
83	Flow Control 20_0.8_30	0.8	20°	$30m/s$
84	Flow Control 00_1.0_10	1.0	0°	$10m/s$
85	Flow Control 00_1.0_20	1.0	0°	$20m/s$
86	Flow Control 00_1.0_30	1.0	0°	$30m/s$
87	Flow Control 10_1.0_10	1.0	10°	$10m/s$
88	Flow Control 10_1.0_20	1.0	10°	$20m/s$
89	Flow Control 10_1.0_30	1.0	10°	$30m/s$
90	Flow Control 20_1.0_10	1.0	20°	$10m/s$
91	Flow Control 20_1.0_20	1.0	20°	$20m/s$
92	Flow Control 20_1.0_30	1.0	20°	$30m/s$

Table 5.5: Overview of platooning experiments with flow control. Platoon consists of two 25° Ahmed vehicles where the front vehicle has flow control applied.

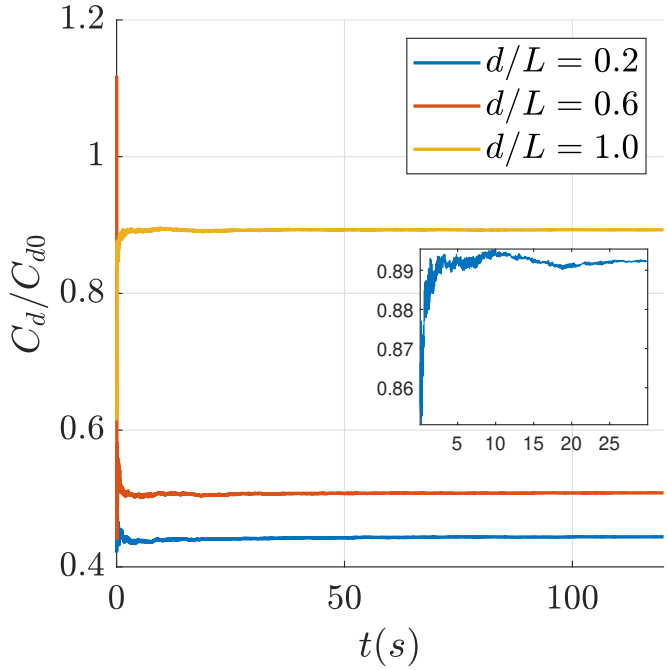

Figure 5.15: Normalised drag coefficient signal as a summed average with respect to time in seconds. Detail highlights oscillations in the average between 0s and 30s. By 30s the average is already beginning to settle.

observed in the measurement therefore, the output data was averaged before being used in the analysis. Figure 5.15 shows the running average for a range of signals. It was observed that once each measurement reached 50s, the average had converged to a steady value showing that a sufficiently long sampling time had been selected.

5.3 Results and discussion

In this section the results of the experimental investigation will be laid out and some discussion for each of the given test cases will be provided. Initially an isolated 25° Ahmed vehicle at each location in the tunnel was analysed. Following this the baseline platoon of two 25° Ahmed vehicles was discussed. After understanding the aerodynamic features of the baseline case the platoon will be altered, initially through modifying the rear slant angle of the front vehicle then by introducing flaps to the front 25° Ahmed vehicle.

5.3.1 Isolated 25° Ahmed vehicle

It has been shown in previous studies that the streamwise location of a model in a wind tunnel can affect the measured drag coefficient. For road vehicle investigations this can be for a number of reasons. The most common reason is due to the development of a boundary layer over the ground plate. As the model moves further downstream, the increased height of the boundary

Re_H	495	1121	1226	1330	1435	1539
	Front	$d/L = 0.2$	$d/L = 0.4$	$d/L = 0.6$	$d/L = 0.8$	$d/L = 1.0$
0.99×10^5	0.410	0.318	0.333	0.351	0.361	0.382
1.98×10^5	0.394	0.292	0.311	0.322	0.341	0.361
2.95×10^5	0.388	0.281	0.300	0.313	0.331	0.350

Table 5.6: Drag coefficient measurements for a 25° Ahmed vehicle in isolation at three Reynolds numbers and over a range of streamwise locations in the wind tunnel test section. Distances were measured from the leading edge of the ground plate to the leading edge of the model and are given in millimetres.

layer can begin to impinge on the leading edge of the vehicle, changing the drag coefficient. In the case of this study, it was shown that the boundary layer height will not increase to a level that will cause large changes in the flow over the leading edge of the vehicle. Additionally, boundary layer effects are significantly reduced in platooning studies as the front vehicle drastically alters the development of a downstream boundary layer. Despite this, another factor that can alter the measured drag coefficient in a platoon is the changing pressure over the length of the test section. This variation can account for as much as a 20% change in drag coefficient depending on the wind tunnel facility and design of experiment [132].

To combat this, the drag of the isolated vehicle was measured at all streamwise locations where, in the later platooning investigations, one of the platoon members would be placed. This then allows for a normalisation of the drag of a platoon member compared to an equivalent isolated 25° Ahmed vehicle in the same location in the tunnel. Whilst most platooning studies quote normalised results with respect to an isolated case, the exact method for normalisation is rarely given. As the drag coefficient of the vehicle is, to some extent, dependant on the streamwise location in the wind tunnel it is hypothesised that this method of normalisation provides the most representative results.

The drag coefficient of the isolated vehicle at different streamwise locations is given in Table 5.6 for the three Reynolds numbers covered in this study. For all Reynolds numbers, the highest drag value is measured in the front position. As can be observed, for the rear positions the drag coefficient gradually climbs as the vehicle moves down the test section from the $d/L = 0.2$ location to the $d/L = 1.0$ location. Between these locations there is a drag increase of 25% (at $Re_H = 2.95 \times 10^5$). It is difficult to determine the exact causes of this increase, but the study by Garry et al. [132] provides some insight. They investigated the effect of the longitudinal position on the drag of simplified road vehicle models for different wind tunnel facilities. They found that the pressure in the diffuser, which is the section of the wind tunnel that slows down the flow of air, can have an impact on the drag of the vehicle model. Additionally, the study found that leakage flows from beneath the ground plate can cause readings to vary by as much as 20% depending on the model position relative to the trailing edge of the ground plate. One potential example of where this can be seen in platooning is the paper by Watkins and Vino

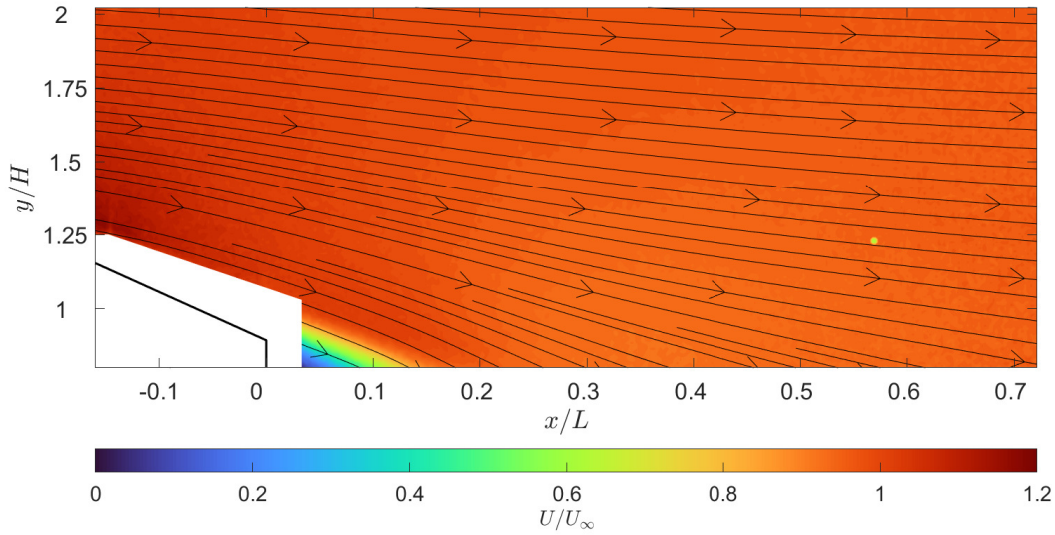

Figure 5.16: PIV image of the normalised velocity magnitude field for a 25° Ahmed vehicle in isolation. The freestream direction is from left to right. For this test case there was a fleck of dust illuminated on the wind tunnel window, this is seen as a small yellow spot in the free stream.

where they report that the drag coefficient of the rear vehicle in the platoon does not return to the isolated drag coefficient value by $d/L = 4.0$. This is in disagreement with some of the literature discussed in section 2.3.

It is obvious that the streamwise location has some effect on the measured drag coefficient, however, no other systematic studies on this phenomenon were found. As discussed above, experimental platooning studies in the literature do not report the dependence of the drag coefficient of an isolated vehicle on the longitudinal position. For this reason, it is suggested that it should be standard practice to report the variation of drag coefficient in future experimental platooning investigations.

Considering the results shown in table 5.6 further, it can be noted that the one outlier of the drag coefficient results is the isolated case in the location of the front vehicle. Whilst the drag coefficient values measured at the front position are of similar magnitude as the other measurements at the same Reynolds number, it does not follow the same increasing trend with longitudinal position. It was shown in section 5.2.5 that a separation bubble exists at the leading edge of the flat plate. Whilst the flow has reattached and settled into a standard attached boundary layer upstream of the leading edge of the model when in the front position, it was speculated that some residual unsteadiness in the flow could explain the outlying result. In addition to this, the mounting system and vehicle model used for at this location is different to all the other locations adding additional variation to the measurement.

Finally, as discussed in section 2.1, the flow over the trailing edge of the 25° Ahmed vehicle should remain attached over the rear slant. This is arguably one of the most important features

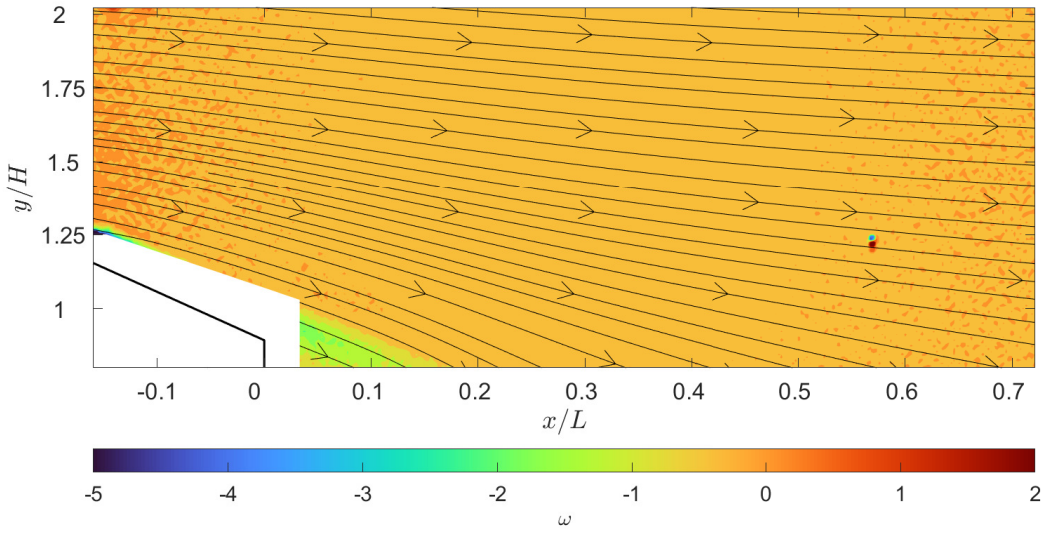

Figure 5.17: PIV image of ω_z for a 25° Ahmed vehicle in isolation. The freestream direction is from left to right.

for this particular experiment, as producing the correct wake conditions is vital for later measuring platoon effectiveness with modified wake structures. Figure 5.16 shows a PIV image of the average velocity field over the rear slant of the Ahmed vehicle in isolation. It is clear that the flow remains attached over the slant, producing a small wake at the base of the vehicle.

Figure 5.17 shows the vorticity for the isolated case. In general, the vorticity in the wake is low. The area of increased vorticity highlights the flow separation at the bottom of the rear slant and indicates that the flow is attached over the rear slant. In general, there is more noise in this figure when compared to the velocity field shown in figure 5.16, this is as a result of the partial differentiation process used to convert the velocity field into a vorticity field (equation 5.6). This is often seen when converting velocity to vorticity and is explained in more detail in the paper by Menter [133]. Similarly, the area around the mask is also effected as the differentiation process does not distinguish between masked and unmasked regions. This causes the effected area to expand. In this scenario, we are using 2D PIV, measuring only v_x and v_y, from which ω_z is calculated as follows:

$$\omega_z = \frac{\partial v_y}{\partial x} - \frac{\partial v_x}{\partial y} \tag{5.6}$$

5.3.2 Baseline platoon

As discussed above, the baseline platoon is a platoon composed of two Ahmed bodies with at 25° rear slant angle. The drag coefficients for each test case discussed in this chapter are given in tables 5.7, 5.8 and 5.9. Figure 5.18 shows the variation of normalised drag coefficient for both 25° Ahmed vehicles in a platoon as a function of the inter-vehicle spacing at a Reynolds number

Case	Front					Rear				
	0.2	0.4	0.6	0.8	1.0	0.2	0.4	0.6	0.8	1.0
Baseline Platoon	0.21	0.21	0.24	0.36	0.38	0.32	0.36	0.37	0.35	0.36
heterogeneous Platoon	0.29	0.22	0.22	0.26	0.31	0.32	0.36	0.37	0.38	0.37
10*mm* Flap 0°	0.23	0.23	0.24	0.28	0.31	0.33	0.36	0.37	0.35	0.36
10*mm* Flap 10°	0.25	0.24	0.25	0.29	0.31	0.33	0.35	0.36	0.35	0.36
10*mm* Flap 20°	0.29	0.27	0.27	0.30	0.32	0.31	0.35	0.36	0.35	0.35
25*mm* Flap 0°	0.26	0.24	0.25	0.29	0.32	0.32	0.35	0.35	0.35	0.36
25*mm* Flap 10°	0.31	0.30	0.29	0.32	0.35	0.29	0.36	0.36	0.35	0.35
25*mm* Flap 20°	0.39	0.36	0.35	0.37	0.39	0.30	0.38	0.37	0.36	0.36

Table 5.7: Drag coefficient for each vehicle in the platoons of the experimental study at $Re = 0.96 \cdot 10^5$.

Case	Front					Rear				
	0.2	0.4	0.6	0.8	1.0	0.2	0.4	0.6	0.8	1.0
Baseline Platoon	0.18	0.18	0.21	0.29	0.35	0.32	0.36	0.37	0.34	0.35
heterogeneous Platoon	0.27	0.19	0.19	0.24	0.28	0.32	0.37	0.38	0.36	0.36
10*mm* Flap 0°	0.20	0.20	0.22	0.25	0.28	0.32	0.35	0.36	0.35	0.35
10*mm* Flap 10°	0.23	0.21	0.23	0.26	0.28	0.32	0.35	0.36	0.35	0.35
10*mm* Flap 20°	0.26	0.25	0.25	0.28	0.30	0.30	0.36	0.36	0.35	0.35
25*mm* Flap 0°	0.23	0.21	0.23	0.26	0.29	0.32	0.35	0.36	0.35	0.35
25*mm* Flap 10°	0.29	0.27	0.27	0.30	0.32	0.30	0.37	0.37	0.35	0.35
25*mm* Flap 20°	0.37	0.34	0.33	0.35	0.37	0.30	0.39	0.38	0.36	0.36

Table 5.8: Drag coefficient for each vehicle in the platoons of the experimental study at $Re = 1.92 \cdot 10^5$.

Case	Front					Rear				
	0.2	0.4	0.6	0.8	1.0	0.2	0.4	0.6	0.8	1.0
Baseline Platoon	0.18	0.17	0.20	0.24	0.32	0.32	0.36	0.36	0.34	0.35
heterogeneous Platoon	0.23	0.18	0.18	0.23	0.27	0.29	0.37	0.38	0.36	0.36
10*mm* Flap 0°	0.19	0.19	0.21	0.24	0.27	0.32	0.36	0.36	0.34	0.35
10*mm* Flap 10°	0.22	0.20	0.22	0.25	0.28	0.32	0.35	0.36	0.34	0.34
10*mm* Flap 20°	0.25	0.24	0.24	0.27	0.29	0.30	0.36	0.36	0.34	0.34
25*mm* Flap 0°	0.22	0.20	0.22	0.26	0.28	0.32	0.35	0.36	0.34	0.34
25*mm* Flap 10°	0.28	0.26	0.26	0.29	0.31	0.29	0.37	0.36	0.35	0.34
25*mm* Flap 20°	0.43	0.33	0.32	0.33	0.36	0.29	0.38	0.38	0.35	0.35

Table 5.9: Drag coefficient for each vehicle in the platoons of the experimental study at $Re = 2.88 \cdot 10^5$.

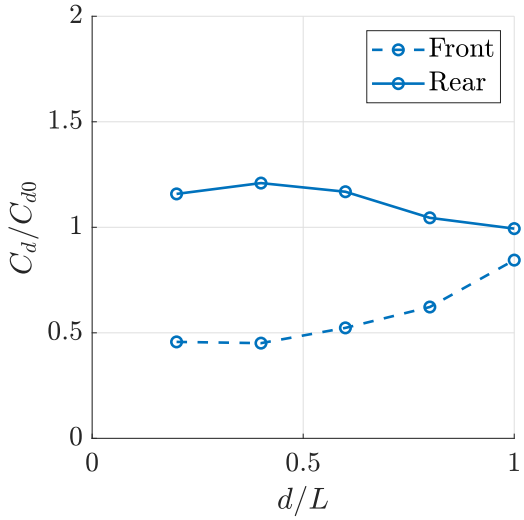

Figure 5.18: Normalised drag coefficient for the baseline platoon of two 25° Ahmed bodies at $Re = 2.88 \cdot 10^5$

of $2.88 \cdot 10^5$ based on the vehicle height. This is a clear example of an inverted platoon, in agreement with other Ahmed vehicle platooning studies discussed in section 2.3.4 [27,109,110]. Each value was normalised with respect to an isolated 25° Ahmed vehicle at the same location on the ground plate as outlined in the previous section (5.3.1).

At inter-vehicle spacing $d/L = 0.2$ and 0.4, the front vehicle receives a drag reduction of 55%. This reduction is a result of two differences between the isolated and platoon cases. For the isolated 25° Ahmed vehicle, the flow remains attached over the trailing edge slant. The critical angle for the rear slant of the isolated Ahmed vehicle is 30°, since at this angle the flow fully separates over the trailing edge slant. When the rear slant is at 25°, the vehicle is required to do a lot of work on the flow to maintain its attachment in this region. When in a platoon, the presence of a second vehicle in the wake of the front vehicle increases the base pressure. This causes the flow to separate over the trailing edge of the front vehicle resulting in a reduction in drag. A comparison can be seen in figure 5.19 where the averaged velocity field of both the the isolated Ahmed vehicle and the platoon at $d/L = 0.4$ is provided. The increase in base pressure also improves the pressure recovery on the front vehicle that, when combined with the effects of flow separation, results in a significant drag reduction for the front vehicle. This is a similar mechanism and wake structure to the isolated, squareback, Ahmed vehicle as discussed in section 2.1 and detailed in figure 2.3

As the vehicles move further apart, the influence between the vehicles weakens. At $d/L = 0.8$ some level of unsteadiness is still visible in the flow over the trailing edge of the front vehicle. However, on average, the flow in this region returns to being attached to the slant surface. For the longest inter-vehicle spacing, $d/L = 1.0$ the flow over the front vehicle has mostly returned the conditions for an isolated body with the normalised drag coefficient approaching 1.

As expected, the baseline platoon exhibits inverted platooning conditions at short inter-

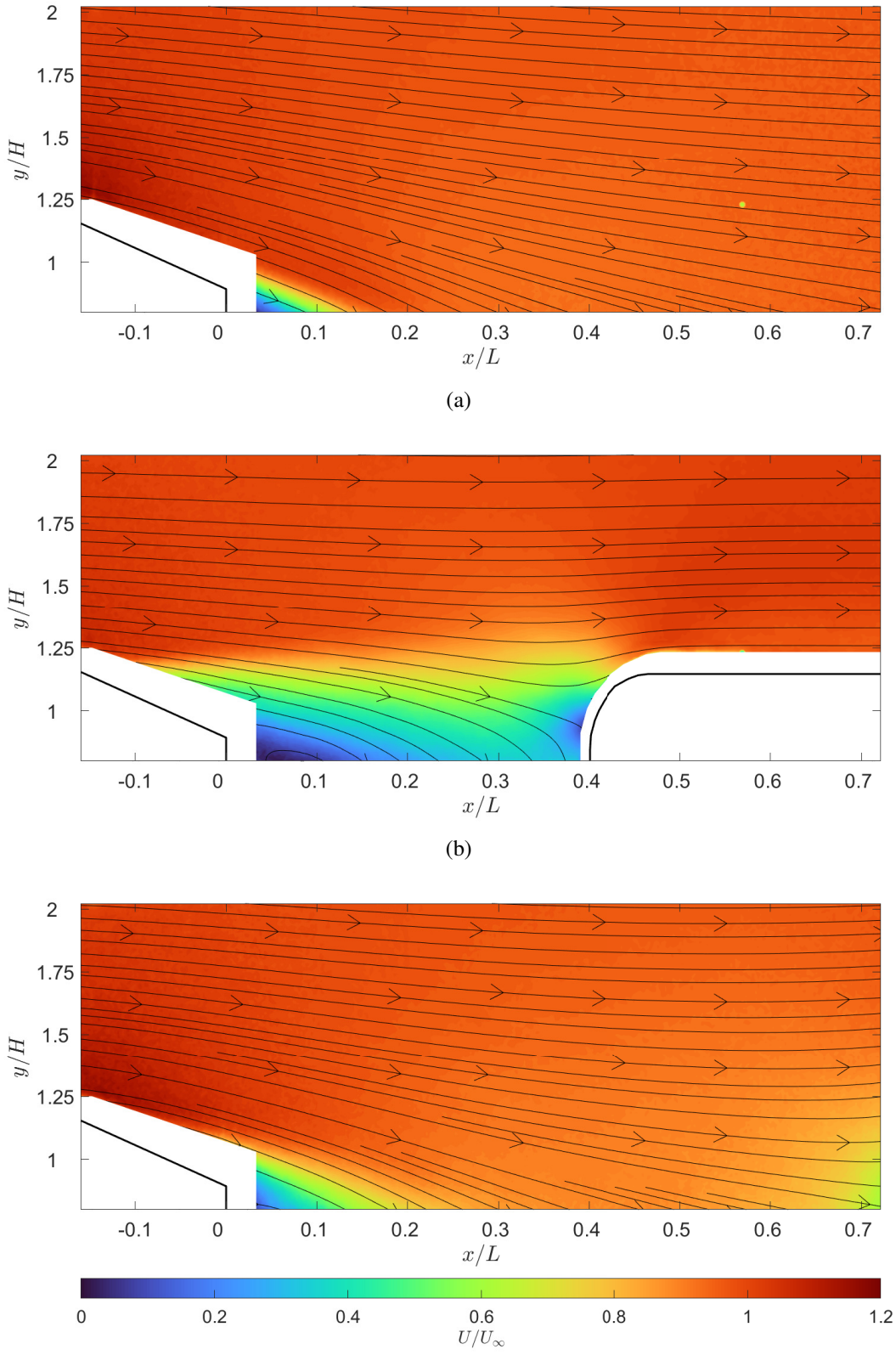

Figure 5.19: PIV images of normalised velocity magnitude field for a 25° Ahmed vehicle in (a) isolation and in a platoon at $d/L =$ (b) 0.4 and (c) 0.8. The freestream direction is from left to right.

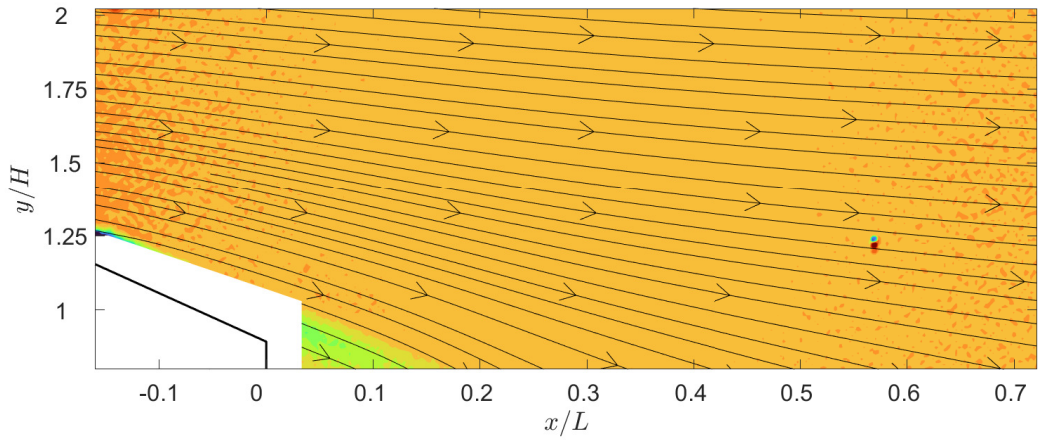

(a)

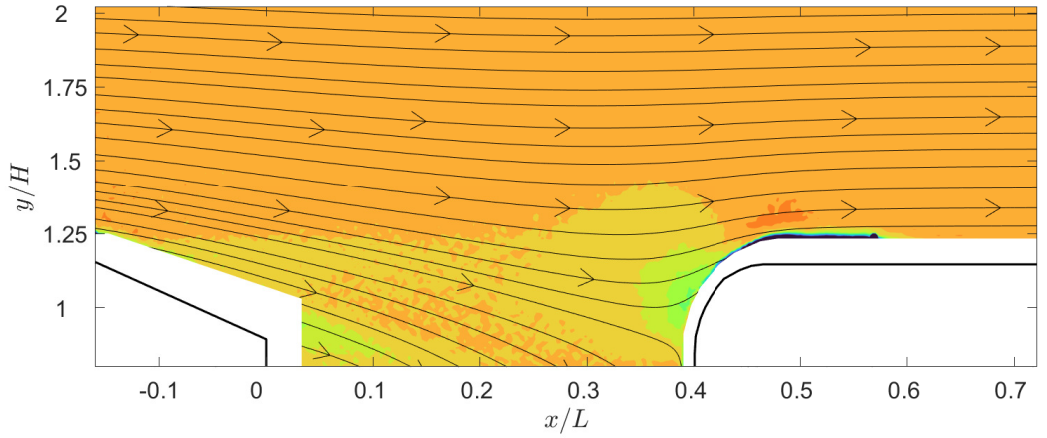

(b)

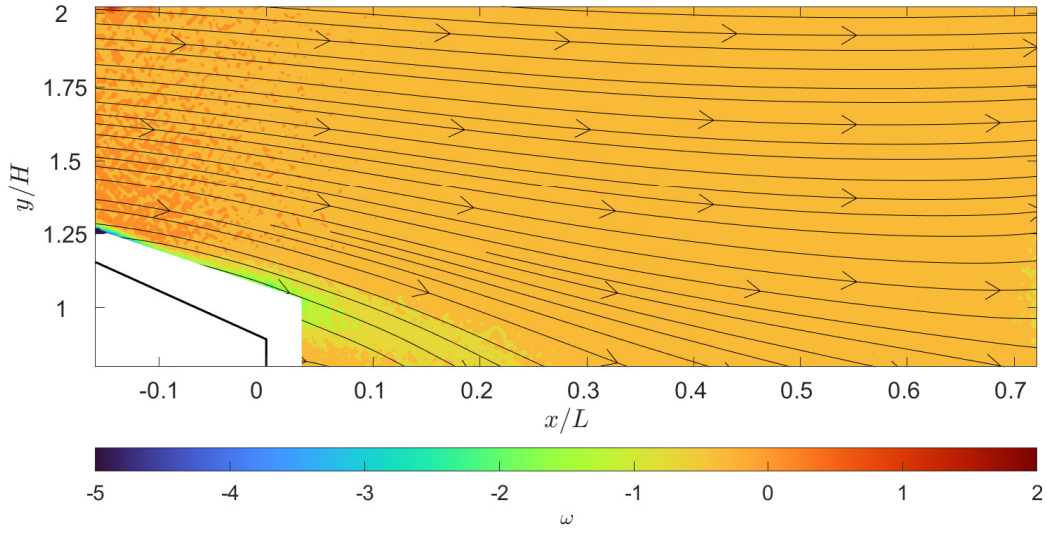

(c)

Figure 5.20: PIV images of ω_z for a 25° Ahmed vehicle in (a) isolation and in a platoon at $d/L =$ (b) 0.4 and (c) 0.8. The freestream direction is from left to right.

vehicle spacing. The normalised drag coefficient of the rear vehicle peaks at $d/L = 0.4$ with an increase of 21% when compared to an isolated vehicle. A similar increase of 16% and 17% was also observed at $d/L = 0.2$ and 0.6 respectively. This increase is most likely due to the interaction of the shear layer trailing from the front vehicle with the rounded leading edge of the rear vehicle, also referred to as wake impingement.

For an isolated Ahmed vehicle, the stagnation of the flow on the flat portion of the leading edge produces a high pressure region. This high pressure is balanced by a region of pressure recovery around each of the curved portions of the leading edge as the attached flow is accelerated. When in a platoon, the stagnation effects of the rear vehicle are reduced (this is the main driving force behind drag reduction in classical platooning examples). Whilst this does provide some benefits, the wake impingement significantly reduces the pressure recovery produced by the flow accelerating around the curved portions of the leading edge of the rear vehicle. A similar mechanism was identified in chapter 4 and was described using a wall normal pressure distribution plot as seen in figure 4.4. When the flow separates over the trailing edge of the front vehicle it produces a thick, unsteady, oscillating shear layer. This can be observed in figure 5.19 where the impingement of this shear layer can clearly be seen at an inter-vehicle spacing of $d/L = 0.4$. Here it can be seen that the stagnation location has shifted high onto the rounded leading edge of the rear vehicle, this interaction destabilises the flow over the rounded leading edge thus negating the pressure recovery seen on the isolated cases. As a result, the drag coefficient of the rear vehicle increases compared to the isolated case.

The importance of the wake-impingement effect at short inter-vehicle spacing is further supported by the results for larger inter-vehicle distances where the influence of wake impingement is removed. At $d/L = 0.8$ the flow of the lead vehicle reattaches over the trailing edge slant, as seen in figure 5.19, significantly reducing the size of the wake of the front vehicle. This coincides with a sharp drop in drag coefficient for the rear vehicle. At this distance the rear vehicle is no longer affected by the impingement of the wake produced by the front vehicle and the normalised drag coefficient of the rear vehicle returns to a value of around 1, i.e., it approaches isolated vehicle conditions.

This result is further highlighted in figure 5.20 where the vorticity on the centre plane is shown. The wake impingement on the leading edge of the rear vehicle at $d/L = 0.4$ can easily be identified by the region of increased vorticity where the shear layer meets the rear vehicle.

The Reynolds number dependency of the platoon was also analysed with the results shown in figure 5.21. Here the drag coefficients are normalised with respect to the drag coefficient at the highest Reynolds number for each case (3×10^5). As discussed in section 2.1, the drag coefficient of the 25° Ahmed body in isolation decreases as Reynolds number increases. This trend is also observed for the front vehicle in the platoon as it is dominated by the incoming flow that remains unchanged in the platoon.

The Reynolds number dependency of the drag coefficient of the front vehicle is quite similar

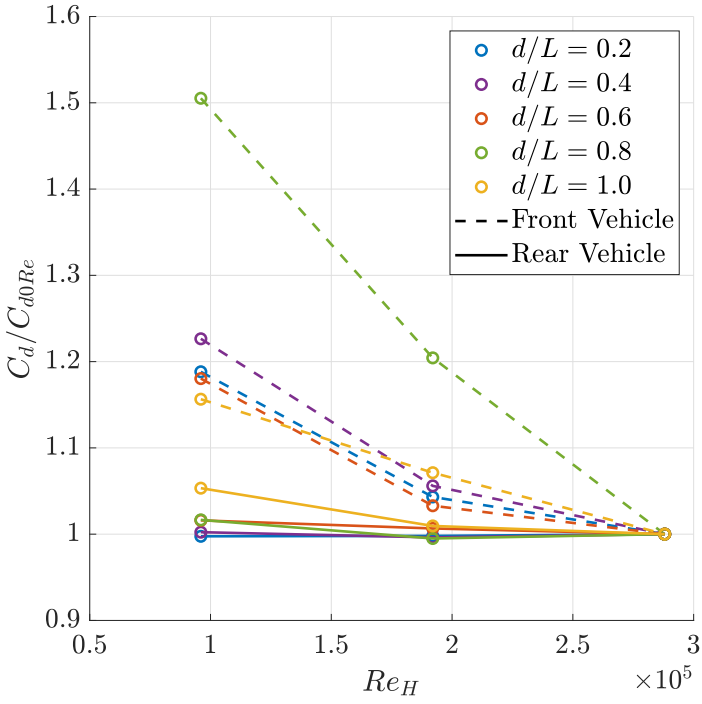

Figure 5.21: Reynolds number dependency of drag coefficients of the baseline platoon. The drag coefficients are normalised with respect to the drag coefficient measured the highest Reynolds number for each case.

for most of the inter-vehicle distances, however, the case of $d/L = 0.8$ is significantly more sensitive to Reynolds number. This outlying result can be explained as follows: Two distinct flow regimes were observed for the front vehicle in this configuration. At the higher Reynolds number of $2.88 \cdot 10^5$ the flow over the front vehicle detaches at the top of the slant whilst at the lower Reynolds number of $0.96 \cdot 10^5$, the flow remains attached over the rear slant before separating. The two different flow regimes result in a much more distinct Reynolds number dependency of the drag coefficient since at this spacing the flow regime changes with Reynolds number. For the intermediate case of $Re_H = 1.92 \cdot 10^5$, a switching behaviour between these two regimes was observed during one test run (3 total test runs of 120s conducted), further highlighting the Reynolds-number sensitivity of this particular platooning arrangement.

In contrast to the front model, the rear model showed little Reynolds number dependency. This is because its aerodynamics are strongly influenced by the wake of the front vehicle. The wake of the front Ahmed body is largely determined by the separation over the rear slant (or absence thereof, depending on inter-vehicle spacing) and it does not vary strongly with Reynolds number. As a result, the incoming flow over the trailing vehicle remains very similar over the investigated Reynolds number range. This is in line with the observation that at the longest spacing, where the rear vehicle is less strongly impacted by the wake, the drag coefficient of the rear model begins to show a stronger Reynolds number dependency.

One would expect the aforementioned switching behaviour of the front vehicle between two

d/L	Isolation	0.2	0.4	0.6	0.8	1.0
Cd	0.269	0.233	0.178	0.177	0.234	0.268

Table 5.10: Drag coefficient measurements for the front squareback Ahmed vehicle in isolation and as part of a heterogeneous platoon for a range of inter-vehicle distances at $Re = 3 \times 10^5$

distinct regimes, seen at $d/L = 0.8$, to also have some residual effect on the Reynolds number sensitivity of the rear vehicle. However, interestingly, no such effect is evident in the results. At this spacing the rear vehicle has already almost recovered isolated conditions and is thus only weakly affected by the wake of the upstream vehicle.

Overall, the results display similar characteristics to the results published by Törnell et al. [18] in their experimental study on a platoon of two, fully articulated, HGV models for a range of Reynolds numbers from $0.95 \cdot 10^6$ to $1.89 \cdot 10^6$. They also found that the front vehicle showed a far stronger Reynolds number dependency with the rear vehicle only deviating in drag coefficient at the largest inter-vehicle distance tested of $4m$ or $d/L = 1.5$

Considering that specific inter-vehicle distances can elicit a strong Reynolds number dependency of a platoon's behaviour, as observed in the present case for the lead vehicle at $d/L = 0.8$, the influence of Reynolds number on platooning is an important area in need of further research. Existing platooning studies typically consider only a single Reynolds number or a cover a limited Reynolds number range like the present study and the work of Törnell et al. [18]. Ideally, a single experiment should be conducted which specifically focuses on capturing a wider range of Reynolds numbers. Whilst there are obvious size and speed limitations in wind tunnel facilities, this type of investigation would be vital to fully understand the effect of Reynolds number on platoon aerodynamics. In addition, the effect of vehicle geometry on Reynolds number dependency also needs to be further understood. Both the current study and the study by Törnell et al. used vehicles with sharp slant edges. Vehicles with more Reynolds number dependent separation locations, e.g., over rounded edges, may yield different results.

5.3.3 Heterogeneous platoon

In order to understand how changing the wake produced by the front vehicle affects the platoon performance, a heterogeneous platoon consisting of a 0° Ahmed vehicle at the front and a 25° Ahmed vehicle at the rear was tested. The drag coefficients for each test case discussed in this chapter are given in tables 5.7, 5.8 and 5.9. Figure 5.22 shows a comparison between the baseline platoon and the new, heterogeneous, platoon over the same range of inter-vehicle distances. It is important to note that the drag coefficients for both vehicles are normalised with respect to the 25° Ahmed vehicle in isolation. This was dont to highlight the absolute differences between the platoons and provide a better comparison. The non-normalised measured drag coefficients for the front vehicle in the heterogeneous platoon are given in table 5.10 for reference and comparison.

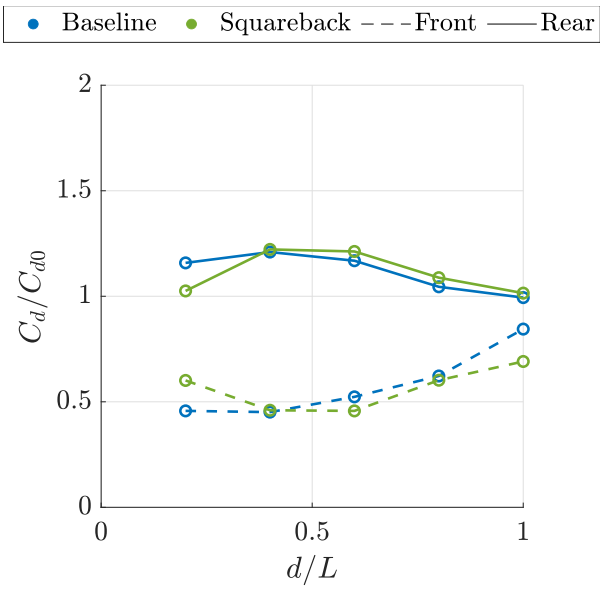

Figure 5.22: Normalised drag coefficient comparison between the baseline platoon and a heterogeneous platoon comprised of a 0° Ahmed front vehicle and a 25° Ahmed rear vehicle at $Re = 2.88 \cdot 10^5$.

Similar to the baseline case, the heterogeneous platoon exhibits inverted platooning conditions where the front vehicle receives a large benefit from the platoon and the rear vehicle experiences an increase in drag coefficient when directly affected by the front vehicle's wake. Whilst the front vehicle in the platoon consistently experiences a drag reduction when compared to a 25° Ahmed vehicle in isolation, the drag coefficient at $d/L = 0.2$ is considerably higher than that at $d/L = 0.4$. This is in contrast to the baseline case where the front vehicle at $d/L = 0.2$ and 0.4 receives approximately the same level of drag reduction. A large proportion of the drag reduction for the front vehicle in the platoon arises from the increase in base pressure resulting from the presence of a second vehicle in the wake of the front vehicle. One would assume that the largest increase in base pressure (and therefore lowest drag coefficient) would coincide with the closest inter-vehicle spacing (i.e., $d/L = 0.2$). However, whilst this holds true for the baseline case it is not true for the heterogeneous platoon. There must be some additional features in the flow that contribute to the drag reduction for the front vehicle. Figure 5.23 shows the average velocity magnitude for the heterogeneous platoon at $d/L = 0.2$ and 0.4. At $d/L = 0.2$ a tight recirculation region forms between the two vehicles, here, the increased recirculation velocity reduces the pressure at the base of the vehicle resulting in an increase in drag.

When moving to the $d/L = 0.4$ case shown in the same figure, it can be observed how the larger distance between the vehicles allows for a slower recirculation than in the previous example, this in turn promotes improved pressure recovery for the front vehicle. This flow regime is continued for the $d/L = 0.6$ case, where further low speed recirculation was observed. The front vehicle at both $d/L = 0.4$ and 0.6 receives a 54% drag reduction compared to the isolated 25° Ahmed vehicle. This equates to a 2% increase and 12.6% reduction in drag coefficient re-

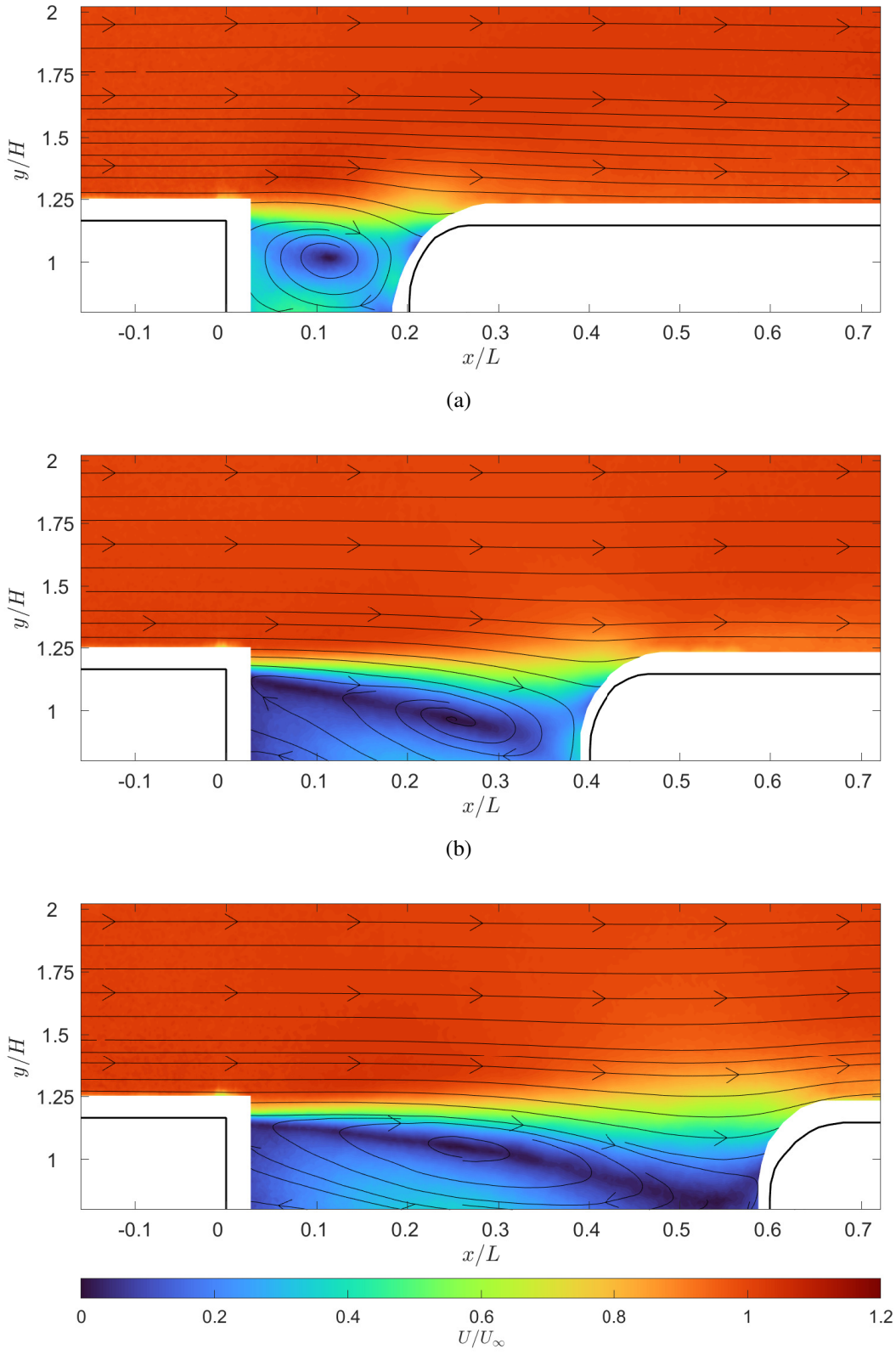

Figure 5.23: PIV images of normalised velocity magnitude field of a heterogeneous platoon of a squareback and 25° Ahmed vehicle at $d/L =$ (a) 0.2, (b) 0.4 and (c) 0.6. The freestream direction is from left to right.

spectively when compared to the baseline. It is difficult to say for certain the exact cause of the difference in drag coefficient between the $d/L = 0.2$ case and the $d/L = 0.4$ and 0.6 cases, however, the difference in the velocity of the recirculation is the only measurable difference obtained. It is clear that a more in depth study will be needed for this particular interaction to be fully understood.

As observed for the baseline case, the drag benefits provided by the platoon for the front vehicle gradually decrease as the inter-vehicle distance increases. In the baseline case, this drop in performance starts at $d/L = 0.4$ whereas for the heterogeneous platoon it is slightly delayed to $d/L = 0.6$. Presumably, this is as a result of the larger wake produced by the squareback vehicle allowing the platoon members to influence each other over a larger range of inter-vehicle distances. By $d/L = 1$, some normalised drag reduction still remains, however, it should be noted that this is no longer as a result of the platoon, but of the chosen normalisation, since in Figure 5.22 the drag of the squareback front vehicle is normalised with respect to an isolated 25° Ahmed vehicle. The squareback vehicle has, as expected based on the results of Ahmed et al. [1], a lower isolated drag coefficient when compared to the 25° Ahmed vehicle, and at long inter-vehicle distances, the drag of the front squareback vehicle is very close to the drag coefficient of a squareback Ahmed body in isolation (see table 5.10).

In the heterogeneous platoon, the rear vehicle is a 25° Ahmed vehicle as in the baseline case, which makes it possible to observe the effects of altering the front vehicle in a platoon and therefore the wake impinging on the rear vehicle. The most notable difference in the results compared to the baseline platoon is seen at $d/L = 0.2$. Although the rear vehicle experiences a drag increase in both the baseline and heterogeneous platoons, the rear vehicle performs significantly better when part of the heterogeneous platoon, experiencing only a 2.5% increase compared to the isolated case. In contrast, a 15.8% increase is observed for the rear vehicle in the baseline platoon. Figure 5.24 compares the flow fields for both cases. As previously discussed, the wake impingement plays a key role in increasing the drag for the rear vehicle. The alteration of the lead vehicle to a squareback shape ensures that the shear layer produced by the separated flow is stable and remains high over the rear vehicle. This in turn produces a more stable reattachment on the rear vehicle. Additionally, when compared to the baseline case, the removal of the rear slant prevents the free stream from being diverted down towards the leading edge of the rear vehicle. This significantly reduces the wake impingement resulting in a lower drag coefficient for the rear vehicle in the heterogeneous platoon when compared to the baseline case.

The improved structure in the wake of the lead squareback vehicle can be seen further in the vorticity field given in figure 5.25. The larger magnitude of vorticity in the heterogeneous case highlights the more structured wake. It is also clear that the vorticity caused due to the wake impingement of the wake onto the rear vehicle is higher on the leading edge of the rear vehicle in the heterogeneous case when compared to the baseline case.

When the inter-vehicle spacing is increased from $d/L = 0.2$ to $d/L = 0.4$, the drag coefficient

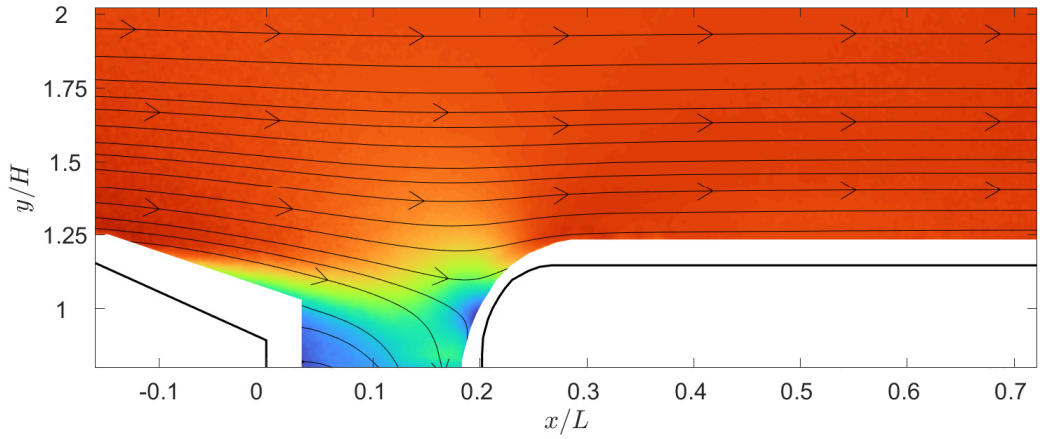

(a)

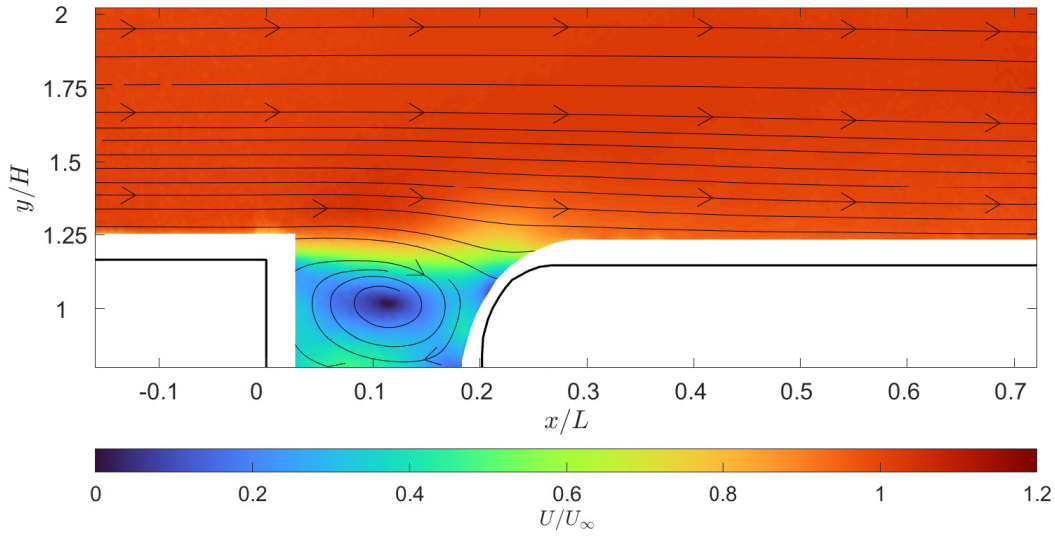

(b)

Figure 5.24: PIV images of normalised velocity magnitude field of the (a) baseline and (b) heterogeneous platoon of a squareback and 25° Ahmed vehicle at $d/L = 0.2$. The freestream direction is from left to right.

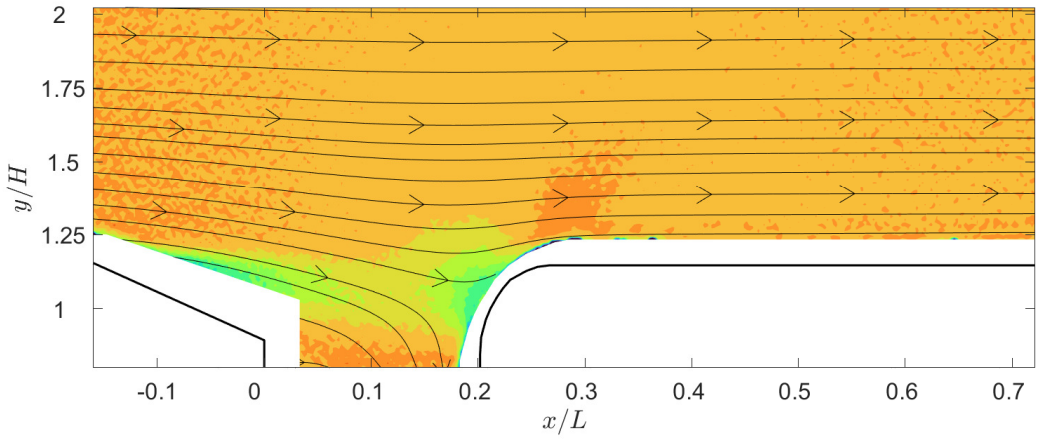

(a)

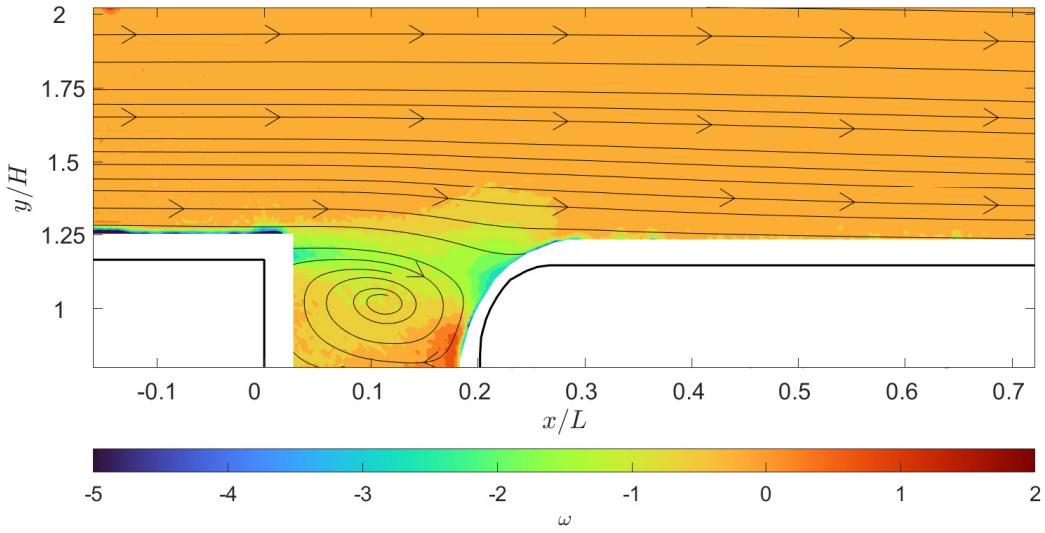

(b)

Figure 5.25: PIV images of ω_z of the (a) baseline and (b) heterogeneous platoon of a squareback and 25° Ahmed vehicle at $d/L = 0.2$. The freestream direction is from left to right.

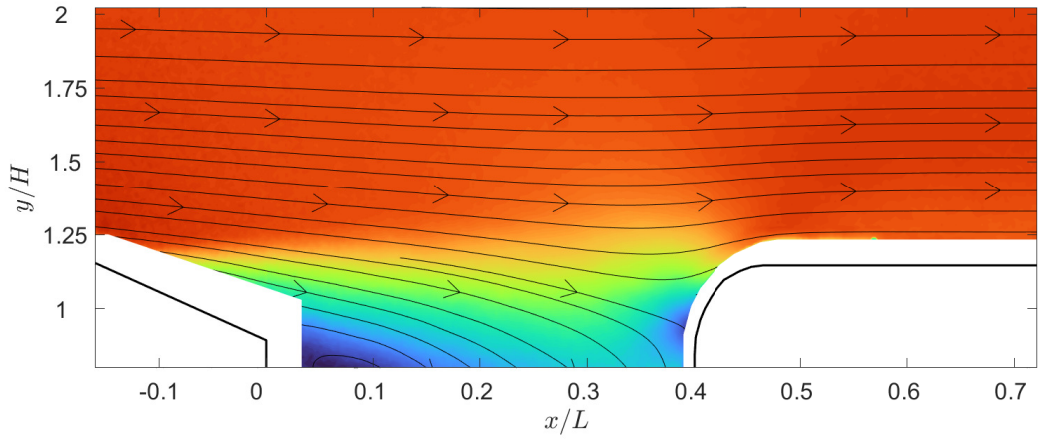

(a)

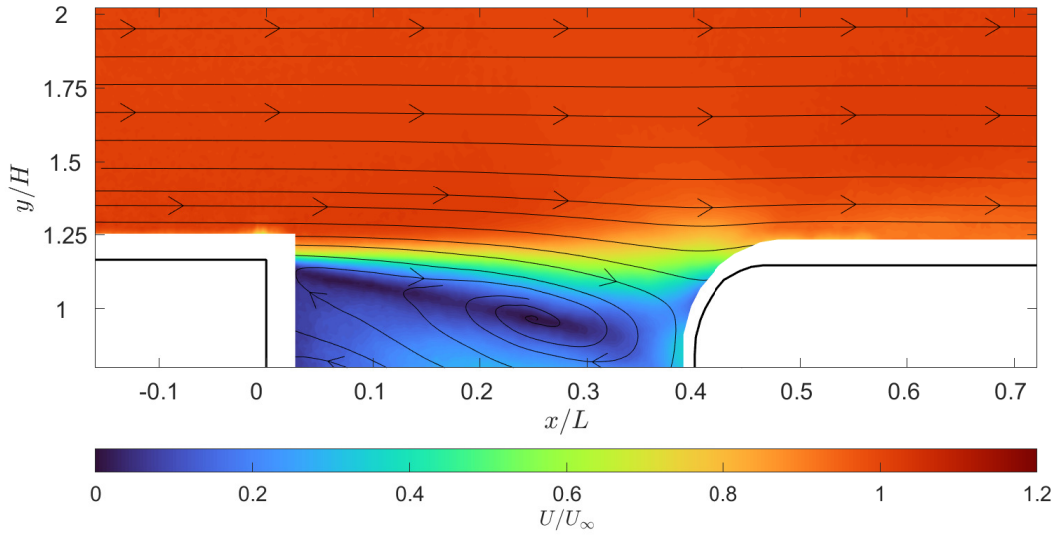

(b)

Figure 5.26: PIV images of normalised velocity magnitude field of the (a) baseline and (b) heterogeneous platoon of a squareback and 25° Ahmed vehicle at $d/L = 0.4$. The freestream direction is from left to right.

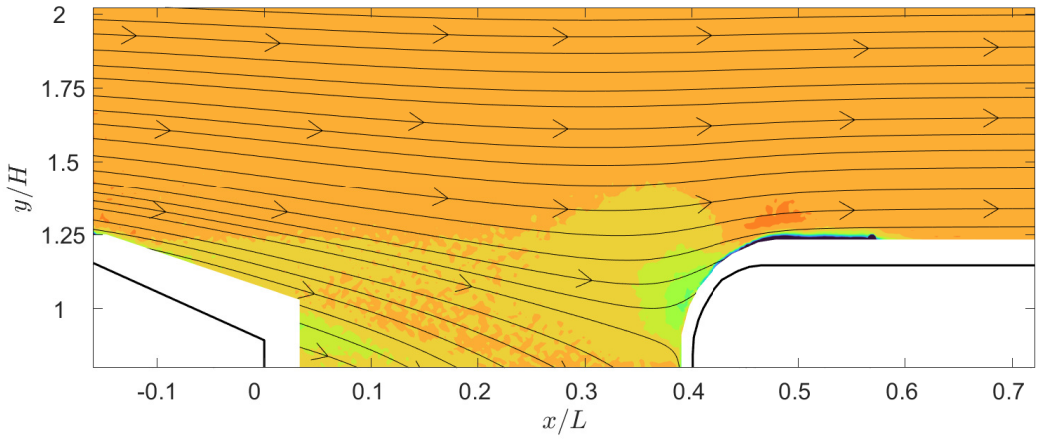

(a)

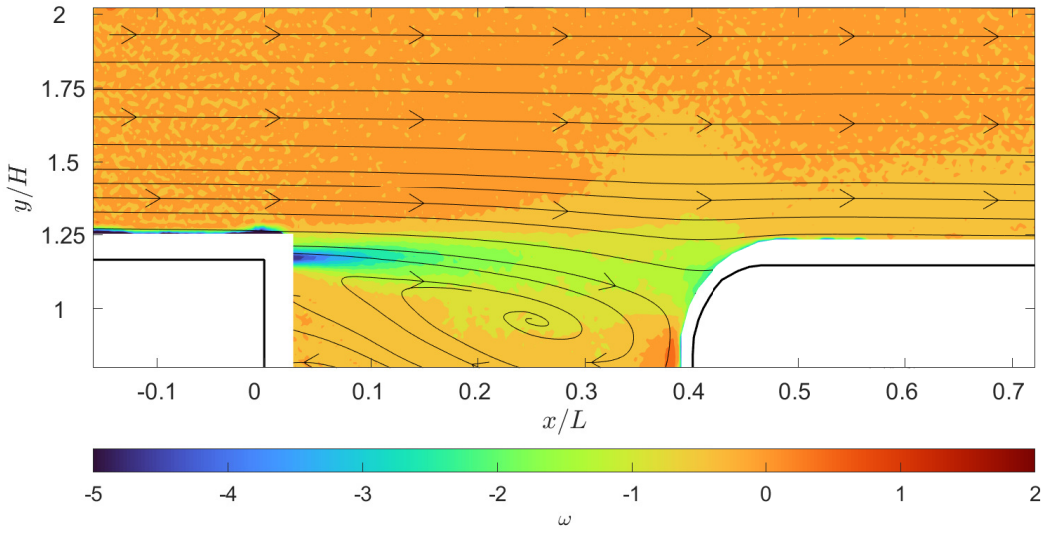

(b)

Figure 5.27: PIV images of ω_z of the (a) baseline and (b) heterogeneous platoon of a squareback and 25° Ahmed vehicle at $d/L = 0.4$. The freestream direction is from left to right.

of the rear vehicle increases sharply and the benefits of the presence of the squareback Ahmed body disappear. The flow fields for each case at $d/L = 0.4$ are compared in figure 5.26. It can be observed that the velocity magnitudes in the inter-vehicle gap are significantly smaller for the longer spacing when compared to the $d/L = 0.2$ cases. In addition, while for $d/L = 0.2$ the outer flow is not significantly disturbed over the inter-vehicle gap, increasing the distance between the vehicles results in an increasing impingement of the shear layer on the upper rounded leading edge of the rear vehicle. This is highlighted in the squareback case where the lower speed recirculation creates less distinction between the free stream flow and the flow in the inter-vehicle gap.

The magnitude of the vorticity in the wake of the heterogeneous case is also increased, both compared to the baseline case at $d/L = 0.4$ and the heterogeneous case at $d/L = 0.2$. In this case, the wake impinges directly onto the curved leading edge of the rear vehicle. The increased vorticity further disrupts the flow in this region resulting in increased drag for the rear vehicle.

As the vehicles move further apart, the rear vehicle of the heterogeneous platoon follows the same trend as the baseline platoon, but, on average, has a 5% higher drag coefficient than the baseline from $d/L = 0.6 - 1.0$. The larger wake created by the squareback vehicle means that the wake impingement of the shear layer persists further downstream, i.e., it impacts the platoon's behaviour more strongly for the longer spacing, and the increased vorticity results in more disruption of the flow over the leading edge of the rear vehicle at larger inter-vehicle distances.

Figure 5.28 shows how the drag coefficient changes with Reynolds number for the heterogeneous platoon. Similar to the baseline case, the values are normalised with respect to the drag coefficient measured at the highest Reynolds number for each case. As expected, the front vehicle shows a stronger Reynolds number dependency than the rear vehicle with the largest changes in drag coefficient occurring between $d/L = 0.2$ to 0.6. It can also be observed that, when the vehicle separation increases to $d/L = 0.8$ and beyond, there is a noticeable decrease in Reynolds number dependency.

The drag coefficient for the front vehicle is dominated by the incoming wind speed in the same way that it would be if it were an isolated vehicle. Despite this, it is clear that the rear vehicle also has some additional influence as Reynolds number changes. At shorter inter-vehicle distances of $d/L \leq 0.6$, the rear vehicle is situated within the wake of the front vehicle, disrupting the shear layer and recirculation region. As Reynolds number changes, the extent of this disruption also changes and makes the drag coefficient of the front vehicle more Reynolds number dependent for these cases. By $d/L = 0.8$ the rear vehicle has cleared the wake of the front vehicle and from here the Reynolds number dependency of the front vehicle is reduced.

The Reynolds number dependency of the rear vehicle can be split into three main regimes: When the vehicles are at their closest, varying Reynolds number has the biggest effect on the rear vehicle with a 10% increase from the highest Reynolds number case to the lowest Reynolds

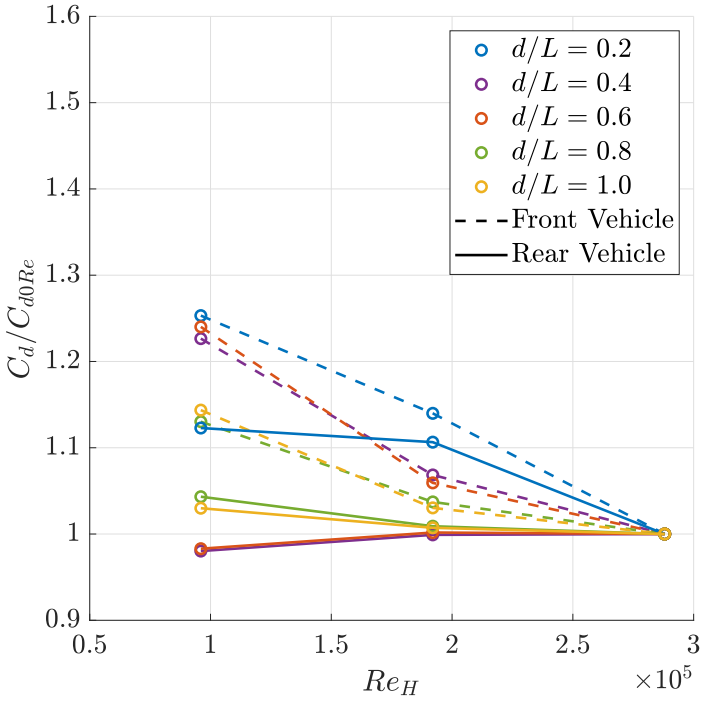

Figure 5.28: Reynolds number dependency of the drag coefficients in a heterogeneous platoon comprised of a 0° Ahmed front vehicle and a 25° Ahmed rear vehicle; the drag coefficients are normalised using the corresponding drag coefficient of each platoon member at the highest Reynolds number.

number case. At $d/L = 0.2$, the shear layer of the incident airflow interacting with the leading edge of the rear vehicle has a large effect on the drag coefficient for the vehicle as a whole. Although the location of flow detachment on the front vehicle is consistent across the range of Reynolds numbers, the energy in the shear layer and how it interacts with the rear vehicle changes considerably causing the rear vehicle to become more Reynolds number dependent at the shortest spacing.

When the distance between the vehicles is increased to $d/L = 0.4$ and 0.6, the rear vehicle becomes significantly less Reynolds number dependent. Instead of the increase in drag seen at shortest spacing, now a weak decrease in drag coefficient can be observed as Reynolds number decreases. As the vehicles move further apart, the incident flow becomes much more consistent across the range of Reynolds numbers, significantly reducing the Reynolds number dependency of the rear vehicle. This is more in line with what was seen in the baseline platoon and the study by Törnell et al. [18].

Another, final, regime change occurs once the inter-vehicle spacing reaches $d/L = 0.8$ and beyond. At this spacing the rear vehicle has left the influence of the wake produced by the front vehicle and begins to tend towards the Reynolds number dependency expected for a 25° Ahmed vehicle in isolation, i.e., the drag coefficient returns to a decrease with increasing *Re*. Nevertheless, the drag coefficient of the rear vehicle continues to be significantly less Reynolds number dependent than what would be expected for a typical 25° Ahmed vehicle in isolation.

5.3.4 Platoon with flow control

The previous section (section 5.3.3) explored how changing the geometry of the front vehicle in a two vehicle platoon changes the efficiency of the rear vehicle in the platoon. The baseline platoon of two 25° Ahmed vehicles showed clear inverted platooning conditions with the rear vehicle experiencing a considerable increase in drag. By simply changing the front vehicle from a Ahmed vehicle with a 25° rear slant to a squareback Ahmed vehicle, the drag of the rear vehicle at $d/L = 0.2$ was reduced by 11.5%. Whilst this reduction is a positive outcome, the rear vehicle still had a drag coefficient that was higher than under isolated conditions, i.e., the platoon continued to experience inverted platooning conditions. Furthermore, at larger inter-vehicle distances the heterogeneous platoon performed worse than the baseline platoon.

The main cause of these changes is the larger wake produced by the squareback vehicle. By diverting the shear layer higher over the curved portion of the leading edge of the rear vehicle. The wake impingement was reduced at the shortest inter-vehicle spacing, thus providing the reduced drag. If, instead of altering the entire geometry of the lead vehicle, it was possible to mimic the benefits of this behavior by adding a simple flap at the trailing edge of a 25° Ahmed vehicle, this would present a significantly more practical solution. In practice, the flap could be deployed to the appropriate angle depending on the inter-vehicle spacing in order to optimise performance for both vehicles in the platoon. In theory could also be stowed when the vehicle

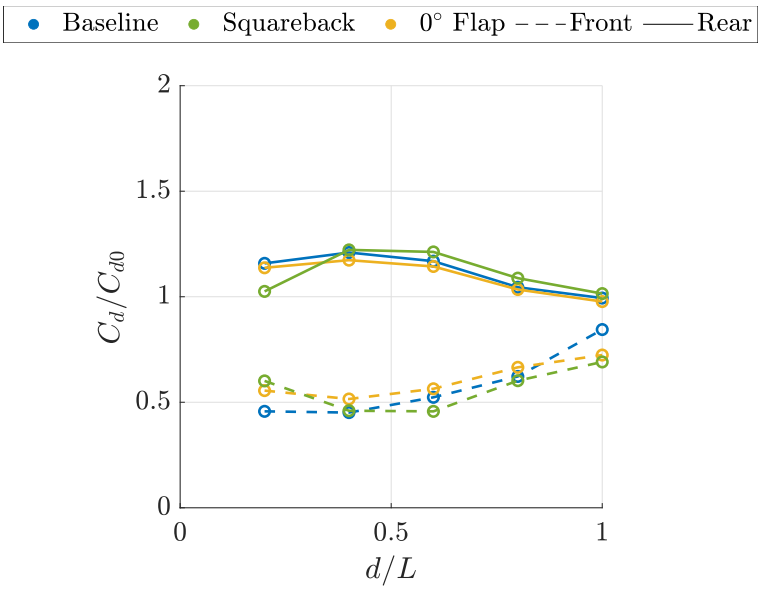

Figure 5.29: Normalised drag coefficient comparison of the baseline, squareback and 25*mm* 10° flap platoon cases.

is not travelling as part of a platoon, similar to modern road vehicles with deployable flaps as discussed in chapter 4.

To explore the efficacy of this concept, the front vehicle was equipped with a flap and a range of flap angles from $0° - 20°$ were tested using two different flaps of length 10*mm* and 25*mm* (corresponding to $0.019L$ and $0.048L$). The different flap lengths were included to also cover flap-length dependency. The drag coefficients for each test case discussed in this chapter are given in tables 5.7, 5.8 and 5.9.

Figure 5.29 compares the results of a 25*mm* flap at 0° to the heterogeneous (squareback) and baseline cases. The most noticeable property in the results provided is that the addition of the flap to the front vehicle is not sufficient to change the raw characteristic of the platoon and inverted platooning conditions still persist.

The largest differences between cases is seen in the front vehicle. The front vehicle with flap is mostly unaffected by the presence of the rear vehicle with a 23% difference between the maximum and minimum normalised drag coefficients over the entire range of inter-vehicle distances tested. This is a significantly lower inter-vehicle spacing dependency than for the baseline case which changes by 46% and the squareback case that changes by 34% over the same region. There are two main reasons for this, primarily, the introduction of the flap provides a sharp point for flow separation resulting in a more consistent wake for all separation distances. The second reason is related to the location of the flap. Whilst the squareback Ahmed vehicle also provides a sharp flow separation point, this occurs at the base of the vehicle. In the case of the 25° Ahmed vehicle with a flap, the separation occurs at the top of the rear slant, some $0.19L$ (100*mm*) upstream of the vehicle's base. The standoff distance of the flap allows the front vehicle to be much less affected by the presence of the rear vehicle.

d/L	Isolation	0.2	0.4	0.6	0.8	1.0
$25°Ahmed$	0.388	0.176	0.174	0.201	0.239	0.325
squareback	0.269	0.233	0.178	0.177	0.234	0.268
$25mm$, $10°$ Flap	0.353	0.215	0.200	0.219	0.258	0.281

Table 5.11: Drag coefficient measurements for the front vehicle in isolation and in the baseline, squareback and $25mm$, $10°$ flap platoons over a range of inter-vehicle distances at $Re = 2.88 \times 10^5$

Whilst the flap case is less affected by the rear vehicle than in other cases, it also obtains less of a benefit when compared to the front vehicle in other two cases. The presence of the rear vehicle helps to increase the base pressure of the front vehicle and promotes flow separation. The combination of these effects is the main factor resulting in the reduction in drag for the front vehicle in the baseline platoon. When a flap is installed, flow separation is no longer induced by the rear vehicle but instead caused by the flap itself, thus negating some of the benefits provided by the rear vehicle. This contributes to the front vehicle performing consistently worse compared to the squareback case and only better than the baseline platoon at the largest inter-vehicle spacing ($d/L = 1.0$).

Table 5.11 gives the drag coefficients for each of the front vehicles in isolation and as part of a platoon. Interestingly, it was observed that at $d/L = 1.0$ the $25°$ Ahmed and flap cases were still receiving some distant benefit from the platoon. In contrast, the drag coefficient of the squareback case at the same distance is equal to its isolated drag coefficient. Of the three cases, the squareback vehicle produces the longest wake. It is therefore unusual that this, of all the lead vehicles considered, is the one least affected by the rear-vehicle at the longest inter-vehicle spacing. Additionally, it also has the lowest drag coefficient at this distance, of the three cases, meaning it is simultaneously the worst option in terms of drag savings and the best option in terms of individual efficiency.

When analysing the rear vehicle's drag coefficient, the difference between the three cases is more subtle. At $d/L = 0.2$ the flap case achieves a similar result to the baseline platoon. This is highlighted in figure 5.30, where it is evident that the flap is promoting flow separation. The flap also creates an area of high vorticity at the point of separation, seen in figure 5.31, however, this does not translate into a stable recirculation region as seen in the wake of the squareback vehicle in the heterogeneous platoon. Whilst the flap is inducing more separation than the baseline case, this fundamentally does not solve the wake impingement problem. It is clear from analysing the location of stagnation on the leading edge of the rear vehicle, that the shear layer produced by the lead vehicle continues to impinge on the rounded leading edge of the rear vehicle. This interaction disrupts the pressure recovery mechanism in this area and resulting in an increase in drag for the rear vehicle.

As the vehicles move further apart, the effectiveness of the flap is mostly unchanged. Over the full range of inter-vehicle distances tested, the rear vehicle in the platoon with flow control

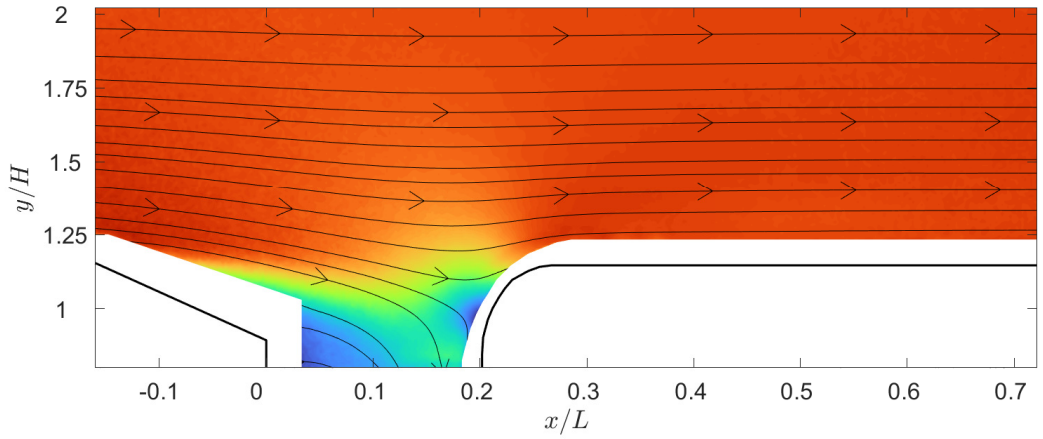

(a)

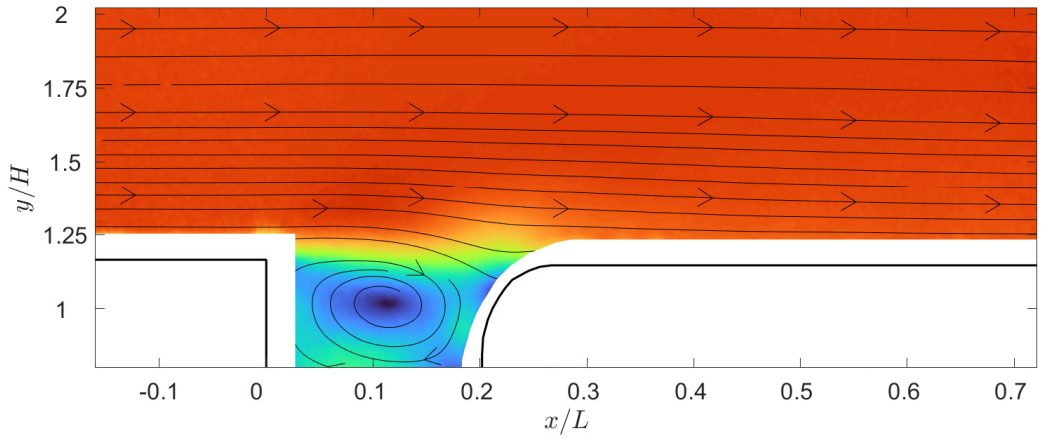

(b)

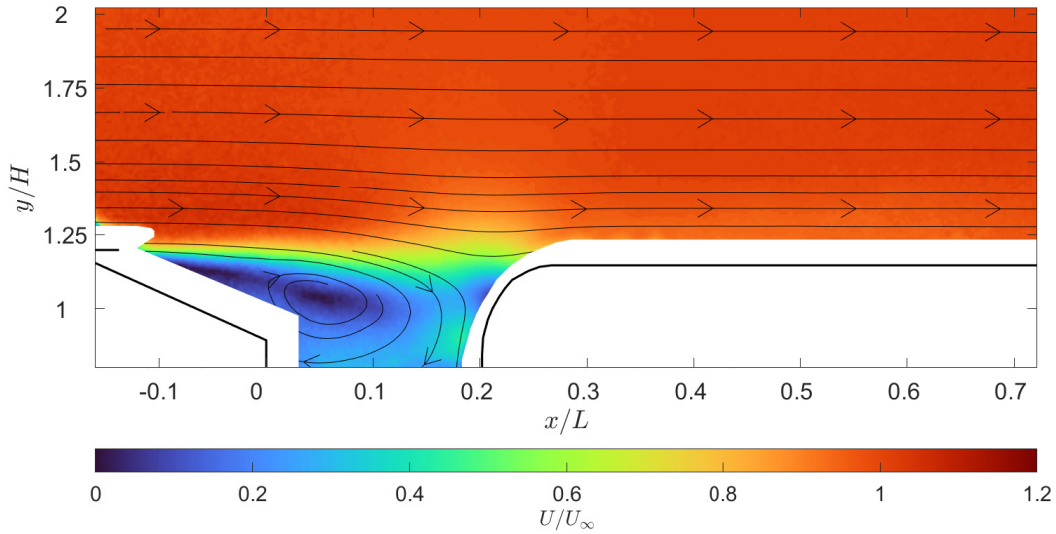

(c)

Figure 5.30: PIV images for comparing normalised velocity magnitude field of the (a) baseline (b) squareback/ heterogeneous and (c) 20*mm* 0° flap platoons at $d/L = 0.2$. Flow goes from left to right

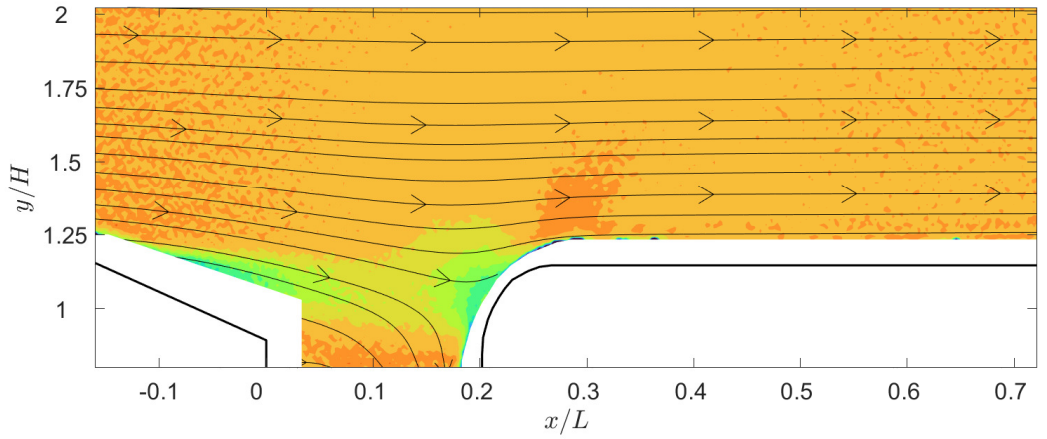

(a)

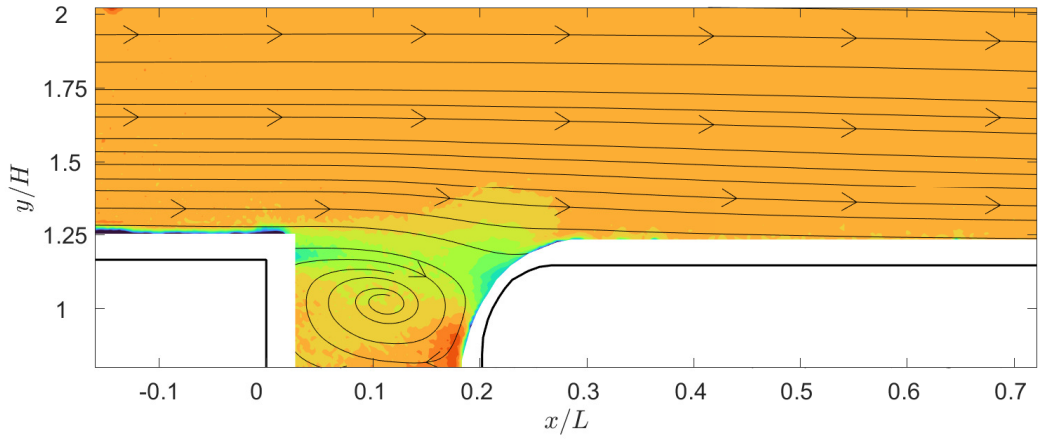

(b)

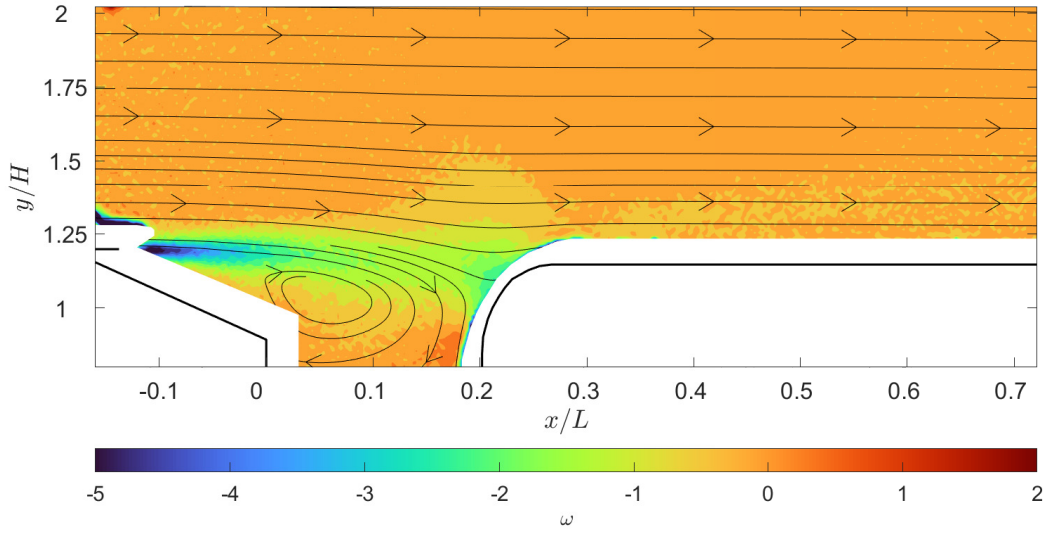

(c)

Figure 5.31: PIV images for comparing the ω_z of the (a) baseline (b) squareback/ heterogeneous and (c) 20*mm* 0° flap platoons at $d/L = 0.2$. Flow goes from left to right

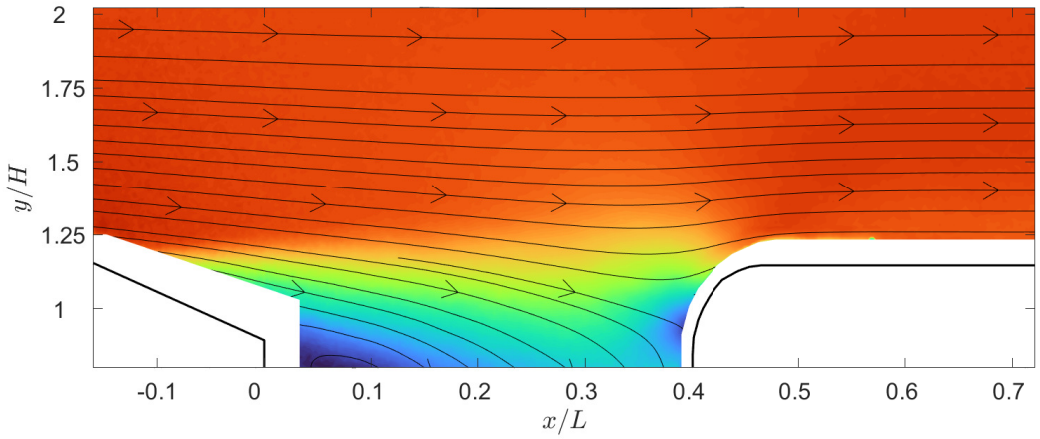

(a)

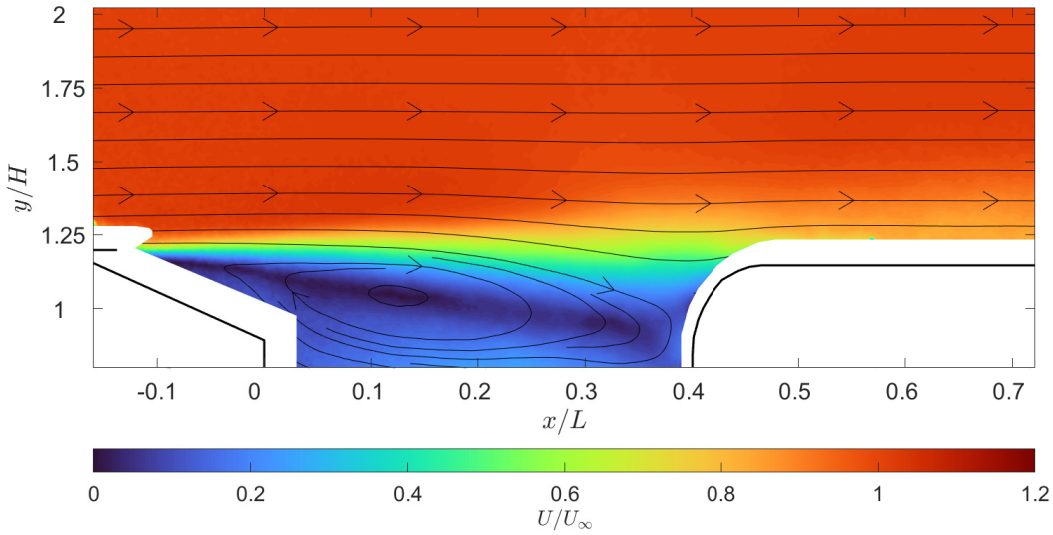

(b)

Figure 5.32: PIV images for comparing normalised velocity magnitude field of the (a) baseline and (b) 20*mm* 0° flap platoons at $d/L = 0.4$. Flow goes from left to right

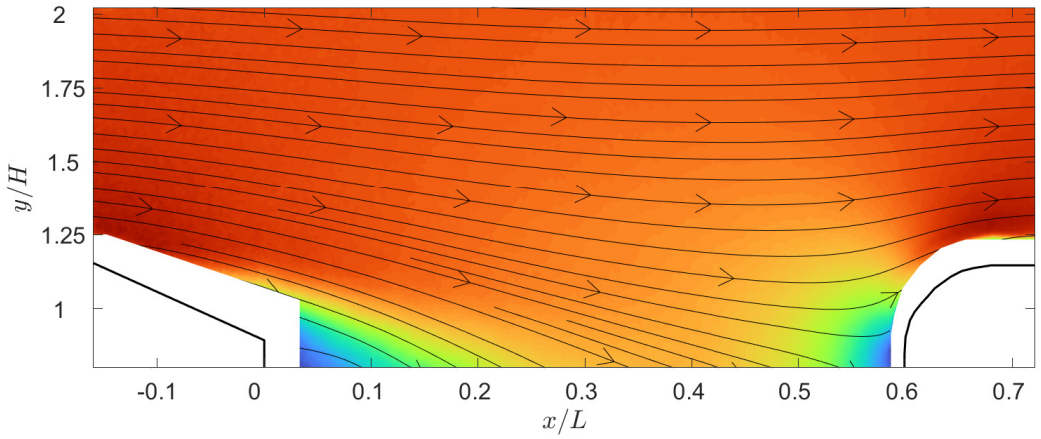

(a)

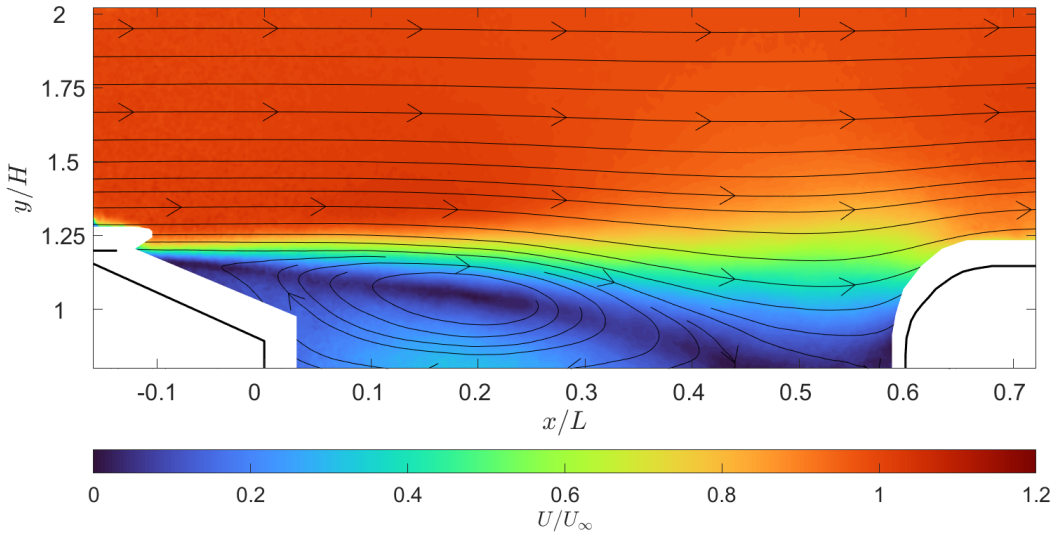

(b)

Figure 5.33: PIV images for comparing normalised velocity magnitude field of the (a) baseline and (b) 20*mm* 0° flap platoons at $d/L = 0.6$. Flow goes from left to right

has a drag coefficient $2-3\%$ lower than the baseline case with a peak of at $d/L = 0.4$.

Figures 5.32 and 5.33 show comparisons of the baseline and flap cases for $d/L = 0.4$ and 0.6 respectively. The flow fields look remarkably different making it surprising that the drag measurements remain so similar. The large wake created by the flap reduces the inflow velocity on the flat, front surface of the rear vehicle which, in theory, should lower its drag coefficient. In addition, at these inter-vehicle distances the flap creates a much more unstable shear layer. This significantly disrupts the flow over the curved surface of the leading edge of the rear vehicle. As discussed previously, a large portion of the pressure recovery for the rear vehicle is generated by accelerating the flow over this curved surface. Thus, disrupting the flow in this region could significantly reduce the aerodynamic efficiency of the rear vehicle. Whilst it cannot be said for certain, it can be hypothesised that this trade-off results in both rear vehicles having a similar net drag coefficient despite the very different flow properties in the inter-vehicle gap.

At inter-vehicle distances of $d/L = 0.8$ and beyond, the rear vehicle is no longer positioned in the recirculation region of the front vehicle. Whilst there are still some distant platooning effects, as seen with the previous platoons, the drag coefficient of the rear vehicle in the platoon with flow control begins to return to a similar value as that of an isolated vehicle.

5.3.5 Investigation of additional flap settings

Throughout this thesis a case has been built that suggested wake impingement on the curved leading edge of the rear vehicle results in an increase in drag coefficient for the rear vehicle. By introducing a flap at the top of the trailing edge slant of the front vehicle, it was shown that the shear layer can be deflected over the rear vehicle, reducing wake impingement and improving the efficiency of the platoon at short inter-vehicle distances. Whilst some success was seen when using a flap to improve the efficiency of the baseline platoon, in general, the influence of the flap was lower than expected.

In this section, the influence of flap angle and flap length is investigated to fully characterise the effectiveness of using a flap as a flow control device in a platooning environment. In the first part of this section, the platoon with a 25*mm* flap is compared to the baseline case for three different flap angles, 0°, 10°, and 20°. Specific emphasis is placed on the mechanisms causing increased or decreased drag. Further information on the Reynolds number dependency of the 25*mm* flap can be found in appendix C. In the second part of this section, the influence of flap length is investigated to establish how much authority a smaller (and thus less intrusive) flap has on the flow when attempting to modify the wake in a similar way. The drag coefficients for each test case discussed in this chapter are given in tables 5.7, 5.8 and 5.9.

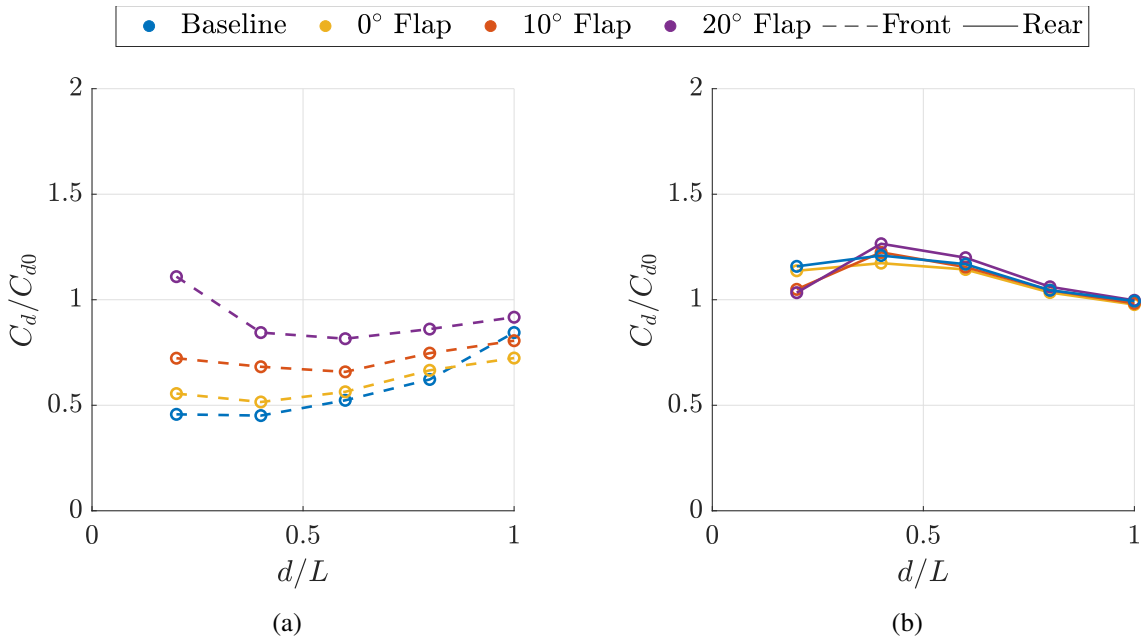

Figure 5.34: Comparison of normalised drag coefficient between the baseline platoon and the platoon with flow control for a range of flap angles over a range of inter-vehicle distances. (a) Front vehicle in the platoon; (b) Rear vehicle in the platoon

Large flap

Figure 5.34 shows a comparison between the normalised drag coefficient of the baseline case and the three flap cases (flap angles 0°, 10°, and 20°). Each case was normalised with respect to an isolated 25° Ahmed vehicle to allow for a direct comparison between cases.

The drag coefficient of the front vehicle increases as the flap angle is increased and, for all inter-vehicle distances less than $d/L = 1.0$, is greater than in the baseline case. As discussed previously, the drag reduction of the front vehicle in the baseline case is a result of the increase in base pressure produced by the presence of the rear vehicle. This base pressure also results in flow separation further lowering the drag coefficient. The addition of the flap also causes the flow to separate over the trailing edge of the front vehicle. Whilst this provides some drag reduction when compared to an isolated Ahmed vehicle, it is less efficient than the baseline case.

While in most cases, the front vehicle with flap still achieves a drag reduction compared to an isolated 25° Ahmed vehicle, at $d/L = 0.2$ the 20° flap setting results in an increase in drag compared to isolated conditions. In this case, the flap protrudes too far into the free-stream leading to an increase in drag.

As the vehicles move further apart, the drag coefficient of the front vehicle with a flap follows a similar trend to the baseline case, slowly tending towards a constant drag coefficient as platooning effects are reduced. By $d/L = 1.0$ the addition of 0° and 10° flaps result in a 4.6% and 14.3% drag decrease respectively from the baseline case and a 19.4% and 27.6% reduction in drag respectively when compared to an isolated Ahmed vehicle. This is primarily due

to the flow separation induced by the flap and no longer an effect of platooning. Flaps have already been shown to be useful tools to help reduce the drag of an isolated 25° Ahmed vehicle [56, 62–64], something discussed in depth in section 2.2.1. Despite this, the lead vehicle in the 20° flap case continues to perform worse than the baseline with a drag increase of 8.6% compared to the baseline at $d/L = 1.0$.

The drag coefficients of the rear vehicle in the platoon are also shown in figure 5.34. At $d/L = 0.2$ the 0° flap case has a drag reduction of 1.8% when compared to the baseline case, with the 10° and 20° cases having a drag reduction of 9.4% and 10.8% respectively. The flow fields of the baseline, 0° and 20° cases at $d/L = 0.2$ are compared in figure 5.35. Here the variation in wake impingement between the three cases can be observed. For the baseline and 0° cases, the free stream is pulled down by the trailing edge slant and the shear layer impinges on the curved leading edge of the rear vehicle. Some of the flow is then diverted over the leading edge whilst the rest is forced down under the rear vehicle. This produces a small stagnation region visible as low velocity flow on the rounded leading edge of the rear vehicle. Overall, the wake impingement results in an increase in drag when compared to the isolated case.

In contrast, the flap in the 10° and 20° cases divert the shear layer over the curved section of the leading edge of the rear vehicle. This improves the efficiency of the rear vehicle when compared to the baseline case. However, it is still not sufficient to result in a drag reduction for the rear vehicle when compared to a vehicle in isolation. One of the key aims for this piece of work was to incorporate flow control into a platoon with the intention of alleviating or eliminating inverted platooning conditions. The platoon utilising a 20° flap on the lead vehicle was the closest result to full elimination of inverted conditions. This setup resulted in 3.3% drag increase for the rear vehicle when compared to an isolated Ahmed vehicle at $d/L = 0.2$, which is a significantly lower drag increase than observed in the baseline platoon.

As the inter-vehicle spacing is increased from $d/L = 0.2$ to $d/L = 0.4$, the best performing configuration changes. Here the 0° case has the lowest drag coefficient, with a drag reduction of 3% when compared to the baseline platoon. The 10° case matches the baseline case and the 20° results in a drag increase of 4.6% when compared to the baseline platoon. Again, this variation in drag stems from wake interactions and the way the wake from the front vehicle impinges on the rear vehicle. What is interesting here is how the effectiveness of each flap angle is almost opposite to the $d/L = 0.2$ results.

More light can be shed on this from analysing the flow fields shown in figure 5.36. For the baseline case, a thick shear layer can be seen to interact with the rounded leading edge of the rear vehicle. In contrast, the 0° case has a much more precise separation point resulting in a thinner shear layer. This, in turn, leads to lower velocity wake impingement on the rear vehicle. Both of these cases have a drag increase when compared to an isolated Ahmed vehicle. However, the smaller shear layer and lower velocity wake impingement seen in the 0° flap case has a slightly lower effect on the pressure recovery mechanism over the rounded leading edge

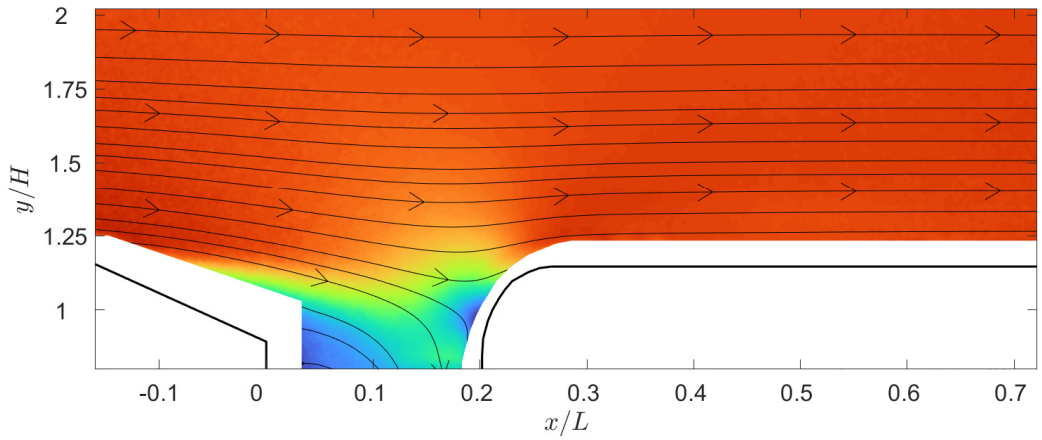

(a)

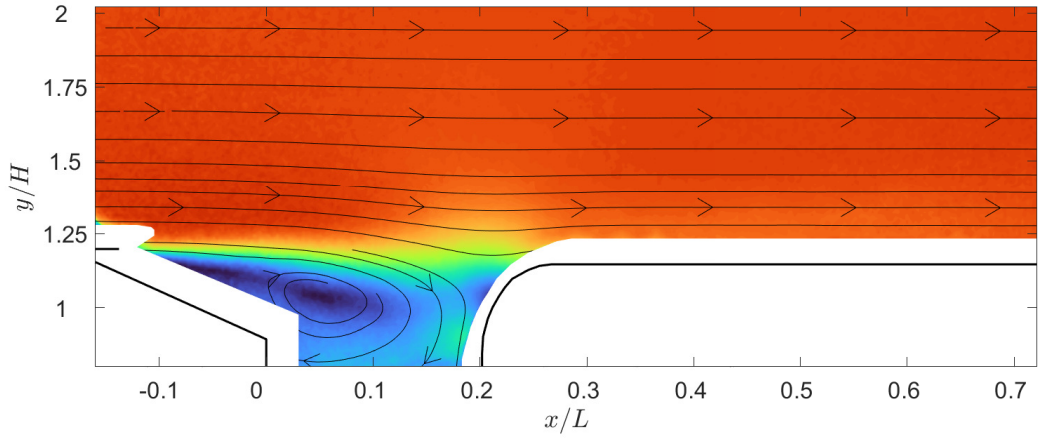

(b)

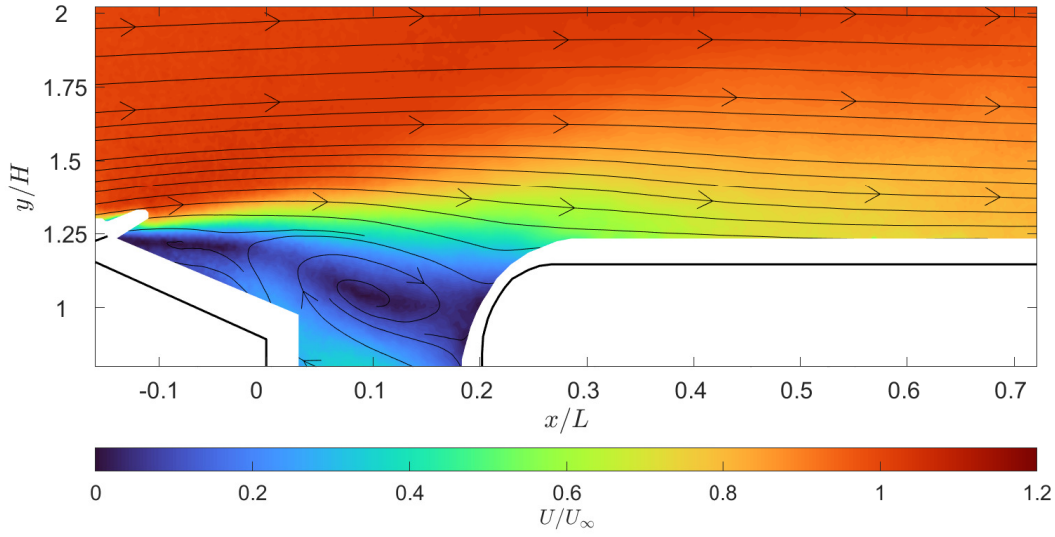

(c)

Figure 5.35: PIV images of the (a) baseline; (b) 0° Flap; (c) 20° Flap platoon at $d/L = 0.2$ for the large, 25*mm*, flap. Flow goes from left to right.

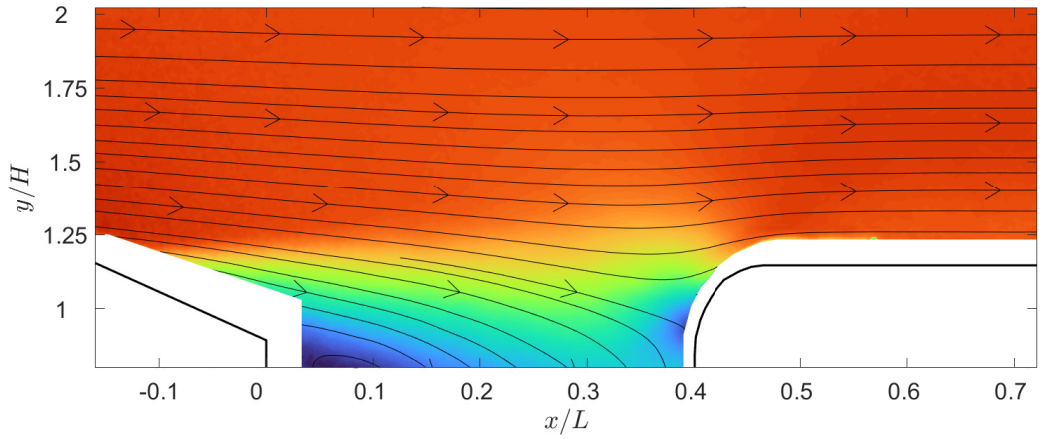

(a)

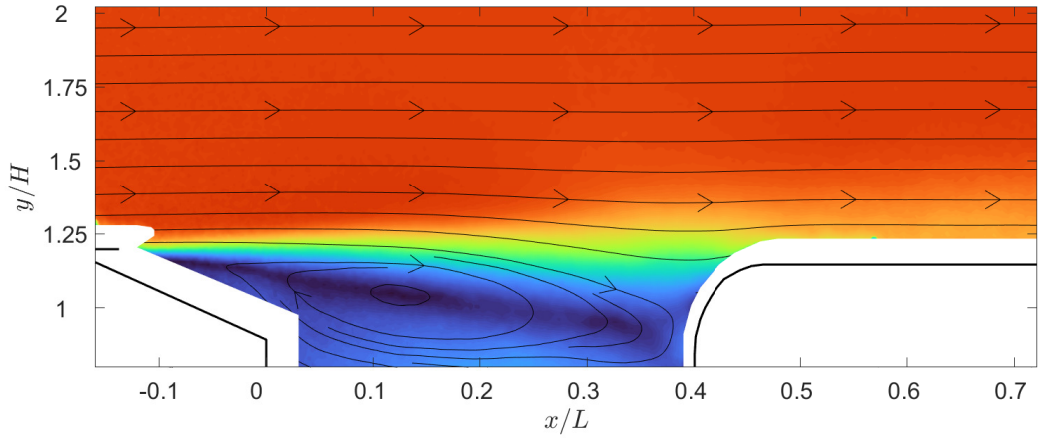

(b)

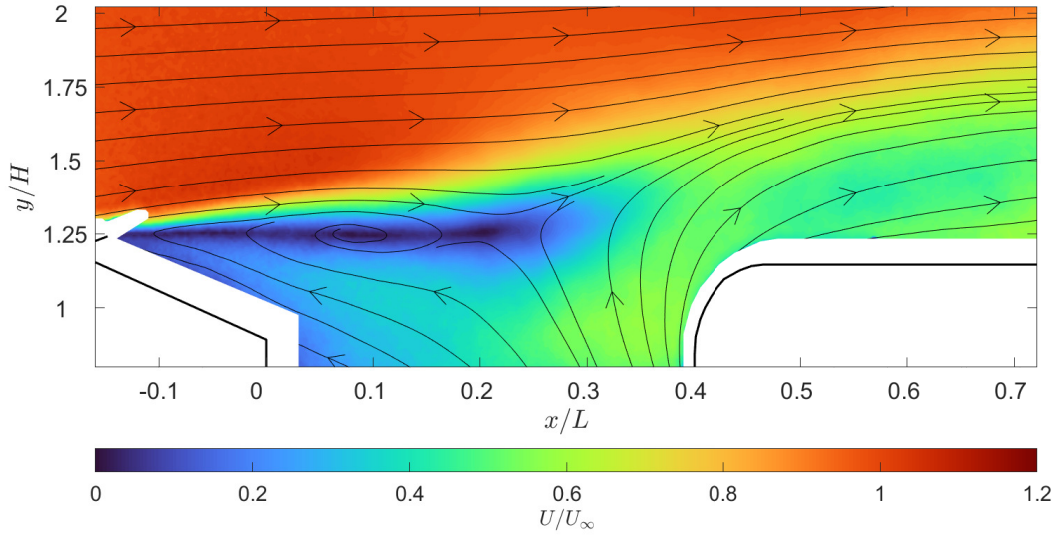

(c)

Figure 5.36: PIV images of normalised velocity magnitude for the (a) baseline; (b) 0° Flap; (c) 20° Flap platoon at $d/L = 0.4$ for the large, 25*mm*, flap. Flow goes from left to right

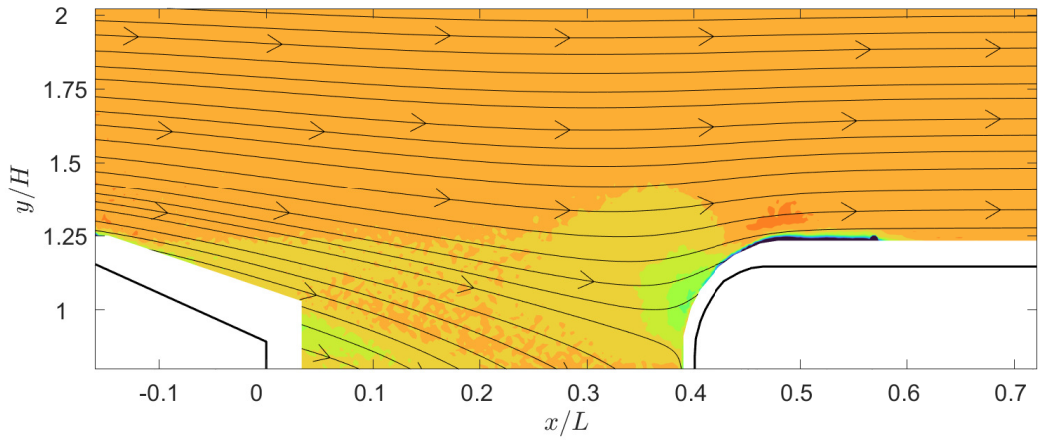

(a)

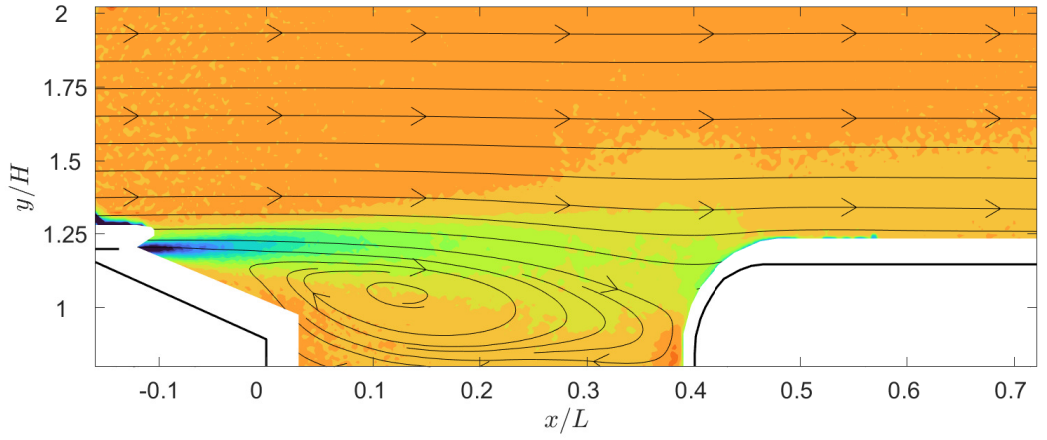

(b)

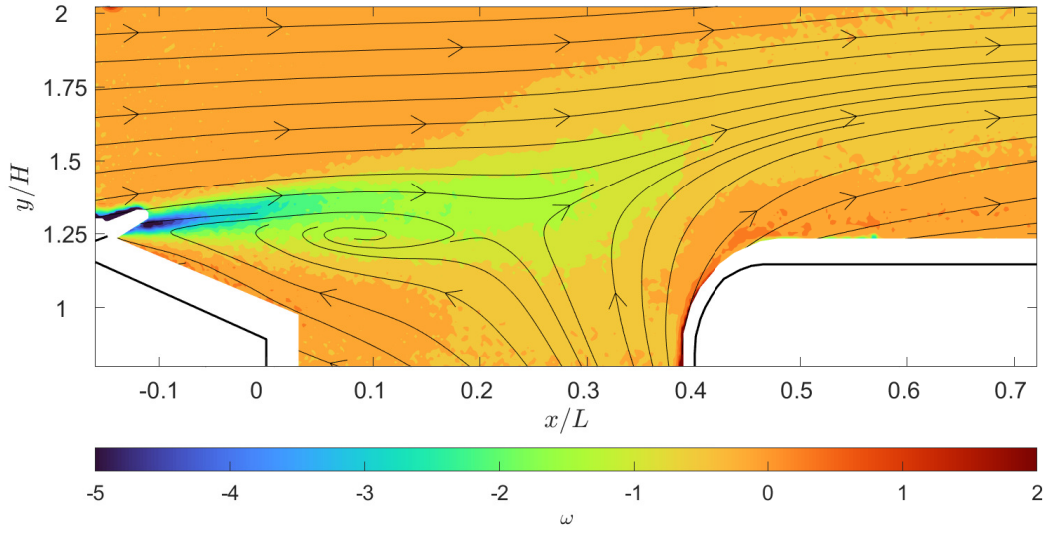

(c)

Figure 5.37: PIV images of ω_z for the (a) baseline; (b) 0° Flap; (c) 20° Flap platoon at $d/L = 0.4$ for the large, 25*mm*, flap. Flow goes from left to right

of the rear vehicle making it perform better than the baseline platooning case at this spacing. This can be seen in the increased vorticity on the rounded leading edge of the rear vehicle in the baseline case when compared to the two flap cases seen in figure 5.37. This increased vorticity indicates that the flow is fully attached to the surface and is being accelerated around the curved section of the leading edge providing increased pressure recovery.

The flow of the 20° flap case at $d/L = 0.4$ is extremely unsteady. In figure 5.36 the flap can be seen to significantly increase the thickness of the shear layer. This unstable flow structure has a negative effect on the rear vehicle and produces an increase in drag when compared to the baseline platoon.

As the vehicles move further apart the platooning effects slowly reduce. Figure 5.38 shows the flow fields for the baseline, 0° and 20° flap cases at $d/L = 0.8$. At this distance the drag coefficients for the rear vehicle of all of the cases are separated by only 2%. Despite this, the wake structure and therefore inflow for the rear vehicle remain quite different. For the baseline case, the flow has reattached over the trailing edge slant, but for the flap cases the flow remains separated. This lowers the velocity of the inflow and, in theory, should lower the drag coefficient of the rear vehicle. It is suspected that some residual unsteadiness in the flow counteracts the benefits of the reduced inflow velocity. The addition of pressure readings on the rear vehicle would provide a clearer picture in the future. Whilst the flap cases induce higher vorticity into the flow (see figure 5.39 this has mostly dissipated by $d/L = 0.7$ and will have little effect on the drag coefficient of the rear vehicle at larger inter-vehicle distances.

Finally, by $d/L = 1.0$ the inter-vehicle distance is sufficiently large to negate all platooning effects for the rear vehicle with all cases tending towards a normalised drag coefficient of 1.

Small flap

In this section, results for a smaller length of flap at the same three angles tested previously will be discussed to ascertain the effect of flap length on the efficiency of this flow control device. The mechanisms for increasing and decreasing drag on each vehicle in the platoon were already discussed above. Therefore, this section focuses more on the differences between the flap configurations as opposed to the absolute effectiveness of the platoon.

Figure 5.40 shows a comparison of the normalised drag coefficient for each vehicle in the platoon over the range of flap settings tested. An interesting observation is that, when the flap is mounted horizontal (i.e., at 0°), flap length has very little effect on the results of the platoon. The front vehicle in the small flap platoon is slightly more efficient whereas the rear vehicle is slightly less efficient than in the larger flap platoon. The reasoning for this becomes more clear when considering the cases with higher flap angles since a stronger flap-length dependency of the results can be observed. As previously mentioned, shear layer interactions on the rear vehicle are the big driving force behind inverted platooning conditions. When the flap is set at a positive angle (i.e., $> 0°$) the longer flap protrudes further into the free stream. In essence, this essentially

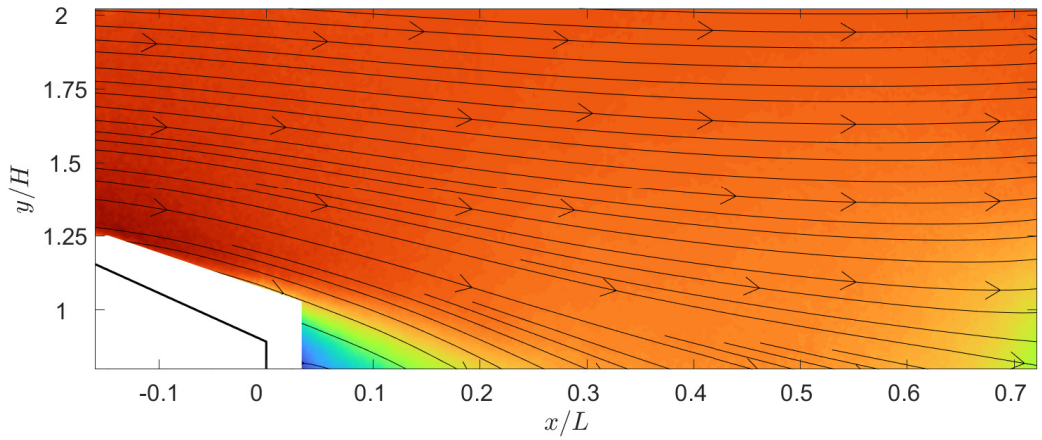

(a)

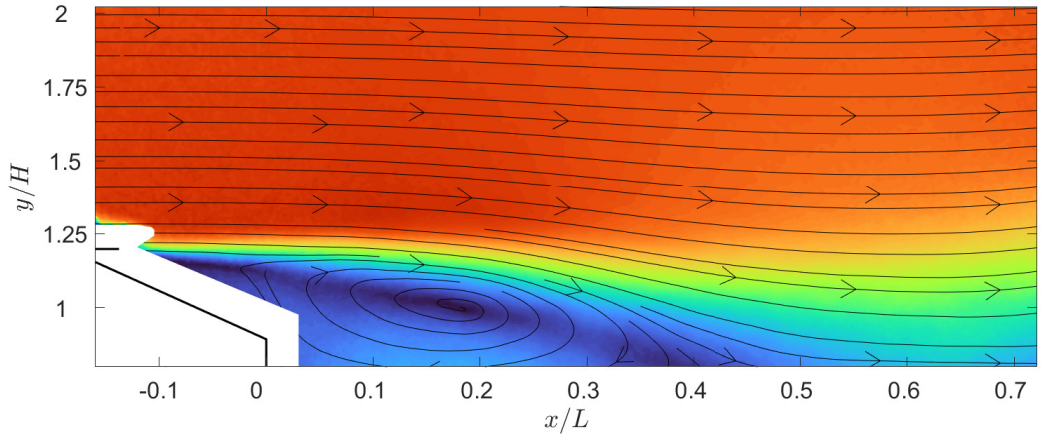

(b)

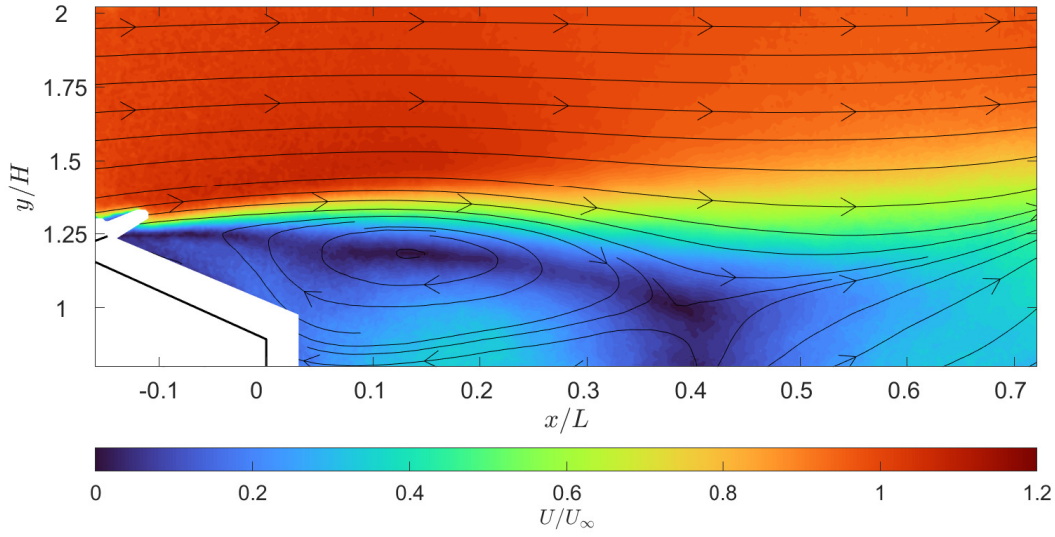

(c)

Figure 5.38: PIV images of the (a) baseline; (b) 0° Flap; (c) 20° Flap platoon at $d/L = 0.8$. here, a flap length of 25*mm* was used. Flow goes from left to right.

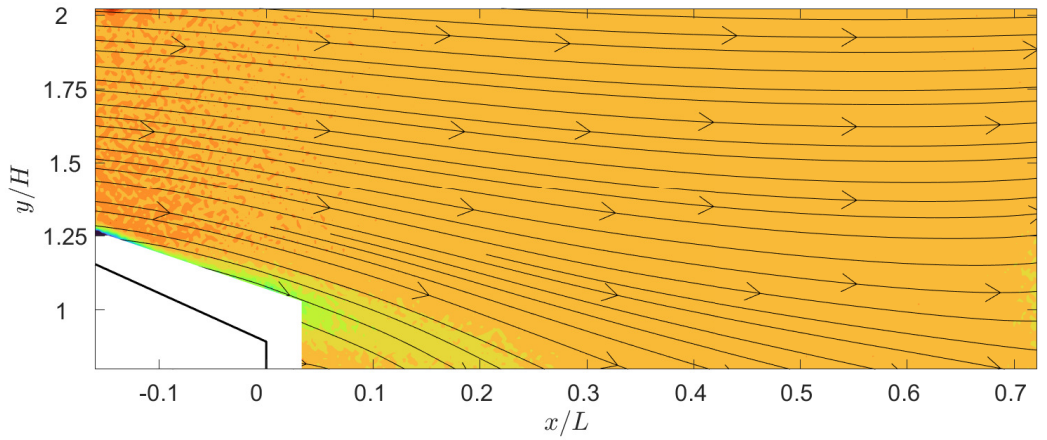

(a)

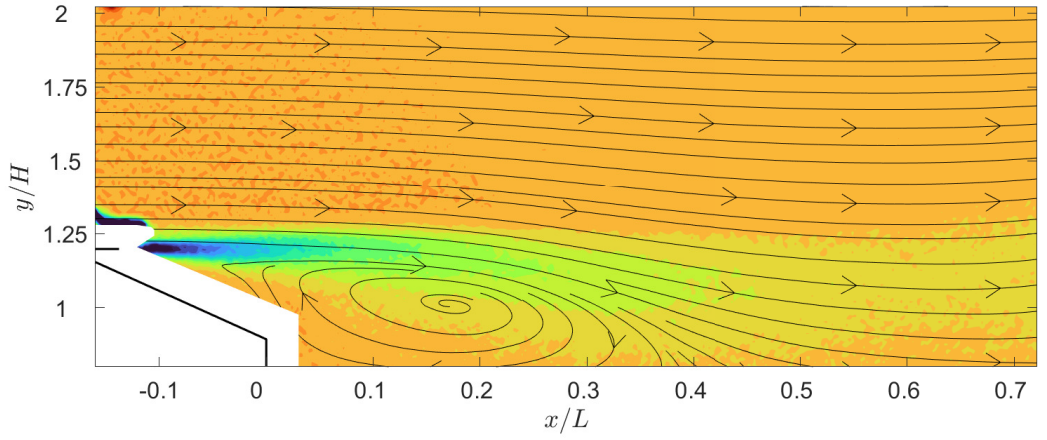

(b)

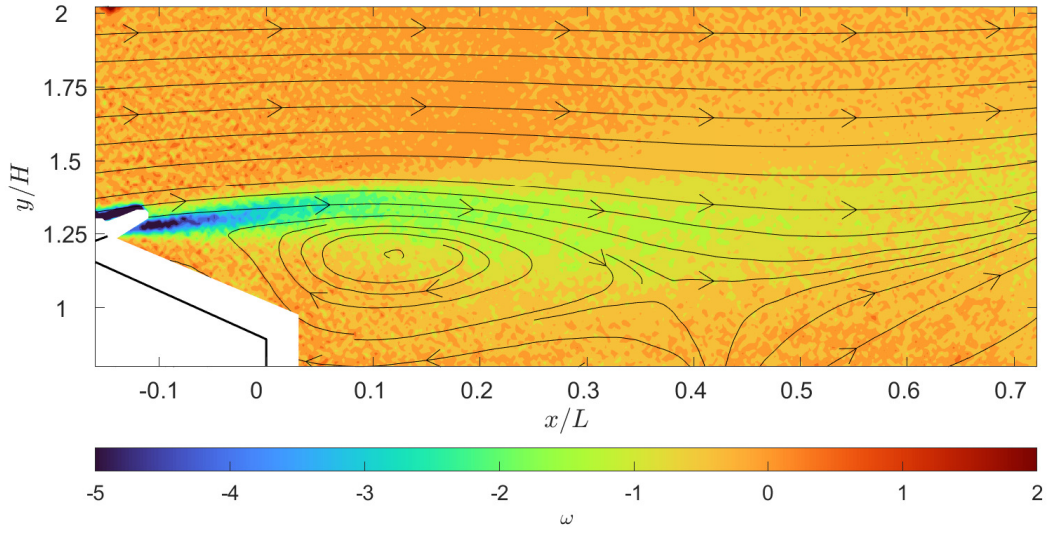

(c)

Figure 5.39: PIV images of ω_z for the (a) baseline; (b) 0° Flap; (c) 20° Flap platoon at $d/L = 0.8$ for the large, 25*mm*, flap. Flow goes from left to right

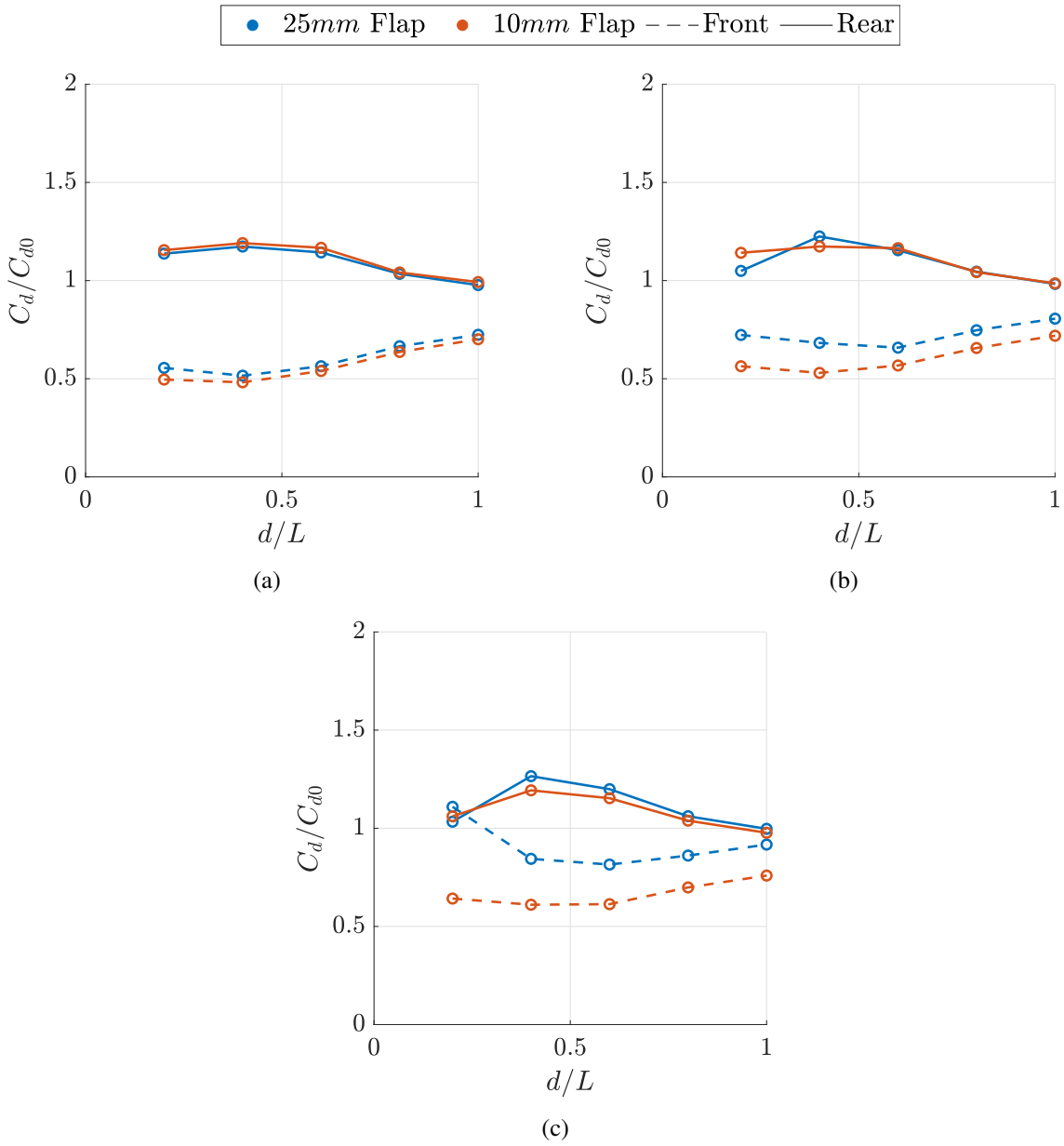

Figure 5.40: Comparison of normalised drag coefficient between the 25*mm* flap platoon and the 10*mm* flap platoon for a range of flap angles over a range of inter-vehicle distances. (a) 0°; (b) 10°; (c) 20°

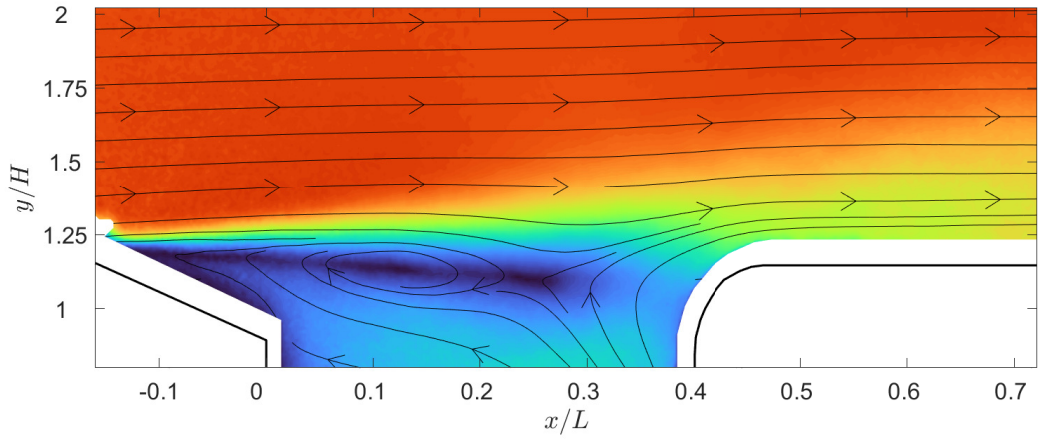

(a)

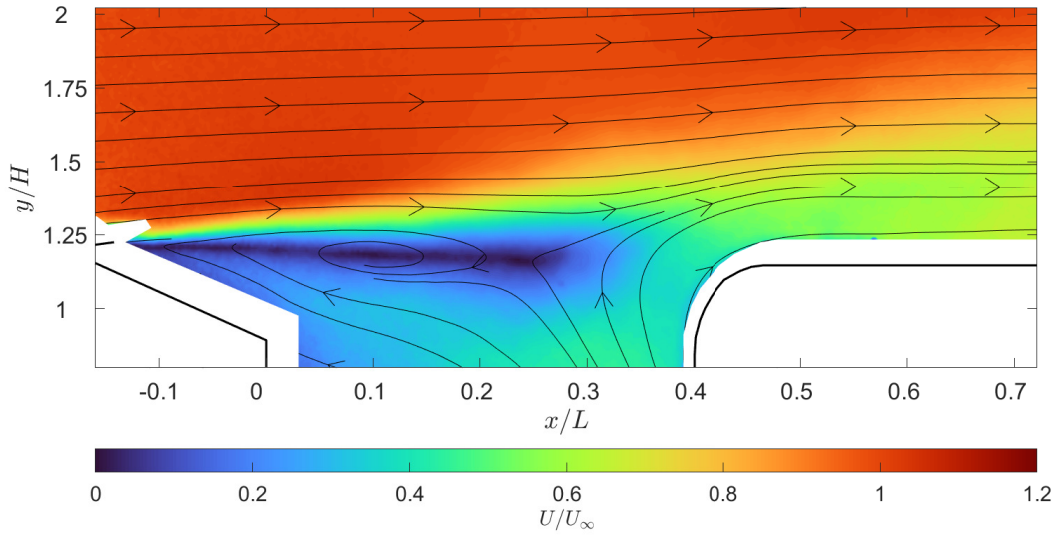

(b)

Figure 5.41: PIV images of the (a) small/10*mm*; (b) large/25*mm* Flap platoon at 10°, $d/L = 0.4$ and $Re_H = 2.88 \times 10^5$. Flow goes from left to right

raises the location of flow detachment at the trailing edge of the front vehicle and, as a result, extends the length of the wake and raises the height of the shear layer. For this reason, it is likely that when the flap is horizontal there is little difference in the height and thickness of the shear layer and therefore little influence of the flap length. In contrast, when the flap is set to 20°, there are much more obvious differences between the two lengths of flap.

As expected for each case, the largest differences in drag coefficient are seen at shorter separation distances (i.e. $d/L = 0.2$ & 0.4). Considering first the 10° case, the length of flap that provides the best results for the rear vehicle changes from first being the 25*mm* flap at $d/L = 0.2$, to the 10*mm* flap at $d/L = 0.4$. At $d/L = 0.2$, the larger flap is able to deflect the shear layer higher over the rounded leading edge of the rear vehicle, allowing it to reattach smoothly and providing a lower drag coefficient than the small flap. As the vehicles move further apart, the

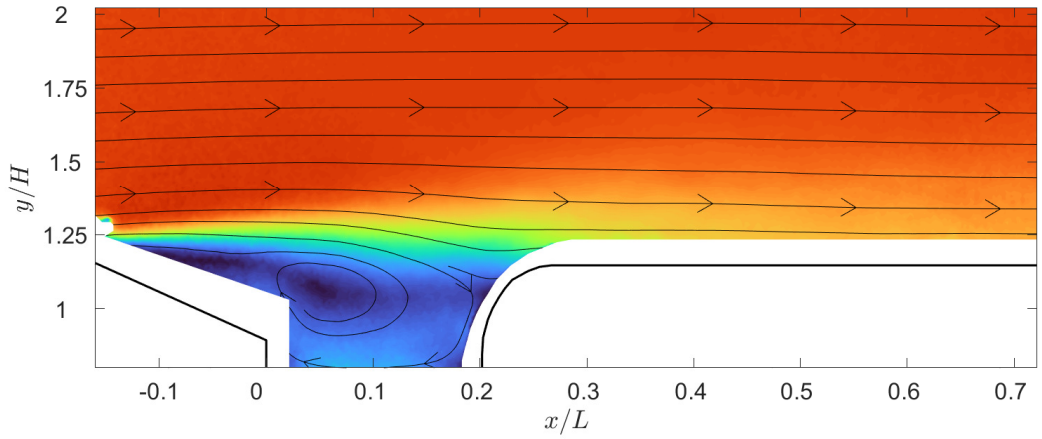

(a)

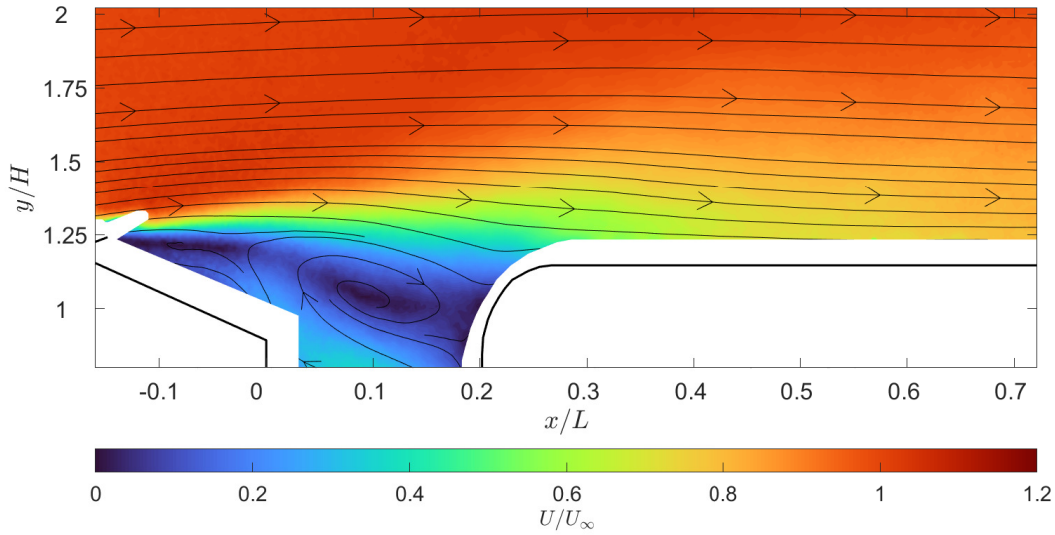

(b)

Figure 5.42: PIV images of the (a) small/10*mm*; (b) large/25*mm* Flap platoon at 20°, $d/L = 0.2$ and $Re_H = 2.88 \times 10^5$. Flow goes from left to right.

larger flap begins to perform worse. The flow fields for each flap length at $d/L = 0.4$ are given in figure 5.41. Here the larger flap protrudes too far into the free stream creating an unsteady flow separation and thick shear layer. When compared to the smaller flap at the same angle, it becomes evident how the thinner, more stable shear layer interaction could provide a more desirable inflow for the rear vehicle.

As the vehicles move further apart still, the rear vehicle begins to move out of the highly turbulent region of the shear layer. Whilst some platooning effects remain, the difference between the flaps at this distance are no longer visible in the drag data.

The 20° case is a more extreme version of the 10° case. The turbulence and general unsteadiness in the shear layer is increased drastically, especially for the larger flap. Whilst this proved to be beneficial for the rear vehicle in the platoon at $d/L = 0.2$, the smaller flap also performs

	Baseline	10*mm* Flap		
		0°	10°	20°
Cd	0.388	0.276	0.305	0.344

Table 5.12: Drag coefficient measurements for each flap case in isolation compared to the drag coefficient of the baseline, 25° Ahmed vehicle in isolation at $Re_H = 3 \times 10^5$

well at this angle with a drag coefficient increase of only 2.7% when compared to the larger flap. Figure 5.42 compares the flow field for both flap lengths at $d/L = 0.2$. Here, both lengths of flap are able to successfully divert the shear layer high over the rear vehicle. Whilst some wake impingement remains for the small flap case, the larger flap does not provide much additional improvement on the deflection of the shear layer. Instead, the biggest change between the small and large flap is the increased shear layer thickness produced by the larger flap case.

Although wake impingement still persists, resulting in an increase in drag for the rear vehicle in the platoon, from $d/L = 0.4$ to $d/L = 1.0$ the smaller flap at 20° consistently outperforms the larger flap. This highlights one of the key factors in using this type of flow control. When intentionally causing flow separation for platooning, one must take care to not generate excessive unsteadiness in the flow. As previously discussed, this disrupts the inflow for the rear vehicle limiting the effects of any pressure recovery mechanisms in the geometry. Whilst this study is only focused on the Ahmed vehicle model, it is suggested that this conclusion is likely to hold true for other geometries and vehicle shapes.

Another observation from the comparison of flap lengths is that when the front vehicle is equipped with the small flap, it always has a lower drag coefficient than for the larger flap at the same angle. Whilst this is a useful insight, i.e., a small flap can produce similar results to the larger flap while being more efficient at doing so, the perceived improvements are not caused by platooning but instead this difference is due to the normalisation of the drag coefficients. Each case was normalised with respect to an isolated 25° Ahmed vehicle. Table 5.12 shows the isolated drag coefficient value for each setting of the smaller flap when compared to the baseline Ahmed vehicle. The improvements for the smaller flap observed here are similar to the improvements measured in the platoon. These results are also in agreement with the work by Beaudoin et al. [56] who studied the effects of different flap configurations on the drag of an Ahmed vehicle. At a similar Reynolds number of $1.2 \cdot 10^6$, they reported drag coefficients for flap angles from 0° to 20° ranging from 0.30 to 0.34.

The final observation from these results is that all of the flow control cases continue to display inverted platooning conditions. By diverting the flow high over the curved leading edge of the rear vehicle (e.g. the 20° flaps at $d/L = 0.2$) the drag coefficient was brought back to a level similar to that of an isolated vehicle. However, once the flow has been diverted to this extent, further savings are difficult to achieve. In addition, diverting the wake in this manner only delays the negative effects of platooning as, at some separation distance, there will be a point at which the shear layer impinges on the rear vehicle thus causing an increase in drag. In practice, this

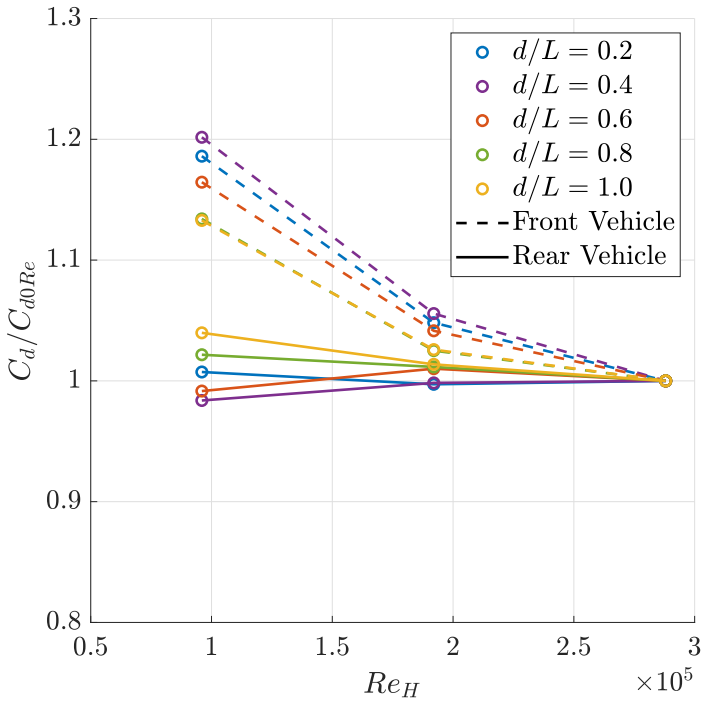

Figure 5.43: Reynolds number dependency of drag coefficients of the platoon with a 25*mm* flap at 0°. The drag coefficients are normalised with respect to the drag coefficient measured the highest Reynolds number for each case.

could be addressed to some degree by adjusting the flap angle depending on the vehicle spacing.

Clearly the flow around platoons that display inverted platooning conditions is extremely complex. To improve this technique further, more sophisticated flow control systems would be required. There will always be some differences in the aerodynamic efficiency of vehicles in a platoon. However, the use of flaps as shown above could be part of a system that works to reduce the drag of all vehicles in a platoon. This could operate in a similar way to current vehicles that have deployable flaps. A proximity sensor could be mounted on the rear of a vehicle. When in isolation the flap could remain retracted but, when said sensor detects a car, the flap could be deployed at the appropriate angle to deflect the air around the vehicle in it's wake.

5.3.6 Effect of Reynolds number on platoons with flow control

This section will discuss the effect of Reynolds number on the platoon cases that implemented the 25*mm* flap. As discussed previously, this area of research is fairly limited. It is also difficult to draw conclusions on Reynolds number dependency across different studies due to the wide range in computational and experimental methods used.

For an isolated road vehicle, the drag coefficient increases as Reynolds number decreases. In general, based on previous results in this chapter, the front vehicle in the platoon shows higher Reynolds number dependency, increasing in a similar fashion to an isolated vehicle. This

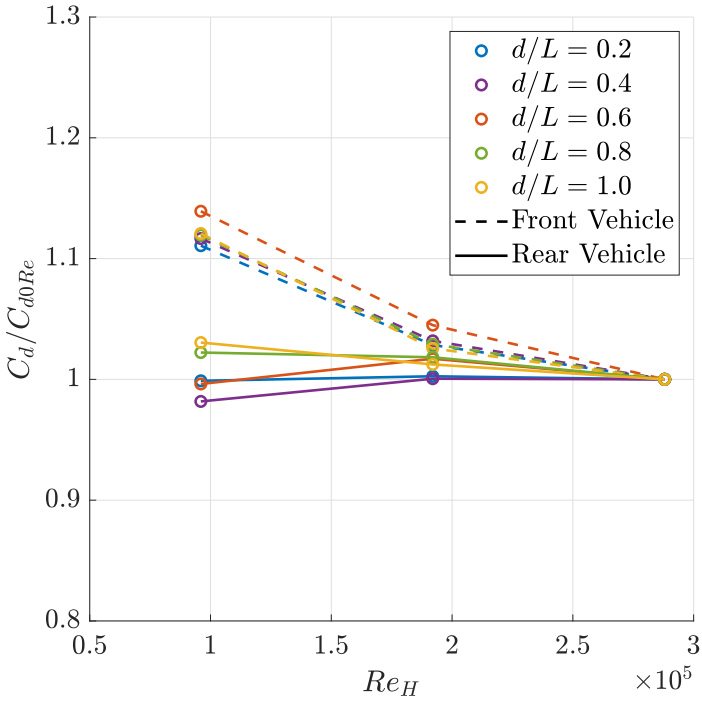

Figure 5.44: Reynolds number dependency of drag coefficients of the platoon with a 25*mm* flap at 10°. The drag coefficients are normalised with respect to the drag coefficient measured the highest Reynolds number for each case.

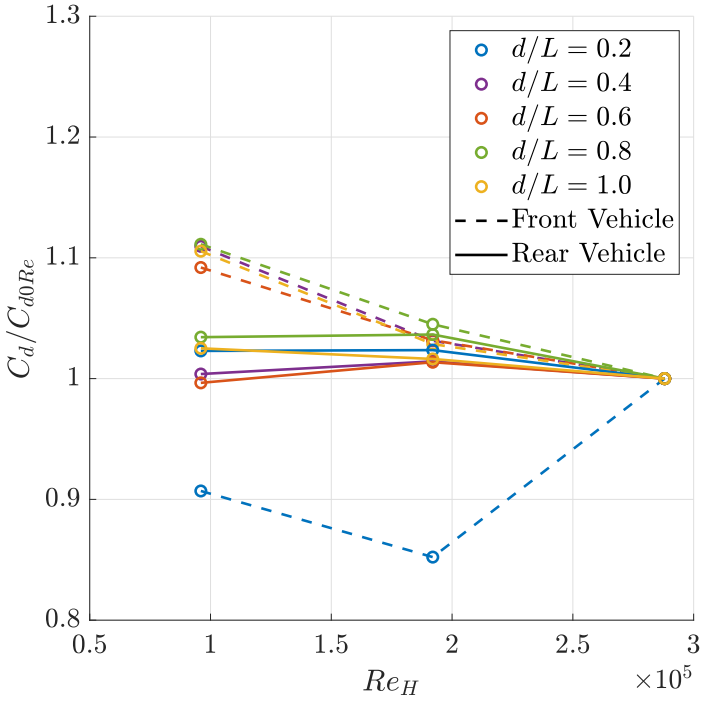

Figure 5.45: Reynolds number dependency of drag coefficients of the platoon with a 25*mm* flap at 20°. The drag coefficients are normalised with respect to the drag coefficient measured the highest Reynolds number for each case.

is reasonably intuitive as the incoming flow changes as Reynolds number changes. The rear vehicle in the platoon is far more sheltered from changing flow conditions therefore, is often unaffected by Reynolds number.

Figures 5.43, 5.44 and 5.45 show the Reynolds number dependency of both vehicles over the range of inter-vehicle distances for the 25*mm* flap at 0°, 10° and 20° respectively. As anticipated from previous data, the front vehicle shows a far larger dependency on Reynolds number than the rear vehicle for all cases.

Comparing the dependency of the front vehicle between the three flap angles, in general, the dependency decreases as flap angle increases. This is again to be expected, as the flap angle increases, the mechanism for flow separation becomes increasingly consistent and predictable making it less dependent on Reynolds number. The outlier in the front vehicle data is the 20° flap case at $d/L = 0.2$. Here, the presence of the rear vehicle in the wake created a much thicker shear layer causing significantly more instability in the flow at high Reynolds numbers. The level of instability is directly related to the Reynolds number resulting in a strong Reynolds number dependency for this configuration.

When comparing the rear vehicles in each case the results are very similar. In the platoon, the drag coefficient of the rear vehicle tends to be greater than the drag coefficient of the vehicle in isolation (inverted platooning conditions). As Reynolds number decreases, the drag coefficient of an isolated vehicle increases. As the rear vehicle in the platoon has no change in drag coefficient at lower Reynolds numbers, this effectively causes a reduction in normalised drag coefficient for the rear vehicle. Similarly, if this experiment was scaled to the Reynolds number of a road vehicle (roughly $8 \cdot 10^6$ for a HGV), it is reasonable to expect an increased normalised drag coefficient for the rear vehicle, strengthining the effects of inverted platooning.

5.4 Conclusions

The results presented in chapter 4 showed great promise for the addition of flow control devices on the lead vehicle of a platoon to eliminate or improve 'inverted' platooning cases. In this chapter an experiment was outlined that was designed to replicate these simulations to give more clarity on the effectiveness of flow control on a platoon.

It was found that thick, unsteady shear layers had a negative influence on the rear vehicle. This effect was amplified by the rounded leading edge of the rear vehicle. In addition, when the wake impinges on this rounded leading edge, the drag of the rear vehicle was significantly increased. This is in line with the conclusions from Chapters 3 and 4.

By implementing a flap on the front vehicle at the top of the trailing edge slant, the shear layer was able to be deflected over the leading edge of the rear vehicle. The combination of a 25*mm* flap at 10° created a strong recirculation region between the vehicles and resulted in a 9.5% reduction in drag for the rear vehicle when compared to the baseline case without flow

control.

In addition, the effectiveness of utilising URANS simulations to provide an experimental scope and assist with the analysis and interpretation of the experimental data was highlighted.

In general, the flaps had a lower influence over the drag coefficients of the rear vehicle than expected. PIV images provided good insight on how the wake was effected by the changing flap configurations. Nevertheless, little difference was seen between results for distances greater than $d/L = 0.6$. For all cases, inverted platooning conditions remained, highlighting how significant the rear geometry is in determining the efficiency of the platoon.

Future flow control efforts could focus more on limiting the interactions between the wake and the rounded leading edge even further. However, more effort should be focused on optimising the leading edge geometry of the rear vehicle as this could provide far more significant drag reductions.

Future work could also investigate how the wake influences the pressure distribution on the leading edge of the rear vehicle through the use of pressure taps. This would provide a more detailed picture of the effects of wake impingement and the mechanisms that create inverted platooning conditions.

Chapter 6

Flow control for platoons: plasma actuators

6.1 Introduction

In the previous chapters, the effect that vehicle shape has on the efficiency of a platoon was explored. It was found that specific geometries produced favorable wakes that improved the drag coefficient of the rear vehicle when compared to a baseline platoon of two 25° Ahmed vehicles. An in-depth analysis on the use of a flap to mimic the positive wake features was given with some success, especially at short inter-vehicle distances.

In this chapter, a more sophisticated method of flow control is proposed. A device that has shown good versatility as a flow control solution is the plasma actuator. This is an electrically controlled device that uses high-voltage electricity to ionise the surrounding air and generate an electric field that induces a jet. The high voltage is generated by spacing two electrodes either side of a thin, non-conductive, dielectric material. One electrode (the 'exposed electrode') is exposed to the surrounding air and is connected to a live high voltage supply, the other is connected to ground (the 'encapsulated electrode') creating the potential difference required to generate plasma. The electric field can then be altered by laterally offsetting the two electrodes inducing flow in the surrounding air.

Plasma actuators have the ability to be mounted directly to a surface, allowing them to be incorporated into a project without altering the geometry. This is very attractive for the automotive industry as vehicle aesthetics are a key component of vehicle design. In addition, as they are eclectically controlled, they are extremely light weight and have short response times to electrical inputs. this opens up the opportunity for incorporating plasma actuators into an active flow control systems. Such a system could have the ability to read upstream flow data and adjust the induced jet of the plasma actuator accordingly to achieve the desired outcome. This, in turn, would optimise the effectiveness of the flow control device. A full description of how plasma actuators function and some of the variables involved is provided in section 2.2.2.

Plasma actuators have wide range of applications outside of the automotive field. For more information, volume 40, number 3, of the journal of physics D: applied physics was dedicated to plasma actuators and provides many interesting articles on the topic [134–136]. Additional review papers by are provided by Cattafesta et al. [97] and Wojewodka et al. [98]

Automotive applications range from the addition of actuators on the leading and trailing edge of HGV's to reduce flow separation [78,82], to improving flow attachment over the trailing edge of a 25° Ahmed vehicle [76,89–91]. One common objective shared between the aforementioned studies is the application of actuators to improve flow attachment. In this chapter, plasma actuators were implimented in a slightly more novel manner to instead induce flow separation.

Whilst extremely versatile, it can be challenging to produce jets with adequate velocity to manipulate the bulk flow using a plasma actuator. When specifically analysing the jet velocity output, Joussot et al. [74] used a serrated type actuator to produce a maximum jet velocity of $6ms^{-1}$. However, the research conducted by Thomas et al. [84] also highlighted the wide range of contributing factors in actuator design making repeatability or comparison between studies more challenging.

In this chapter, an experimental investigation will first be conducted to provide a velocity profile of a plasma induced jet. Following this, the velocity profile will be incorporated into a URANS platooning investigation to provide an indication of the effectivness of using plasma actuators as a flow control device for platoons.

Initially, two serrated actuators with different dielectric layers were investigated. Each actuator was characterised over a range of electrical inputs to fully understand the maximum induced velocity capabilities of this technology. In addition, the effect of duty cycle and modulation frequency on the induced velocity of the actuator were analysed.

This work was then continued into a CFD study analysing the effect of induced velocity on a platoon of two 25° Ahmed vehicles, similar to that done using flaps in section 4.

6.2 Experimental Methodology

6.2.1 Electrical equipment setup

To generate the voltage required for a plasma actuator, a series of electrical components were used. Initially, a signal generator is used to provide a high frequency wave to the low voltage circuit board. In addition to this, a $20V$ DC power supply is also connected to the low voltage board. These two inputs are passed to a high voltage board that steps the voltage up to $20kV$ AC. Both circuit boards are housed inside a Faraday cage to limit the influence of the high voltage electricity interfering with any of the other electrical equipment. An insulated high voltage cable is used to pass the $20kV$ supply to the exposed electrode of the actuator. The grounded electrode is then earthed generating a $20kV$ alternating potential difference between the two electrodes.

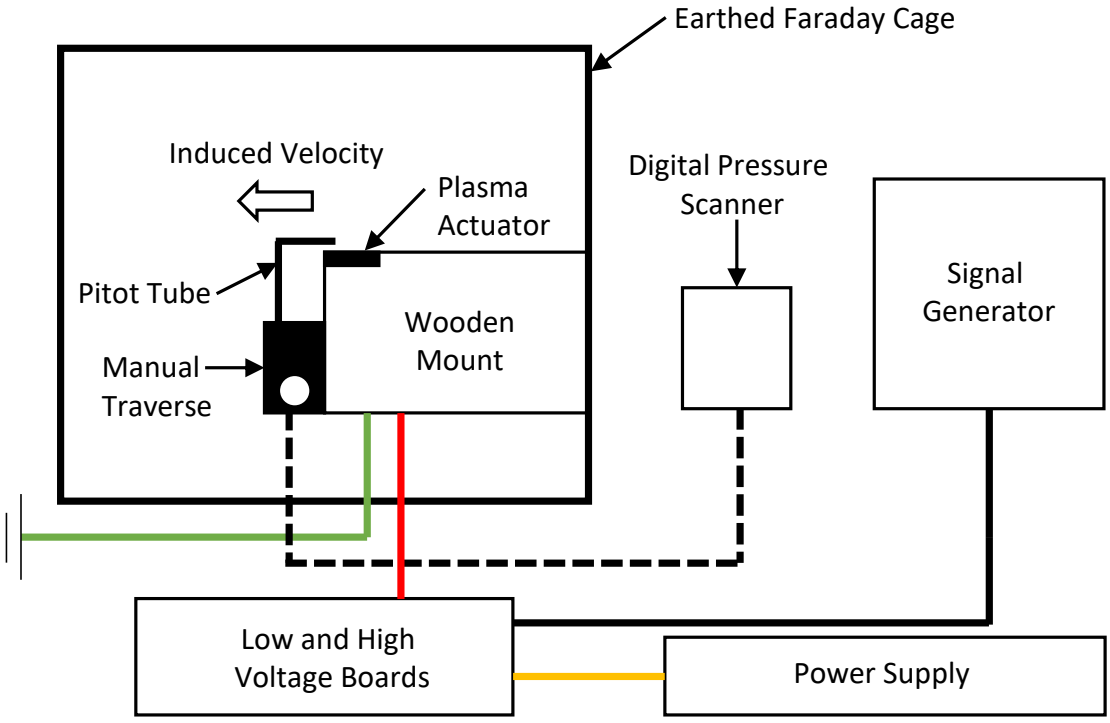

Figure 6.1: Schematic of plasma actuator experimental setup. High voltage wiring is shown in red with earthed wiring shown in green.

This setup is depicted in figure 6.1

Design of electrodes

The electrodes themselves are a serrated design based on the studies conducted by Joussot et al. [74] and Liu et al. [75]. Figure 6.2 shows the dimensions of the electrodes. The encapsulated electrode is rectangular and offset 8mm from the exposed electrode. There is some overlap between the electrodes, however, the offset allows the electric field created to drive the induced flow into a jet.

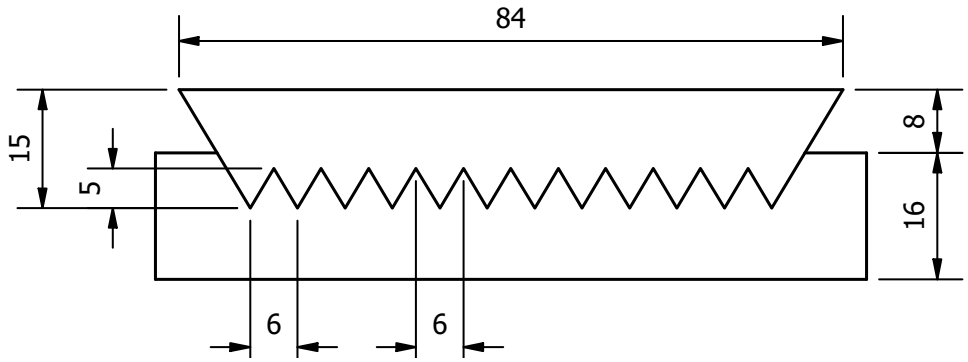

Figure 6.2: Serrated actuator design with associated dimensions (in mm); the induced flow direction is from top to bottom.

Actuator Makeup

Two different actuators with the same electrode design were manufactured. The first actuator used adhesive copper tape for the exposed and encapsulated electrodes, cut to the required dimensions on a computer numerical control (CNC) cutter. The dielectric layer was constructed of $500\mu m$ Mylar sandwiched between $55\mu m$ Kapton tape (one layer on either side), similar to the description in the paper by Joussot et al. [74]. In the Joussot study they refer to this actuator as KMK, describing the dielectric structure of the actuator (e.g. Kapton, Mylar, Kapton).

In the research by Thomas et al. [84], it was shown how the use of Kapton as a dielectric layer limited the maximum voltage put through the actuator before the dielectic layer breaks down. For this reason, a second actuator, made of FR4 Epoxy glass laminate, was also constructed. This is a printed circuit board (PCB) material with with a $35\mu m$ layer of copper on each side. The electrode designs were then etched out of the copper surfaces to produce the finished actuator.

6.2.2 Measurement setup

Pitot tubes

Pitot tube measurements were used to characterise the actuator's induced velocity. Pressure measurements were taken using a quartz Pitot tube with a 90-degree bend, 60 mm and 150 mm straight sections, an inner height of 0.3 mm and an outer height of 1.2 mm. The Pitot tube was mounted $10mm$ downstream of the actuator on a single component manual traverse with a scale accurate to 0.5mm. Measurements were taken on the centre line of the actuator at four vertical locations: $0.6mm$, $1.1mm$, $1.6mm$ and $2.1mm$ above the surface of the actuator. A FLUKE 922 digital airflow meter was used to measure the difference in stagnation pressure of the Pitot tube and atmospheric pressure to a resolution of 1Pa, this equates to a measurement uncertainty of $0.6ms^{-1}$.

Pressure measurements were later transformed into velocities using equation 6.2.2, a rearrangement of the Bernoulli equation where U is the horizontal component of velocity, ΔP is the change in pressure measured by the Pitot tube and ρ is the density of air. Pressure and temperature readings were also taken during the experiment to later calculate the appropriate density using the perfect gas law.

$$U = \sqrt{2\frac{\Delta P}{\rho}} \tag{6.1}$$

6.2.3 Experimental procedure

This experiment was designed to characterise a serrated plasma actuator. The induced velocity was measured to provide a comparison between cases and was utilised in a later chapter to assess the feasibility of using a DBD plasma actuator as a flow control device on a platoon of road vehicles. Two different dielectric structures were used to make the actuators as outlined previously in section 6.2.1.

The first component of the characterisation was the frequency dependency of each actuator. To achieve this, a range of frequencies from $1-9kHz$ were tested. Three input wave-forms were also tested: square, saw-tooth and sinusoidal. Additionally, duty cycle and modulation frequency were analysed.

The duty cycle describes the percentage of time that the actuator is powered (for example, a duty cycle of 50% implies that over 2 seconds the actuator would be powered for a total of 1 second and off for a total of 1 second). This duty cycle can be modulated allowing the actuator to switch between on and off states at a range of frequencies. This process is outlined in figure 6.3 where a number of signal plots are provided for comparison. Modulation frequencies of $10, 50$ and $100Hz$ were used for a range of duty cycles from $10-90\%$. The signals in the centre column all have the same duty cycle with the modulation frequency increasing from top to bottom. The signals in the middle row all have the same modulation frequency with duty cycle increasing from left to right.

Each test case was repeated 3 times to ensure the repeatability of the experiments.

6.3 Experimental results and discussion

6.3.1 Effect of dielectric material on induced velocity

In this section the induced velocity of both the PCB and KMK type actuators described in section 6.2.1 will be compared. Figure 6.4 shows how the induced velocity changes as input frequency changes for both types of actuator. As predicted by Thomas et al. [84], the actuator that utilises a KMK dielectric layer broke down at a much lower frequency than was achieved by the PCB actuator. The KMK actuator produced a peak velocity of $3.1ms^{-1}$ at $3kHz$. This was slightly higher than the induced velocity of the PCB actuator at $3kHz$ however, the induced velocity quickly reduced thereafter with the dielectric material breaking down at $6kHz$. The PCB type actuator was much more resilient to input frequency, only beginning to deteriorate at around $10kHz$, with a peak induced velocity of $6.2ms^{-1}$ occurring at $6.5kHz$. Appendix B shows photos of some of the scarring on both actuators due to arcing when frequencies were increased past the dielectric material's threshold.

The thinner dielectric layer of the KMK actuator, in general, provided a higher induced velocity than the thicker PCB actuator for the same input parameters. However, as mentioned

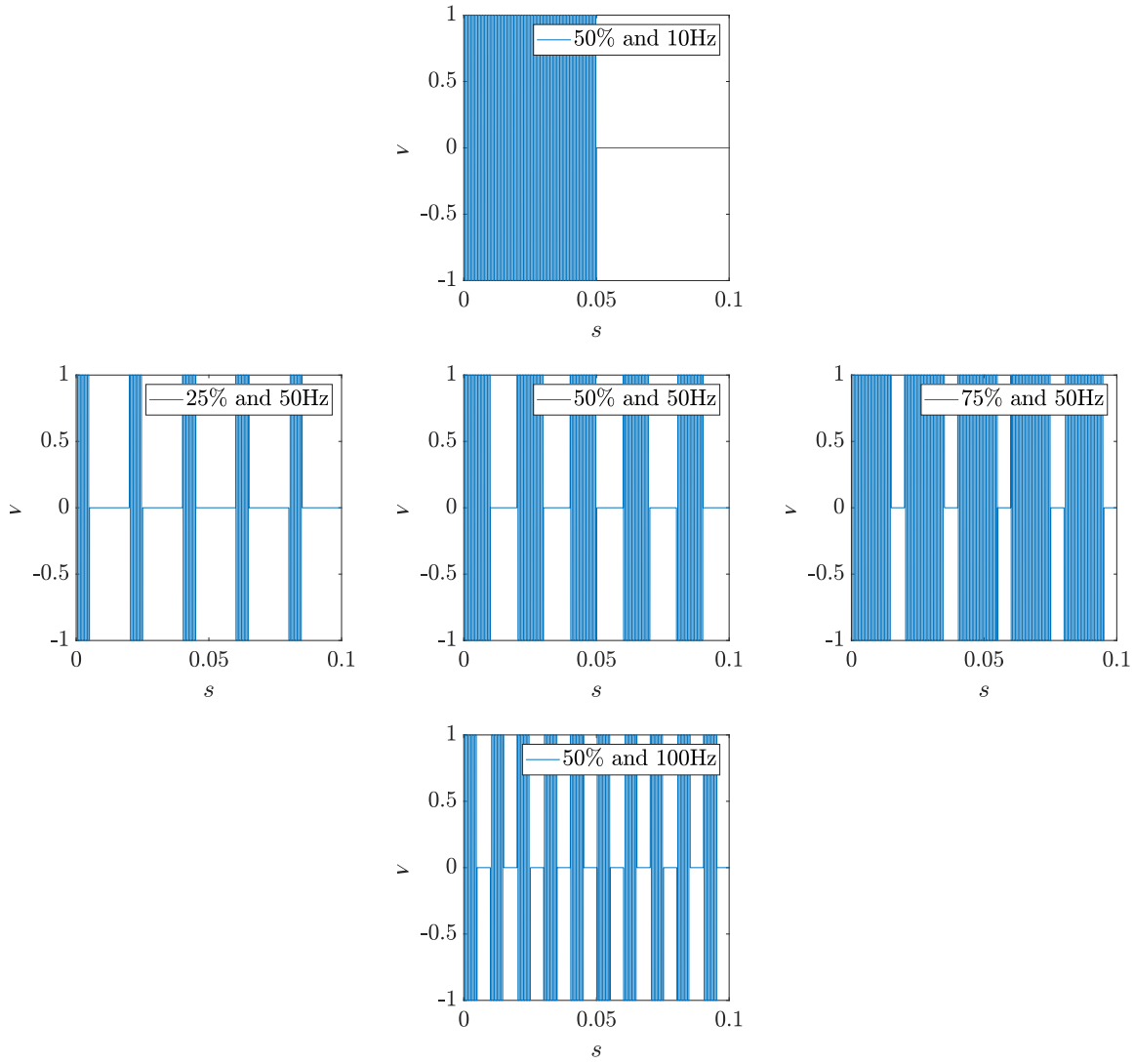

Figure 6.3: Examples of normalised input square wave signals produced by the signal generator for a 0.1s sample. All vertical signals have the same duty cycle and increasing modulation frequency from top to bottom. Horizontally, each figure has the same modulation frequency with different levels of duty cycle increasing from left to right.

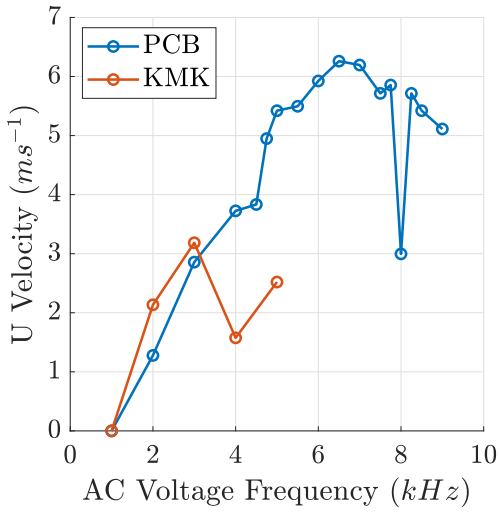

Figure 6.4: U component of induced velocity over a range of input frequencies for two plasma ctuators using different dielectric materials. Namely PCB and KMK.

previously, the dielectric layer began to break down at much lower frequencies resulting in a much lower peak induced velocity. The plasma actuator works in a very similar way to a capacitor with two electrodes separated by a dielectric layer. The material properties of the dielectric can be described using the dielectric coefficient which contributes to the overall capacitance of the actuator. At high voltages, as the frequency is increased, the dielectric coefficient drops. Eventually this leads to a breakdown of the dielectric material and it looses the ability to hold any capacitance. This is sometimes referred to as saturation and at this point, the actuator will no longer be able to function. In general, thinner dielectric layers have a lower dielectric coefficient, causing them to breakdown at lower frequencies. The PCB actuator's ability to withstand these higher frequencies is the fundamental reason why it performs better than its KMK counterpart.

6.3.2 Effect of voltage inputs on induced velocity

Input frequency

In addition to a comparison between dielectric materials, figure 6.4 also provides a good visualisation for the frequency dependency of plasma actuators. Many studies discuss saturation as one reason why the induced velocity does not increase indefinitely as frequency increases [77, 82–85]. Although this may also be the case in the present study, there is an additional, peculiar, non-linear nature to the results. A sharp increase in the PCB induced velocity between 4.5 and $5kHz$ and similarly, a sharp minimum at $8kHz$, combined with relatively constant velocities between 4 and 4.5 and 5 and $5.5kHz$ paint an unusual picture. It is hypothesise that the geometry of the exposed electrode, combined with the quantity of metal, creates certain harmonics that can be excited by the input frequency. This hypothesis would also help to explain why each different setup reported in the literature appears to produce slightly different outputs

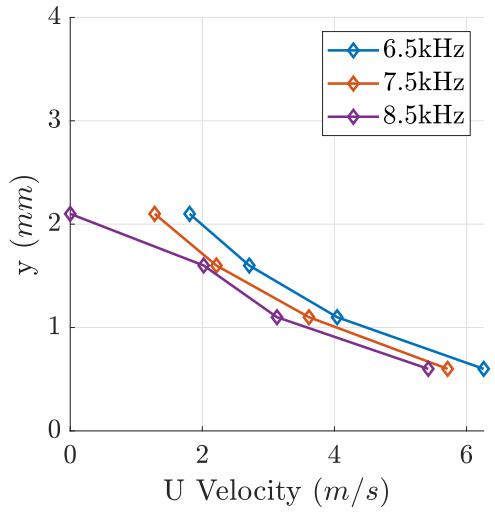

Figure 6.5: Profiles of the U component of induced velocity over a range of input frequencies from 6.5kHz to 8.5kHz for the PCB serrated electrode plasma actuator.

and optimum frequencies. Unfortunately, this avenue of investigation was outwith the scope of the current study, however, it would be of interest for future work.

Figure 6.5 shows the velocity profile for a select range of input frequencies, namely 6.5, 7.5 and $8.5kHz$. This was achieved by measuring the pressure over a range of vertical locations using a pitot tube. These results show averaged data over 3 runs and the four vertical readings for each case were not taken instantaneously, instead a manual traverse was used to reposition the pitot tube between each run.

Here, the velocity profiles are reasonably consistent between each run with a constant velocity offset as the frequency increases. The outlier in these results is the $8.5kHz$ case at $2.1mm$ above the surface where the induced velocity measurement drops to $0ms^{-1}$. It is interesting that, as saturation builds through the three cases, not only the induced velocity but also the height of the jet induced is effected.

Another important note to take from this figure is the lack of data between $0.6mm$ and the surface of the actuator. In this case, readings were limited by the size of the pitot tube however, this leaves the true peak velocity of the jet unknown. Whilst it is theoretically possible to use Laser based measurement techniques such as PIV or LDA to obtain this data, the feasibility of measuring velocities near the surface is still challenging. A big limiting factor is the process of plasma generation as it emits light, disrupting the optical equipment used for these techniques.

The final outcome of note from the frequency characterisation is the comparison with the literature. The two key papers that also studied this type of serrated actuator, Joussot et al. [74] and Liu et al. [75], both reported a maximum induced velocity of around $6ms^{-1}$. Although these studies use different dielectric materials that are both again different from the current study, all three (including the current study) recorded similar peak induced velocities. This was unexpected as it has been shown how the change in dielectric makeup can have a strong effect

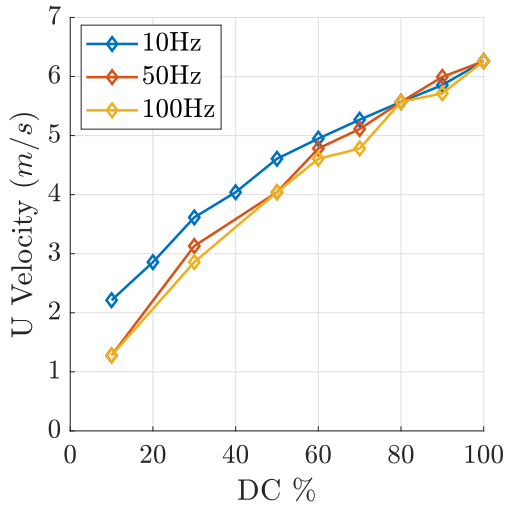

Figure 6.6: U velocity measurements for a range of duty cycles at various modulation frequencies from $10Hz$ to $50Hz$.

on the induced velocity. This trend may also suggest that electrode geometry could be a factor that limits the maximum induced jet.

Modulation and duty cycle

When the plasma actuator is initially activated a visual spike in plasma generated was observed accompanied by an audible increase in noise. This would last for less than a second before the plasma generation drops to a consistent rate. It was hypothesised that for this short time, there would be increased velocity induced by the actuator. To characterise this further, some modulation was introduced causing the actuator to switch on and off at a range of frequencies. This technique can also be used in flow control to excite harmonics in shear layers and promote boundary layer attachment [72, 77, 79].

Figure 6.6 shows how the duty cycle effected the induced velocity for three different modulation frequencies for the PCB actuator at $6.5kHz$. Duty cycle essentially describes how long the actuator is active, therefore as duty cycle is decreased, so to does the induced velocity. It is also evident that the $10Hz$ modulation performs better than the other modulation frequencies, especially at lower duty cycles.

The induced velocity reduces slowly as duty cycle reduces making it a good method for power saving. However, the hypothesised improvements by pulsing the actuator did not come to fruition. These measurements were taken using a Pitot tube, which is adequate for the primary focus was optimising the average velocity output of the actuator; for a more detailed time resolved measurement, LDA could be utilised.

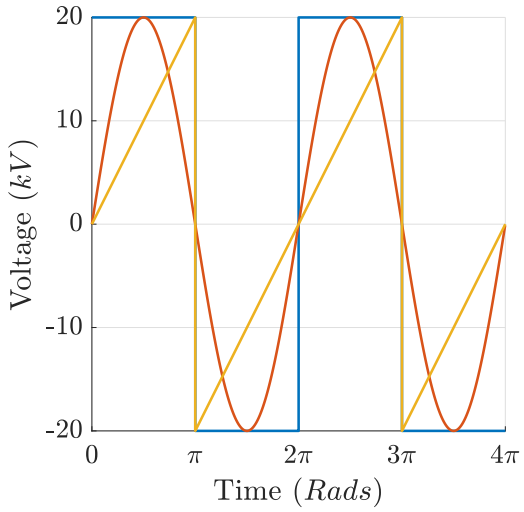

Figure 6.7: An example of the square, sinusoidal and sawtooth input waveforms used for the PCB actuator in the waveform sensitivity study.

Input waveform

In addition to duty cycle and modulation, the effect that input waveform has on the induced velocity of the actuator was also analysed. Figure 6.7 outlines the three waveforms used; square, sinusoidal and sawtooth. Figure 6.8 shows the induced velocity of the PCB actuator for each of the input waveforms over a range of frequencies. For the square wave, a peak velocity of $6.2ms^{-1}$ was achieved at $6.5kHz$. The sine and sawtooth waveforms produced a lower induced velocity, each around $4ms^{-1}$ at $3kHz$ and $1.2kHz$ respectively.

When comparing the waveforms, the square wave is always at peak power (either positive or negative) whereas the other two waves build up to a peak and drop off again. Taking the integrals, the area of the sine wave is 64% of the square wave with the sawtooth being 50%. The visible drop in performance for these waves is likely due to this offset. Despite this, sinusoidal waveforms are often used in the literature so future work should focus on a more rigorous testing of this hypothesis to fully understand the role that the input waveform plays on induced velocity.

6.4 Conclusions from experimental characterisation

By investigating the effects of dielectric material, input frequency, duty cycle, modulation frequency and input waveform a serrated plasma actuator was fully characterised. It was found that, using a PCB material with input parameters of $20kV$, $6.5kHz$ square wave and no modulation, a maximum jet velocity of $6.2ms^{-1}$ could be achieved.

The comparison between the PCB and KMK type actuators showed that the PCB actuator performed better in terms of frequency resilience, with a higher peak induced velocity of $6.2ms^{-1}$ at $6.5kHz$ compared to the KMK actuator's peak velocity of $3.1ms^{-1}$ at $3kHz$. The

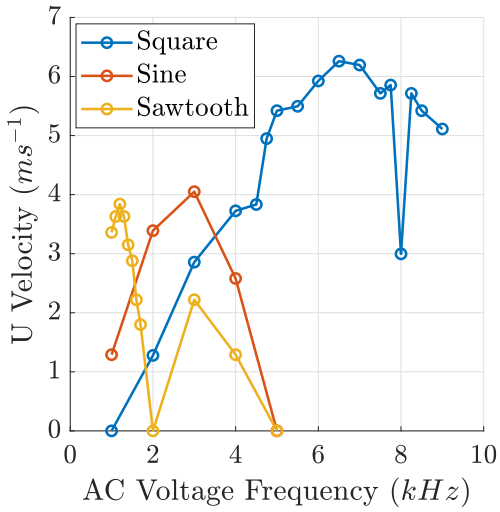

Figure 6.8: U component of induced velocity for a $20kV$ input voltage using a square, sinusoidal and sawtooth waveform tested on the PCB actuator at 100% duty cycle over a range of input frequencies

thinner dielectric layer of the KMK actuator resulted in a higher induced velocity at specific frequencies, but also a lower breakdown frequency.

Whilst the general trend in results indicated that higher frequencies produced larger induced velocities, the results also showed some non-linear behavior in the induced velocity over the range of input frequencies. This may be explained by the electrode's geometry and metal quantity creating harmonics. The effect of voltage inputs on induced velocity was also studied, with the results showing that a modulation frequency of $10Hz$ performed better than others, however, the addition of any modulation or duty cycle had a negative effect on the induced velocity.

The comparison with the literature also provides some interesting conclusions. This is now one of three studies that used the same serrated electrode design. Using very different electrical setups and input parameters each study recorded a maximum induced velocity of around $6ms^{-1}$. This would insinuate that the peak induced velocity of a plasma actuator is somehow limited by the electrode design, however, this seems unlikely and would need extensive further testing to verify.

Plasma actuators are an extremely innovative flow control solution, however, there are still many challenges to overcome. In general, the power used by the actuator is greater than the power saved through aerodynamic drag reductions by virtue of the actuator. This technology is still going through a lot of development and it is expected that the power consumption and efficiency of the actuators will improve in the future. Whilst it is possible to conduct experimental testing of plasma actuators in a controlled lab environment, it is another challenge completely to implement them in a safe manner on any consumer product. This is due to the nature of the high voltage, high frequency supply that is particularly good at breaking down insulation materials. The best way to minimise the risks is to keep the high voltage end of the equipment as close

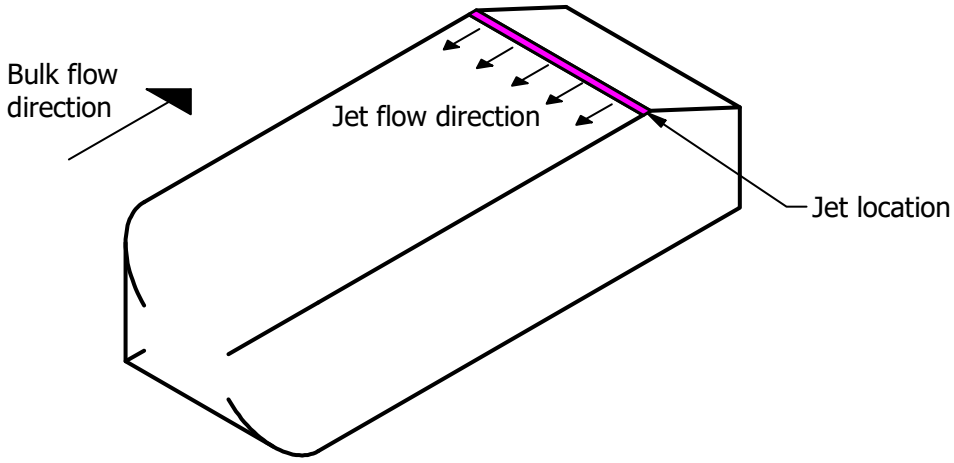

Figure 6.9: Location and direction of velocity inlet for the jet flow control device. Mounted on the front vehicle in the platoon, only. Flow is from left to right.

together as possible, this allows for shorter runs of high voltage cable and a smaller danger area. If the electrical equipment required to produce the high voltage supply was reduced in size this could provide a huge breakthrough in the ease of implementation of this technology. This was unfortunately an area of study that was outwith the scope of the current research. In the near future, however, plasma actuators would be ideal for implementation in controlled environments such as various military applications.

6.5 Computational Methodology

As discussed previously, the plasma actuator is a highly attractive piece of flow control however, it is also very challenging to implement experimentally. Whilst it was possible to conduct experimental testing on the actuator in a controlled environment, incorporating them into a full wind tunnel investigation adds an additional level of complexity.

The effectiveness of said plasma actuator was instead studied through the use of a series of URANS CFD simulations. This was achieved by simulating a simplified representation of the jet produced by the plasma actuator. The jet was applied to the trailing edge of the front vehicle in a platoon of two 25° Ahmed vehicles in a similar fashion to the implementation of the flaps discussed in chapter 4. The intention was to induce flow separation and create the desired flow features in the wake of the front vehicle of the platoon. The jet profile in section 6.3.2 was first implemented with two additional jet velocities also investigated to characterise the influence that jet velocity has on the effectiveness of the flow control technique.

6.5.1 Modifications to the URANS simulations

The initial set up used for this computational investigation was adapted from the methods used in chapters 3 and 4 and a more detailed explanation of meshing strategy and boundary conditions can be found there.

In order to model the near wall jet, a new surface section was created on the roof of the Ahmed vehicle at the beginning of the rear slant as depicted in figure 6.9. This surface was the same width as the vehicle, $15mm$ long and was given a velocity inlet boundary condition. The jet was then angled so that it would be directed horizontally upstream, to disrupt the boundary layer as it approaches the rear slant.

Most of the complex flow produced by the jet should be captured by the prism layers as this is designed to capture changes in the boundary layer. In order to accommodate the increased flow complexity in the surrounding region, the mesh was slightly refined to provide better resolution of the flow causing the cell count to increase. This modification resulted in the mesh size changing from $4.3m$ cells to $4.6m$ cells.

Some studies also incorporate plasma actuators on the side of vehicles [96]. This tends to shrink the recirculation region providing pressure recovery at the base of the vehicle. As the aim of this investigation is to grow the wake and induce flow separation, the actuators were only implemented on the roof of the front vehicle. As seen in the previous flow control examples, changes in the spanwise flow have a smaller effect on the drag coefficient of the rear vehicle and the main intention of this study is to induce flow separation over the trailing edge of the front vehicle.

6.5.2 Validation of approach

The original jet profile envisioned for these simulations was designed to match the peak velocity profile induced by the plasma actuator characterised in chapter 6. Figure 6.10 compares the horizontal component of the plasma induced jet to the jet profile used in the simulations. The main difference between the simulated and experimental jets is the location of the core of the jet. The true location of the jet core for the plasma actuator is unknown as the closest possible measurement to the surface is limited by the thickness of the Pitot tube. This leaves some uncertainty as to what the jet profile at the surface of the actuator looks like as a standard no slip assumption may be invalid due to the effects of the electric field.

The best match between the measured jet profile and simulated jet profile coincided with a nozzle velocity of $10ms^{-1}$. The jet closely matches the profile of the plasma induced jet for the measured heights above the surface of $0.6mm - 2.6mm$. This would suggest that, when modeling a plasma actuator, there may not be a need to include the complex physical properties relating to the generation of the plasma and that a simple induced jet may suffice.

A plasma actuator generates heat when in operation, although it has been shown that heat can

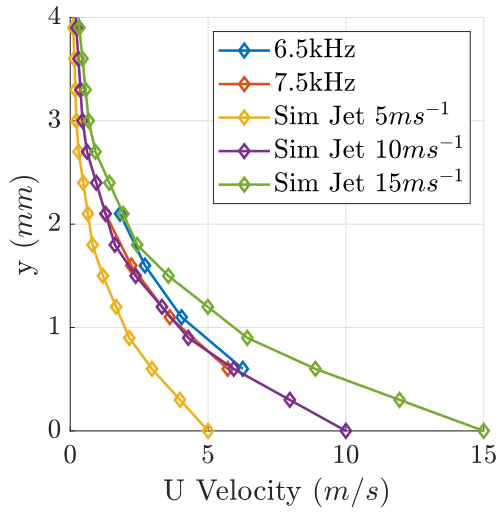

Figure 6.10: Profiles of the U component of induced velocity over a range of input frequencies for a serrated electrode plasma actuator showing a comparison of the experimental results from chapter 6 and the simulated jets from the current investigations.

increase the jet velocity induced, the temperature changes do not present any real changes to the mean flow physics or temperature and have therefore been neglected in this investigation [137].

In addition to the $10ms^{-1}$ jet, nozzle velocities of $5ms^{-1}$ and $15ms^{-1}$ were proposed. The three velocities correspond to $0.125U_\infty$, $0.25U_\infty$ and $0.375U_\infty$. The addition of a range of velocities allows us to test how the plasma could be used at varying induced velocities in order to alter the wake of the front vehicle in the platoon. The $15ms^{-1}$ jet is a higher velocity than the measured maximum velocity from the plasma characterisation in chapter 6. As the knowledge of plasma actuators grows, it is hoped that this increased velocity profile could be achieved. This simulation will therefore highlight if serious gains could be achieved at this new velocity. In addition, a lower velocity of $5ms^{-1}$ was also tested to provide a more general understanding of the effects of varying induced velocity.

6.6 Computational results and discussion

The introduction of a counter flow jet upstream of the trailing edge slant was proposed as a less invasive way to promote flow detachment over the trailing edge of the front Ahmed vehicle in order to improve the performance of the platoon. The results are compared to a baseline platoon of two 25° Ahmed vehicles that was discussed in detail in section 4.4.1

6.6.1 Proof of concept

Initially, the effects of the $10ms^{-1}$ jet were analysed as this matches the jet profile measured experimentally. This will act as a proof of concept for plasma actuators as a flow control device.

Case	Front					Rear				
	0.2	0.4	0.6	0.8	1.0	0.2	0.4	0.6	0.8	1.0
Ahmed-25° – 25°	0.08	0.10	0.14	0.20	0.25	0.38	0.40	0.38	0.32	0.29
$5ms^{-1}$ Jet	0.12	0.13	0.14	0.17	0.21	0.27	0.30	0.34	0.35	0.31
$10ms^{-1}$ Jet	0.12	0.13	0.14	0.17	0.21	0.26	0.30	0.33	0.35	0.32
$15ms^{-1}$ Jet	0.12	0.13	0.14	0.17	0.21	0.27	0.30	0.33	0.35	0.32

Table 6.1: Drag coefficient for each vehicle in platoon with simulated plasma actuators as flow control.

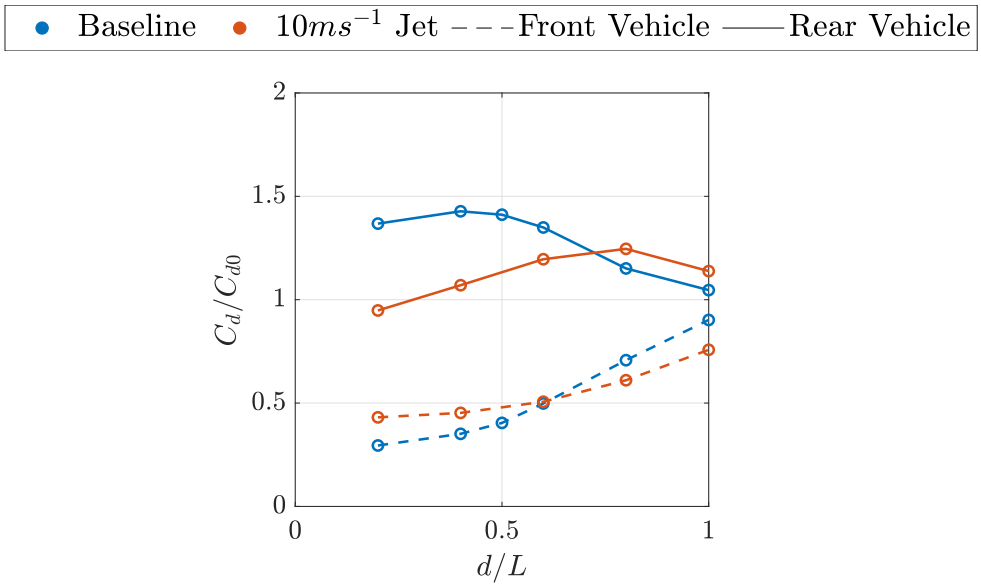

Figure 6.11: Comparison of normalised drag coefficient as a function of inter-vehicle spacing for (a) the baseline platoon of two 25° Ahmed vehicles (b) a platoon of two 25° Ahmed vehicles with a $10ms^{-1}$ jet as flow control.

The drag coefficients for all of the test cases in this chapter is given in table 6.1. Figure 6.11 shows the normalised drag coefficients for both the baseline platoon and a platoon of two 25° Ahmed vehicles where the front vehicle has been fitted with a $10ms^{-1}$ jet inducing flow control device. In this section, all values are normalised with respect to the isolated 25° Ahmed vehicle to highlight the true effect of the flow control.

As seen in the previous Ahmed vehicle platoons, inverted platooning conditions were observed, however, the addition of the jet has a notable influence over the drag coefficient. For the front vehicle in the platoon, the introduction of the induced jet initially produces a drag increase of around 45% at $d/L = 0.2$ and 29% at $d/L = 0.4$ when compared to the baseline platoon. As discuss in section 4.4.1, the front vehicle in the baseline case receives a large amount of it's drag reduction at short inter-vehicle distances due to the increased base pressure caused by the presence of the rear vehicle in it's wake. This promotes flow separation over the trailing edge slant, further reducing the drag coefficient of the vehicle. When a jet is added to this system, it is the jet that induces flow separation. This reduces the effectiveness of the pressure recovery provided by the rear vehicle. It does, however, continue to provide a significant drag reduction when compared to the isolated case in the region of 55%. In addition to this, at larger inter-vehicle distances (e.g. $d/L \geq 0.8$), the maintained flow separation results in a drag reduction of 14% when compared to the baseline and 25% when compared to the isolated Ahmed vehicle.

When analysing the rear vehicle, initially, a drag reduction of 31% is measured when compared to the rear vehicle in the baseline case at $d/L = 0.2$. This equates to a 5% reduction in drag when compared to the isolated 25° Ahmed vehicle.

As the vehicles move further apart, the drag coefficient of the rear vehicle in the flow control case gradually increases and, by $d/L = 0.8$, the addition of flow control results in a drag increase of 8% for the rear vehicle when compared to the baseline case.

Figure 6.12 compares the normalised velocity field for the baseline and induced jet cases at $d/L = 0.2$. A large component of the drag increase for the rear vehicle in the baseline platoon is the wake impingement of the shear layer of the front vehicle. This is visible in figure 6.13 as the turbulent separated flow is angled down towards the curved section of the leading edge of the rear vehicle. In contrast, the induced separation caused by the jet results in a far more structured wake with the turbulent sheer layer diverted high over the rounded leading edge of the rear vehicle. It is hypothesised that this additional sheltering is the key component that results in the significant reduction in drag between the baseline and flow control case at this inter-vehicle distance.

This is further emphasised when analysing the wall normal pressure distribution over the leading edge of the rear vehicle for both cases, as depicted in figure 6.14. Here, the wake impingement has been altered by the addition of the induced jet flow control. The rear vehicle in the baseline case has a large spike in pressure over the rounded leading edge however, this is significantly reduced in the flow control case. In addition, the location of the pressure increase

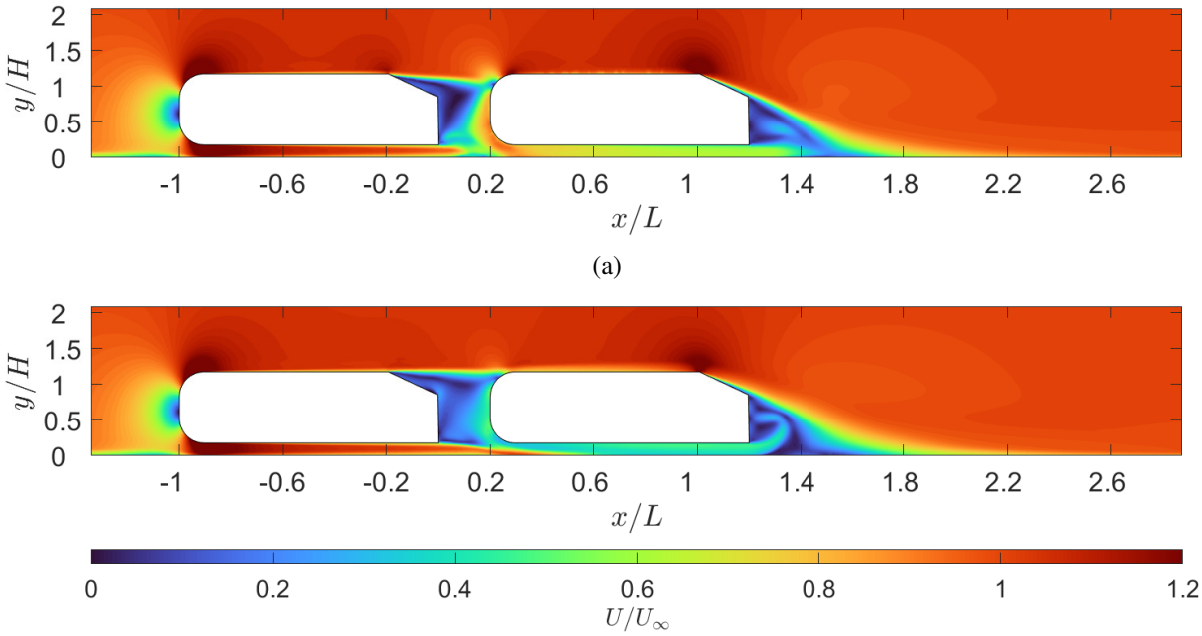

(a)

(b)

Figure 6.12: Average normalised velocity field comparison of the (a) baseline platoon (b) platoon with a $10ms^{-1}$ jet at $d/L = 0.2$. Flow direction is left to right.

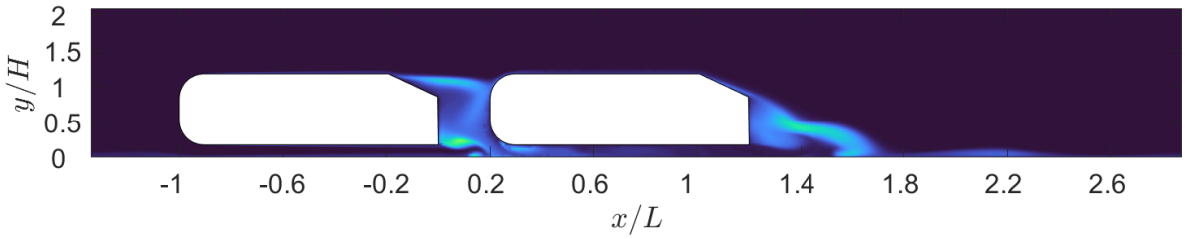

(a)

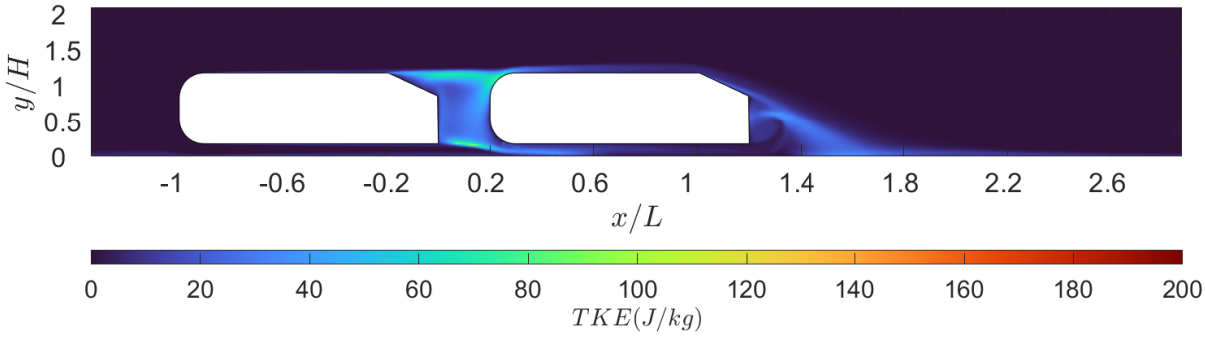

(b)

Figure 6.13: Turbulent kinetic energy field comparison of the (a) baseline platoon (b) platoon with a $10ms^{-1}$ jet at $d/L = 0.2$. Flow direction is left to right.

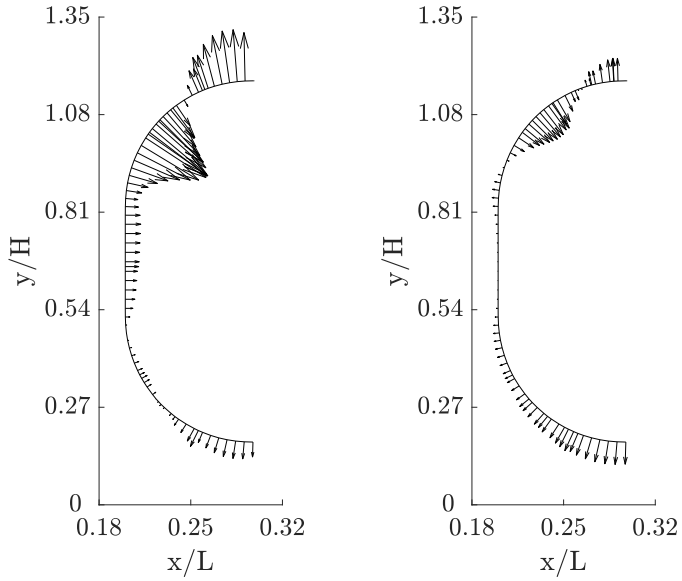

Figure 6.14: Wall normal pressure distribution across the centre plane on the leading edge of the rear vehicle in the (a) baseline platoon (b) platoon with a $10ms^{-1}$ jet as flow control at $d/L = 0.2$. Here an arrow facing into the surface represents a pressure greater than the reference pressure and an arrow pointing away from the surface denotes a pressure less than the reference pressure. The length of each arrow describes the magnitude of the pressure difference.

caused by wake impingement has been moved higher on the curved leading edge. This was also highlighted in chapter 3 as a technique that can help to prevent inverted platooning conditions. The final notable difference is the increased region and magnitude of pressure recovery seen on the lower portion of the leading edge of the rear vehicle in the flow control case. The combination of these two elements results in the large drag reductions discussed previously.

In the spanwise plain, the effect of the induced jet is far more subtle. The primary difference is the absence of the C-pillar vortices seen on the baseline case in figure 6.16. This allows the wake to diverge slightly more around the leading edge of the rear vehicle in the jet case (see figure 6.15)

As the vehicles move further apart, the drag coefficient of the rear vehicle in the flow control case gradually climbs. Where, at $d/L = 0.2$, the increased size of the wake helped to reduce wake impingement and sheltered the rear vehicle, at larger inter-vehicle distances, the wake of the front vehicle begins to impinge on the rear vehicle. This can be seen in figure 6.17 where the averaged flow field of the $d/L = 0.2$ and $d/L = 0.6$ configurations are compared. As the vehicles move further apart, the shear layer from the front vehicle moves progressively lower on the leading edge of the rear vehicle. This results in a gradual increase of the drag coefficient for the rear vehicle as predicted by the earlier study on the shape dependency of vehicle platooning in chapter 3.

From $d/L = 0.6$ to 0.8, the drag coefficient of the rear vehicle in the baseline case drops

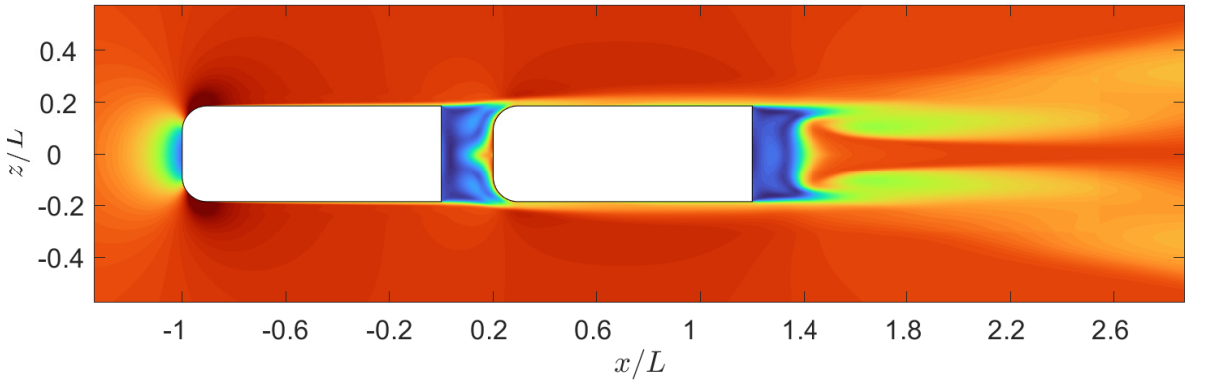

(a)

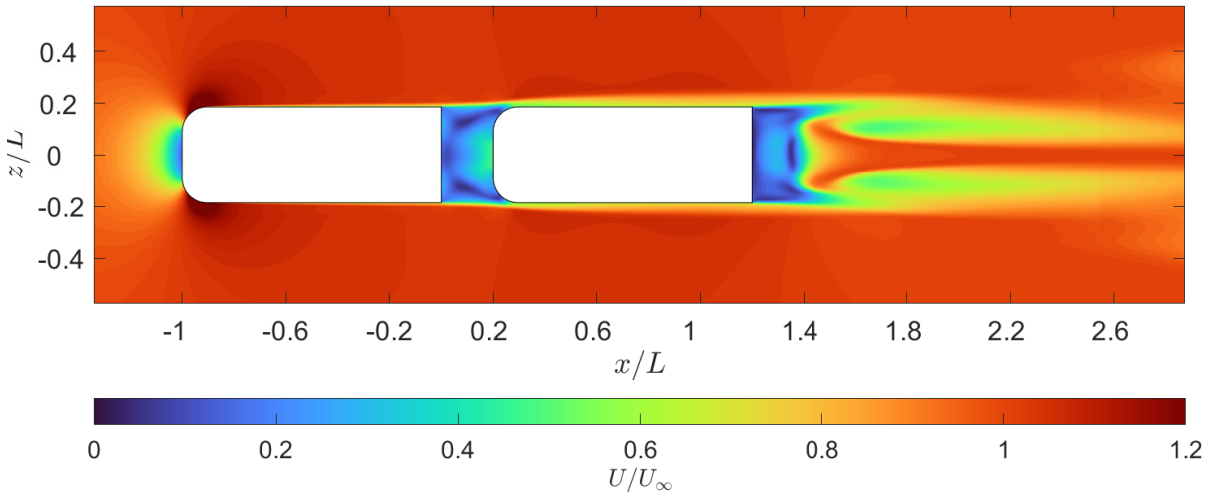

(b)

Figure 6.15: Average normalised velocity field comparison on a spanwise plane at $y = 0.15m$ for the (a) baseline platoon (b) platoon with a $10ms^{-1}$ jet at $d/L = 0.2$. Flow direction is left to right.

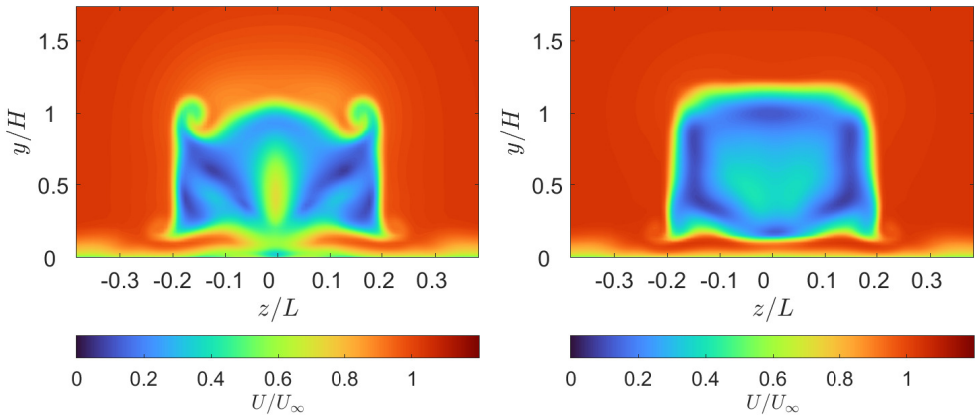

Figure 6.16: Average normalised velocity field comparison on a spanwise plane at $x = 0.15m$ for the (a) baseline platoon (b) platoon with a $10ms^{-1}$ jet at $d/L = 0.2$. Flow direction is left to right.

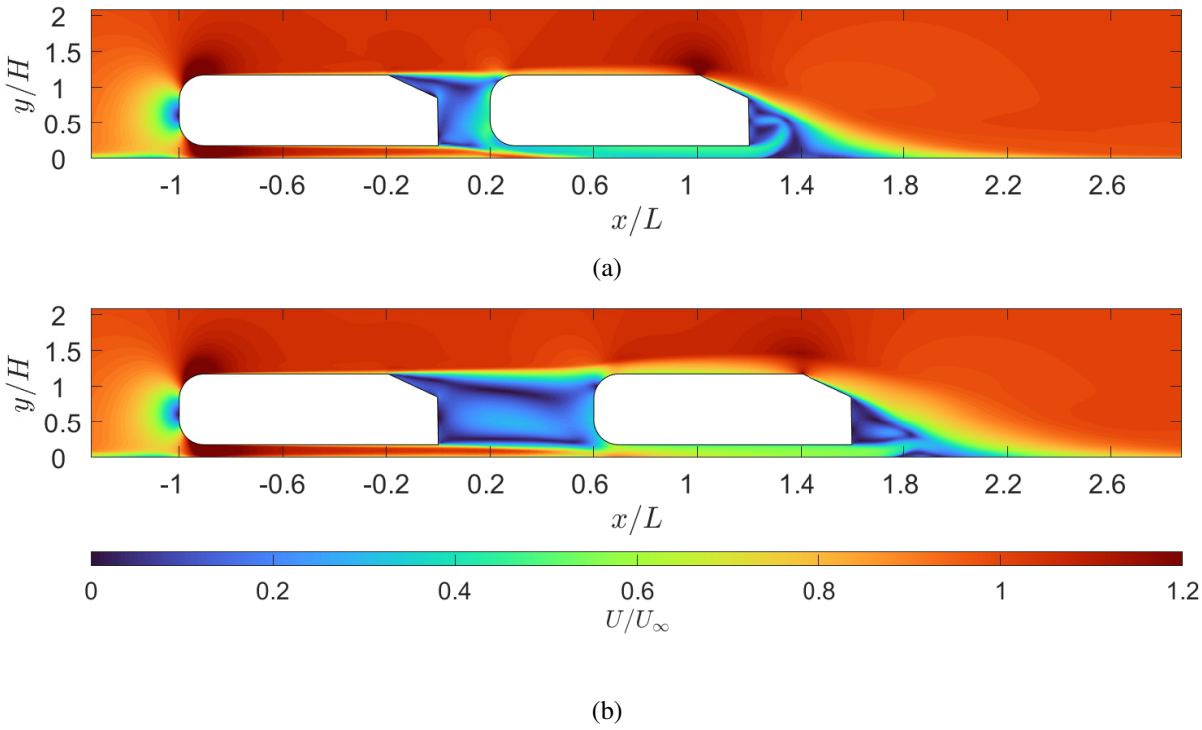

Figure 6.17: Average normalised velocity field comparison of a platoon where the front vehicle has a $10ms^{-1}$ jet flow control device for an inter-vehicle distance of (a) $d/L = 0.2$ (b) $d/L = 0.6$. The flow direction is left to right.

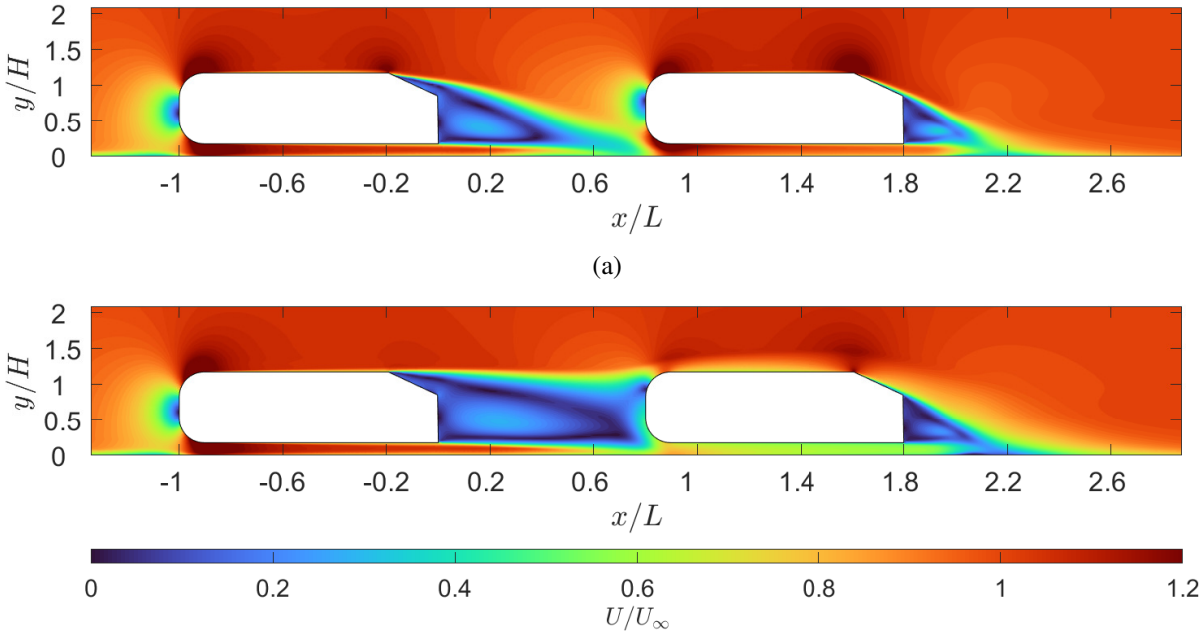

(a)

(b)

Figure 6.18: Average normalised velocity field comparison between (a) the baseline platoon and (b) a platoon where the front vehicle has a $10ms^{-1}$ jet flow control device for an inter-vehicle distance of $d/L = 0.8$. The flow direction is left to right.

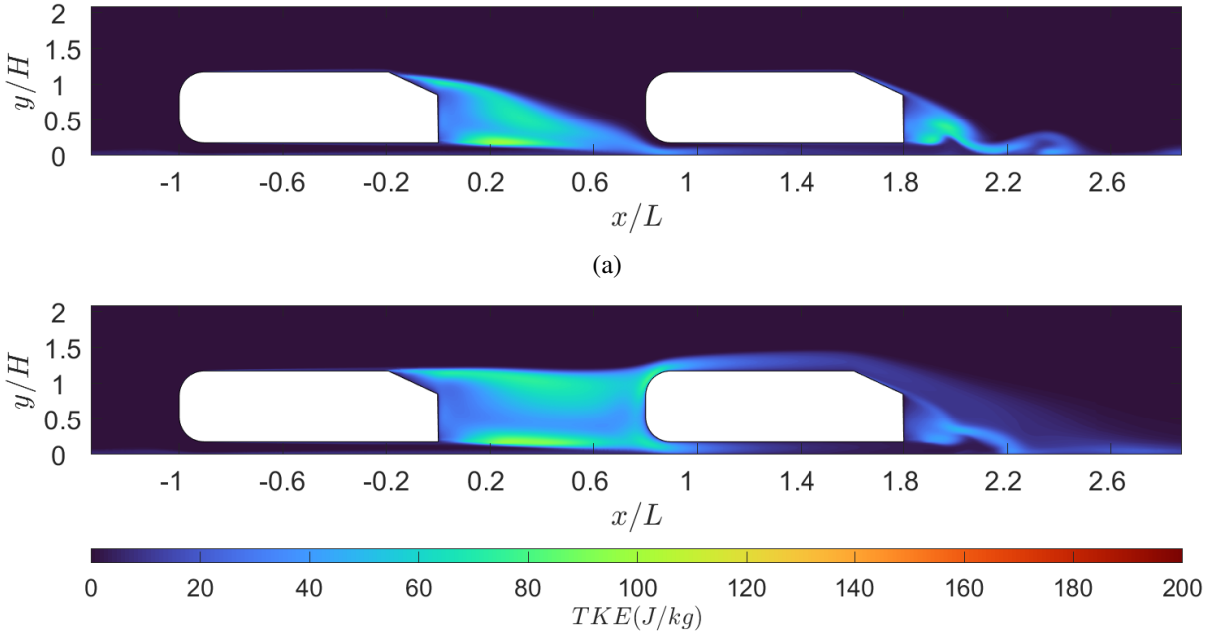

(a)

(b)

Figure 6.19: Turbulent kinetic energy field comparison of the (a) baseline platoon (b) platoon with a $10ms^{-1}$ jet at $d/L = 0.8$. Flow direction is left to right.

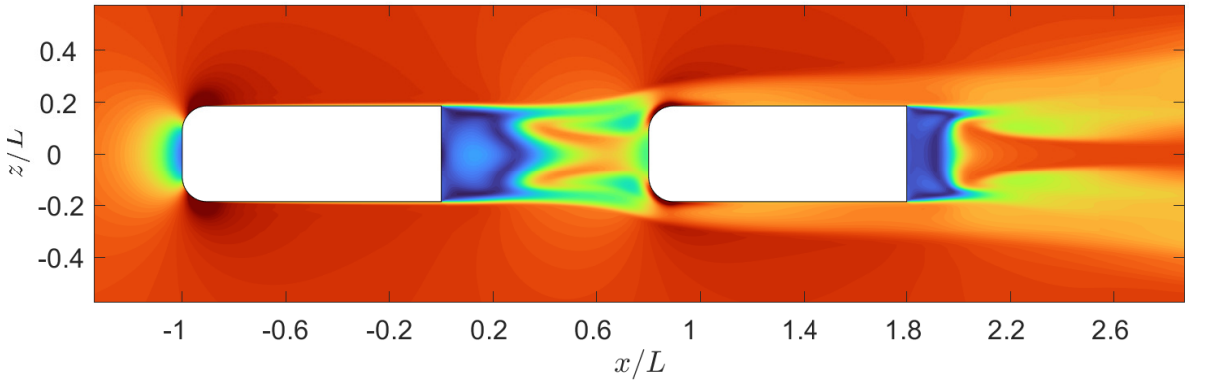

(a)

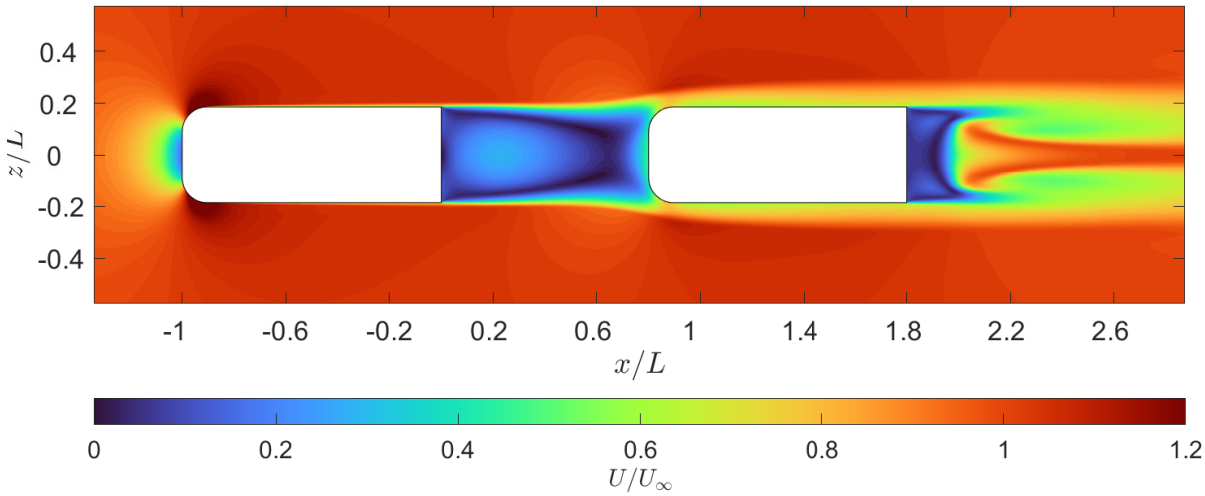

(b)

Figure 6.20: Average normalised velocity field comparison on a spanwise plane at $y = 0.15m$ for the (a) baseline platoon (b) platoon with a $10ms^{-1}$ jet at $d/L = 0.8$. Flow direction is left to right.

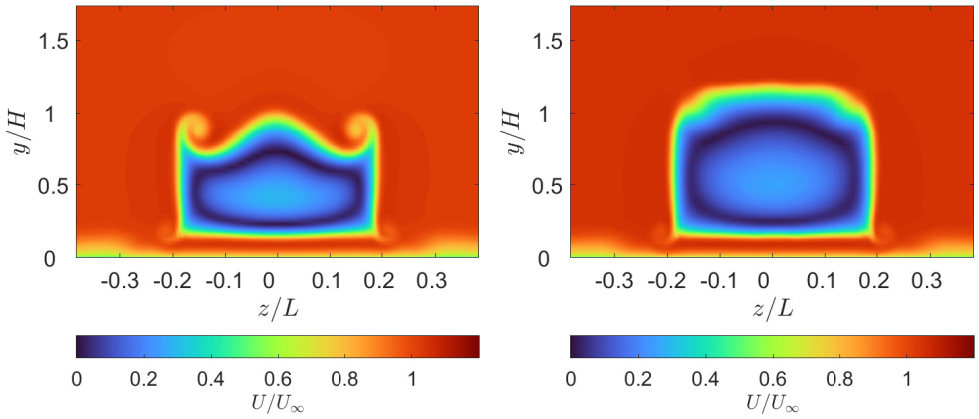

Figure 6.21: Average normalised velocity field comparison on a spanwise plane at $x = 0.15m$ for the (a) baseline platoon (b) platoon with a $10ms^{-1}$ jet at $d/L = 0.8$. Flow direction is left to right.

dramatically. This coincides with the flow reattaching to the rear slant of the front vehicle, significantly reducing the wake interactions between the two vehicles. For the flow control case, the flow separation is not induced by the presence of the rear vehicle, it is instead induced by the flow control device, therefore, flow separation persists through all of the inter-vehicle distances tested. Where this was a benefit over the shorter inter-vehicle distances, at $d/L = 0.8$ it becomes a hindrance. Figure 6.18 shows the normalised velocity field for the baseline and jet cases at $d/L = 0.8$. At this distance, the difference between cases is not particularly subtle. The wake impingement caused by the separated flow in the jet case is clearly visible, with stagnation occurring on the rounded portion of the leading edge of the rear vehicle. This rounded section of the rear vehicle provides a large portion of pressure recovery when the vehicle is in isolation, the introduction of the wake impingement disrupts the pressure recovery mechanism and results in an increase in drag of 25% when compared to an isolated 25° Ahmed vehicle.

In contrast, whilst the flow for the baseline case is not fully attached, the reduced wake size allows the rear vehicle to avoid the negative impact of wake impingement and instead returns to near isolated conditions. This difference between the two cases is clearest when analysing the turbulent kinetic energy shown in figure 6.19. In this example, the turbulent wake extends much further downstream for the flow control case, disrupting the pressure recovery mechanism of the rear vehicle.

The differences between the baseline case and the case with an induced jet are also visible in the spanwise direction. The introduction of the induced jet maintains flow separation over the trailing edge of the front vehicle. This helps to eliminate the C-pillar vortices and reduce the down-wash in the wake. This results in a much taller and wider wake in the inter-vehicle gap when compared to the baseline case (see figures 6.20 and 6.21).

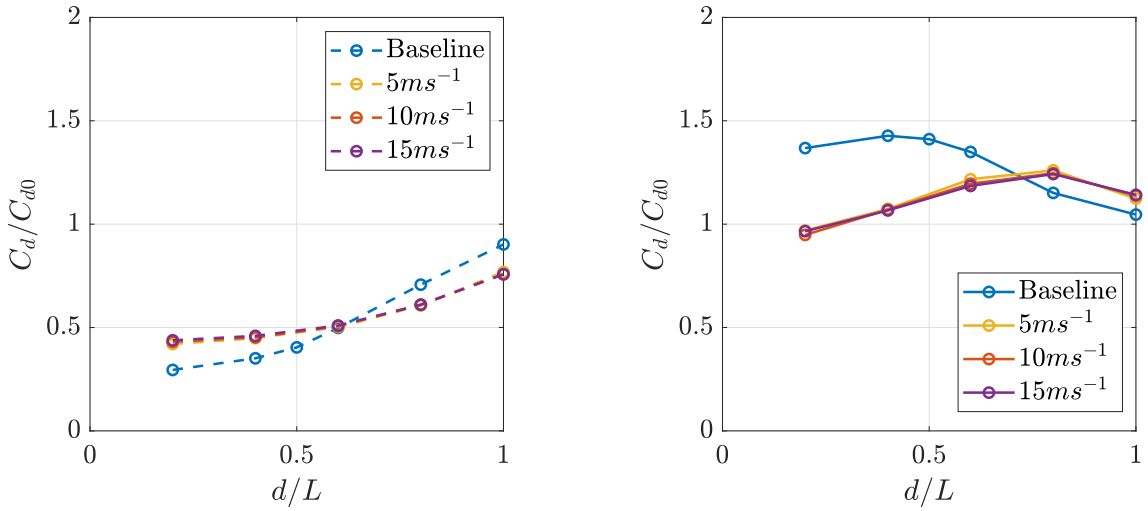

Figure 6.22: Normalised drag coefficient as a function of inter-vehicle spacing for a range of jet velocities for the (a) front and (b) rear vehicles in a platoon of two 25° Ahmed vehicles compared to the baseline case.

Although not perfect, this initial study clearly indicates the great potential that this type of flow control has in modifying the wake of the front vehicle in a platoon. The remainder of this section will investigate the effect that varying the flow control set up can have on the performance of the platoon.

6.6.2 Effect of jet velocity

The introduction of a counter flow jet upstream of the trailing edge slant was proposed as a less invasive way to promote flow detachment over the trailing edge of the front Ahmed vehicle. The intention of this was to increase the size of the wake produced by the front vehicle thus improving the performance of the platoon. The previous section highlighted the effectiveness of this technique by significantly reducing the drag coefficient of the rear vehicle when compared to the baseline platoon at short inter-vehicle distances (e.g. $d/L \leq 0.6$)

To further characterise the effect that the induced velocity produced by this flow control device has on the drag coefficient of the platoon vehicles, two additional jet velocities were used. These were $5ms^{-1}$ and $20ms^{-1}$ corresponding to $0.125U_\infty$ and $0.5U_\infty$ respectively. The drag coefficients for all of the test cases in this chapter is given in table 6.1. A comparison of the normalised drag coefficients for each vehicle is given in figure 6.22. Here, an interesting and unexpected result was observed. Whilst it is true that this type of flow control is effective at reducing the drag coefficient of the rear vehicle in a platoon, the result for the range of induced velocities are indistinguishable from one another. Our hypothesis for this is as follows: The flow over the 25° Ahmed vehicle is stable however is very susceptible to flow separation as the rear slant angle is near the critical angle of 30°. This has been discussed in a number of studies that

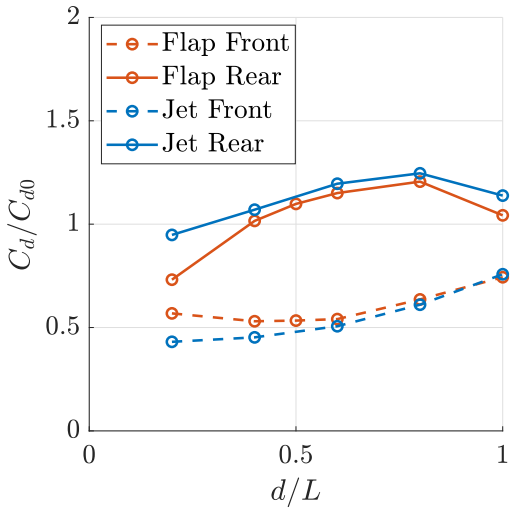

Figure 6.23: Normalised drag coefficient as a function of inter-vehicle spacing for platoon of two 25° Ahmed vehicles using (a) a 10°, 20*mm* flap (b) an $10m/s$ induced jet as a flow control device on the front vehicle.

highlight a small separation bubble that forms at the top of the trailing edge slant for the 25° Ahmed vehicle case [76, 89–91]. In essence, this means that even with a low velocity jet, in the region of $5ms^{-1}$, flow separation can be induced over the trailing edge of the vehicle.

Conversely, whilst the low velocity jets are strong enough to induce flow separation, once the flow has separated, their influence over the flow appears to be greatly diminished. This could be for two reasons; firstly as the jets are directed upstream, they will have limited influence over the downstream flow and secondly, the induced jets are not of a high enough velocity to have any lasting influence as the shear layer propagates downstream.

As a proof of concept, this shows that plasma actuators and other jet production mechanisms are capable of inducing flow separation and providing significant gains for platoons that suffer from inverted platooning conditions. This also indicated that the induced jets measured in the plasma actuator experiments in chapter 6 are of a high enough velocity to be applicable for this application.

6.6.3 Comparison of flow control

In this section, the differences between a representative platoon with an induced jet as flow control and a platoon with a flap as flow control will be compared. This will allow us to understand the differences in the application and analyse how each is effecting the profile of the front vehicle's wake. The 10°, 20*mm* flap and the induced jet at $10m/s$ were used for this study.

The normalised drag coefficient of the two platoons is compared in figure 6.23. Here both types of flow control perform similarly. The front vehicle in the jet case has a slightly lower drag coefficient with the opposite being true for the rear vehicles. The largest difference between the

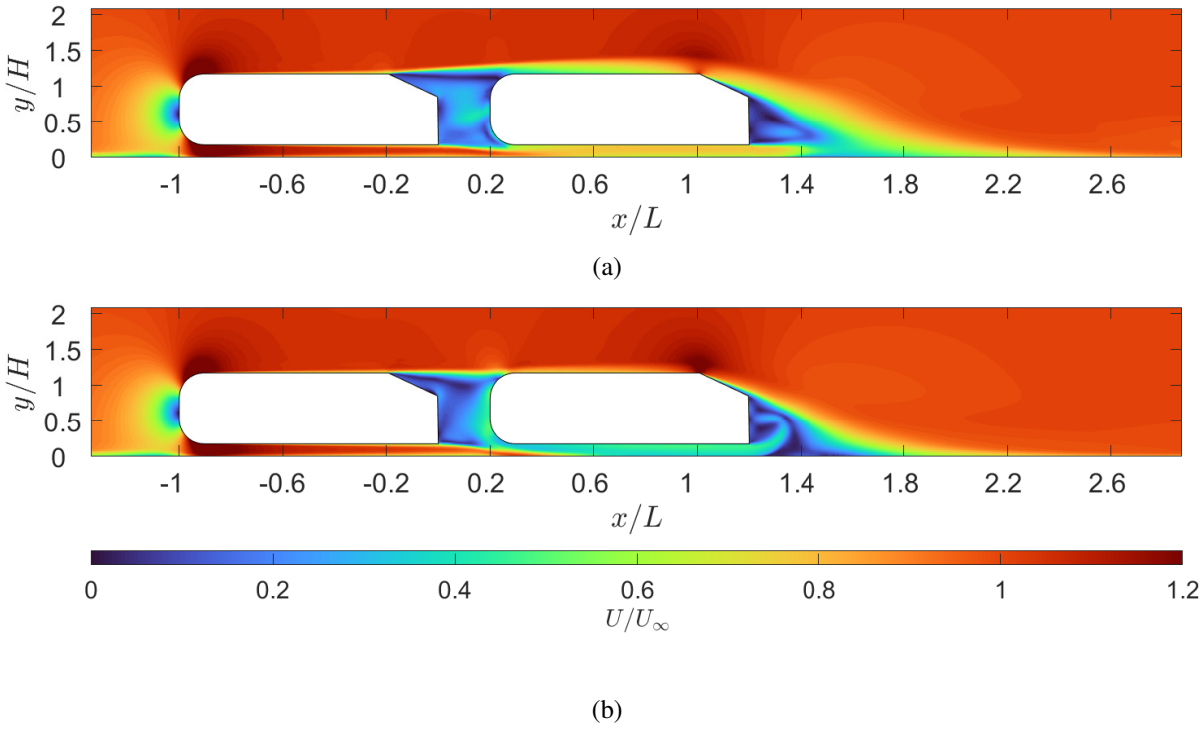

Figure 6.24: Average normalised velocity field comparison between (a) the baseline platoon and (b) a platoon where the front vehicle has a $10ms^{-1}$ jet flow control device for an inter-vehicle distance of $d/L = 0.2$. The flow direction is left to right.

two cases is seen at $d/L = 0.2$ where the rear vehicle in the flap case has a 25% lower drag coefficient.

Figures 6.24 and 6.25 show the normalised velocity field and turbulent kinetic energy respectively in the streamwise direction. The main cause of the difference in drag coefficient comes from the angle of the flap, deflecting the turbulent shear layer over the leading edge of the rear vehicle. It is also clear that the flap results in an increase in turbulent kinetic energy where the flow comes off of the flap. The jet case does not deflect the shear layer as high and this results in increased wake impingement and a higher drag coefficient for the rear vehicle.

As both flow control devices are designed to effect the flow in the streamwise direction, it is of no surprise that the spanwise flow is relatively unchanged between the two flow control cases. Figures 6.26 and 6.27 show the flow in the spanwise direction, the only clear difference is the inclusion of two small vortices forming off of the edges of the flap. These are not present in the induced jet case.

As the vehicles move further apart, the angled shear layer caused by the flap helps to reduce the level of wake impingement on the rear vehicle. Conversely, the separation caused due to the induced jet creates a slightly lower wake, this increases the wake impingement and results in a slightly higher drag coefficient for the rear vehicle in this case (see figures 6.28 and 6.29).

Similarly to the shorter spacing, the wake profile in the spanwise direction remains relatively unchanged between the two different flow control cases (see figure 6.30). The small vortices

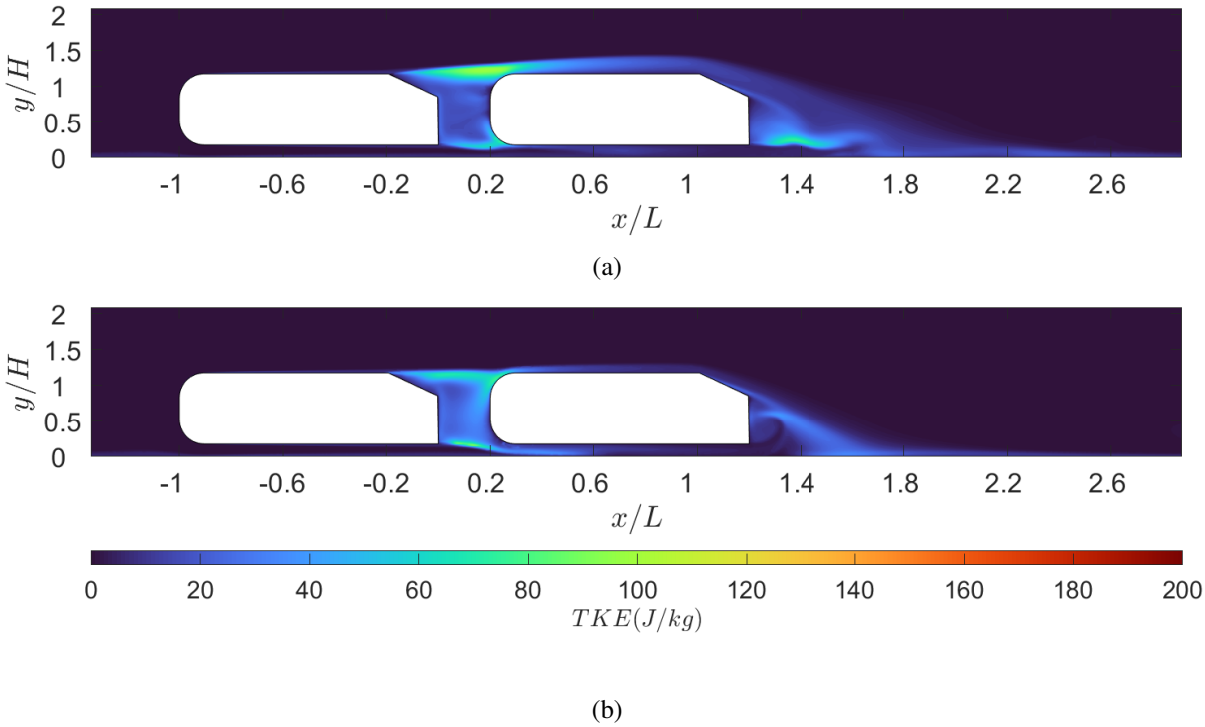

(a)

(b)

Figure 6.25: Turbulent kinetic energy field comparison of the (a) baseline platoon (b) platoon with a $10ms^{-1}$ jet at $d/L = 0.2$. Flow direction is left to right.

generated by the flap are still visible in figure 6.31 at $d/L = 0.8$ however this will have a very limited impact on the drag coefficient of the rear vehicle.

In a more general sense, it was shown that the proposal of increasing the size of the front vehicle's wake to reduce the level of wake impingement on the rounded leading edge of the rear vehicle is an effective way to improve the efficiency of a platoon. However, it could be possible to achieve greater drag reductions through the use of a flow control device that has a greater influence over the detached flow and shear layer of the front vehicle. In addition, whilst this method of flow control application was able to alleviate some of the negative effects of inverted platooning, more work is still required to create a flow control system where both of the vehicles in the platoon receive a consistent drag reduction over a wide range of inter-vehicle distances.

6.7 Conclusions

The aim of this chapter was to asses the application of a different flow control device on a platoon of two 25° Ahmed vehicles. Initially an experimental characterisation of a plasma actuator was conducted and a velocity profile was measured. This velocity profile was then adapted into a boundary condition for the application on the baseline platoon.

Plasma actuators were selected as an alternative flow control device as they have the benefit of being able to operate actively. This means they can adapt to the current flow conditions or be used in a pulsing manner to excite different natural frequencies in the wake shedding. This is

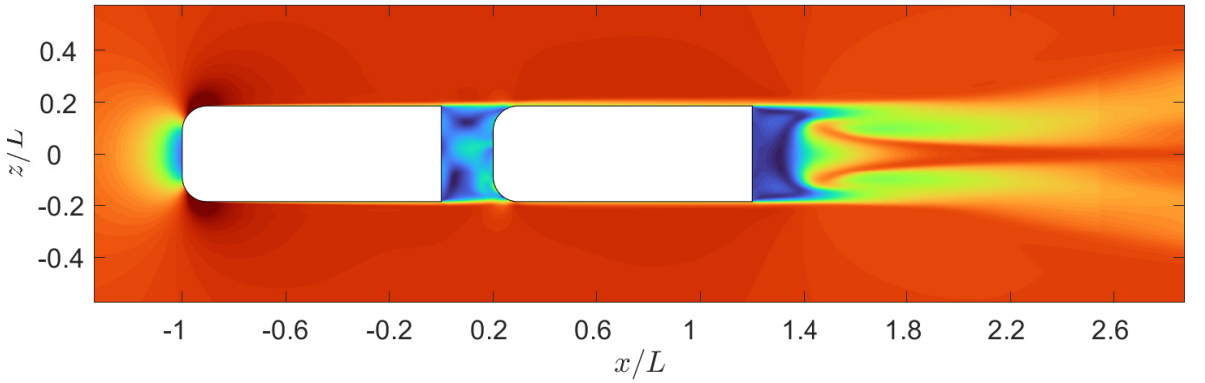

(a)

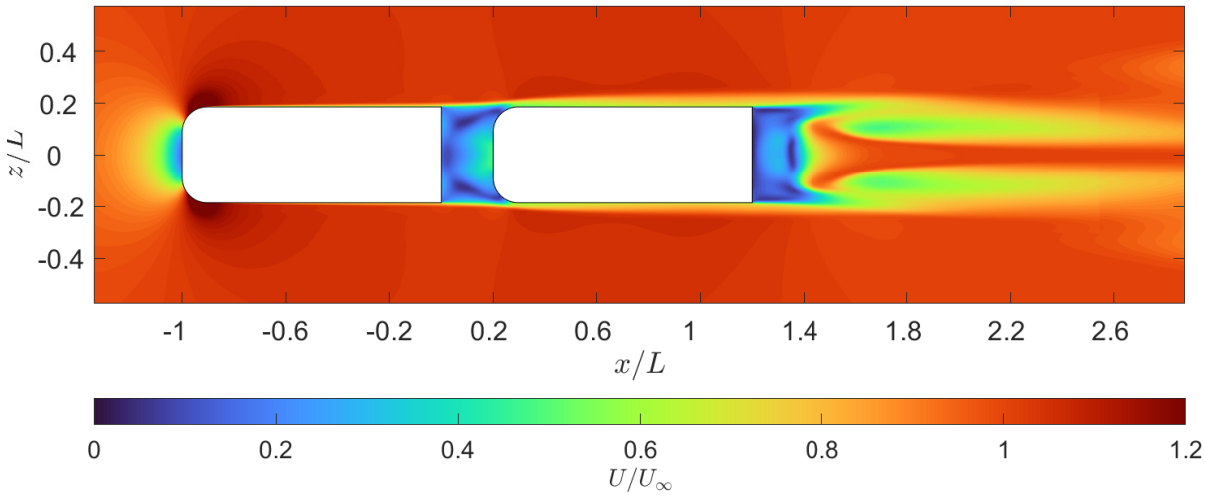

(b)

Figure 6.26: Average normalised velocity field comparison on a spanwise plane at $y = 0.15m$ for the (a) baseline platoon (b) platoon with a $10ms^{-1}$ jet at $d/L = 0.2$. Flow direction is left to right.

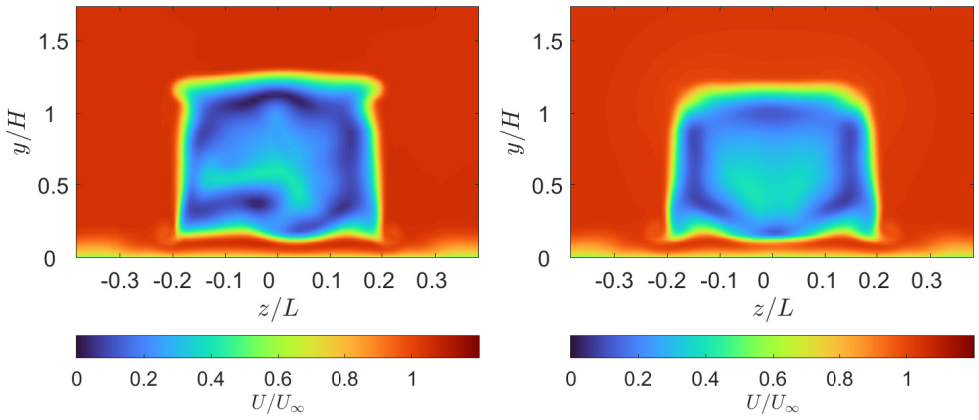

Figure 6.27: Average normalised velocity field comparison on a spanwise plane at $x = 0.15m$ for the (a) baseline platoon (b) platoon with a $10ms^{-1}$ jet at $d/L = 0.2$. Flow direction is left to right.

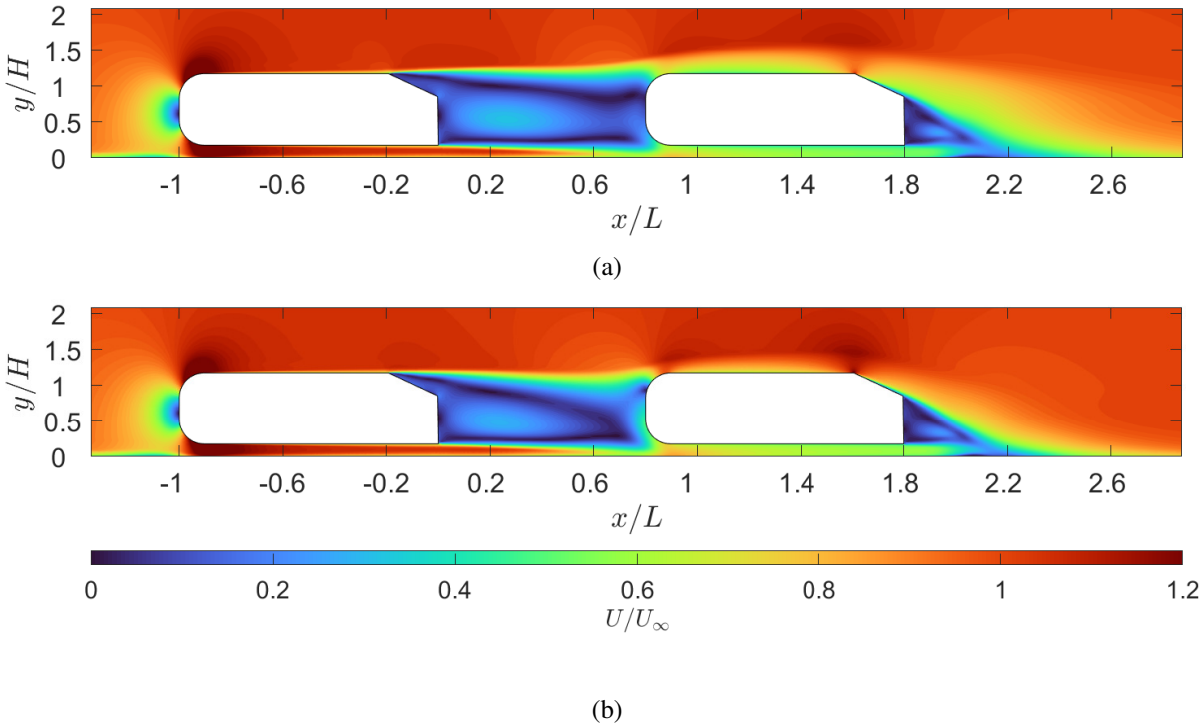

Figure 6.28: Average normalised velocity field comparison between (a) the baseline platoon and (b) a platoon where the front vehicle has a $10ms^{-1}$ jet flow control device for an inter-vehicle distance of $d/L = 0.8$. The flow direction is left to right.

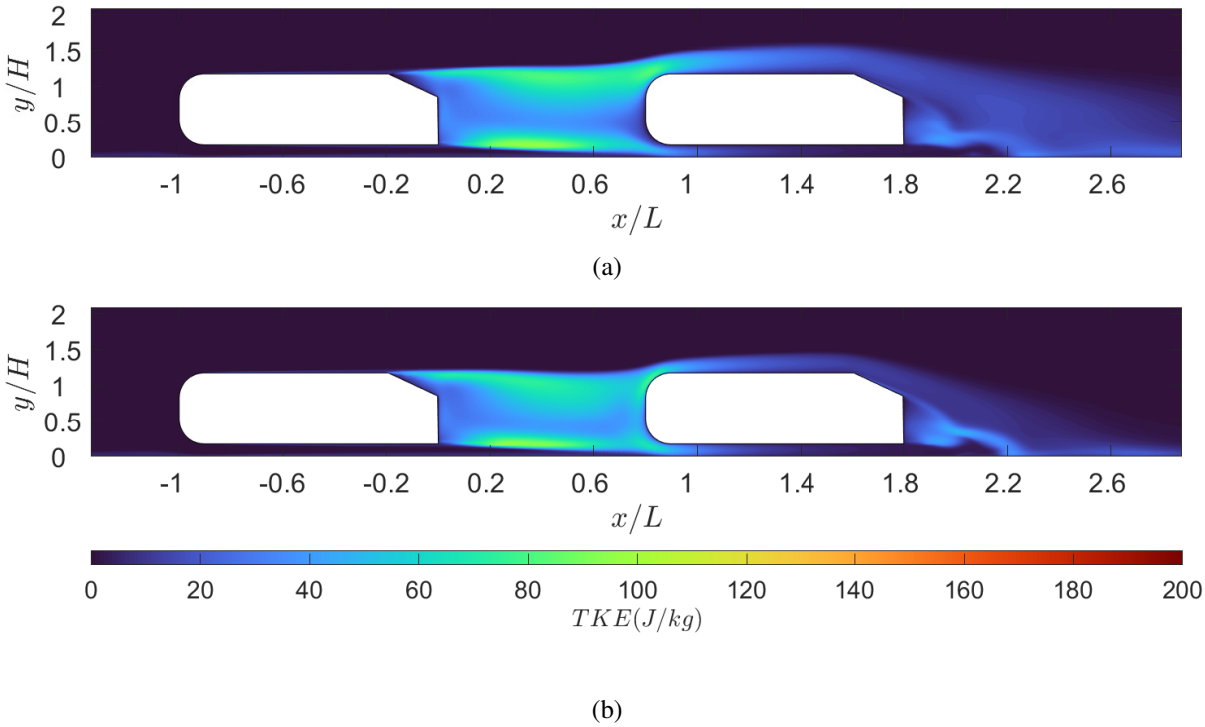

(a)

(b)

Figure 6.29: Turbulent kinetic energy field comparison of the (a) baseline platoon (b) platoon with a $10ms^{-1}$ jet at $d/L = 0.8$. Flow direction is left to right.

definitely an area with great possibilities that should be that investigating more thoroughly in the future. Plasma actuators are still in the early stages of development and although they present a very exciting solution to flow control, there are also still many challenges to overcome. The primary challenge is the much increased safety requirement, not just in a real world setting but also in a wind tunnel environment as plasma actuators utilise high voltage electricity.

Through the implementation of an upstream facing jet with the same velocity profile as measured experimentally by the plasma actuator, the drag coefficient of the rear vehicle in a platoon of two 25 Ahmed vehicles was reduced by as much as 25% at short inter-vehicle distances. As the inter-vehicle distance increased, the drag benefits slowly reduced, eventually causing the rear vehicle to have an increased drag coefficient at $d/L = 0.8$ and 1.0.

Although showing real promise as a flow control solution, varying the induced velocity had no effect on the measured drag coefficients for either vehicle. This implies that the flow control device, whilst initially good at causing flow separation, has very little authority over the post separated flow. Despite this, plasma actuators remain an extremely versatile flow control solution. This study presents a first look into one way jets could be applied to the problem of inverted platooning, further flow authority could be achieved by pulsing the actuator and exciting harmonic frequencies in the shear layer however this was out-with the scope of this particular study.

This concept was envisioned as an alternative to the implementation of a flap as flow control. When comparing the two types of flow control it is clear that the jets were less effective as a

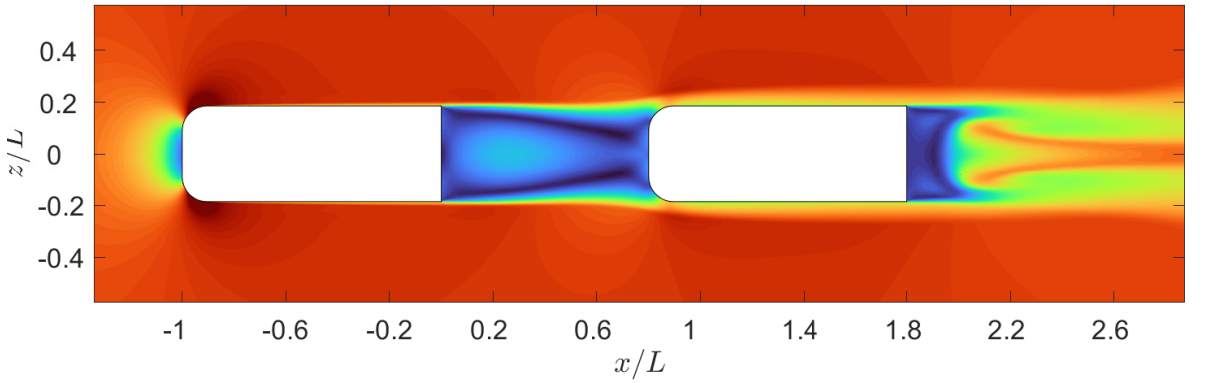

(a)

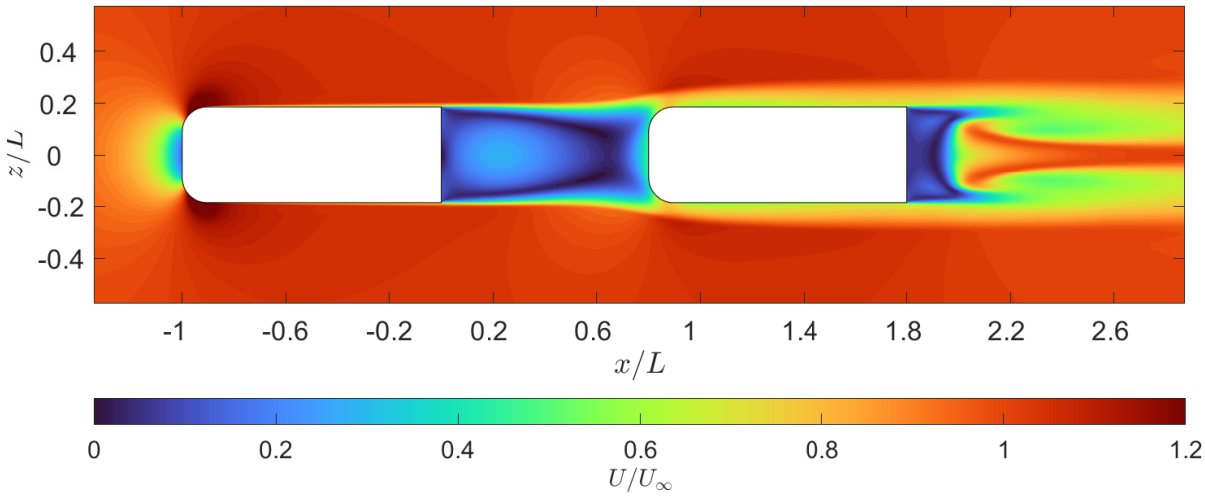

(b)

Figure 6.30: Average normalised velocity field comparison on a spanwise plane at $y = 0.15m$ for the (a) baseline platoon (b) platoon with a $10ms^{-1}$ jet at $d/L = 0.8$. Flow direction is left to right.

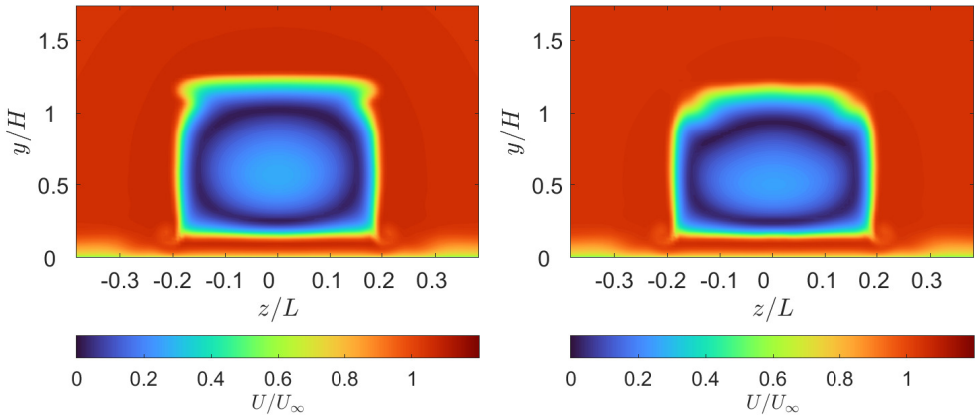

Figure 6.31: Average normalised velocity field comparison on a spanwise plane at $x = 0.15m$ for the (a) baseline platoon (b) platoon with a $10ms^{-1}$ jet at $d/L = 0.8$. Flow direction is left to right.

flow control device for this application. Whist they were able to promote flow separation in the same way as the flaps, they had little influence over the detached flow ultimately resulting in higher drag coefficients for the rear vehicle when comparing the two flow control techniques. Although the flaps were able to manipulate the detached flow, their effectiveness was still less than anticipated.

In the short term, plasma actuators would be well suited to applications in very controlled environments such as military applications however would be far less suited to be used as a consumer product. Whilst flaps are more limited in terms of their active flow control capabilities, they are far simpler to implement in a wind tunnel and are much more likely to pass regulatory requirements for passenger vehicles. Many road vehicles like the Audi TT, BMW M4 or Mercedes-AMG GT R already implement deployable flap like spoilers therefore, although these vehicles are in the higher price bracket in terms of cars, it would not be too big a step to introduce flaps as a flow control solution in the near future.

Chapter 7

Conclusion

This thesis presented the results of an experimental and computational investigation on the complex aerodynamics of vehicle platooning. Two main areas were addressed: the dependency of platooning outcomes on vehicle geometry and the potential of flow control to improve adverse platooning outcomes. Along with the conclusions provided at the end of each chapter, this chapter will provide a compiled version of the key outcomes with an explanation of how each objective was completed. This is followed by a section detailing suggestions for future work.

7.1 Summary of key outcomes

7.1.1 Effects of platoon geometry

One of the key objectives of this work was the investigation of the geometric features that create inverted platooning in order to provide a better understanding of its causes. By systematically morphing a cuboid into a 25° Ahmed vehicle in a parametric, URANS-based simulation study, new light was shed on how classical platooning conditions can be changed to inverted platooning conditions by simple changes in geometry. The main outcome was that vehicle geometry plays a key role in determining the effectiveness of a platoon. In general, more streamlined vehicle geometries tended to perform worse in platoons than bluff vehicles. Focusing on the aerodynamic features, it was shown how wake impingement on the rounded leading edge of a trailing Ahmed vehicle causes a dramatic localised increase in surface pressure. This fundamentally increased the overall drag of the vehicle. From this, study a much clearer idea of the mechanisms that cause inverted platooning was obtained.

The main motivation for this research comes from the ground transport sector, where platooning has the potential to provide significant fuel savings. Modern car design is focused on achieving low drag coefficients by using curved surfaces to maintain flow attachment and reduce recirculation regions. In contrast, the morphing study showed that this type of design will be much more susceptible to inverted platooning conditions. In reality, a ground vehicle will - even

with the widespread implementation of platooning - travel in isolation a lot of the time, therefore, maintaining a streamlined vehicle shape would still be highly desirable. As a consequence, alternative methods for improving platooning outcomes, such as the application of flow control, are of high interest.

7.1.2 Computational exploration of flow control in platoons

Equipped with improved understanding of inverted platooning provided by the vehicle morphing study outlined in chapter 3, the secondary aim was to explore how to utilise flow control with the intention of alleviating or eliminating inverted platooning conditions. In addition, this extra data would also contribute to achieving the primary aim of further understanding the complex aerodynamics of simplified vehicle platoons.

The results of the previous chapter highlighted a range of positive and negative flow features that can occur in platooning. Flow control devices could be one solution used to trigger flow behaviour that is beneficial in the context of vehicle platooning. Flaps were implemented as a simple method of flow control. These were tested at 3 angles (0°, 10° and 20°) and for 3 flap lengths ($0.005L$, $0.01L$ and $0.02L$). Using flaps as flow control, a maximum drag reduction of 50% was achieved for the rear vehicle compared to the baseline platoon at short inter-vehicle distances. Although the flow control was effective at alleviating adverse platooning results over short distances, it was relatively ineffective for inter-vehicle distances of $d/L > 0.5$.

To the best of our knowledge, this was the first study to implement flow control on a platoon of two 25° Ahmed vehicles and the first study to investigate flaps as a flow control option on any platoon. The use of the flaps to induce flow separation and create a larger wake was inspired by the improved understanding of the effects of vehicle geometry. For this reason, the flaps were designed to reduce the effects of wake impingement on the rear vehicle of the platoon. The implementation of flaps on a ground vehicle would also face much lower regulatory hurdles compared to plasma actuators since flap-like devices, such as deployable spoilers, already exist on some sports cars.

7.1.3 Experimental platoon proof of concept

The final objective of this study was to conduct a wind tunnel investigation to follow on from the computational results. Additionally, the experiments were to provide a proof of concept for the use of flow control on platoons due to the known limitations of URANS in modelling complex turbulent flows. Initially, analysing the flow around an isolated Ahmed vehicle highlighted that the model's streamwise location in the wind tunnel has a significant effect on the measured drag coefficient. This is an important measurment that is rarely mentioned in papers on platooning experiments and may thus have been neglected in some previous studies. A possible consequence of neglecting this position dependency could be an incorrect interpretation of the drag

measurements at longer inter-vehicle distances. As platooning investigations usually report drag measurements as normalised drag coefficients, having an understanding of the effect of streamwise location for each vehicle provided a more representative normalisation technique. It was concluded that more emphasis should be put on this step for future experimental work.

Following this, a baseline platoon consisting of two 25° Ahmed vehicles was characterised using drag force and PIV measurements. A Reynolds number range of $1 \cdot 10^5$ to $3 \cdot 10^5$ was covered: a strong Reynolds number dependence was found for the front vehicle in the platoon with a far lesser dependence on Reynolds number for the rear vehicle. The Reynolds number dependency of the rear vehicle grew at larger inter-vehicle distances. At higher Reynolds numbers, platooning effects could be maintained over longer inter-vehicle distances. In addition, some platooning configurations showed a far stronger Reynolds number dependence, for example, in the case of the baseline platoon at $d/L = 0.8$, a switching between two distinct flow regimes was observed over the investigated Reynolds number range.

A similar investigation was then carried out for an heterogeneous platoon. Here a squareback Ahmed vehicle was used as the front vehicle in the platoon. The sharp corner at the trailing edge of the squareback Ahmed vehicle produced a flow separation that was much less Reynolds number dependent. Therefore, this platooning configuration was far less Reynolds number dependent in general. This again highlighted the requirement for further research on the Reynolds number dependency of platoons. On the roads, there are a wide range of vehicle shapes which will potentially influence each other differently dependent on the speed they are travelling at.

In the final stage of the project, the potential of flow control using flaps was investigated for a platoon composed of two 25° Ahmed vehicles. To the best of our knowledge, this was the first experimental investigation of its kind. Through the use of loadcell measurements and PIV the influence of introducing a flap as flow control on the top of the trailing edge slant of the front vehicle of the platoon was investigated. Three flap angles were tested, 0°, 10° and 20° to line up with the previous computational URANS investigation. In addition, two flap lengths of $0.02L$ and $0.05L$ were tried. This method was successful in its objective of reducing the extent of the impingement of the wake from the front vehicle on the leading edge of the rear vehicle as seen in the corresponding PIV measurements. However, while some drag coefficient improvements of the rear vehicle were achieved when compared to the baseline platoon, the flow control was in general less successful at reducing the effects of inverted platooning than predicted by the earlier URANS simulations. Some success was observed for the 10° and 20° flaps at $d/L = 0.2$ where the drag coefficient of the rear vehicle was reduced by around 9% compared to the baseline result. Whilst drag reductions were lower than expected, the experiments nevertheless provided a proof of concept for platoons with flow control. This study thus represents the first step in the development of flow control targeted at improving the outcomes of platoons subject to 'inverted' platooning conditions.

7.1.4 Alternative flow control solutions for platooning

Flaps are a very simple form of flow control and were shown to have measurable success in adapting the wake of the front vehicle to produce more favorable platooning conditions. A more complex alternative flow control device that was of interest was the plasma actuator due to its high versatility and its previous successful application to flow control on HGV models. Chapter 6 provided a comprehensive characterisation of a serrated plasma actuator to be used as a flow control device. In the field of plasma actuator research, experimental setup can vary greatly between investigations making it challenging to quantitatively compare studies. By maintaining a consistent setup, a detailed understanding of the effects of electrical input frequency, electrical input waveform, dielectric material construction, modulation frequency and duty cycle was achieved.

A key finding was that the input frequency required to produce the peak induced velocity varies for each actuator and is dependant on electrode design and dielectric construction. In addition, it was found that whilst a material with a lower dielectric coefficient (like Kapton) is more efficient at inducing a jet, it breaks down more readily, ultimately resulting in reduced performance. The maximum induced flow speed were found to match previous results published in the literature for this design. In general, the results indicate that the plasma actuator can be an extremely versatile tool for flow control applications if the safety concerns can be mitigated.

Following this, the induced jet produced by the plasma actuator was mimicked using a tangential surface velocity boundary condition in URANS simulation. The resulting simple induced jet above the surface provided a good approximation of the experimental velocity profile of the induced jet produced by the serrated plasma actuator. Induced jets at speeds of 5, 10 and 20ms^{-1} were tested as flow control devices at the top of the trailing edge slant of the front vehicle in a platoon composed of two Ahmed vehicles with 25° rear slant angle. The jets were directed upstream to trigger the early separation of the flow. Using this method, drag reductions of up to 31% for the rear vehicle compared to the result for the baseline platoon without flow control were achieved.

7.2 Suggestions for future work

This study contributed to identification of the mechanisms causing ‘inverted’ platooning by conducting both computational and experimental investigations of inverted platoons with special focus on the complex flow in the inter-vehicle gap between two platoon members. Simple methods of flow control were explored which were successful in improving inverted platooning conditions.

Going forward, future research on this topic should put more emphasis on understanding the interaction between the shear layer produced by the front vehicle, and the leading edge of the rear vehicle. It is important to remember that, initially, the Ahmed vehicle was designed

to understand the effects of rear slant angle on the drag coefficient of the vehicle. Whilst the Ahmed body is one of the most commonly used simplified vehicle models for both isolated and platooning investigations, for the study of geometry effects on platooning it would be highly desirable to have a vehicle geometry that also allows a systematic variation of the leading edge of the body, e.g., different degrees of streamlining, not only the modification of the rear of the body as is the case for the Ahmed body. Nevertheless, future research can only progress to more complex models and platooning configurations once the fundamentals have been fully understood. It is therefore perhaps worthwhile to first understand to what extent the rounded leading edge affects the platoon and to what extent this behaviour is applicable to more realistic road vehicles.

Whilst URANS simulation was an effective tool to cover the large range of test cases proposed in this thesis, in the future, more advanced computational methods could be utilised to provide additional detail of the complex flow of platoons. As discussed in section 2.1.3, the implementation of LES or IDDES computational methods is not a quick fix for URANS simulations, however, if done correctly and with larger resources, they could prove to be an invaluable asset for more detailed analysis the flow structures in the wake of platooning vehicles.

This could also be achieved through the use of additional experimental measurement techniques. Although adding to the complexity and expense of model design, the addition of pressure tappings on the vehicles in a platoon platoon would provide additional insight onto the velocity field PIV measurements. Whilst pressure measurements on each surface of both vehicles would be an ideal scenario, the inclusion of some pressure data on the rounded leading edge of the rear vehicle would provide valuable insight into the effect of wake impingement on the rear vehicle.

In addition, the inclusion of cross-plane or stereo-PIV measurements could help further inform the analysis by shedding light on the three dimensional nature of the flow in the wake of an Ahmed vehicle with a 25° rear slant. These techniques again add additional complexity to the experimental setup with caution having to be taken to ensure optical access and laser safety. These limitations make the techniques unfeasible in the current Handley-Page wind tunnel facility without significant investment, however, there are many facilities that boast these capabilities.

This study presented one of the first, tentative, steps into introducing flow control on platoons. Whilst an extensive computational investigations comparing two different flow control techniques was conducted, the scope of the wind tunnel investigation was limited to the use of flaps. Our primary suggestion for future work in this regard would be to introduce plasma actuators, a much more versatile form of flow control, to a platoon. The simulation work in this thesis showed some promise for this area of research. Plasma actuators could not only be applied in a steady configuration, but could be applied in pulsating mode to disrupt or enhance specific modes in the shear layer. However, compared to a simple flap there are many important safety hurdles to overcome for plasma actuator experiments in a wind tunnel, which is why this

direction could not be explored within the time frame of this project.

Future work in platooning should take a more in-depth look at flow control implementation in general. By analysing frequency responses of the shear layer a more targeted approach could be achieved. It was hypothesised that flow control intended to disturb specific oscillation frequencies in the wake of the front vehicle could potentially yield improved outcomes. There are a number of ways this could be achieved, many of which are outlined in the literature review on flow control on flows past bluff bodies (see section 2.2.2), from plasma actuators to pulsed jets or pneumatic flaps.

In the field of plasma actuators, two avenues for future investigation were highlighted. Primarily, this involved continuing the previous work on input waveform. It was observed that the velocity of the induced jet is affected by the type of waveform used and this input parameter could be further optimised. In addition, a more rigorous test of the theory regarding 'harmonic' frequencies causing an irregular relationship between the frequency of input voltage and the induced jet is required. This could be achieved by altering the size or quantity of metal used for the electrodes to ascertain whether this has an effect on the optimum inputs for the device.

On a more general note, it is vital to obtain a better experimental understanding of how Reynolds number affects platooning. Ideally, a large range of Reynolds numbers would be tested on the same experimental setup. This is difficult to achieve since test section length and size play a big factor in dictating the available range of Reynolds numbers. However, wind tunnel facilities like the GVPM Wind Tunnel at the Politecnico di Milano exist where a large platoon could be tested. Similarly the 'TRAIN' test rig utilised by Robertson et al. [104] could be a possible alternative solution to the problem. Such larger facilities would also allow to go beyond two body platoons to the investigation of platoons composed of three or more vehicles.

In the wider context of platooning, aerodynamics is just one of the building blocks that will go toward making platooning a reality on modern roads. The further development of a wide range of engineering systems is also required. Primarily, the consistent improvement of automated or semi-automated vehicles is vital to allow platoons to travel at the shorter inter-vehicle distances required for optimum efficiency in a safe manner. This could be helped by the adaption of road infrastructure to include specific lanes for automated or platooning vehicles. However, these techniques will be limited without the implementation of a common protocol allowing vehicles to communicate not just with vehicles by the same manufacturer but across manufacturing platforms. One of the final building blocks is of course the legislation requirements and social acceptance of platooning. The ideas discussed previously may seem quite radical however, with each research paper a stronger case for platooning is made and the appropriate legislation should follow.

Appendix A

Detailed description of meshing scheme

In the following appendix, we will provide additional data to support the description of the meshing scheme outlined in section 3.2.2. Here we will discuss the dimensions of each volume refinement for the case of an isolated 25° Ahmed vehicle, along with the associated maximum cell size for each refinement region. We will then detail the surface refinement strategy outlining prism layer dimensions.

A.1 Volumetric refinement

A staggered volumetric refinement approach was implemented using 4 refinement regions as detailed in figure A.1. The base cell size for the domain began at $0.5H$. From here, the first refinement region reduced the cell size to $0.25H$. This region extended from $x = -2.4$ to $x = 3.378$, was $2m$ wide (centred along the centre plane) and was the full height of the domain.

The cell size for each refinement step continued to reduce by half, starting from $0.25H$ and ending at $0.03H$ at the smallest refinement region. A full description of the size of each region is given in table A.1. The length of each refinement region was extended by varying amounts when introducing a second vehicle for the platooning studies. This was to maintain an

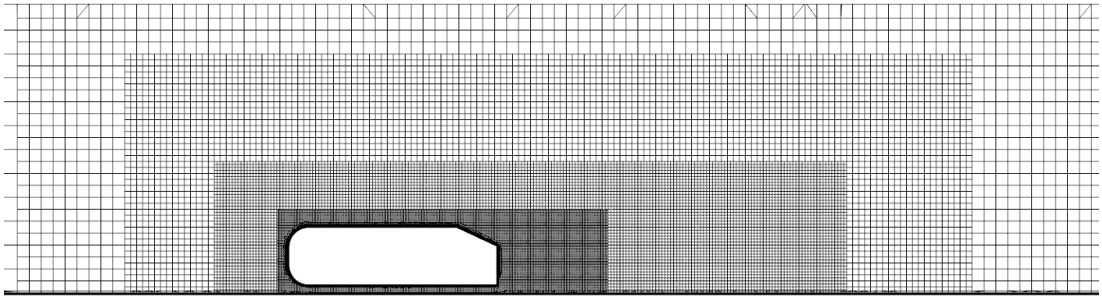

Figure A.1: Illustration of volumetric refinements over an isolated Ahmed vehicle with a 25° rear slant. Similar to figure 3.4 but repeated here for reference during discussion of meshing scheme.

Refinement region	x upstream	x downstream	Width	Height	Cell size
Region 1	-2.40	3.38	2.00	1.46	$0.250H$
Region 2	-1.85	2.38	1.70	1.18	$0.125H$
Region 3	-1.39	1.75	1.36	0.67	$0.063H$
Region 4	-1.10	0.56	0.60	0.43	$0.031H$

Table A.1: Dimensions for volumetric refinement regions the the computational investigation of an isolated 25° Ahmed vehicle. All dimensions are in meters.

Refinement surface	Number of layers	Stretching Coefficient	Total Thickness [m]
Vehicle Body	11	1.2	0.025
Vehicle Base	9	1.2	0.025
Road	6	1.5	0.02

Table A.2: Prism layer settings for the surface refinement in the the computational investigation of an isolated 25° Ahmed vehicle.

appropriate level of refinement downstream of the rear vehicle and was achieved by adding one vehicle length plus the distance between the vehicles to the downstream x coordinate of each refinement region.

A.2 Surface refinement

A prism layer refinement strategy was employed in order to provide an improved representation of boundary layer development along the no-slip surfaces. The surface refinements were split into three distinct categories: the vehicle body, the vehicle base and the road surface.

Over the main portion of the vehicle, 11 prism layers were used with a stretching coefficient of 1.2. This implies that the height of each cell, as one moves away from the model surface, will be 1.2 times larger than the cell previous. The total thickness of this prism layer was capped at $0.025m$.

The 'base' of the vehicle, including both the rear slant and the base, had significantly more, low velocity, detached flow than over the rest of the vehicle. To accommodate for this, slightly larger cells were used to maintain the appropriate wall y+ approximations. Here 9 prism layers were used however the stretching and total thickness was kept consistent to improve the transition between the two prism layer schemes used on the vehicle.

Finally, the flow over the road was captured using 6 prism layers with a total thickness of $0.02m$ and a stretching coefficient of 1.5. The dimensions for each surface refinement are outlined in table A.2.

The total mesh size for this simulation was 3.6 million cells. When expanded to incorporate additional vehicles for the platooning study, the mesh size grew to around 4 million cells, depending on the inter-vehicle distance selected. Using a time step of $0.0005s$, a convective Courant number of 1.081 was achieved.

Appendix B

Photographs of arcing on plasma actuators

This appendix is included to provide additional visual representations of arcing as discussed in section 6.3.1. We found a number of scenarios that induced arcing on our plasma actuators. Primarily, saturation and the resultant breakdown of the dielectric material was the main instigator for arcing to occur. This can be seen in figure B.1 (a) where a black spot is visible on the tip of the serrated exposed electrode. This example is of the KMK actuator, the thinned dielectric layer made the actuator very susceptible to this type of failure which is ultimately why they performed worse than their PCB counterpart.

Another cause for arcing was the addition of excess metal near the exposed electrode. As seen in figure B.1 (b), along the top edge of the actuator a small portion of copper was left after the etching process. Although not connected to any wiring, this tended to promote arcing with some spectacular consequences. Future iterations of this design took special care to remove all excess copper before installation and operation of the actuators.

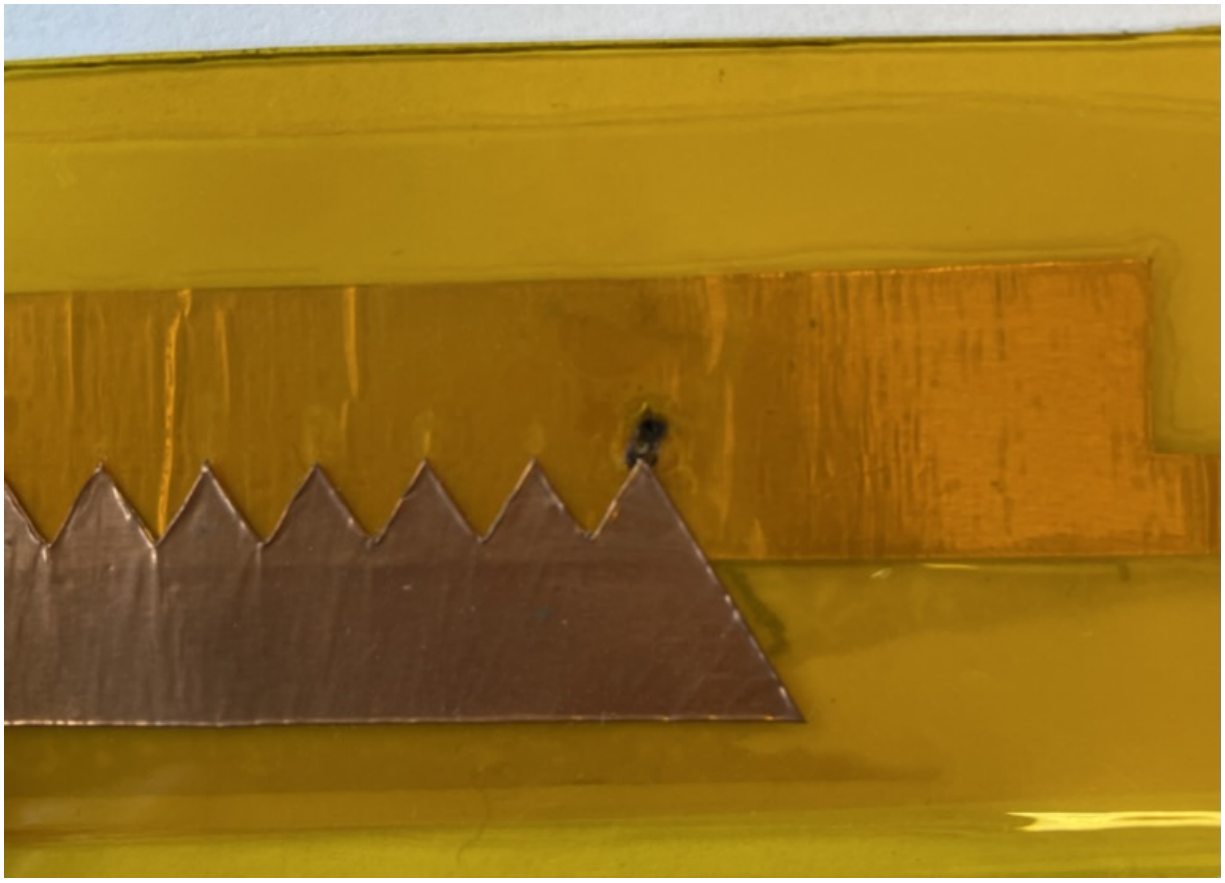

(a)

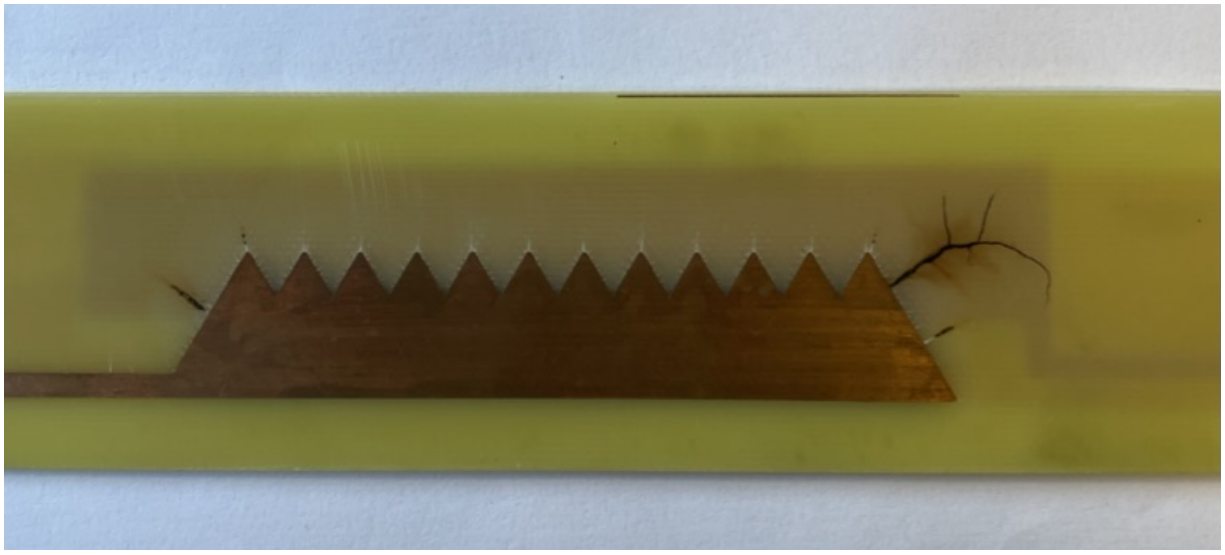

(b)

Figure B.1: Examples of arcing on the (b) KMK and (b) PCB based plasma actuators.

Appendix C

Experimental platooning measurements at lower Reynolds numbers

To provide additional perspective on the Reynolds number dependency of platoons, the data for a selection of lower Reynolds number platoons with a 25*mm* flap as flow control are laid out in the following appendix. This data was omitted from the main thesis as the discussion surrounding the aerodynamics of these platoons is broadly similar to their higher Reynolds number counterparts outlined in detail in section 5.3.4.

Figure C.1 gives a comparison between the baseline case and three flap angle cases for the platoon with a 25*mm* flap as flow control at a Reynolds number of $1 \cdot 10^5$. Figure C.2 shows the same four cases at a Reynolds number of $1.9 \cdot 10^5$. Whilst the results are fairly similar to the flap cases discussed in section 5.3.4, some additional insight on the Reynolds number dependency of the results can be gained by comparing both figures together.

For the lowest Reynolds number case, we observe that the platooning effects on the rear vehicle are significantly reduced. Here the drag coefficient remains fairly similar to the isolated Ahmed vehicle, especially for inter-vehicle distances greater than $d/L = 0.4$. As Reynolds number increases to from $1{\cdot}^5$ to $1.9{\cdot}^5$, we see a general increase of $10-15\%$ for all of the rear vehicle drag coefficients. This highlights that platooning interactions are stronger at higher Reynolds numbers. As This platoon exhibits inverted platooning conditions, the stronger influence of platooning has a negative effect on the rear vehicle however, for other platooning configurations the opposite could occur. This further underlines the importance of improving our understanding of the Reynolds number dependency of platooning as real world scenarios will occur at at even higher Reynolds numbers where the influence of platooning conditions are stronger.

A comparison of the front vehicles at each Reynolds number is less interesting. A slight decrease in drag coefficient of around 5% is seen for each case at $Re_H = 1.9 \cdot 10^5$ when compared to the $Re_H = 1.0 \cdot 10^5$ cases. For the isolated Ahmed vehicle, drag coefficient decreases as Reynolds number increases (as discussed in section 2.1); this result follows that trend.

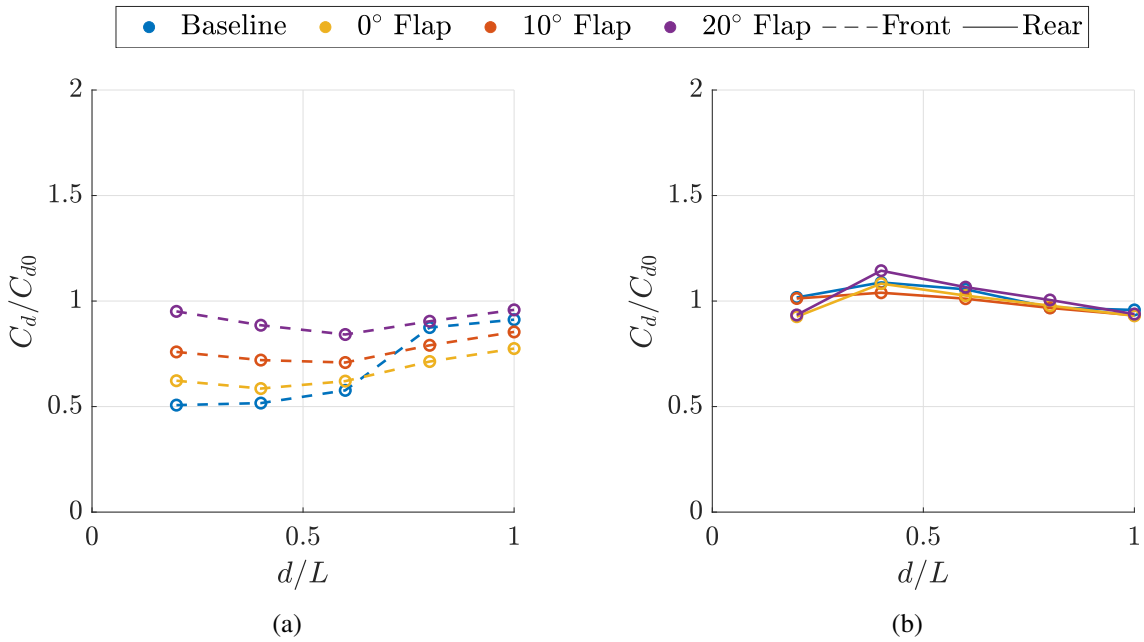

Figure C.1: Comparison of normalised drag coefficient between the baseline platoon and the platoon with a 25*mm* flap as flow control for a range of flap angles over a range of inter-vehicle distances at a Reynolds number of $1.0 \cdot 10^5$. (a) Front vehicle in the platoon; (b) Rear vehicle in the platoon

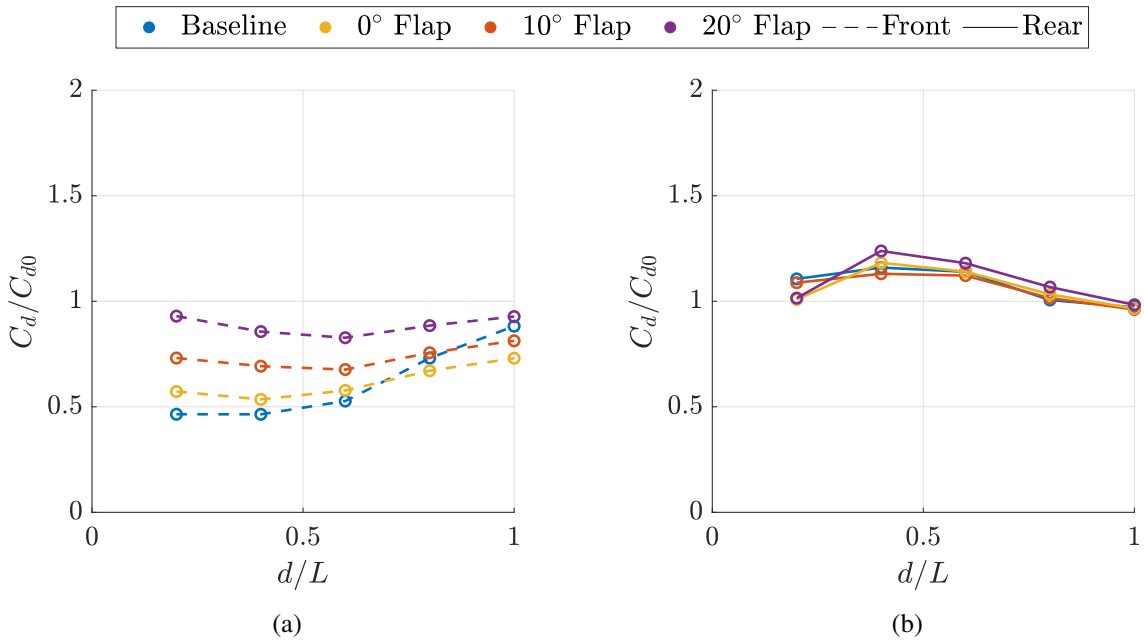

Figure C.2: Comparison of normalised drag coefficient between the baseline platoon and the platoon with a 25*mm* flap as flow control for a range of flap angles over a range of inter-vehicle distances at a Reynolds number of $1.9 \cdot 10^5$. (a) Front vehicle in the platoon; (b) Rear vehicle in the platoon

Bibliography

[1] S R Ahmed, G Ramm, and G Faltin. Some Salient Features of the Time-Averaged Ground Vehicle. *SAE Transactions*, 93:473–503, 1984.

[2] W. Meile, G. Brenn, A. Reppenhagen, B. Lechner, and A. Fuchs. Experiments and numerical simulations on the aerodynamics of the ahmed body. *CFD Letters*, 3(1):32–38, 2011.

[3] Hermann Lienhart and Stefan Becker. Flow and turbulence structure in the wake of a simplified car model. *SAE transactions*, pages 785–796, 2003.

[4] Juan D'Adamo, Roberto Sosa, and Guillermo Artana. Active control of a backward facing step flow with plasma actuators. *Journal of Fluids Engineering, Transactions of the ASME*, 136(12), 12 2014.

[5] United Nations. Paris agreement. https://unfccc.int/process-and-meetings/the-paris-agreement/the-paris-agreement, 12 2015. Date accessed: 11 February 2023.

[6] Scottish Parliament. Climate change (emissions reduction targets) (Scotland) Act 2019. https://www.legislation.gov.uk/asp/2019/15/enacted, October 2019. Accessed on 9 February 2023.

[7] Office for National Statistics. Road transport and air emissions. https://www.ons.gov.uk/economy/environmentalaccounts/articles/roadtransportandairemissions/2019-09-16, 2019. Date accessed: 11 February 2023.

[8] Office for National Statistics - Department for Business, Energy and Industrial Strategy. Provisional uk greenhouse gas emissions national statistics 2021. https://www.gov.uk/government/statistics/provisional-uk-greenhouse-gas-emissions-national-statistics-2021, 2022. Date accessed: 11 February 2023.

[9] Xiao-Yun Lu and Steven E Shladover. Automated truck platoon control and field test. *Road Vehicle Automation*, pages 247–261, 2014.

[10] Stanley W Smith, Yeojun Kim, Jacopo Guanetti, Ruolin Li, Roya Firoozi, Bruce Wootton, Alexander A Kurzhanskiy, Francesco Borrelli, Roberto Horowitz, and Murat Arcak.

Improving urban traffic throughput with vehicle platooning: Theory and experiments. *IEEE Access*, 8:141208–141223, 2020.

[11] Highways Agency and DVSA. Highways Agency warns tailgaters that 'only a fool breaks the 2-second rule' . https://www.gov.uk/government/news/highways-agency-warns-tailgaters-that-only-a-fool-breaks-the-two-second-rule, 5 2014. Date accessed: 11 February 2023.

[12] Gereon Meyer and Sven Beiker. *Road vehicle automation*, volume 201955. Springer, 2019.

[13] Tom Robinson, Eric Chan, and Erik Coelingh. Operating platoons on public motorways: An introduction to the sartre platooning programme. In *17th world congress on intelligent transport systems*, volume 1, page 12, 2010.

[14] Eric Chan. Overview of the SARTRE platooning project: Technology leadership brief. SAE Technical Paper Series 2012-01-9019, Society of Automotive Engineers, 2012.

[15] Kuo Yun Liang, Jonas Martensson, and Karl H. Johansson. Experiments on platoon formation of heavy trucks in traffic. In *IEEE Conference on Intelligent Transportation Systems, Proceedings, ITSC*, pages 1813–1819. Institute of Electrical and Electronics Engineers Inc., 12 2016.

[16] Kuo Yun Liang, Jonas Mårtensson, and Karl H. Johansson. Heavy-Duty Vehicle Platoon Formation for Fuel Efficiency. *IEEE Transactions on Intelligent Transportation Systems*, 17(4):1051–1061, 2016.

[17] The Engineer. Mercedes Benz debuts truck platooning system with automated airfield snow clearance demo. https://www.theengineer.co.uk/content/news/mercedes-benz-debuts-truck-platooning-system-with-automated-airfield-snow-clearance-demo/, October 2017. Accessed on 9 February 2023.

[18] Johannes Törnell, Simone Sebben, and Per Elofsson. Experimental investigation of a two-truck platoon considering inter-vehicle distance, lateral offset and yaw. *Journal of Wind Engineering and Industrial Aerodynamics*, 213:104596, 2021.

[19] Fred Browand, Charles Radovich, Tai Merzel, Dennis Plocher, Rose McCallen, Kambiz Salari, Jason Ortega, Paul Castellucci, John Paschkewitz, Craig Eastwood, Anthony Leonard, Mike Rubel, James Ross, J. T. Heineck, Stephen Walker, Bruce Storms, W. David Pointer, Christopher Roy, David Whitfield, Ramesh Pankajakshan, Lafayette Taylor, Kidambi Sreenivas, Robert Englar, Larry Dechant, and Basil Hassan. DOE's effort to reduce truck aerodynamic drag through joint experiments and computations. In

2005 SAE Commercial Vehicle Engineering Conference. SAE International, November 2005.

[20] Ekene F Ozioko, Julian Kunkel, and Fredric Stahl. Road intersection coordination scheme for mixed traffic (human driven and driver-less vehicles): A systematic review. In *Intelligent Computing: Proceedings of the 2022 Computing Conference, Volume 3*, pages 67–94. Springer, 2022.

[21] BBC News. First full-size driverless bus trials to begin in Scotland. https://www.bbc.co.uk/news/uk-scotland-edinburgh-east-fife-61216302, 4 2022. Date accessed: 11 February 2023.

[22] Department for Transport. Rules on safe use of automated vehicles on GB roads. https://www.gov.uk/government/consultations/safe-use-rules-for-automated-vehicles-av/rules-on-safe-use-of-automated-vehicles-on-gb-roads, 2022. Date accessed: 11 February 2023.

[23] Michael Zabat, Nick Stabile, Stefano Frascaroli, and Frederick Browand. The Aerodynamic Performance of Platoons: Final Report. 1995.

[24] Brian R McAuliffe, Mark Croken, Mojtaba Ahmadi-baloutaki, and Arash Raeesi. Fuel-economy testing of a three-vehicle truck platooning system. *National Research Council Canada. Aerospace. Aerodynamica Laboratory*, page 64, 2017.

[25] John Nuszkowski, Harlan Smith, Michael McKinney, Nicholas McMahan, Benjamin Wilder, Eric Boehringer, Blair Clarkson, Cutler Littleton, and Kyle Parker. Increasing the on-road fuel economy by trailing at a safe distance. *Proceedings of the Institution of Mechanical Engineers, Part D: Journal of Automobile Engineering*, 231(9):1303–1311, 8 2017.

[26] Department for Transport and Driver and Vehicle Standards Agency. The highway code. https://www.highwaycodeuk.co.uk/, 2022. Date accessed: 11 February 2023.

[27] Simon Watkins and Gioacchino Vino. The effect of vehicle spacing on the aerodynamics of a representative car shape. *Journal of Wind Engineering and Industrial Aerodynamics*, 96(6-7):1232–1239, 6 2008.

[28] Geoff Le Good, Max Resnick, Peter Boardman, and Brian Clough. Effects on the aerodynamic characteristics of vehicles in longitudinal proximity due to changes in style. SAE Technical Paper Series 2018-37-0018, Society of Automotive Engineers, 2018.

[29] Jeff Howell and Derek Hickman. The Influence of Ground Simulation on the Aerodynamics of a Simple Car Model. In *SAE Technical Papers*, number 970134, 2 1997.

[30] John Davis. *Wind Tunnel Investigation of Road Vehicle Wakes*. PhD thesis, University of London, 1982.

[31] American Society of Mechanical Engineers. *Experimental and Numerical Investigation of the DrivAer Model*, volume Volume 1: Symposia, Parts A and B of *Fluids Engineering Division Summer Meeting*, 07 2012.

[32] Dirk Wieser, Hanns-Joachim Schmidt, Stefan Mueller, Christoph Strangfeld, Christian Nayeri, and Christian Paschereit. Experimental comparison of the aerodynamic behavior of fastback and notchback drivaer models. *SAE International Journal of Passenger Cars-Mechanical Systems*, 7(2014-01-0613):682–691, 2014.

[33] Michael John, Stefan-Daniel Buga, Indro Monti, Timo Kuthada, Felix Wittmeier, Markus Gray, and Vincent Laurent. Experimental and numerical study of the drivaer model aerodynamics. SAE Technical Paper Series 2018-01-0741, Society of Automotive Engineers, 2018.

[34] T Gheyssens and G Van Raemdonck. Effect of the Frontal Edge Radius in a Platoon of Bluff Bodies. *SAE Int. J. Commer: Veh.*, 9(2):371–380, 2016.

[35] Kin Hing Lo and Konstantinos Kontis. Flow around an articulated lorry model. *Experimental Thermal and Fluid Science*, 82:58–74, 2017.

[36] Mingzhe He, Shen Huo, Hassan Hemida, Frederick Bourriez, Francis H. Robertson, David Soper, Mark Sterling, and Chris Baker. Detached eddy simulation of a closely running lorry platoon. *Journal of Wind Engineering and Industrial Aerodynamics*, 193:103956, 2019.

[37] Xiao Tian Zhang, Francis H. Robertson, David Soper, Hassan Hemida, and Shi Di Huang. Investigation of the aerodynamic phenomena associated with a long lorry platoon running through a tunnel. *Journal of Wind Engineering and Industrial Aerodynamics*, 210:104514, 3 2021.

[38] Geoffrey M Le Good and Kevin P Garry. On the Use of Reference Models in Automotive Aerodynamics. *SAE Technical Paper Series*, (2004-01-1308):246, 2004.

[39] Emmanuel Guilmineau. Computational study of flow around a simplified car body. *Journal of Wind Engineering and Industrial Aerodynamics*, 96(6-7):1207–1217, 2008.

[40] Tural Tunay, Bulent Yaniktepe, and Besir Sahin. Computational and experimental investigations of the vortical flow structures in the near wake region downstream of the Ahmed vehicle model. *Journal of Wind Engineering and Industrial Aerodynamics*, 159:48–64, 12 2016.

[41] Maryam Mirzaei, Siniša Krajnović, and Branislav Basara. Partially-Averaged navier-stokes simulations of flows around two different ahmed bodies. *Computers and Fluids*, 117:273–286, 8 2015.

[42] Ilhan Bayraktar, Drew Landman, and Oktay Baysal. Experimental and Computational Investigation of Ahmed Body for Ground Vehicle Aerodynamics. SAE Technical Paper Series 2001-01-2742, Society of Automotive Engineers, 2001.

[43] M. Corallo, J. Sheridan, and M. C. Thompson. Effect of aspect ratio on the near-wake flow structure of an Ahmed body. *Journal of Wind Engineering and Industrial Aerodynamics*, 147:95–103, 12 2015.

[44] M. Grandemange, M. Gohlke, and O. Cadot. Turbulent wake past a three-dimensional blunt body. Part 1. Global modes and bi-stability. *Journal of Fluid Mechanics*, 722:51–84, 2013.

[45] Giancarlo Pavia, Martin Passmore, and Costantino Sardu. Evolution of the bi-stable wake of a square-back automotive shape. *Experiments in Fluids*, 59(1), 1 2018.

[46] M. Grandemange, O. Cadot, A. Courbois, V. Herbert, D. Ricot, T. Ruiz, and R. Vigneron. A study of wake effects on the drag of Ahmed's squareback model at the industrial scale. *Journal of Wind Engineering and Industrial Aerodynamics*, 145:282–291, 2015.

[47] B. F. Zhang, Y. Zhou, and S. To. Unsteady flow structures around a high-drag Ahmed body. *Journal of Fluid Mechanics*, 777:291–326, 8 2015.

[48] Lars Larsson, Leif Broberg, and Carl-Erik Janson. A zonal method for predicting external automobile aerodynamics. *SAE transactions*, pages 704–721, 1991.

[49] Stephen B Pope and Stephen B Pope. *Turbulent flows*. Cambridge university press, 2000.

[50] Eric Serre, Matthieu Minguez, Richard Pasquetti, Emmanuel Guilmineau, Gan Bo Deng, Michael Kornhaas, Michael Schäfer, Jochen Fröhlich, Christof Hinterberger, and Wolfgang Rodi. On simulating the turbulent flow around the ahmed body: A french–german collaborative evaluation of les and des. *Computers & Fluids*, 78:10–23, 2013.

[51] Philippe R. Spalart, W-H Jou, Michael Strelets, and Steven Allmaras. Comments on the Feasibility of LES for Wings, and on a Hybrid RANS/LES Approach. In *Advances in DES/LES*, 1997.

[52] N. Ashton, A. West, S. Lardeau, and A. Revell. Assessment of RANS and DES methods for realistic automotive models. *Computers and Fluids*, 128:1–15, 2016.

[53] Emmanuel Guilmineau, Ganbo Deng, Alban Leroyer, P Queutey, J Wackers, and Michel Visonneau. Assessment of rans and des methods for the ahmed body. In *ECCOMAS Congress 2016-VII European Congress on Computational Methods in Applied Sciences and Engineering*, 2016.

[54] E. Guilmineau, G. B. Deng, A. Leroyer, P. Queutey, M. Visonneau, and J. Wackers. Assessment of hybrid RANS-LES formulations for flow simulation around the Ahmed body. *Computers and Fluids*, 176:302–319, 11 2018.

[55] N. Ashton and A. Revell. Key factors in the use of DDES for the flow around a simplified car. *International Journal of Heat and Fluid Flow*, 54:236–249, 2015.

[56] Jean François Beaudoin and Jean Luc Aider. Drag and lift reduction of a 3D bluff body using flaps. *Experiments in Fluids*, 44(4):491–501, 4 2008.

[57] Robert J Englar. Development of pneumatic aerodynamic devices to improve the performance, economics, and safety of heavy vehicles. Technical report, Georgia Tech Research Institute, Atlanta, GA (US), 2000.

[58] Mohammad El-Alti, Valery Chernoray, Per Kjellgren, Linus Hjelm, and Lars Davidson. Computations and full-scale tests of active flow control applied on a volvo truck-trailer. In *The Aerodynamics of Heavy Vehicles III: Trucks, Buses and Trains*, pages 253–267. Springer, 2015.

[59] Erik Wassen and Frank Thiele. Road vehicle drag reduction by combined steady blowing and suction. In *39th AIAA Fluid Dynamics Conference*, page 4174, 2009.

[60] Charles-Henri Bruneau, Emmanuel Creusé, Delphine Depeyras, Patrick Gilliéron, and Iraj Mortazavi. Active procedures to control the flow past the ahmed body with a 25° rear window. *International Journal of Aerodynamics*, 1(3-4):299–317, 2011.

[61] Bahram Khalighi, S Zhang, C Koromilas, SR Balkanyi, Luis P Bernal, G Iaccarino, and P Moin. Experimental and computational study of unsteady wake flow behind a bluff body with a drag reduction device. *SAE transactions*, pages 1209–1222, 2001.

[62] Jie Tian, Yingchao Zhang, Hui Zhu, and Hongwei Xiao. Aerodynamic drag reduction and flow control of ahmed body with flaps. *Advances in Mechanical Engineering*, 9(7):1687814017711390, 2017.

[63] N. A. Siddiqui and M. A. Chaab. A Simple Passive Device for the Drag Reduction of an Ahmed Body. *Journal of Applied Fluid Mechanics*, 14(1):147–164, 1 2021.

[64] Ankush Raina, G. A. Harmain, and Mir Irfan Ul Haq. Numerical investigation of flow around a 3D bluff body using deflector plate. *International Journal of Mechanical Sciences*, 131-132:701–711, 10 2017.

[65] Grégoire Fourrié, Laurent Keirsbulck, Larbi Labraga, and Patrick Gilliéron. Bluff-body drag reduction using a deflector. *Experiments in Fluids*, 50(2):385–395, 2 2011.

[66] G. Pujals, S. Depardon, and C. Cossu. Drag reduction of a 3D bluff body using coherent streamwise streaks. *Experiments in Fluids*, 49(5):1085–1094, 2010.

[67] Siniša Krajnović. Large eddy simulation exploration of passive flow control around an Ahmed body. *Journal of Fluids Engineering, Transactions of the ASME*, 136(12), 12 2014.

[68] Babak Mohammadikalakoo, Paolo Schito, and Mahmoud Mani. Passive flow control on ahmed body by rear linking tunnels. *Journal of Wind Engineering and Industrial Aerodynamics*, 205:104330, 2020.

[69] R. Ruisi, H. Zare-Behtash, K. Kontis, and R. Erfani. Active flow control over a backward-facing step using plasma actuation. *Acta Astronautica*, 126:354–363, 9 2016.

[70] Hürrem Akbiyik, Hakan Yavuz, and Yahya Erkan Akansu. A study on the plasma actuator electrode geometry configurations for improvement of the aerodynamic performance of an airfoil. *Journal of Mechanical Engineering*, 64(12):719–725, 2018.

[71] A R Hoskinson and N Hershkowitz. Differences between dielectric barrier discharge plasma actuators with cylindrical and rectangular exposed electrodes. *Journal of Physics D: Applied Physics*, 43(6):065205, 2 2010.

[72] Mark Riherd and Subrata Roy. Serpentine geometry plasma actuators for flow control. *Journal of applied physics*, 114(8):083303, 2013.

[73] Arnob Das Gupta and Subrata Roy. Effect of plasma actuator control parameters on a transitional flow. *Journal of Physics D: Applied Physics*, 51(13), 3 2018.

[74] R. Joussot, A. Leroy, R. Weber, H. Rabat, S. Loyer, and D. Hong. Plasma morphology and induced airflow characterization of a DBD actuator with serrated electrode. *Journal of Physics D: Applied Physics*, 46(12), 2013.

[75] Zhifeng Liu, Mingming Zhang, and Lianze Wang. Investigation on 3D flow field induced by a plasma actuator with serrated electrode. *Science Bulletin*, 61(6):481–487, 3 2016.

[76] Dongri Kim, Hyungrok Do, and Haecheon Choi. Drag reduction on a three-dimensional model vehicle using a wire-to-plate DBD plasma actuator. *Experiments in Fluids*, 61(6), 6 2020.

[77] Subrata Roy and Chin-Cheng Wang. Bulk flow modification with horseshoe and serpentine plasma actuators. *Journal of Physics D: Applied Physics*, 42(3):032004, 2008.

[78] Julie A. Vernet, Ramis Örlü, David Söderblom, Per Elofsson, and P. Henrik Alfredsson. Plasma Streamwise Vortex Generators for Flow Separation Control on Trucks: A Proof-of-concept Experiment. *Flow, Turbulence and Combustion*, 100(4):1101–1109, 6 2018.

[79] R. J. Durscher and S. Roy. Three-dimensional flow measurements induced from serpentine plasma actuators in quiescent air. *Journal of Physics D: Applied Physics*, 45(3), 1 2012.

[80] Mark Riherd and Subrata Roy. Damping tollmien–schlichting waves in a boundary layer using plasma actuators. *Journal of Physics D: Applied Physics*, 46(48):485203, 2013.

[81] Mark Riherd and Subrata Roy. Stabilization of boundary layer streaks by plasma actuators. *Journal of Physics D: Applied Physics*, 47(12):125203, 2014.

[82] Subrata Roy, Pengfei Zhao, Arnob DasGupta, and Jignesh Soni. Dielectric barrier discharge actuator for vehicle drag reduction at highway speeds. *Aip Advances*, 6(2):025322, 2016.

[83] Rasool Erfani, Tohid Erfani, Sergei V. Utyuzhnikov, and Konstantinos Kontis. Optimisation of multiple encapsulated electrode plasma actuator. *Aerospace Science and Technology*, 26(1):120–127, 4 2013.

[84] Flint O. Thomas, Thomas C. Corke, Muhammad Iqbal, Alexey Kozlov, and David Schatzman. Optimization of dielectric barrier discharge plasma actuators for active aerodynamic flow control. *AIAA Journal*, 47(9):2169–2178, 9 2009.

[85] FF Rodrigues, JC Pascoa, and Michele Trancossi. Experimental analysis of alternative dielectric materials for dbd plasma actuators. In *ASME International Mechanical Engineering Congress and Exposition*, volume 52002, page V001T03A005. American Society of Mechanical Engineers, 2018.

[86] Cameron Tropea, Alexander L Yarin, John F Foss, et al. *Springer handbook of experimental fluid mechanics*, volume 1. Springer, 2007.

[87] Romain Futrzynski and Gunilla Efraimsson. Effect of a SDBD on the drag of a half-submerged cylinder in crossflow. In *Fluids Engineering Division Summer Meeting*, volume 1C of *Proceedings of the 4th Joint US-European Fluids Engineering Division Summer Meeting collocated with the ASME*, August 2014.

[88] Samuel Gottfarb Bart. Optimal placement of plasma actuators on trucks: A drag reduction study using adjoint methods, 2016.

[89] Pierric Joseph, Xavier Amandolèse, and Jean Luc Aider. Drag reduction on the 25° slant angle Ahmed reference body using pulsed jets. *Experiments in Fluids*, 52(5):1169–1185, 5 2012.

[90] B. F. Zhang, K. Liu, Y. Zhou, S. To, and J. Y. Tu. Active drag reduction of a high-drag Ahmed body based on steady blowing. *Journal of Fluid Mechanics*, 856:351–396, 12 2018.

[91] Bing xin Wang, Zhi gang Yang, and Hui Zhu. Active flow control on the 25°Ahmed body using a new unsteady jet. *International Journal of Heat and Fluid Flow*, 79:108459, 10 2019.

[92] Dongri Kim, Hoon Lee, Wook Yi, and Haecheon Choi. A bio-inspired device for drag reduction on a three-dimensional model vehicle. *Bioinspiration and Biomimetics*, 11(2), 3 2016.

[93] Haecheon Choi, Woo-Pyung Jeon, and Jinsung Kim. Control of flow over a bluff body. *Annu. Rev. Fluid Mech.*, 40:113–139, 2008.

[94] Ben L. Clapperton and Peter W. Bearman. Control of circular cylinder flow using distributed passive jets. *Journal of Fluid Mechanics*, 848:1157–1178, 8 2018.

[95] Anthony R. Oxlade, Jonathan F. Morrison, Ala Qubain, and Georgios Rigas. High-frequency forcing of a turbulent axisymmetric wake. *Journal of Fluid Mechanics*, 770:305–308, 2015.

[96] Kin-Hing Lo, Rengarajan Sriram, and Konstantinos Kontis. Wake flow characteristics over an articulated lorry model with/without ac-dbd plasma actuation. *Applied Sciences*, 9(12), 2019.

[97] Louis N. Cattafesta and Mark Sheplak. Actuators for active flow control. *Annual Review of Fluid Mechanics*, 43:247–272, 1 2011.

[98] Michael M Wojewodka, Craig White, Shahrokh Shahpar, and Konstantinos Kontis. A review of flow control techniques and optimisation in s-shaped ducts. *International Journal of Heat and Fluid Flow*, 74:223–235, 2018.

[99] Lun Tsuei and Ömer Savaş. Transient aerodynamics of vehicle platoons during in-line oscillations. *Journal of Wind Engineering and Industrial Aerodynamics*, 89(13):1085–1111, 2001.

[100] Kenji Tadakuma, Mitsuhisa Shida, Kazuhiro Maeda, et al. Aerodynamic drag reduction in vehicle platooning-effect on lateral position of following vehicle. In *18th ITS World CongressTransCoreITS AmericaERTICO-ITS EuropeITS Asia-Pacific*, 2011.

[101] K Tadakuma, T Doi, M Shida, and K Maeda. Aerodynamic Drag Reduction in Vehicle-Platoon Driving (second Report) - Effect of Several-Vehicle Platooning. 47(1):195–201, 2016.

[102] David Uystepruyst and Siniša Krajnović. LES of the flow around several cuboids in a row. *International Journal of Heat and Fluid Flow*, 44:414–424, 12 2013.

[103] Hesham Ebrahim and Robert Dominy. Wake and surface pressure analysis of vehicles in platoon. *Journal of Wind Engineering and Industrial Aerodynamics*, 201, 6 2020.

[104] Francis H. Robertson, Frederick Bourriez, Mingzhe He, David Soper, Chris Baker, Hassan Hemida, and Mark Sterling. An experimental investigation of the aerodynamic flows created by lorries travelling in a long platoon. *Journal of Wind Engineering and Industrial Aerodynamics*, 193, 10 2019.

[105] F. H. Robertson, D. Soper, and C. Baker. Unsteady aerodynamic forces on long lorry platoons. *Journal of Wind Engineering and Industrial Aerodynamics*, 209:104481, 2 2021.

[106] Bert Blocken, Yasin Toparlar, and Thomas Andrianne. Aerodynamic benefit for a cyclist by a following motorcycle. *Journal of Wind Engineering and Industrial Aerodynamics*, 155:1–10, 8 2016.

[107] Bert Blocken, Yasin Toparlar, Thijs van Druenen, and Thomas Andrianne. Aerodynamic drag in cycling team time trials. *Journal of Wind Engineering and Industrial Aerodynamics*, 182:128–145, 11 2018.

[108] David Uystepruyst and Siniša Krajnović. Numerical simulation of the transient aerodynamic phenomena induced by passing manoeuvres. *Journal of Wind Engineering and Industrial Aerodynamics*, 114:62–71, 2013.

[109] Maryam Mirzaei and Siniša Krajnović. Large Eddy Simulations of flow around two Generic vehicles in a platoon. In *5th International Conference on Jets, Wakes and Seperatwed Flows*, volume 185, pages 283–288. Springer Science and Business Media, LLC, 2016.

[110] Renata Gnatowska and Marcin Sosnowski. The influence of distance between vehicles in platoon on aerodynamic parameters. In *EPJ Web of Conferences*, volume 180, page 02030. EDP Sciences, 6 2018.

[111] Charles Henri Bruneau, Khodor Khadra, and Iraj Mortazavi. Flow analysis of square-back simplified vehicles in platoon. *International Journal of Heat and Fluid Flow*, 66:43–59, 8 2017.

[112] Jianbin Luo, Ke Mi, Dongli Tan, Zhiqing Zhang, Mingsen Li, Jun Qing, and Huiqiong Huang. Investigation of the Aerodynamic Characteristics of Platoon Vehicles Based on Ahmed Body. *Shock and Vibration*, 2022, 2022.

[113] Fudhail Abdul Munir, Muhammad Najhi Fauzi, and Ridhwan Jumaidin. Numerical Study of The Effects of Vehicle Arrangement on Aerodynamics Resistance. *Journal of Advanced Research in Fluid Mechanics and Thermal Sciences*, 98(1):67–72, 2022.

[114] Michele Segata, Andrea Stedile, and Renato Lo Cigno. Modeling Slipstreaming Effects in Vehicle Platoons. In *IEEE Vehicular Networking Conference, VNC*, volume 2020-December. IEEE Computer Society, 12 2020.

[115] Geoffrey Le Good, Peter Boardman, Max Resnick, and Brian Clough. An investigation of aerodynamic characteristics of three bluff bodies in close longitudinal proximity. In *SAE Technical Papers*, volume 2019-April. SAE International, 4 2019.

[116] James MacAskill, Geoffrey Le Good, and Remus Cirstea. An investigation of aerodynamic characteristics of two bluff bodies in close longitudinal proximity-sensitivity to front-end geometry. Technical report, SAE Technical Paper, 2022.

[117] Hesham Ebrahim and Robert Dominy. The effect of afterbody geometry on passenger vehicles in platoon. *Energies*, 14(22), 11 2021.

[118] Ivo Džijan, Aleksandar Pašić, Andrija Buljac, and Hrvoje Kozmar. Aerodynamic characteristics of two slipstreaming race cars. *Journal of Mechanical Science and Technology*, 35(1):179–186, 1 2021.

[119] Maryam Mirzaei and Siniša Krajnović. Numerical study of aerodynamic interactions in a homogeneous multi-vehicle formation. In *Proceedings of the 5th International Conference on Jets, Wakes and Seperated Flows*, volume 185, pages 289–294. Springer Science and Business Media, LLC, 2016.

[120] Hesham M Ebrahim, Robert G Dominy, and Pak S Leung. Evaluation of Vehicle Platooning Aerodynamics using Bluff Body Wake Generators and CFD. In *International Conference for Students on Applied Engineering (ICSAE)*, pages 218–223, Newcastle Upon Tyne, UK, 2016.

[121] Siemens Digital Industries Software. Simcenter STAR-CCM+ User Guide, version 15.04.010. In *Simulating Physics*, pages 3067–3200. Siemens, 2021.

[122] J. Ha, S. Jeong, and S. Obayashi. Drag reduction of a pickup truck by a rear downward flap. *International Journal of Automotive Technology*, 12(3):369–374, June 2011.

[123] Zulfaa Mohamed-Kassim and Antonio Filippone. Fuel savings on a heavy vehicle via aerodynamic drag reduction. *Transportation Research Part D: Transport and Environment*, 15(5):275–284, 2010.

[124] EN and BS. EN 1991-1-4: Eurocode 1: Actions on structures - Part 1-4: General actions - Wind actions. Technical report, 1991.

[125] W H Hucho, L J Janssen, and G Schwartz. The Wind Tunnel's Ground Plane Boundary Layer - Its Interference with the Flow Underneath Cars. *SAE Transactions*, 84:380–389, 1975.

[126] Jewel B Barlow, William H Rae, and Alan Pope. *Low-Speed Wind Tunnel Testing*. Wiley, New York, 1999.

[127] Laura M Hudy, Ahmed M Naguib, and William M Humphreys Jr. Wall-pressure-array measurements beneath a separating/reattaching flow region. *Physics of Fluids*, 15(3):706–717, 2003.

[128] Ludwig Prandtl. Motion of fluids with very little viscosity. Technical report, National Advisory Committee for Aeronautics, 1928. [German to English translation of "Ueber Flussigkeitsbewegungg bei sehr kleiner reibung" from "Vier Abhandlungon zur Hydrodynamik und Aerodynamik" pp. 1-8, Göttingen, 1904].

[129] Charles Borden Johnson and Dennis M. Bushnell. *Power-law velocity-profile-exponent variations with Reynolds number, wall cooling, and Mach number in a turbulent boundary layer*. National Aeronautics and Space Administration, 1969.

[130] David J. Pickles, Daniele Zagaglia, Angela Busse, and Richard B. Green. Vortex ring state of a shrouded rotor: an experimental survey. *Experiments in Fluids*, 64(4):69, 2023.

[131] RICHARD B. GREEN, ERIC A. GILLIES, and RICHARD E. BROWN. The flow field around a rotor in axial descent. *Journal of Fluid Mechanics*, 534:237–261, 2005.

[132] KP Garry, KR Cooper, A Fediw, SB Wallis, and DJ Wilsden. The effect on aerodynamic drag of the longitudinal position of a road vehicle model in a wind tunnel test section. *SAE transactions*, pages 478–489, 1994.

[133] F. R. Menter. Two-equation eddy-viscosity turbulence models for engineering applications. *AIAA Journal*, 32(8):1598–1605, 1994.

[134] Eric Moreau. Airflow control by non-thermal plasma actuators. *Journal of physics D: applied physics*, 40(3):605, 2007.

[135] Arvind Santhanakrishnan and Jamey D Jacob. Flow control with plasma synthetic jet actuators. *Journal of Physics D: Applied Physics*, 40(3):637, 2007.

[136] A Labergue, E Moreau, N Zouzou, and G Touchard. Separation control using plasma actuators: application to a free turbulent jet. *Journal of Physics D: Applied Physics*, 40(3):674, 2007.

[137] R. Erfani, H. Zare-Behtash, and K. Kontis. Plasma actuator: Influence of dielectric surface temperature. *Experimental Thermal and Fluid Science*, 42:258–264, 2012.